The Thesis Committee for Ryan Lee Harbor
Certifies that this is the approved version of the following thesis:

Facies Characterization and Stratigraphic Architecture of Organic-Rich Mudrocks, Upper Cretaceous Eagle Ford Formation, South Texas

APPROVED BY

SUPERVISING COMMITTEE:

Supervisor:

William L. Fisher

Co-Supervisor:

Stephen C. Ruppel

Ronald J. Steel

Facies Characterization and Stratigraphic Architecture of Organic-Rich Mudrocks, Upper Cretaceous Eagle Ford Formation, South Texas

by

Ryan Lee Harbor, B.S.

Thesis

Presented to the Faculty of the Graduate School of

The University of Texas at Austin

in Partial Fulfillment

of the Requirements

for the Degree of

Masters of Science in Geological Sciences

The University of Texas at Austin

August 2011

Acknowledgements

I would like to acknowledge the help of my supervisor, Dr. Stephen Ruppel, for his continued support and thoughtful guidance throughout this study. I would also like to thank the Jackson School of Geosciences and Bureau of Economic Geology for providing the resources, facilities, and support for me to pursue my interest in my graduate work. Thank you to the industry members of the MSRL Consortium for their helping fund this research and for their collaborative efforts during the duration of this study. Members include Anadarko, BP, Chesapeake, Chevron, Cima, Cimarex, ConocoPhilips, Cypress, Devon, Encana, EOG, EXCO, Husky, Marathon, Pangaea, Penn Virginia, Penn West, Pioneer, Shell, StatOil, Texas American Resources, The Unconventionals, US EnerCorp, Valence, and YPF. My gratitude is also due to Dr. Kitty Milliken, Dr. Bob Loucks, professor Charlie Kerans, Dr. Seay Nance, Dr. Scott Hamlin, and Tucker Hentz for their willingness to teach and help answer my many questions during the progression of this thesis. I would also like to offer a special thanks to ConocoPhillips for providing the SPIRIT scholarship program and sponsoring multiple trips that enriched my graduate student experience.

Abstract

Facies Characterization and Stratigraphic Architecture of Organic-Rich Mudrocks, Upper Cretaceous Eagle Ford Formation, South Texas

Ryan Lee Harbor, MSGeoSci

The University of Texas at Austin, 2011

Co-Supervisors: Stephen C. Ruppel and William L. Fisher

The Eagle Ford is a well-known source rock for both sandstone (Woodbine) and carbonate (Austin and Buda) hydrocarbon reservoirs in East and South Texas. Recent discoveries have demonstrated that source rocks, such as the Eagle Ford, are capable of producing significant volumes of gas and oil. At the same time, variations in well producibility indicate that these rocks, like conventional reservoirs, display considerable geological heterogeneity. Yet, only limited research has been published on the subsurface stratigraphy and character of Eagle Ford facies. Understanding the types, controls, and distribution of these heterogeneities requires in-depth rock-based studies.

In order to characterize Eagle Ford facies, 27 cores from 13 counties were investigated for rock textures, fabrics, sedimentary structures, and fossil assemblages. These studies were supported by light and electron microscopy as well as analysis of elemental chemistry and mineralogy. Regional subsurface stratigraphic correlations and facies distributions were defined using wireline logs calibrated from core studies.

In South Texas, the Eagle Ford Formation was deposited during a second-order transgressive/regressive cycle on the flooded, oxygen-restricted Comanche Shelf. Nine depositional facies consisting predominately of organic-rich, fine-grained (5.0 % TOC) to coarser-grained (3.05 % TOC) fabrics were identified. Facies developed in low-energy environments episodically interrupted by higher-energy, event sedimentation (current winnowing, cohesive and non-cohesive density flows, and turbidity flows). Locally, these rocks show evidence of early diagenetic recrystallization of calcite.

Concurrent water anoxia and organic matter preservation persisted locally into later Austin deposition, resulting in formation of a three-fold division of the Cenomanian-Coniacian Eagle Ford Formation. Common facies of lower and upper Eagle Ford members include (1) unlaminated, fissile, clay- and silica-rich, organic-rich mudrocks, (2) laminated, calcareous, organic-rich mudrocks, and (3) laminated, foraminifera- and peloid-rich, organic-rich packstones. The transitional Eagle Ford member consists of highly-cyclic (1) ripple-laminated, organic-rich wackestone (cycle base) and (2) burrowed, organic-lean lime wackestones (cycle top). Transitional Eagle Ford facies developed in oxygen-restricted, basinal depositional environments as distal equivalents to burrowed, foraminiferal lime wackestones of the Austin Formation.

Facies complexities in the Eagle Ford stem from complicated and interrelated processes of sediment production and distribution, diagenesis, and water column chemistry. Integrated core studies shed light on both controls of facies formation and their spatial distribution. These findings provide a framework for upscaling the fine-scale, heterogeneous character of shelfal Eagle Ford mudrocks; thus allowing development of predictive models into the distribution of key reservoir properties in the subsurface.

Table of Contents

List of Figures

List of Tables

INTRODUCTION

The Upper Cretaceous Eagle Ford of Central and South Texas is a mixed siliciclastic/carbonate system currently being explored for both oil and natural gas. Whereas previous studies have concentrated on the outcrop character (Dawson, 1997 & 2000) and wireline log stratigraphy (Surles, 1987) of the Eagle Ford in East Texas, heterogeneous facies distributions and minimal subsurface stratigraphic framework in South Texas necessitate further consideration. This study was undertaken as a core-based investigation into the character of subsurface facies variability and to define the stratigraphy of the Eagle Ford in areas actively being explored for oil and natural gas. The fundamental objectives were to (1) use subsurface cores to identify and describe depositional facies, (2) interpret paleoenvironments and active sediment delivery processes during Eagle Ford deposition, (3) characterize trends of key rock properties including textural fabric, mineralogy, elemental chemistry, TOC, and organic matter type (4) define regional subsurface stratigraphy, and (5) construct process-based depositional models allowing prediction into the relative distributions of source rock and reservoir character across the shelf.

The traditional association of organic-rich shales as monotonous, fine-grained successions that show little lithological variability does not apply to the Eagle Ford Formation. Heterogeneous facies assemblages identified in subsurface Eagle Ford cores include fine-grained clay to calcite-rich mudrocks, peloidal packstones, and skeletal lime wackestones to grain-dominated packstones. Each of these facies exhibit characteristic sedimentary structures resulting from primary sediment delivery processes coupled with evidence of post-depositional reworking and resedimentation. Bedding structures allow interpretations of the depositional controls that contributed to their formation. Study of

diagenetic features such as concretionary fabrics and calcite cements provides geochemical indicators into the processes active in Eagle Ford rocks extending from the sediment-water interface to those related to oxidation of organic matter in the subsurface.

The collection of subsurface cores utilized during this study cover a wide variety of depositional settings and geographic locations that afford a regional look into the lithologic variability present in the Eagle Ford Formation. Comparison of facies from proximal (highly variable lithologies) and distal (more uniform lithologies) depositional environments, coupled with along strike variability helps put subtle character changes seen in cores from producing zones into a broader perspective. In-depth rock studies help define and characterize facies types; but also identify important rock properties such as mineralogy, organic matter content, and organic matter type. Also, calibration of wireline logs with detailed rock descriptions allows better interpretations of the subsurface when core is not available.

This study is unique because it is the first rock-based study of the subsurface Eagle Ford with the purpose of modeling regional facies distributions and diagnosing controls on their formation. Construction of process-based mudrock depositional models will allow better understanding of how these systems formed in the ancient and depositional controls on rock properties. The distribution of key reservoirs properties is controlled by rock character, which results from depositional and diagenetic processes developed in varied paleoenvironments. Shifts in water-column chemistry also determine rock character through controlling production and preservation of organic matter; and regulating faunal abundance which in turn governs burrowing. In-depth rock studies such as this allow understanding of types, controls, and distributions of mudrock heterogeneity, thus providing predictive power into the spatial distribution of key reservoir properties.

OIL AND GAS RESOURCES OF THE EAGLE FORD

Unconventional shale resource plays are gaining importance and popularity as hydrocarbon reservoirs both within the United States and internationally. In Texas, the Barnett, Haynesville/Bossier, Woodford, and Pearsall Formations are established unconventional resource reservoirs with proven hydrocarbon production. The Eagle Ford is the most recent, large discovery in Texas and "is quickly becoming one of the hottest shale plays in North America" (Pioneer Natural Resources, 2011).

Exploration in the Eagle Ford began in late 2008 when Petrohawk Energy Corporation drilled a discovery well, the STS-2411 #1H, in LaSalle County, Texas (Durham, 2010). Initial flow from the well was 7.6 MMcf of gas and 250 barrels of condensate per day (Durham, 2010). This discovery area was soon designated part of the Hawkville Field, which now covers an area of 90 miles east-west and 15 miles north-south (Durham, 2010) in central La Salle and McMullen Counties.

Early exploration in the Eagle Ford spread from this LaSalle County discovery, centering in South Texas and extending from the Mexican border several counties into Texas (Durham, 2010). These early wells were commonly drilled in areas of high thermal maturity and dominantly produced dry gas or gas in conjunction with natural gas liquids. In early 2009, EOG Resources began producing from their own discovery well updip from the majority of previous exploration activity in the less mature oil window. The discovery and ability to produce oil from shale reservoirs with peak rates of 2,000 barrels per day and gas to oil ratios of 1,000-4,000 (Cherry, 2011) further increased interest in the Eagle Ford. Mark Papa, president of EOG resources, said that the discovery of oil in the Eagle Ford "represents one of the most significant oil discoveries in the lower 48 during the last 40 years" (EOG Resources, 2011).

Since its discovery in 2008, the Eagle Ford play area has expanded and continues to expand into East Texas; it now covers an area 400 miles long, 50 miles wide (Fig. 1), and possesses an average thickness of 250 ft (Railroad Commission of Texas, 2011). Hydrocarbon production in the Eagle Ford has shown established oil and dry gas windows (Fig.1). Wells drilled in intermediate zones between the oil and gas windows often leads to production of liquids-rich crude, condensate, and natural gas liquids.

Today, there are currently 16 fields producing from the Eagle Ford (Railroad Commission of Texas, 2011). Drilling permits in the Eagle Ford have increased rapidly from 26 in 2008 to 1,010 in 2010 and 743 already issued in the first 4 months of 2011 (Railroad Commission of Texas, 2011). As companies begin to bring these early wells into production, increases in production of oil, condensate, and gas have progressed rapidly (Fig. 2). With increased drilling activity and improvements in completion methods, these numbers will likely continue rapid grow into the foreseeable future.

Interest in the geology of the Eagle Ford arises from variable well flow and efforts to optimize production over large play areas. Oil and gas discoveries have led to rapid increases in drilling programs; yet, few published rock-based studies of the Eagle Ford inhibit the formation of accurate geologic models. One of the early aspects of the Eagle Ford that attracted attention was its high calcite content and its ability to propagate stimulated fracturing (Cherry, 2011). Rock-based studies allow identification and understanding of the controlling processes behind the distribution of key rock character, such as mineralogy. Documenting the geographic and stratigraphic extent of trends in subsurface rock character facilitates the formation of geologic models in three-dimensional space.

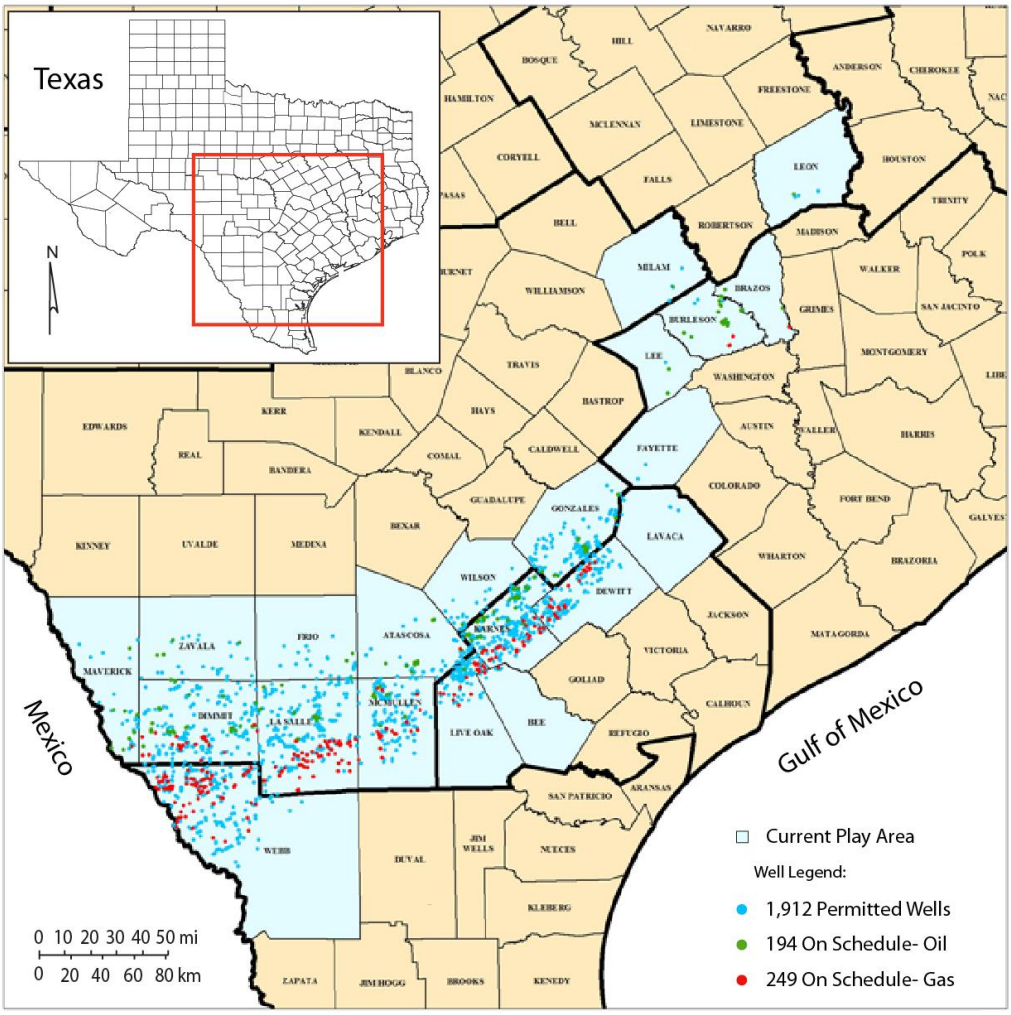

Figure 1: Map showing the location of Eagle Ford drilling activity and geographical coverage of the play area extending from the Texas/Mexico border into East Texas, as of June 2, 2011. Dark outlines represent Railroad Commission Districts. After Railroad Commission of Texas (2011).

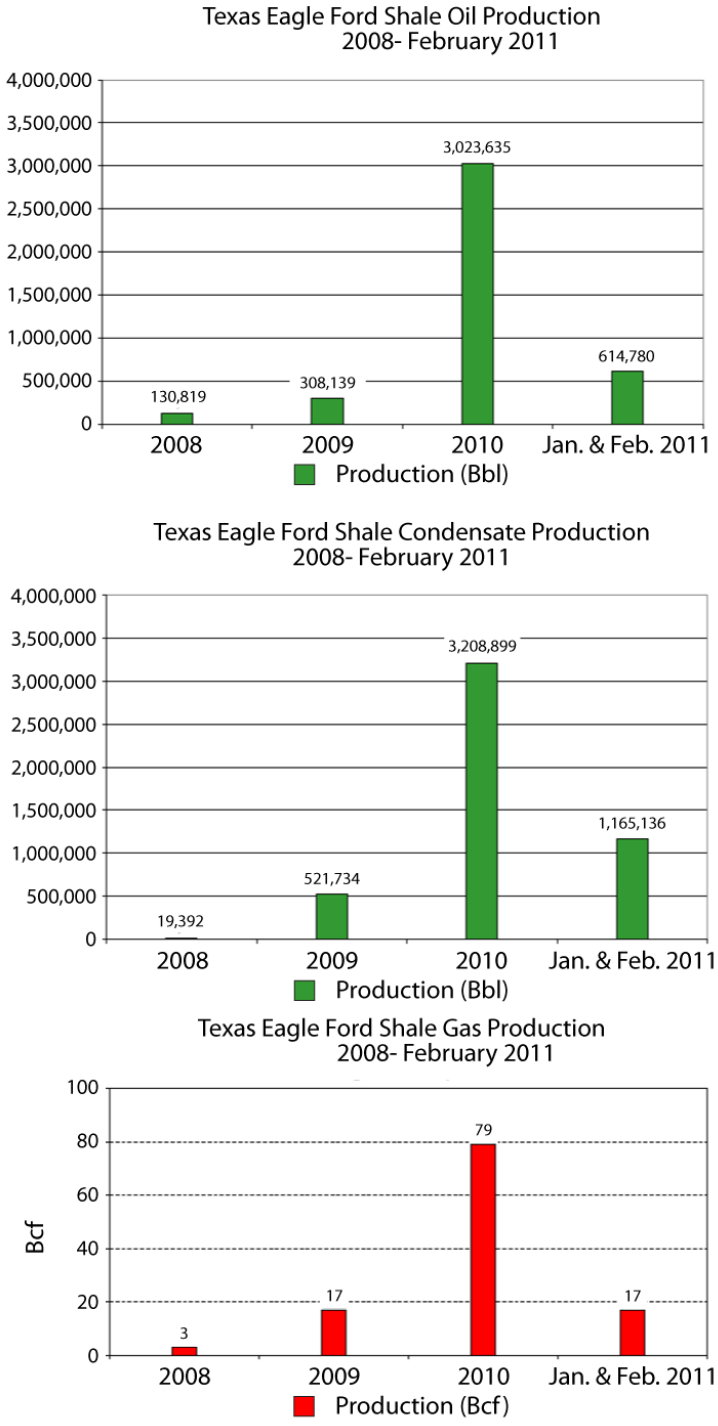

Figure 2: Beginning with its discovery in 2008, the Eagle Ford Formation has shown steady increases in production of oil, condensate, and natural gas in Texas. After Railroad Commission of Texas (2011).

STUDY LOCATION

The Eagle Ford Formation and time equivalent deposits are found in the subsurface as a continuous unit stretching across Texas (Fig. 3). Although most of the Eagle Ford possesses elevated organic matter content, thickness and rock character differences have led current exploration for oil and natural gas to concentrate southwest of the San Marcos Arch. These areas of current exploration and production were chosen as key localities when establishing the bounds of this project.

The study area encompasses subsurface shelfal Eagle Ford mudrocks (Fig. 4) extending from the shallow subsurface east of the Upper Cretaceous outcrop trend. The outcrop trend consists of a southwest-northeast trending belt consisting of the Buda, Eagle Ford, and Austin Formations in South Texas (Fig. 3). In East Texas, the Woodbine Group is included in this trend. Additional Eagle Ford equivalent strata in West Texas have received little published recognition and were not included in the identified outcrop trend. The outcrop trend and the shallow subsurface surrounding them offer valuable interpretation tools because they commonly exhibit sedimentation styles from the most proximally preserved Eagle Ford depositional settings.

From the outcrop trend, subsurface Eagle Ford rocks dip gently to the east and southeast toward the Gulf of Mexico Basin. The study area extends distally to the Late Cretaceous shelf edge, coincident with the Edwards/Stuart City reef and the Sligo reef margins (Fig. 3). Depths of up to 14,000 ft are attained along the shelf margin. In the southern extent of the study area, the Stuart City and Sligo reef margins are separated by a maximum distance of approximately 30 miles and converge to the northeast near Live Oak and Bee Counties. This separation led to the formation of a large submarine plateau which permitted thick accumulation of Eagle Ford sediment (Fig. 3, 4).

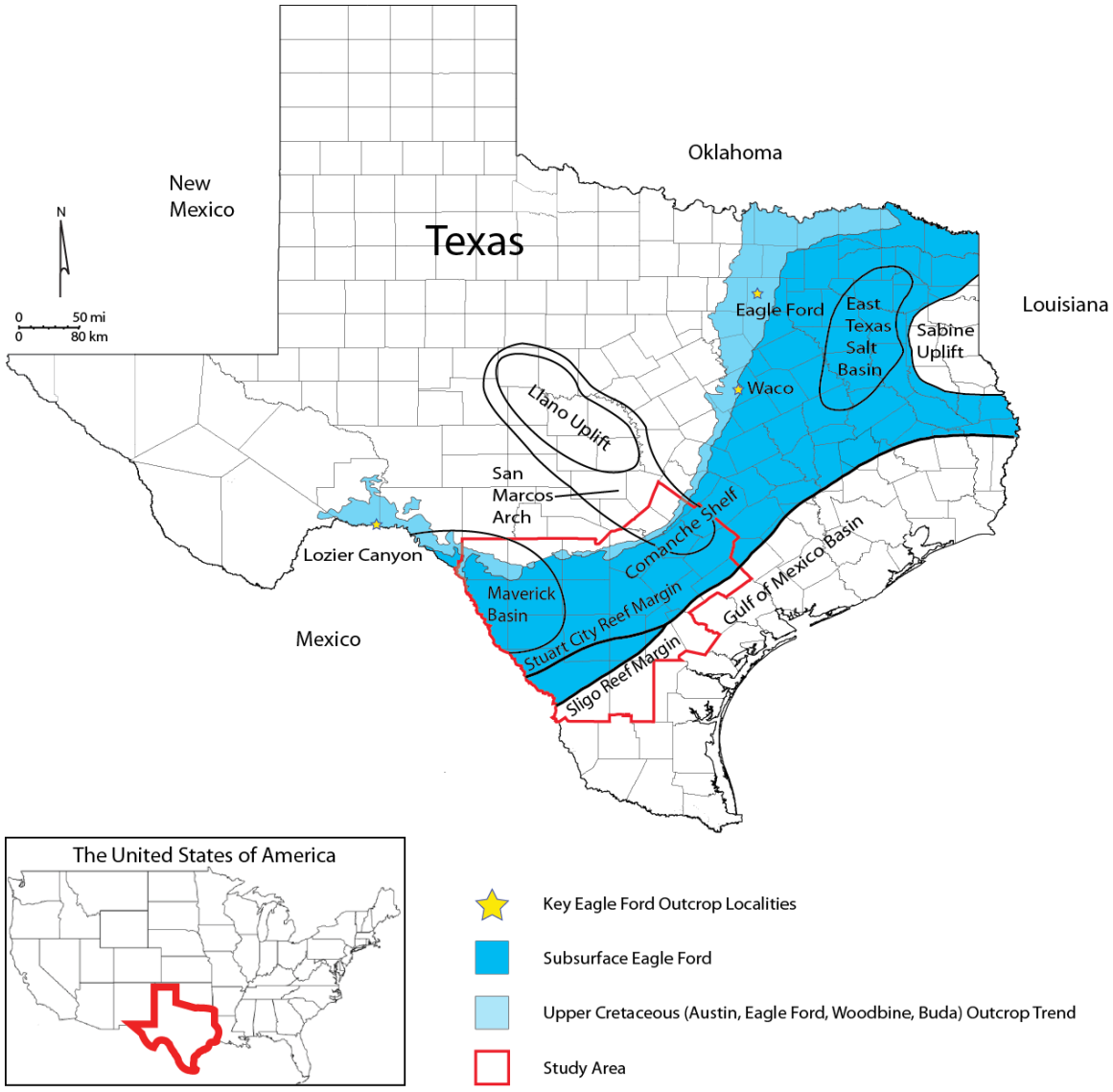

Figure 3: Map showing distribution of the Eagle Ford and related rocks in outcrops and the subsurface of Texas. Major structural features affecting rock thickness and rock character distributions during (Maverick Basin, Comanche Shelf, Cretaceous reef margins, San Marcos Arch, East Texas Salt Basin) and following (Sabine Uplift) deposition are shown. Adapted from Geology of Texas Map (1992), Montgomery (1991), and Phelps (2011).

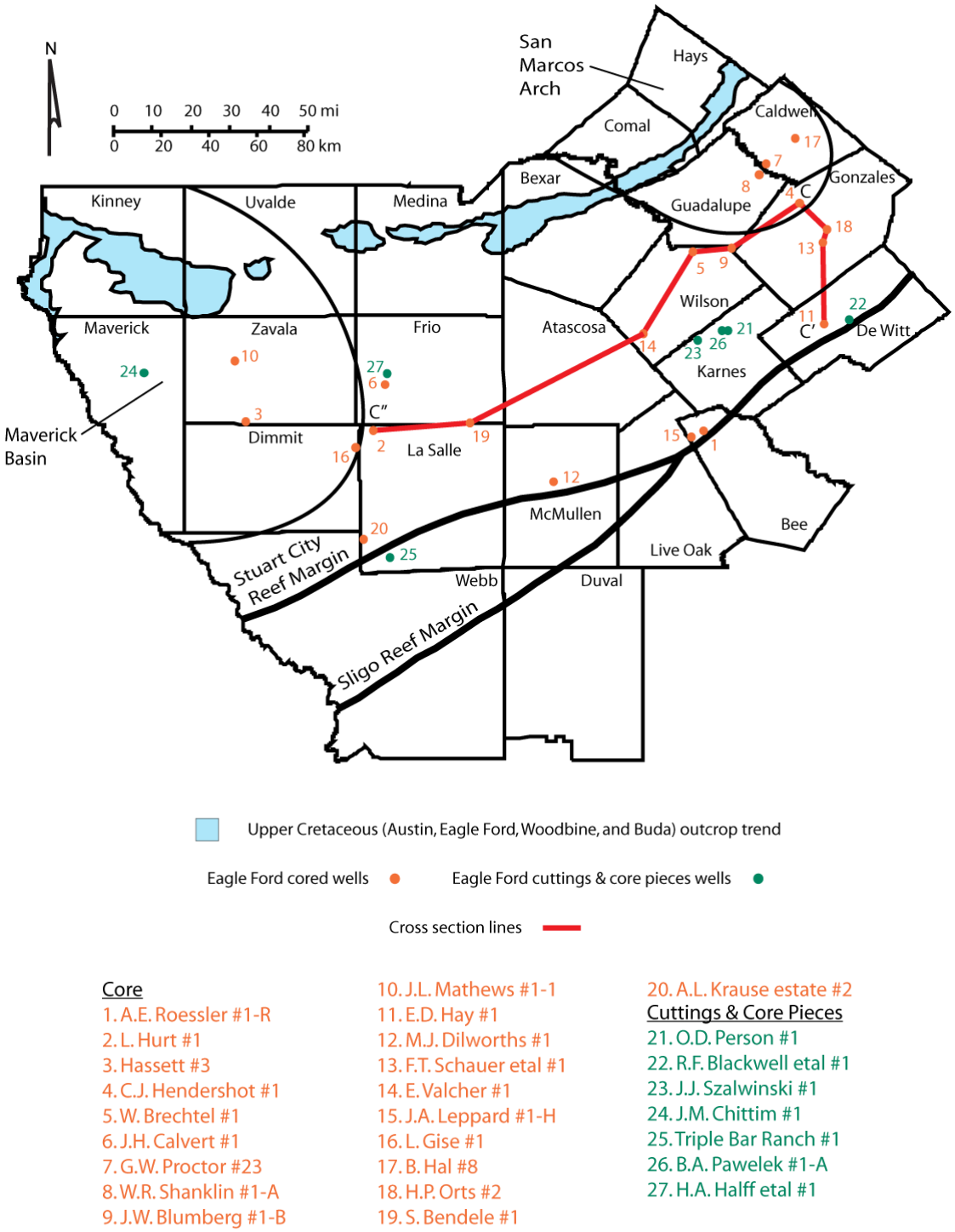

Core
1. A.E. Roessler #1-R
2. L. Hurt #1
3. Hassett #3
4. C.J. Hendershot #1
5. W. Brechtel #1
6. J.H. Calvert #1
7. G.W. Proctor #23
8. W.R. Shanklin #1-A
9. J.W. Blumberg #1-B
10. J.L. Mathews #1-1
11. E.D. Hay #1
12. M.J. Dilworths #1
13. F.T. Schauer etal #1
14. E. Valcher #1
15. J.A. Leppard #1-H
16. L. Gise #1
17. B. Hal #8
18. H.P. Orts #2
19. S. Bendele #1
20. A.L. Krause estate #2

Cuttings & Core Pieces
21. O.D. Person #1
22. R.F. Blackwell etal #1
23. J.J. Szalwinski #1
24. J.M. Chittim #1
25. Triple Bar Ranch #1
26. B.A. Pawelek #1-A
27. H.A. Halff etal #1

Figure 4: Map of Eagle Ford study area showing sampled wells and the location of regional cross sections. Location of study area in Texas is shown in Figure 3. Adapted from Geology of Texas Map (1992).

The northeast and southwest margins of the study area are bounded by major structural features. The San Marcos Arch, a paleogeographic/ bathymetric high, marks the northeastern extent of the study area. The Maverick Basin and Texas/Mexico border combine to form the southwestern extent of this study (Fig.4).

PREVIOUS WORK

Organic-rich mudrocks of the Eagle Ford have drawn periodic attention in the literature over the past 150 years. Until recently, the majority of work has concentrated on Eagle Ford outcrops rimming the western margin of the East Texas Basin (Fig. 3). These areas have been of particular interest because of the proximity and association of Eagle Ford source rocks with oil accumulations in siliciclastic reservoirs of the East Texas Salt Basin (Fig. 3). Early descriptions of the Eagle Ford as "black shale with fish remains" were made by Ferdinand Roemer as early as 1852. These observations were followed by R.T. Hill, who in 1887, established a type locality and applied the name of Eagle Ford Shale at Eagle Ford near Dallas, Texas (Fig. 3). In 1901, Hill noted the bituminous nature and occurrence of the Eagle Ford within the Upper Cretaceous section surrounding the Red River area of North Texas.

In 1932, Sellards, Adkins, and Plummer introduced the work of W.L. Moreman, dividing the Eagle Ford Shale within northern East Texas into the Tarrant, Britton, and Arcadia Park Formations. His divisions of the Eagle Ford and subsequent recognition as a group represent early attempts to subdivide the Eagle Ford based on lithologic variability. Moreman also identified characteristic outcrop stratigraphic relationships and thickness trends for the Eagle Ford. Most notably he recognized distinct thinning of the uppermost Eagle Ford from about 100 ft near Dallas, Texas to 10 ft in Austin, Texas. Emerging from these observations, Moreman interpreted the contact between the Arcadia

Park Formation and the overlying Austin Group as unconformable. A thin, approximately 1 ft, transition zone consisting of clay, gypsum, phosphatic nodules, reworked pelecypods, and fish remains mark this unconformity.

Highly variable Eagle Ford thicknesses and sharp lithologic boundaries continued to generate interest in the nature of the contact between the Eagle Ford and the overlying Austin. Stephenson (in Sellards et al., 1932) noted in Hays and Travis counties that borings from the base of the Austin Group extend down up to 18" into the Eagle Ford and were filled with glauconitic chalk of the basal Austin. In 1962, Brown and Pierce concluded that southward thinning of the Eagle Ford onto the San Marcos Arch was due to nondeposition at the base and truncation at the top. Montgomery, 1991, also reported a clear unconformity between the Eagle Ford and Austin Formation around the San Marcos Arch; but suggested gradational contacts in the Maverick Basin/Rio Grande Embayment area (Fig. 3).

Jiang (1989) conducted a regional study of outcrop-based biostratigraphic data (ammonites and planktonic foraminifera) for the Eagle Ford and Austin. His outcrop work in the proximity of the San Marcos Arch showed that Turonian upper Eagle Ford rocks are unconformably overlain by the Coniacian Austin Formation. Based on these outcrop studies, Jiang assigned the Eagle Ford Group an age of Cenomanian to Turonian.

More recent work on characterizing the lithologic variability of the Eagle Ford Group was completed by Dawson (1997, 2000). He utilized outcrops spanning from Dallas to Austin, Texas and a subsurface core from La Salle County, Texas to define Eagle Ford microfacies. Dawson's division of Eagle Ford facies once again represent an important recognition of the heterogeneous character of the Eagle Ford and the need to better define lithologic character. Dawson's divisions of the Eagle Ford in East Texas into six shale and three end-member limestone microfacies, with accompanying

mineralogical and TOC data, provide a reference to which valuable geographic and stratigraphic comparisons can be drawn.

Understandably, much of the characterization efforts on the Eagle Ford have exclusively centered on outcrop successions. Few published correlations for subsurface Eagle Ford rocks exist, especially in South Texas. From the subsurface correlations that do exist, some of the earliest were produce by Winter (1961) while studying the Austin Formation in South Texas. Winter's paper illustrated early correlations and thicknesses of the Eagle Ford based on internal log markers. His correlations show truncation of the upper markers toward the San Marcos Arch due to an unconformity placed between the Eagle Ford and overlying Austin. Grabowski's (1984) work on the Austin Formation also established early Eagle Ford subsurface correlations based on a Cenomanian lower member and Turonian upper member. His division of the Eagle Ford into lower and upper members is still widely accepted today and is utilized in this paper.

Surles (1987) mapped the regional stratigraphy and source rock potential of the Eagle Ford Group in the East Texas Basin (Fig. 3). Although his study centered on identifying net sand thicknesses for the Tarrant, Britton, Arcadia Park, and primarily the sub-Clarksville Formations of the Eagle Ford Group; his regional correlations and inclusion of geochemical data once again acknowledged the extent and hydrocarbon generating potential of Eagle Ford source rocks. Surles, citing Cotera (1956) and Beall (1964), suggested terrigenous sourcing from the Ouachitas and southern Appalachians during Eagle Ford time. Nichols (1964) and Oliver (1971) showed that following the marine transgression that deposited the Buda Limestone, northeast Texas was subjected to uplift that resulted in erosion of Paleozoic rocks of the Ouachita Mountains in southern Oklahoma and Arkansas. Based on outcrop and log studies, Surles identified several

fluvial mud-dominated deltas that prograded from the north (Ouachita Mountains) and west. These deltas acted as active clastic sediment sources during Eagle Ford deposition.

Hentz and Ruppel (2010) established a wireline log based regional lithostratigraphic framework for subsurface Eagle Ford rocks in Texas. Their efforts to correlate subsurface Eagle Ford rocks lithostratigraphically across the San Marcos Arch are useful in identifying regional rock character and thickness trends between South and East Texas. Stemming from these correlations, they generated several regional structure contour maps, lower and upper Eagle Ford thickness isopach maps, and regional wireline cross sections identifying the distribution of lower and upper Eagle Ford facies stretching from the Maverick Basin to the East Texas Salt Basin.

Donovan and Staerker (2010) conducted an outcrop study of the Boquillas Formation (Eagle Ford equivalent) in Lozier Canyon, Terrell County, West Texas (Fig. 3). Proceeding from their outcrop-based sedimentological and biostratigraphic work, distinction of three transgressive-regressive cycles within the Boquillas Formation were identified. Donovan and Staerker also suggested nomenclature changes of the Rock Pens and Langtry Members of the Boquillas Formation to the Eagle Ford Formation and Langtry Formation, respectively. The Eagle Ford and Langtry Formations were incorporated into a sequence stratigraphic framework and correlated into the subsurface of South and Central Texas.

METHODS OF INVESTIGATION

Data for this study was collected from subsurface cores (22) and core pieces and cuttings (5) located at the Core Research Center, J.J. Pickle Research Campus, The University of Texas at Austin (Fig. 4). Core investigations of both whole and partial Eagle Ford sections included identification of sedimentological character, fossil

assemblages, mineral assemblages, defining properties of both clastic and carbonate facies, and identifying vertical facies stacking patterns. A modified Dunham (1962) depositional fabric classification scheme was utilized in rock classification. However, the common association of the Dunham classification with shallow water carbonate depositional environments does not apply to Eagle Ford facies and this assumption was not intended.

Facies stacking patterns and facies proportions were utilized in identifying key stratigraphic surfaces and developing a regional stratigraphic framework. Core descriptions were also utilized in building wireline log calibrations. Once complete, these calibrations assisted in developing a sampling regime, defining regional lithologic variability, and building stratigraphic correlations. Preliminary studies of additional Eagle Ford cores north of the San Marcos Arch (East Texas) and outcrop studies (West Texas) helped add to interpretations of lithologic variability, depositional process, and stratigraphy; but are not addressed in detail in this report.

Samples collected for thin section preparation and petrographic analysis were coupled with analyses of TOC (total organic carbon), Rock-Eval, XRD (X-ray diffraction), XRF (X-ray fluorescence), and stable isotopes. Thin sections were utilized as part of detailed facies descriptions by determining rock fabric, grain type and abundance, mineralogical content, and biotic content. Pore type was identified where applicable. Thin section preparation was completed by Spectrum Petrographics and National Petrographic Services. Each thin section was prepared with a thickness of 25 μm (micrometer). High resolution photomicrographs were produced from thin sections at the Bureau of Economic Geology, using a Nikon Eclipse LV 100 POL microscope and Nikon DS-Ril camera.

TOC and Rock Eval analyses were performed by GeoMark Research, Ltd. and used in determining relevant rock properties such as total organic carbon, percent carbonate, calculated thermal maturity, hydrogen index, oxygen index, S1, S2, and S3 values. Measurements of TOC were performed using a Leco TOC apparatus, which utilizes a combustion method of TOC analysis. Approximately 10 grams of sample were crushed and treated with hydrochloric acid (HCl) to remove inorganic carbon. The Leco instrument was calibrated with standards having known carbon contents. Combustion of unknowns was then completed and compared to that of the calibration standard, thus determining the TOC of the unknown sample.

Rock-Eval analyses include thermal vaporization of volatiles (the S1 peak, residual free oil) as well as pyrolysis of kerogen (the S2 peak, remaining generation potential). S2 values are used to compute Hydrogen Index (HI) by normalization involving TOC values ((HI=S2/TOC x 100 with units of mg (milligram) HC/g (gram) TOC)). Estimations of thermal maturity are generated from the temperature at peak generation of S2 hydrocarbons, the Tmax ((in ^{o}C (Celsius)) value. Tmax is a kinetic value and varies depending on kerogen type. The S3 peak ("organic" carbon dioxide yield during initial pyrolysis process) was used to compute the Oxygen Index (OI) by normalization with the TOC content (OI=S3/TOC x 100 with units of mg CO_2/g TOC) (Brian Jarvie, personal communication, February, 2010).

Samples collected for TOC analysis were also commonly analyzed for XRD and XRF, providing mineral phase and elemental abundance, respectively. XRD analyses were conducted by Dr. N. Guven at The University of Texas, San Antonio. X-ray diffraction studies were performed using a Rigaku-Ultima IV diffractometer. The scanning range was initially limited from 2° to 44°/2 Θ and then, depending on need, extended to 62°/2Θ. Scanning speeds ranged from 1°/2Θ to 2°/2Θ per minute.

To prepare for XRD analyses, core samples were cleaned with acetone and then gently ground to a fine powder. Core samples showing extensive cementation were ground in an acetone solution. The fine sample powder was then x-rayed in two or three successive modes, depending on the presence or absence of swelling clay minerals.

In the first scanning mode, a fine sample powder was loaded in a special glass holder with a rough surface to minimize the preferred orientation of the sample. In the second scanning mode, oriented slides were prepared from the stable suspensions of clays or acid residues of carbonates. Approximately 1-1.5 g of the powder were suspended in 0.01N (normality) solution of sodium pyrophosphate for about 24 hours. If the suspensions of the clays and those of acid residues flocculated, the liquid was replaced with a fresh solution. This process was repeated until a workable suspension was generated. Next, particles coarser then 4 (sometimes 2) μm where allowed to settle out of suspension. The suspending liquid was then transferred to a glass slide and then gently heated to about 50-60 ^{o} C to dry the suspension. Glass slides covered with dried, thin clay films were then x-rayed.

If there was an indication of swelling clay minerals, preparation for the third scanning mode included finely spraying the clay slide with ethylene glycol (EG) and allowing to sit for another 24 hours in a pot half filled with EG. The clay film saturated with EG was then x-rayed again. This third scanning mode reveals the presence of swelling clay minerals like smectites and mixed-layer illlite/smectites (Nicep Guven, personal communication, July, 2011).

X-ray intensities were used to differentiate sample mineralogies. Randomly packed sample powders were used to identify non-clay minerals. Clay minerals were identified using oriented slides described in scanning mode two and three. Quantification of diffraction patterns involved interpretations aided by computer software. Elemental

XRF analyses were carried out by Henry Francis at the University of Kentucky, Lexington. XRF analyses provide constraints in quantitative XRD estimations. XRF scanning of Eagle Ford cores was done by Dr. Harry Rowe and students from the University of Texas, Arlington. Detailed descriptions of XRF scanner methodology can be found in the unpublished thesis of Hughes (2011).

Samples collected for inorganic carbon and oxygen isotope analysis were acquired from five Eagle Ford cores based on geographic location and stratigraphic position. Whole rock samples were collected on a 1 ft interval using a handheld drill. Concretionary fabrics were also preferentially sampled in each core. Sample analyses were performed in the lab of Dr. Harry Rowe at The University of Texas at Arlington, Arlington, Texas. "Each powdered sample was analyzed using a UIC, Inc. coulometer in order to determine the total inorganic carbon (%TIC) concentration. Weighed samples (3-5mg) were reacted in 10% H_3PO_4 at 70°C during the coulometric measurement. The standard deviation of %TIC measurements of carbonate-rich samples is typically on the order of 0.25% (absolute percentage). The %TIC measurement assisted in optimizing the weight for stable isotopic analysis. Depending upon the sample %TIC, approximately 200- 450 μg (microgram) of sample were weighed into LABCO Exetainer vials, capped, and purged with ultra high-purity helium gas for three minutes each. Samples were subsequently acidified with three drops of 100% H_3PO_4 and equilibrated at 50°C for 13.5 hours. Samples were subsequently analyzed using a ThermoFinnigan GasBench II peripheral connected to a ThermoFinnigan Delta-V isotope ratio mass spectrometer (IRMS). An in-house standard (UTAH) calibrated to Vienna-PDB (Pee Dee Belemnite) was used to standardize stable carbon ($\delta^{13}C$) and oxygen ($\delta^{18}O$) isotopic results. Errors for standards and samples are ±0.1 for both $\delta^{13}C$ and $\delta^{18}O$" (Harry Rowe, personal communication, February, 2011).

GEOLOGIC SETTING

In South Texas, the Comanche Shelf (Fig. 3) developed as a thick, prograding carbonate succession deposited during multiple transgressive-regressive events. Two dominant end-member shelfal depositional profiles emerged as (1) flat-topped reef-rimmed platforms and (2) storm-dominated ramps (Fig. 5). Reef-rimmed platforms were dominant during low-order regressive events while transgressive and early highstand deposits produced storm-dominated ramp profiles. Architectural differences between these systems were driven by biotic (flat-topped platforms) and physical (ramp) processes.

Carbonate platforms of the Comanche Shelf appeared during the early Cretaceous Hauterivian Stage with the development of the Sligo Limestone (Fig. 5) (Salvador and Muñeton, 1989). The Sligo developed as a raised-rim, prograding reef margin that marked a significant shift in the depositional architecture of platform, platform margin, and slope sediments (Galloway, 2008). Nearly continuous reef-rimmed platform architecture existed from the Hauterivian through the Albian and into the early Cenomanian (Fig. 5) (Salvador and Muñeton, 1989). Back-stepping of the platform was accompanied by periods of organic-rich sedimentation on the platform top. The Pine Island and Bexar members of the Pearsall Formation, Del Rio Formation, and the Eagle Ford Formation each represent periods of organic-rich deposition initiated during marine transgression (Fig. 5).

Cenomanian paleogeographic changes along the Texas Gulf Coast transformed the depositional architecture of the platform (Fig. 5, 6). Prior to Eagle Ford deposition, uplift coupled with eustatic regression produced exposure past the shelf edge and one of the major discontinuities in the Mesozoic record of the Gulf (Sohl et al., 1991, Galloway,

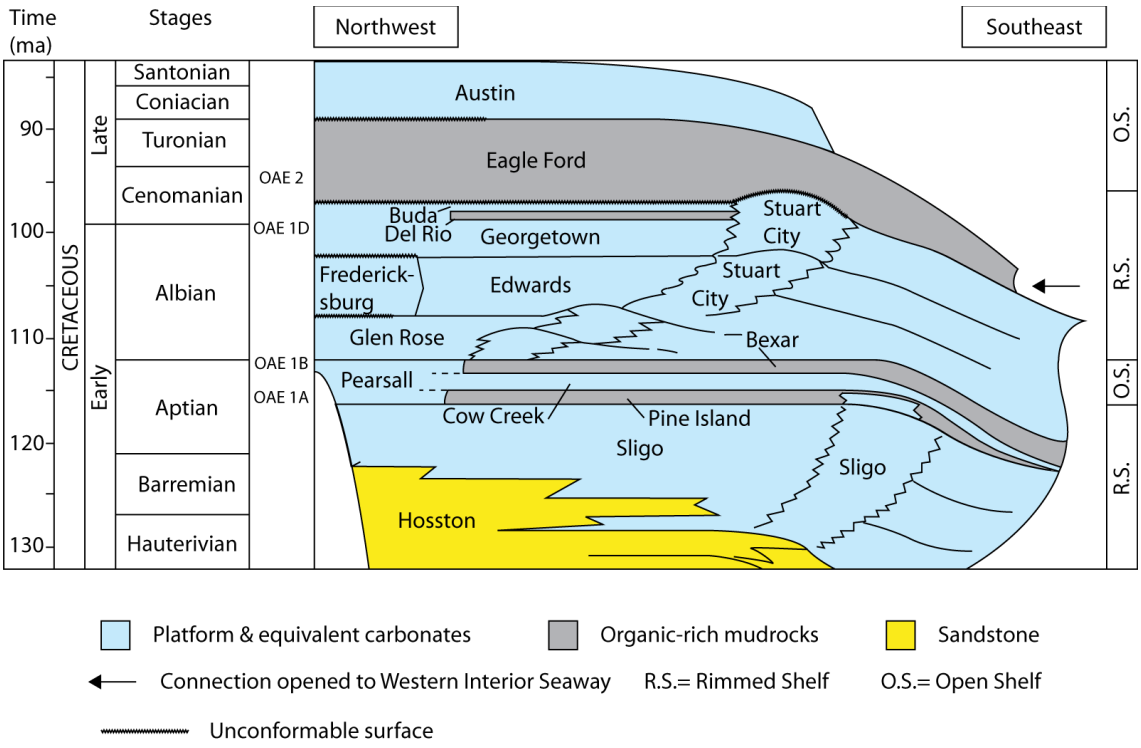

Figure 5: Architecture of Gulf Coast Cretaceous depositional systems. The Comanche Shelf of South Texas emerged as a series of platform carbonates and organic-rich mudrocks. Organic-rich mudrocks coincide with OAE events and commonly occur at the boundary between open shelf and rimmed shelf platform architecture. Modified after Galloway (2008) and Salvador and Muñeton (1989).

2008). This depositional break represented a shift from broad, reef-rimmed carbonate platforms to a ramp profile with alluvial, deltaic, and coastal depositional systems (Wu et al., 1990, Galloway, 2008). Eagle Ford sedimentation began during the Middle to Late Cenomanian as part of a major transgression of the Upper Comanche Shelf. This transgression generated a shift in platform architecture and drove primary sedimentation from the shelf margin toward intrashelf depocenters (Galloway, 2008), such as the Maverick Basin in South Texas and East Texas Salt Basin in Northeast Texas. As a result, the thickest and furthest encroaching succession of organic-rich mudrocks along the Gulf Coast was deposited during Eagle Ford time (Galloway, 2008). Although limestone deposition returned during the Coniacian, the marine transgression associated with the Eagle Ford drowned the platform and platform-rimming reef development did not return.

In South Texas, the Eagle Ford commonly overlies the Buda Formation (Sohl et al., 1991). Buda facies consist of light grey, very fine textured, dense, micritic limestones with abundant stylolites (Snyder and Craft, 1977). The Buda Formation commonly pinches out as it approaches the Stuart City reef margin (Fig. 5). At the shelf margin, Eagle Ford facies are found directly overlying the rudist-rich reefs of the Stuart City (Phelps, 2011). Here, a significant unconformity marks the basal Eagle Ford contact. Overlying the Eagle Ford is the regionally extensive Austin Formation. The Austin consists of highly burrowed coccolith-rich limestone, concentrated microfossil remains (echinoids, mollusks, ostracods, bryozoans), localized sedimentary structures indicative of bottom transport, and is commonly interbedded with shale and ash (Montgomery, 1990).

CLIMATIC EVENTS

Recognition of globally correlative climatic events, known as ocean anoxic events (OAEs), began in the Cretaceous section of Texas with the work of Schlanger and Jenkyns (1976) who identified two intervals (Aptian/Albian & Cenomanian/Turonian) that exhibited widespread organic-rich black shale deposition. Since that time, recognition of OAE events in the Cretaceous section of South Texas have grown to include the Late Aptian OAE 1A (Pine Island), Aptian/Albian OAE 1b (upper Bexar /lower Glen Rose), Albian/Cenomanian OAE 1d (Upper Georgetown/Del Rio), and the Cenomanian/ Turonian OAE 2 (Eagle Ford) (Phelps, 2011).

Global drivers for intensified organic matter burial include increased sea-floor spreading rates and surface volcanic activity that released large amounts of CO_2. Additional influx of greenhouse gases into the atmosphere increased global temperatures, which resulted in increasing disappearance of polar ice caps (Arthur et al., 1985). This absence of polar ice stalled oceanic circulation rates due to the lack of oxygenated sea water circulating the sea floor. Marine transgression generated by melting of polar ice coupled with poor circulation patterns formed intensified oxygen minimum zones that underwent geographical and vertical expansion during OAEs (Schlanger and Jenkyns, 1976). Basinal upwelling of waters rich in nitrogen and phosphate (Wignall, 1994) led to increased productivity. Shelfal areas with high productivity generated expanded oxygen minimum zones where accumulation and preservation of organic matter accounts for globally correlative organic matter enrichment (Schlanger and Jenkyns, 1976). In areas with strong upwelling conditions, deposition of organic-rich sediments began before and continued after the OAE event (Schlanger et al., 1987).

Figure 6: Paleogeography of North America during the Late Cretaceous. After R. Blakey (1994).

One of these periods of increased organic matter burial, OAE 2, occurred near the Cenomanian-Turonian boundary. Globally, the Cenomanian-Turonian (90.5-91.5 mya) boundary is marked by a recognizable $\delta^{13}C$ excursion in marine carbonate, marine, and terrestrial organic matter (Arthur et al., 1988). This 1 million year period is evident by a $\delta^{13}C$ increases in carbonate from 2.0‰-3.0‰ to 4.0‰-5.0‰ (Schlanger et al., 1987). The positive $\delta^{13}C$ excursion is related to the excess burial of organic carbon (Jenkyns, 1980). Increased organic-carbon burial prevented the recycling of C12 included in the organic components of marine plankton, increasing C13 values of remaining seawater (Schlanger et al., 1987). Classically, the onset and maximum isotope excursion of OAE 2 are identifiable, while no firm chemostratigraphic marker exists for the end of the positive excursion (Tsikos et al., 2004).

Whereas the Cenomanian-Turonian OAE 2 event has historically been recognized by a positive carbon isotope excursion, OAE events from the early Albian, early Aptian, and early Toarcian show both positive and negative excursions (Jenkyns, 2010). Negative excursions in previous anoxic events have been ascribed to huge amounts of CO_2 being released into the atmosphere by subaerial volcanism and the formation of large igneous provinces (Kuroda et al., 2007). The Cenomanian/Turonian boundary is a recognized period of increased volcanism in large igneous provinces, including the Caribbean and Ontong-Java oceanic plateaus and the Madagascar flood basalts (Sinton and Duncan, 1997). However, the effect of these large igneous provinces on $\delta^{13}C$ values near the Cenomanian/Turonian boundary commonly goes unrecognized in the literature.

TECTONICS

Prominent structural features active during Eagle Ford deposition coupled with pre-existing platform rimming biologic build-ups that acted to control the thickness and

lateral distribution of Eagle Ford facies are shown in Figures 7. The San Marcos Arch is an extension of the Paleozoic Llano Uplift that trends southeast-northwest and separates the Maverick Basin/Rio Grande Embayment area and the East Texas Basin (Fig. 7) (Dravis, 1980). Decreased subsidence along the San Marcos Arch led to its expression as a minor topographic high and a shallow water shelf flanked by deeper shelf basinal areas on the east, south, and west (Seewald, 1958, Tyler and Ambrose, 1986).

Tectonic activity also led to the formation of intra-shelf depocenters such as the Maverick Basin in South Texas. The Maverick Basin originating from basement structures developed during the failed Rio Grande rift (Rose, 1972, Donovan and Staerker, 2010). Active salt withdrawal led to prolonged accommodation development and deposition within the Maverick Basin. The effect of these large structurally generated features is still evident in a base Eagle Ford contour map (Fig. 8) and allows inference into what depositional profiles may have looked like during the Eagle Ford.

A series of southwest-northeast fault systems possibly produced during the Ouachita orogeny (Montgomery, 1990) cuts through most of the study area. These fault systems include the Fashing Fault Zone, Charlotte Fault Zone, Luling Fault Zone, and the shallow Balcones Fault Zone. Aside from the Balcones, these fault systems formed in the proximity of up-dip Triassic/Jurassic salt and result from basinward salt movement (Montgomery, 1990). Within the Balcones Fault Zone, individual faults are discontinuous (Muehlberger and Kurie, 1956) while the zone as a whole is laterally extensive and stretches from Del Rio through Central Texas to Waco and possibly into northeastern Texas (Reaser, 1961). Balcones faulting consists of normal, downthrown to the southeast faults forming an arcuate pattern concave to the Llano uplift (Zink, 1957). The Luling Fault System parallels the Balcones Fault System and is separated by 10 to 20 miles (Zink, 1957). Faults are landward dipping, producing grabens between the Luling and

Balcones Fault Zones. Faulting initiated during the Late Jurassic to Early Cretaceous and remained active into the Cenozoic (Murray, 1961). The Charlotte Fault System lies on the southern end of the San Marcos Arch in Atascosa and Frio counties. This fault system, also recognized as the Atascosa Trough, consists of a complex network of basinward and landward dipping normal faults with graben development between (Zink, 1957). The Fashing Fault Zone, also known as the Karnes Trough, similarly forms a network of basinward and landward dipping normal faults leading to graben formation. Although unique in location and throw, each of these fault systems remained active during Eagle Ford sedimentation and produced locally thickened Eagle Ford sections (Eaton, 1956 & Corbett, 2010) potentially ideal for hydrocarbon exploration.

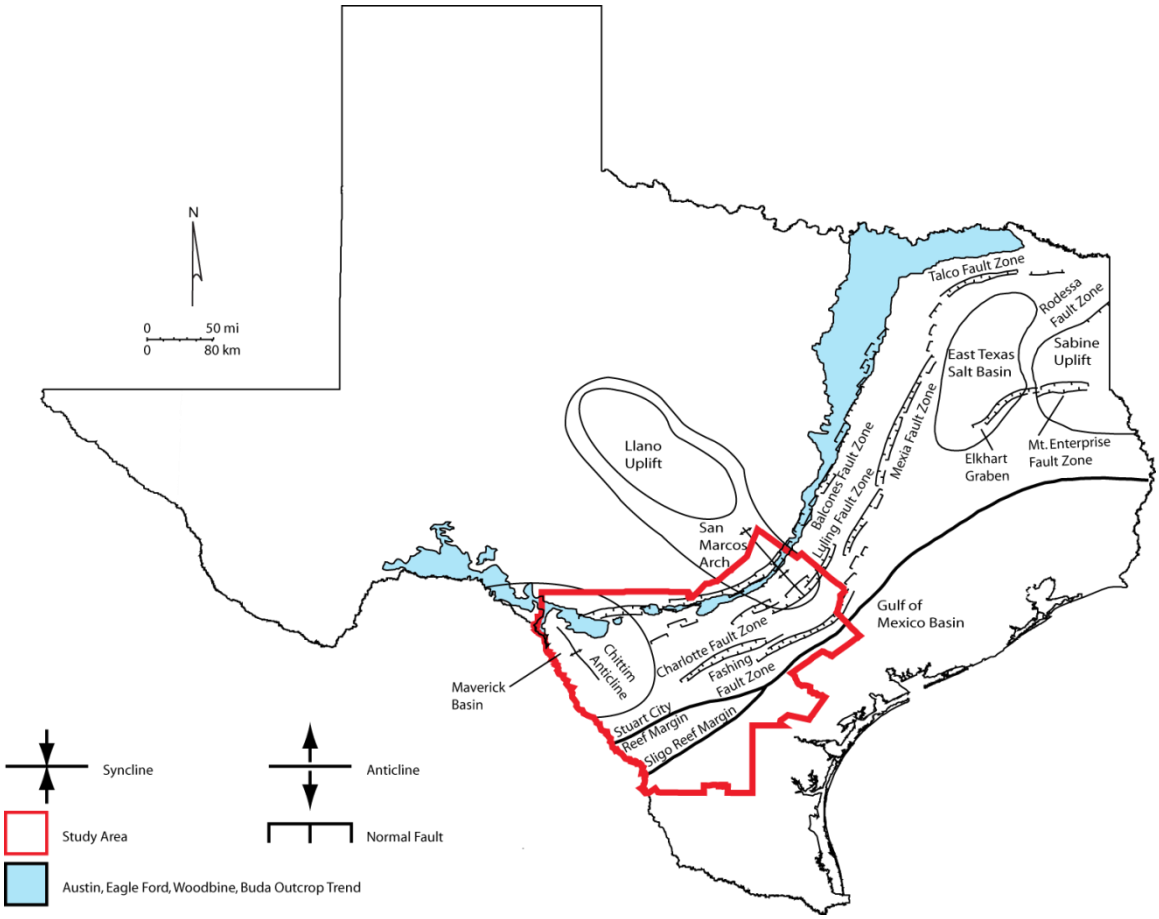

Figure 7: Map showing structural features in Texas. Active structural, paleogeographic, and bathymetric features exerted control on thicknesses and facies distributions of the Eagle Ford. Modified after Montgomery (1990) and Phelps (2011).

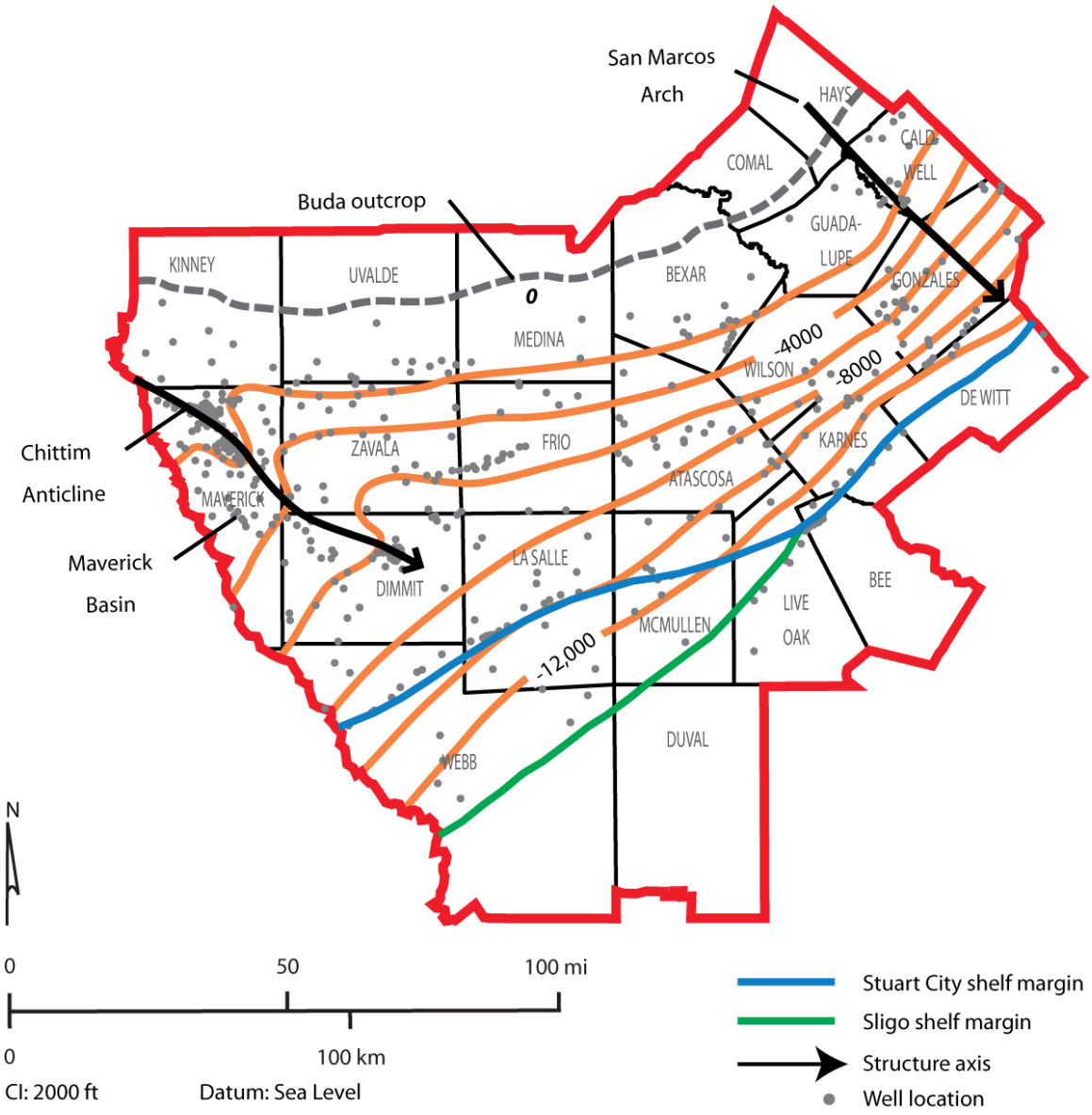

Figure 8: Isopach map of the Eagle Ford Formation based on wireline logs. Recognizable structural features active during Eagle Ford deposition include the San Marcos Arch and the Maverick Basin. Secondary features such as the Chittim Anticline, an inverted graben associated with Laramide compression, developed post-depositionally. Location of study area is shown in Figure 7. Modified after Hentz and Ruppel (2010).

REGIONAL EAGLE FORD STRATIGRAPHY

Outcrops rimming the East Texas Basin and in West Texas have historically served as type localities for the development of Eagle Ford nomenclature and understanding of stratigraphic relationships. However, description of the physical character and recognition of stratigraphic divisions in these geographically and lithologically distinct areas were developed independent of one another and exhibit variable group, formation, and member names. In order to better delineate the stratigraphic relationships between Eagle Ford type localities, and in an effort to connect these with the subsurface of South Texas, a consolidated stratigraphic chart showing conventional Eagle Ford nomenclature and lithostratigraphy is shown in Figure 9. Comparison of regional trends in sediment type and distribution provide a framework with which to better constrain variability identified in South Texas subsurface core investigation.

EAST TEXAS

Recognition of the Eagle Ford as a group emerged from the work of Moreman (in Sellards et al., 1932) through identification of the Tarrant, Britton, and Arcadia Park Formations in outcrops rimming the western margin of the East Texas Basin (Fig. 10). The type locality of the Tarrant sandy clay and limestone, the basal unit of the Eagle Ford Group, is located in Tarrant County where it is typically 15 ft thick. Here, the lithology of the Tarrant Formation is grey to brown-grey sandy clays with intermittent thin brown limestone strata and calcareous concretions (Sellards et al., 1932). The middle unit, the Britton clay, has a type area in northwestern Ellis County where it is 250 ft thick and consists of mostly blue clay with flaggy limestones and calcareous concretions increasing

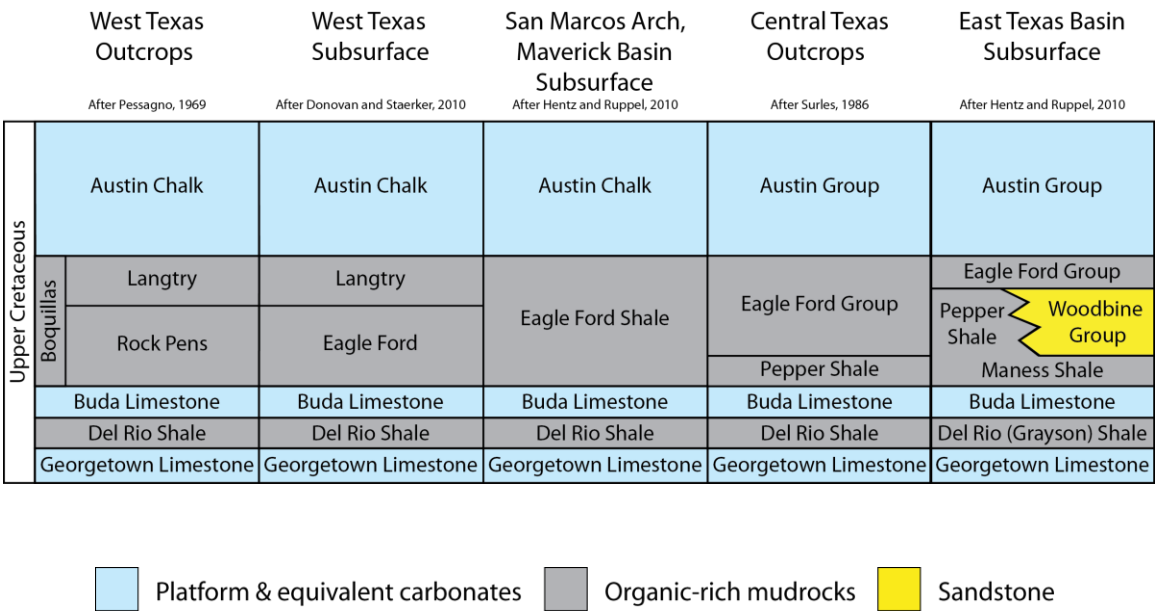

Figure 9: Chart of stratigraphic nomenclature for the Eagle Ford and related units. In the San Marcos Arch and Maverick Basin area of South Texas, the Eagle Ford Formation commonly overlies subtidal platform carbonates of the Buda Formation and is overlain by subtidal platform carbonates of the Austin Formation. Outcrop locations shown in Figure 3.

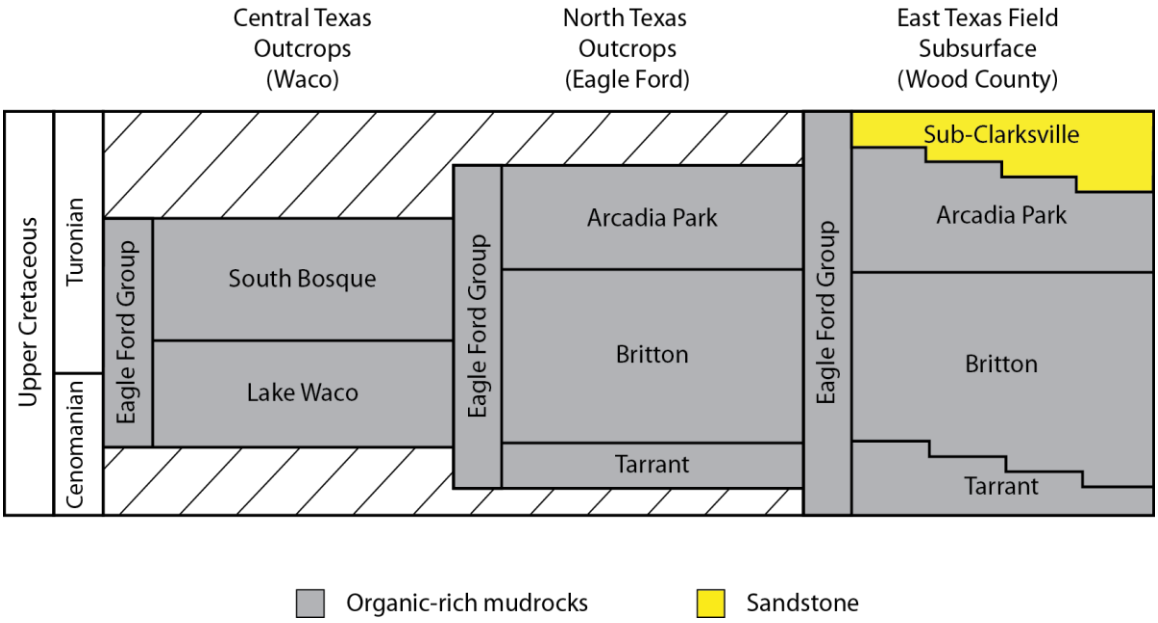

Figure 10: Chart of Eagle Ford stratigraphic nomenclature in Central, North, and East Texas. Outcrop locations shown in Figure 3. After Surles (1986).

in abundance near the top of the unit (Sellards et al., 1932). The uppermost Eagle Ford consists of the Arcadia Park shale, with its type section in central Dallas County consists of a 20 ft lower blue clay, 1-3 ft limestone flags, and 75 ft blue shale with numerous calcareous concretions (Sellards et al., 1932).

The Tarrant, Britton, and Arcadia Park Formations undergo marked lithology shifts and associated name changes to the southwest toward the San Marcos Arch (Fig. 10). From Waco to Austin, Texas the Eagle Ford Group consists of the Lake Waco and South Bosque Formations (Fig. 10). The Lake Waco Formation was introduced by Adkins and Lozo (1951) in the Waco area of Texas as "grayish white to brownish grey, arenaceous, flaggy limestone and dark to bluish gray, silty, calcareous shale with bentonite" (Jiang, 1989). The South Bosque Marl was identified earlier by Prather in 1902 as "the marl below the base of the Austin Chalk", but was later expanded by Adkins and Lozo (1951) into two parts; a "dark gray to black, massive to blocky, fossiliferous but not particularly calcareous shale or mudstone and laminated calcareous shale, interbedded with few silty limestone flags and thin bentonite seams" (Jiang, 1989). The equivalent relationships of the South Bosque Formation with the Arcadia Park Formation and the Lake Waco Formation with the Britton Formation were later established by Jiang (1989).

Formations of the Eagle Ford identified in the western outcrop trend are continuous into the subsurface of the East Texas Basin. Here, addition of the Sub-Clarksville Sands constitutes the upper-most formation in the Eagle Ford Group (Fig. 10). This Sub-Clarksville Formation is not present in the western outcrop belt, but is seen well-developed in subsurface cores and in the northern outcrop belt where it is further subdivided into a lower Bells Sandstone Member and an upper Maribel Shale Member (Surles, 1987).

In East Texas, the Eagle Ford Group shares the Buda to Austin stratigraphic interval with the Pepper Shale and Maness Formations (Fig. 9). The type section of the Pepper Shale Formation is located in Bell County, Texas and was defined by Adkins (1932) as a 50 ft "non-calcareous, blue-purplish clay shale". Due to a lack of outcropping Maness Shale, a subsurface type locality was defined from the Shell Oil Company's Maness No. 1 (Bailey et al., 1945). Here, the 61 ft thick Maness consists of "faintly laminated to massive, bronze or copper-colored and dark gray, somewhat calcareous clay shale and claystone" (Bailey et al., 1945).

The Maness Shale of the subsurface East Texas Basin is commonly separated from the overlying Eagle Ford and Pepper Shale by the coarse siliciclastic-rich Woodbine Group (Fig. 9) (Hentz and Ruppel, 2010). Southwestern pinch-out of Woodbine clastics leads to juxtaposition of the Eagle Ford Group, Pepper Shale, and Maness Shale to the north of the San Marcos Arch (Hentz and Ruppel, 2010). Occasionally, the Maness Shale and Pepper Shale Formations are included in the lowermost Eagle Ford Group (Ambrose et al., 2009).

WEST TEXAS

In West Texas, well-preserved outcrops of Eagle Ford equivalent strata have been periodically studied since Udden's (1907) initial description and identification of a type locality for the Boquillas Flags Formation in Brewster County, Texas. More recent studies by Pessagno (1969) identified a type locality for the Boquillas Formation at Lozier Canyon, Terrell County, Texas (Fig. 3). Here, the Boquillas consists of a lower Rock Pens and an upper Langtry member (Fig. 9). At the type section, Pessagno defined the 150 ft Rock Pens Member as "medium- to thick-bedded grey calcareous siltstones, mudstones, and limestone beds" with the overlying 38 ft thick Langtry Member as "thin-

bedded and buff colored, calcareous mudstones, marls, and chalky limestones" (in Donovan and Staerker, 2010).

Donovan and Staerker (2010) further studied the Boquillas type locality at Lozier Canyon and subdivided the Boquillas into two formations, the Eagle Ford and the Langtry, which they correlated into the subsurface of West and South Texas (Fig. 9). An important aspect of their research was application of biostratigraphic studies to better constrain the regional stratigraphy and equivalence of Eagle Ford mudrocks. Their Eagle Ford Formation is age equivalent (Cenomanian-Turonian) with conventional understanding of outcropping Eagle Ford rocks on the San Marcos Arch (Jiang, 1989). While the Langtry Formation, consisting of a transgressive-regressive cycle that grades into the overlying Austin, is biostratigraphically dated late Turonian to Coniacian (Donovan and Staerker, 2010).

SOUTH TEXAS

Beyond Austin, Texas few rock characterization or stratigraphic studies tie the Lake Waco and South Bosque Formations of the Eagle Ford Group with the Rock Pens and Langtry Members of the Boquillas Formation of West Texas (Fig. 9). Lack of correlativity between these type sections likely exists due to the changing lithologic character of the Eagle Ford and insufficient outcrop and core data. As a result, the Eagle Ford Group and any potentially equivalent strata to the Pepper Shale Formation of Central and East Texas have classically been included in the Eagle Ford of the subsurface of South Texas (Fig. 9).

Classically, the names Eagle Ford Shale and Eagle Ford have been used interchangeably in the subsurface of South Texas. In order to avoid confusion these will exclusively be referred to as the Eagle Ford Formation in this study. Based on wireline

log response, the Eagle Ford Formation of South Texas is divided into lower and upper members (Grabowski, 1984). Descriptions of facies character by Dawson (1997, 2000) suggest that lower and upper Eagle Ford members of South Texas are correlative with the Lake Waco and South Bosque Formations of Central Texas, respectively. These interpretations were later supported by correlations of South Texas Eagle Ford nomenclature into East Texas by Treadgold et al. (2011).

The most comprehensive subsurface correlations showing the log character of the Eagle Ford in South Texas were recently published by Hentz and Ruppel (2010) and are shown in Figures 11 and 12. Recognition of the lower and upper Eagle Ford members in the subsurface of is facilitated by characteristic gamma ray and resistivity log response (Fig 11, 12). Lower Eagle Ford deposition occurred during a second-order transgressive system tract recording dark grey, well-laminated shales (Dawson, 2000 and Phelps, 2011) and commonly exhibits high gamma ray response (Hentz and Ruppel, 2010). The upper Eagle Ford was deposited during marine regression (Dawson, 2000) and consists of interbedded dark grey, high gamma ray and light grey, low gamma-ray mudrock (Hentz and Ruppel, 2010).

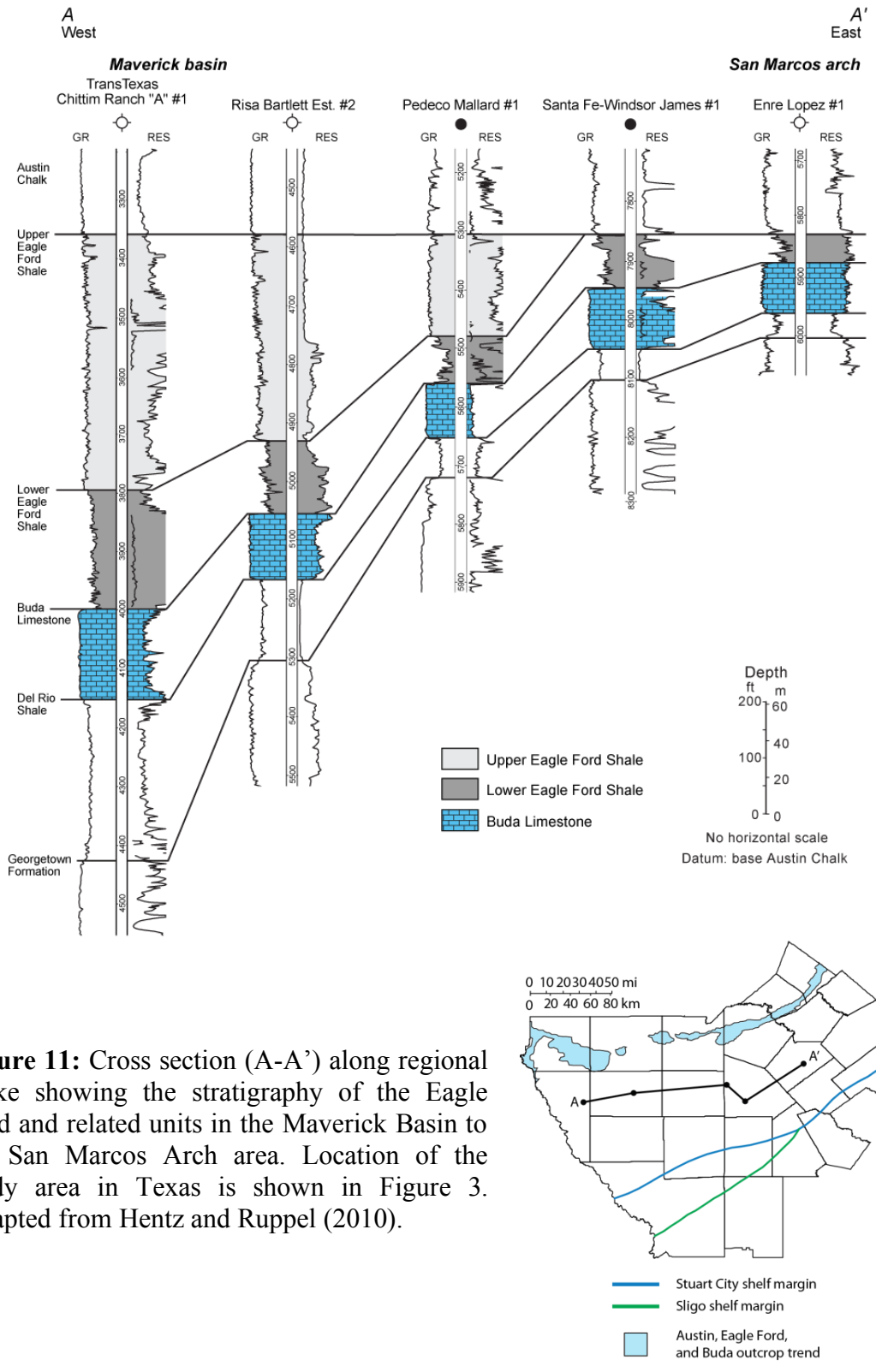

Figure 11: Cross section (A-A') along regional strike showing the stratigraphy of the Eagle Ford and related units in the Maverick Basin to the San Marcos Arch area. Location of the study area in Texas is shown in Figure 3. Adapted from Hentz and Ruppel (2010).

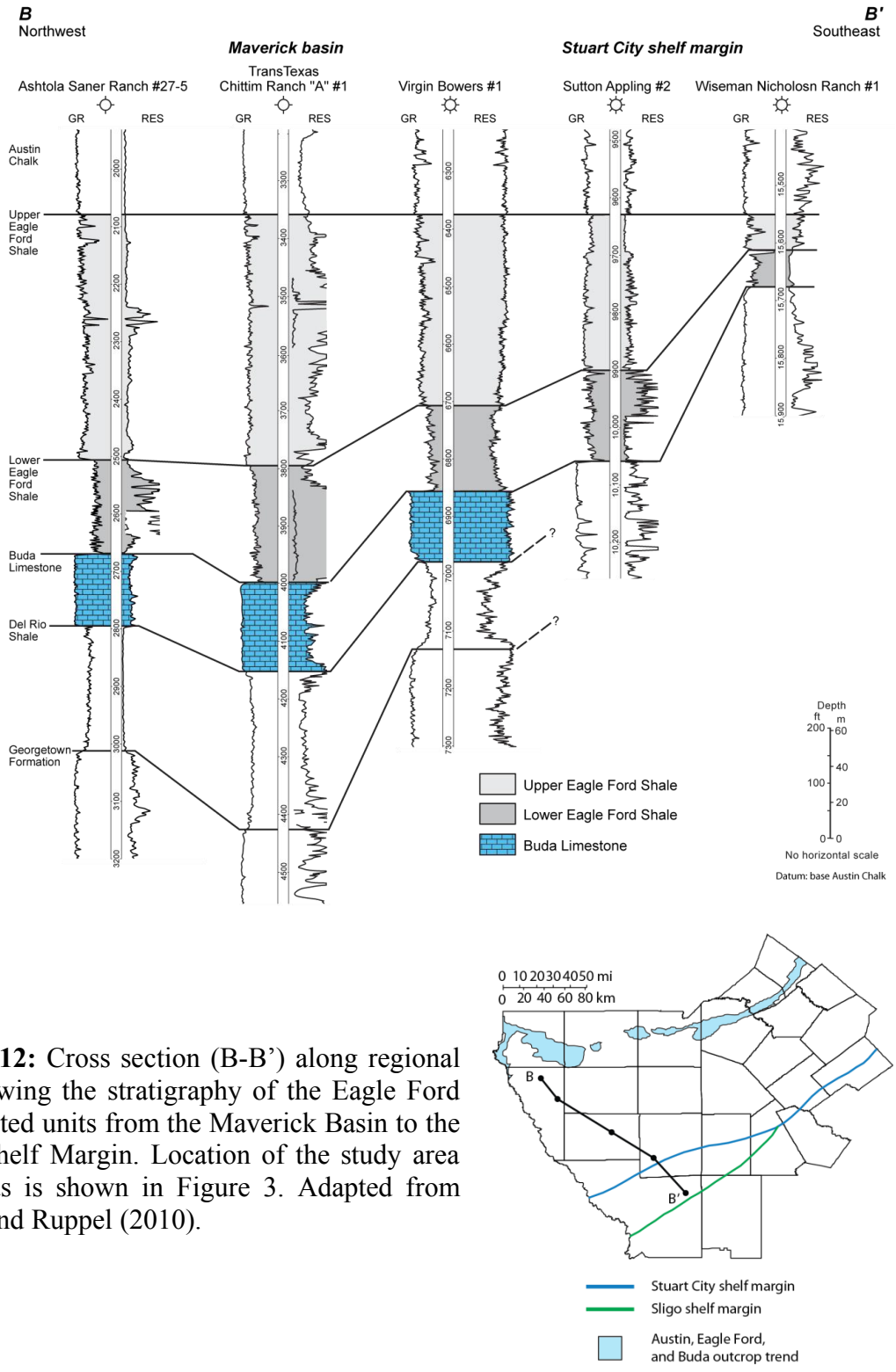

Figure 12: Cross section (B-B') along regional dip showing the stratigraphy of the Eagle Ford and related units from the Maverick Basin to the Sligo Shelf Margin. Location of the study area in Texas is shown in Figure 3. Adapted from Hentz and Ruppel (2010).

SUBSURFACE EAGLE FORD FACIES AND STRATIGRAPHY

FACIES

An important aspect of unconventional reservoir characterization and modeling is understanding the underlying sedimentological processes responsible for organic-rich mudrock deposition and preservation in the subsurface. Eagle Ford facies were identified from core and petrographic investigation using grain type, size, and abundance, textural fabric, and sedimentary structures. XRD analyses also contributed in distinguishing mineralogical abundance of fine-grained depositional and diagenetic minerals within the mudrock matrix. Individual Eagle Ford facies were defined by distinct rock character developed in unique depositional environments with characteristic sediment delivery processes. Nine depositional facies were recognized and are listed in general order of occurrence, beginning in the basal lower Eagle Ford:

1) Massive Argillaceous Mudrock
2) Laminated Calcareous Foraminiferal Mudrock
3) Laminated Fossiliferous Wackestone/Packstone
4) Laminated Foraminiferal and Peloidal Packstone
5) Massive to Bioturbated Kaolinitic Claystone
6) Laminated Wackestone
7) Disrupted Bedded Foraminiferal Packstone
8) Massive Inoceramid Packstone
9) Bioturbated Lime Wackestone

Facies	Color	Dominant Mineralogy (Average %)	Sedimentological Character	Primary Grain Type	Occurrence (by abundance)	Depositional Setting	Total Organic Carbon
1. Massive Argillaceous Mudrock	Green to Dark Grey	Clay, Quartz (45, 32)	Massive bedded, Fissile	Quartz	LEF, UEF	Proximal	5.1% (n=8)
2. Laminated Calcareous Foraminiferal Mudrock	Dark Grey to Brown	Carbonate, Clay (54, 25)	Planar laminated, mm scale	Globigerinid foraminifera, inoceramid bivalves	LEF, UEF	Distal	5% (n=68)
3. Laminated Fossiliferous Wackestone/Packstone	Dark Grey and Brown Couplets	Carbonate, Clay (55, 30)	Ripple laminated skeletal debris, cm scale	Oysters, inoceramid bivalves, phosphatic bioclasts,	LEF, UEF	Proximal to Distal	7.2% (n=2)
4. Laminated Foraminiferal and Peloidal Packstone	Light and Dark Grey Couplets	Carbonate, Clay (69, 18)	Ripple and cross laminated, mm to cm scale, Planar laminated, mm scale	Globigerinid foraminifera, inoceramid bivalves	LEF, UEF	Distal	4.6% (n=6)
5. Massive to Bioturbated Kaolinitic Claystone	Light Green to Grey	Clay (91)	Massive bedded, Locally burrowed	N/A	LEF, UEF	Distal	N/A
6. Laminated Wackestone	Grey	Carbonate, Clay (66, 19)	Ripple laminated, mm scale, Scour surfaces, Locally burrowed	Globigerinid foraminifera, inoceramid bivalves, phosphatic bioclasts	TEF, UEF	Proximal	1.6% (n=6)
7. Disrupted Bedded Foraminiferal Packstone	Brown and Light Grey Couplets	Carbonate, Clay (59, 29)	Folded and disrupted ripple laminae, cm scale, Soft sediment deformation and slumping	Globigerinid foraminifera, inoceramid bivalves	UEF	Proximal	8.1% (n=2)
8. Massive Inoceramid Packstone	Brown	Carbonate, Clay (70, 25)	Massive, Intraclasts	Inoceramid bivalves	UEF	Proximal	1.3% (n=1)
9. Bioturbated Lime Wackestone	White to Light Grey	Carbonate (90)	Heavily bioturbated	Globigerinid foraminifera, inoceramid bivalves, coccoliths, ostracodes, echinoids	TEF, UEF, LEF	Proximal	0.88% (n=2)

Table 1: Types and characteristics of dominant depositional facies in the Eagle Ford Formation.

FACIES 1: MASSIVE ARGILLACEOUS MUDROCK

In hand specimen, massive argillaceous mudrock facies is dark green to grey, fissile, and massive bedded (Fig. 13). Comparison of thin sections with normalized XRD analyses show this facies consists predominately of clay minerals (avg. 45%, range 30-75%), quartz, plagioclase, and K-feldspar (avg. 32%, range 22-50%), and marine carbonate (avg. 23%, range 3-41%). Clay mineral compositions are nearly equally divided between illite, illite/smectite mixed layer, and kaolinite. Accessory grains include silt to fine-sized quartz grains and authigenic framboidal pyrite. The calcareous skeletal component consists of coccoliths, multi-chambered planktonic foraminifera and ostracods, with widespread pyritization of skeletal tests (Fig. 13). Ammonite impressions are identifiable between shale partings in hand specimen.

This facies is locally enriched in organic matter with an average TOC of 5.1 % (8 samples). High TOC zones consist of bedding-parallel, laterally discontinuous organic matter "streaks" developing weak laminae that are laterally discontinuous over 200-300 μm (Fig. 13). The character of organic matter streaks suggest formation occurred post-depositionally due to compactional forces. However, the presence of organic matter laminae in an otherwise massive fabric indicates the rock texture likely did not originate during intense bioturbation, but rather records clastic dilution related to varying depositional rates with proximity to terrigenous point sources.

The massive argillaceous mudrock facies exists as a relatively thick succession in the basal lower Eagle Ford surrounding the San Marcos Arch, resting sharply on the Buda Limestone. Along the dip axis of the San Marcos Arch, this facies appears continuous from the shallow subsurface to near the deeply buried shelf margin. Minimal thickness changes of 10-15 ft accompany this shift from on top of the arch to near the platform edge. This facies is also continuous in basal lower Eagle Ford mudrocks off

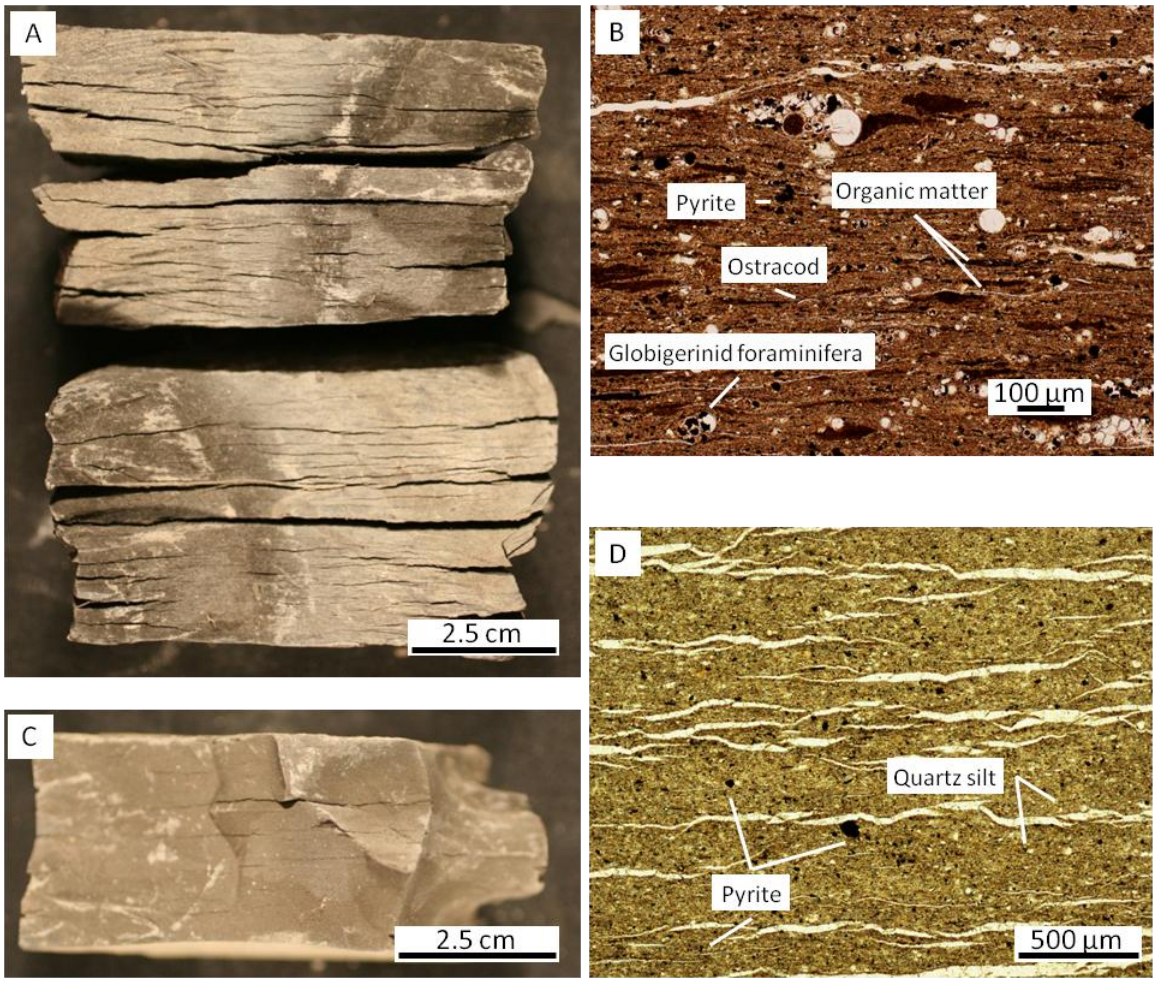

Figure 13: Photographs of massive argillaceous mudrock facies. (A) Slab photo of massive bedded, organic-rich, dark grey mudrock with fissile character, lower Eagle Ford, Orts #2, 7753.6'; (B) Photomicrograph illustrating planktonic globigerinid foraminifera and ostracods within an organic-rich, clay mineral matrix, lower Eagle Ford, Orts #2, 7753.6'; (C) Slab photo of massive bedded, green argillaceous mudrock, lower Eagle Ford, Shanklin #1, 2139.3'; (D) Photomicrograph showing detrital terrigenous material and clay mineral matrix with accessory pyrite, lacking calcareous skeletal material and organic matter seen in finer-grained distal facies, lower Eagle Ford, Shanklin #1, 2139.9'.

the San Marcos to the southwest, showing rapid thickening toward the Maverick Basin. Proximal to distal transects extending from the San Marcos Arch show decreasing detrital quartz grain size, grain abundance, and increasing organic matter (Fig. 13). Distally, massive argillaceous mudrock facies appear to be gradational with laminated calcareous foraminiferal mudrock facies.

Other than the basal lower Eagle Ford, this facies also exists as isolated beds 6" to 5 ft in thickness within distal lower and upper Eagle Ford laminated calcareous foraminiferal mudrock facies. This expression of massive argillaceous mudrock facies is largely confined to distal depositional environments near the Stuart City reef margin in the northeastern corner of the study area. These isolated beds of massive argillaceous mudrock facies exhibit similar widespread organic enrichment, but appear to lack the regional continuity seen in the basal Eagle Ford argillaceous mudrocks.

This facies is interpreted to represent deposition in low-energy, below storm wave base depositional environments. The presence of organic matter, absence of burrowing, and complete lack of current-generated structures indicate anoxic conditions prevailed in these low-energy settings. In basal Eagle Ford thickly bedded facies, increased detrital quartz grain abundance coupled with increased grain size approaching the San Marcos Arch represent sedimentation in closer proximity to terrigenous clastic sources than more calcareous, finer-grained Eagle Ford mudrocks. In these proximal environments, the general lack of calcareous fauna indicates terrigenous driven environments not suitable for carbonate production or organic matter accumulation.

The occurrence of distal, thinly bedded massive argillaceous mudrock facies suggests episodic increases in siliciclastic input and sedimentation in low-energy environments. Oliver (1971) showed that rejuvenation of sediment source areas in Oklahoma and Arkansas occurred periodically, producing multiple events of increased

terrigenous shedding into the East Texas Basin. Increased sediment input into the East Texas Basin likely led to increased terrigenous siliciclastic flux toward the San Marcos Arch and occasional transport beyond the arch.

FACIES 2: LAMINATED CALCAREOUS FORAMINIFERAL MUDROCK

The laminated calcareous foraminiferal mudrock facies is characterized by brown to dark grey, mixed calcite and clay mineral matrix with millimeter (mm) scale planar laminations (Fig. 14). Laminations commonly consist of globigerinid foraminifera and are laterally continuous, yet show variable vertical thicknesses and concentrations throughout this facies. Bedding parallel inoceramid shells, phosphatic bioclasts, and authigenic pyrite are common textural components (Fig. 14). Ostracods are locally present proximal to the San Marcos Arch, but are only locally abundant and were likely transported into these depositional environments. Thin-shelled inoceramid bivalves are common, showing extensive compaction and existing as bedding parallel, flattened shell pieces (Fig. 14). Normalized XRD analyses shows increased carbonate (avg. 54%, range 28-76%) accompanies clay (avg. 25%, range 7-50%) and quartz, plagioclase, and K-feldspar (avg. 16%, range 5-28%) within the rock matrix. TOC values for laminated calcareous foraminiferal mudrock facies range from 1.79-10.90% (68 samples) and average 5.0%. TOC values over 4.0% are prevalent and occur 74% of the time.

The laminated calcareous foraminiferal mudrock facies is the most abundant facies identified within the Eagle Ford Formation. This facies is interpreted to be the most distally deposited Eagle Ford shelfal mudrock facies and is found extensively in both the lower and upper Eagle Ford members. Proximal to the San Marcos Arch, this facies possesses a silt-rich fabric and medium brown color due to increased siliciclastic

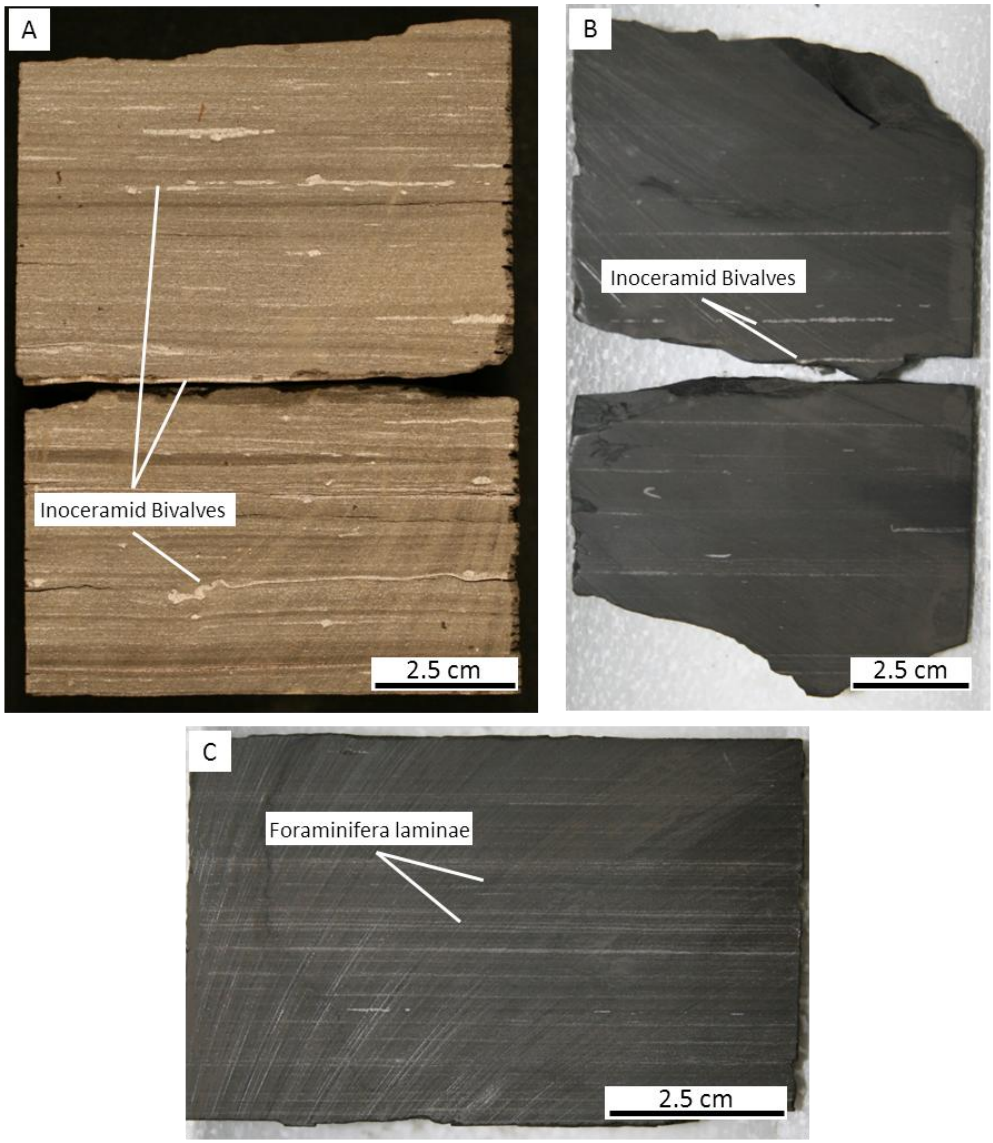
A
Inoceramid Bivalves
2.5 cm
B
Inoceramid Bivalves
2.5 cm
C
Foraminifera laminae
2.5 cm
D
Quartz silt
Globigerinid foraminifera
500 µm
E
Phosphatic bioclast
Globigerinid foraminifera
500 µm

Figure 14: (Previous page) Photographs of laminated calcareous foraminiferal mudrock facies. (A) Slab photo of proximal, weakly laminated, brown mudrock with flattened, bedding parallel inoceramid shells, lower Eagle Ford, Brechtel #1, 3295.9'; (B) Slab photo of weak planar laminations in distal, dark grey mudrock with flattened, bedding parallel inoceramid shells, lower Eagle Ford, Hassett #3, 6220.4'; (C) Slab photo of well-developed planar laminations in dark grey mudrock, Halff etal. #1, 6451.0'; (D) Photomicrograph showing developed coarser-grained foraminifera laminations within organic and clay-size mudrock matrix, lower Eagle Ford, Hassett #3, 6212.8'; (E) Photomicrograph illustrating weak foraminifera laminations within organic and clay-sized mudrock matrix, lower Eagle Ford, Hassett #3, 6220.4'.

content (Fig. 14A). Distal to the arch, this facies is a dark grey mudrock with increased calcite input from calcareous marine sources and decreased clay content (Fig. 14B). Despite these differences, high organic matter content is ubiquitous.

This facies has been interpreted to represent deposition in below storm wave base, anoxic depositional environments. Bioturbation is generally absent, but thin, isolated zones with nearly horizontal *Chondrites* burrows 1-2 centimeters (cm) thick are identifiable. Isolated zones of bioturbation and believed to be associated with short lived oxygenation events, which are well documented during OAEs (Schlanger et al., 1987). However, reoxygenation events during Eagle Ford deposition represent only short durations and rarely detract from widespread organic matter preservation.

Dominant sediment delivery processes include hemipelagic and pelagic sedimentation of marine carbonate, and terrigenous clay and silt-sized quartz. The fine-grained matrix represents both primary sedimentation and resedimentation of the smallest fraction of storm-entrained sediment and fair-weather current transport (Kreisa, 1981). Low sedimentation rates coupled with deposition from waning turbidity flows initiated in more proximal, shallower water environments likely led to the formation of fine (mm scale) laminae of silt-sized globigerinid foraminifera. A full spectrum of lamination

development makes distinguishing between the combined effects of slow sedimentation rates and event-driven turbidity deposition difficult. Due to the lack of well-developed coarser-grained facies, scour surfaces, and peloids seen in higher-energy facies; the effects of current winnowing and resedimentation are interpreted to be minimal in this facies.

FACIES 3: LAMINATED FOSSILIFEROUS WACKESTONE/PACKSTONE

The laminated fossiliferous wackestone/packstone facies is characterized by organic-rich clay- and silt- sized matrix with abundant whole and fragmented skeletal material (Fig. 15). Small fining upward sequences are common and composed of medium grey (silt-sized) to brown (clay-sized) couplets. Bed thickness ranges 10-15 cm with individual couplets measuring < 3 cm and <1 cm (Fig. 15). Proximal to the San Marcos Arch, well-preserved fossiliferous beds consisting of inoceramids and thin-shelled oysters compose most of the whole skeletal component. In distal basinal settings, inoceramid bivalve shells and phosphatic bioclasts constitute the dominate skeletal contribution. Globigerinid foraminifera, phosphatic bioclasts, carbonate intraclasts, ostracods, and echinoid fragments contribute common accessory grains. Normalized XRD analysis shows that carbonate (avg. 55%, range 56-75%), clay minerals (avg. 30%, range 16-42%), and quartz, plagioclase, and K-feldspar (avg. 15%, range 8-26%) constitute the rock matrix.

Shells appear with both random and bedding parallel orientations, indicative of waxing and waning energy conditions (Fig. 15). The thickest fossiliferous wackestone/packstone beds are laterally extensive in the lower Eagle Ford resting on top of massive argillaceous mudrock facies. Thinner (<1 cm), skeletal-rich laminae are

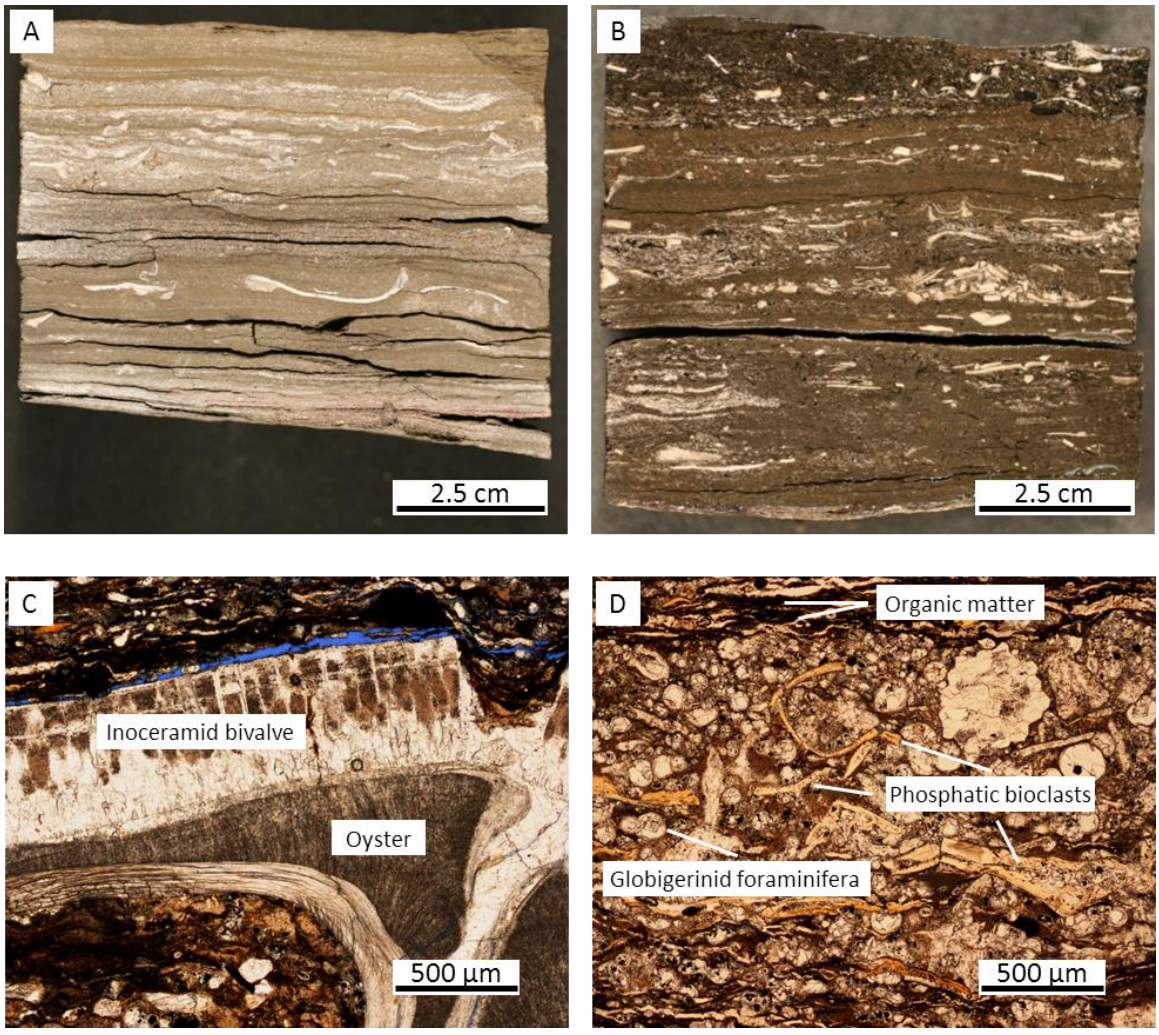

Figure 15: Photographs of laminated fossiliferous wackestone/packstone facies. (A) Slab photo showing whole and fragmented oyster and inoceramid shells within a mudrock matrix, lower Eagle Ford, Hendershot #1, 4771.1'; (B) Slab photo with couplets of fragmented shell debris and mudrock matrix, lower Eagle Ford, Orts #2, 7746.1'; (C) Photomicrograph showing skeletal component consisting of inoceramid and oysters shells with small undifferentiated skeletal debris within mudrock matrix, lower Eagle Ford, Brechtel #1, 3311.5'; (D) Photomicrograph of a coarser-grained couplet consisting of planktonic foraminifera, and phosphatic bioclasts, lower Eagle Ford, Proctor #1, 1961.8'.

found locally interstratified with foraminiferal laminated calcareous mudrock facies of the lower and upper Eagle Ford, but lack abundant thin-shelled oysters . TOC values for fossiliferous wackestone/packstone facies are elevated at 7.2 % (2 samples), with both measured and observed increases in organic matter content along proximal to distal transects of the San Marcos Arch.

Sharply defined bases and normal grading into weakly defined upper contacts within fossiliferous wackestone/packstone facies is interpreted to represent event sedimentation (Flügel, 2009). Graded couplets form when storm-generated turbulence weakens and sediment begins to drop out of suspension clouds (Kreisa, 1981). Between higher-energy laminae, planar laminated, finer-grained mudrocks of fossiliferous wackestone/packstone represent slow sediment accumulation between higher-energy events (Fig. 15). Oxygen-dependent benthic fauna found as randomly oriented, whole and fragmented oysters, ostracods, and echinoids were likely transported from proximal, more oxygenated environments and carried basinward into anoxic depositional environments under which this facies accumulated. Here, oxygen-dependent fauna mixed with pelagic and/or less oxygen-dependent fauna including inoceramid bivalves, phosphatic bioclasts originating from fish, and globigerinid foraminifera under slow sedimentation rates. Evidence of continued anoxia prevailing during deposition of this facies includes elevated organic matter and lack of bioturbation.

FACIES 4: LAMINATED FORAMINIFERAL AND PELOIDAL PACKSTONE

The laminated foraminiferal and peloidal packstone facies, composed of two subfacies, is characterized by light grey, ripple and low angle cross laminated limestone beds within dark grey, organic-rich peloidal packstone matrix. These deposits are typically associated with the dark grey, planar laminated calcareous mudrock facies (Fig.

16). Skeletal packstone beds dominantly consist of well sorted globigerinid foraminifera, fragmented to whole inoceramids, and phosphatic bioclasts of fish bones and teeth. Skeletal packstone beds are typically mm to cm scale but upward ranges of individual beds reach 15 cm in localities proximal to the San Marcos Arch. Skeletal beds show irregular upper and lower bounding contacts. Nearly bimodal grain size distributions across much of the shelf likely are responsible for the observed sharp contacts between skeletal packstone and interstratified peloidal packstones (Fig. 16).

Dark grey, organic-rich peloidal packstone matrix consists of abundant flattened peloids, floating globigerinid foraminifera, phosphatic bioclasts, and bedding parallel organic matter (Fig. 16). Peloids typically range from 50-400 μm in length and <150 μm in height. Compaction of unlithified peloids produces bedding-parallel, elongate forms which manifest as fine-scale, lenticular laminae draped by organic matter (Fig. 16). Organic matter preservation is high at 4.6 % (6 samples). Locally, poorly sorted ellipsoidal carbonate intraclasts consisting of micritic carbonate are present and range in size from 75-150 μm. Carbonate intraclasts likely originated during post-sedimentary reworking of partially cemented calcite and clay matrix, thus lack compactional forms observed in peloids.

The laminated foraminiferal and peloidal packstone facies is found in both lower and upper Eagle Ford rocks where it is appears to grade distally into the laminated calcareous foraminiferal mudrock facies. Distal, weakly developed packstones (Fig. 16C) possess similar mineralogical and TOC compositions to laminated calcareous foraminiferal mudrock facies. However, proximal, well-developed packstone beds (Fig. 16A) within laminated foraminiferal and peloidal packstone facies possess concentrated calcareous tests, skeletal debris, and early diagenetic calcite showing increased carbonate content (avg. 69%, range 47-94%) and decreased organic matter preservation. Organic

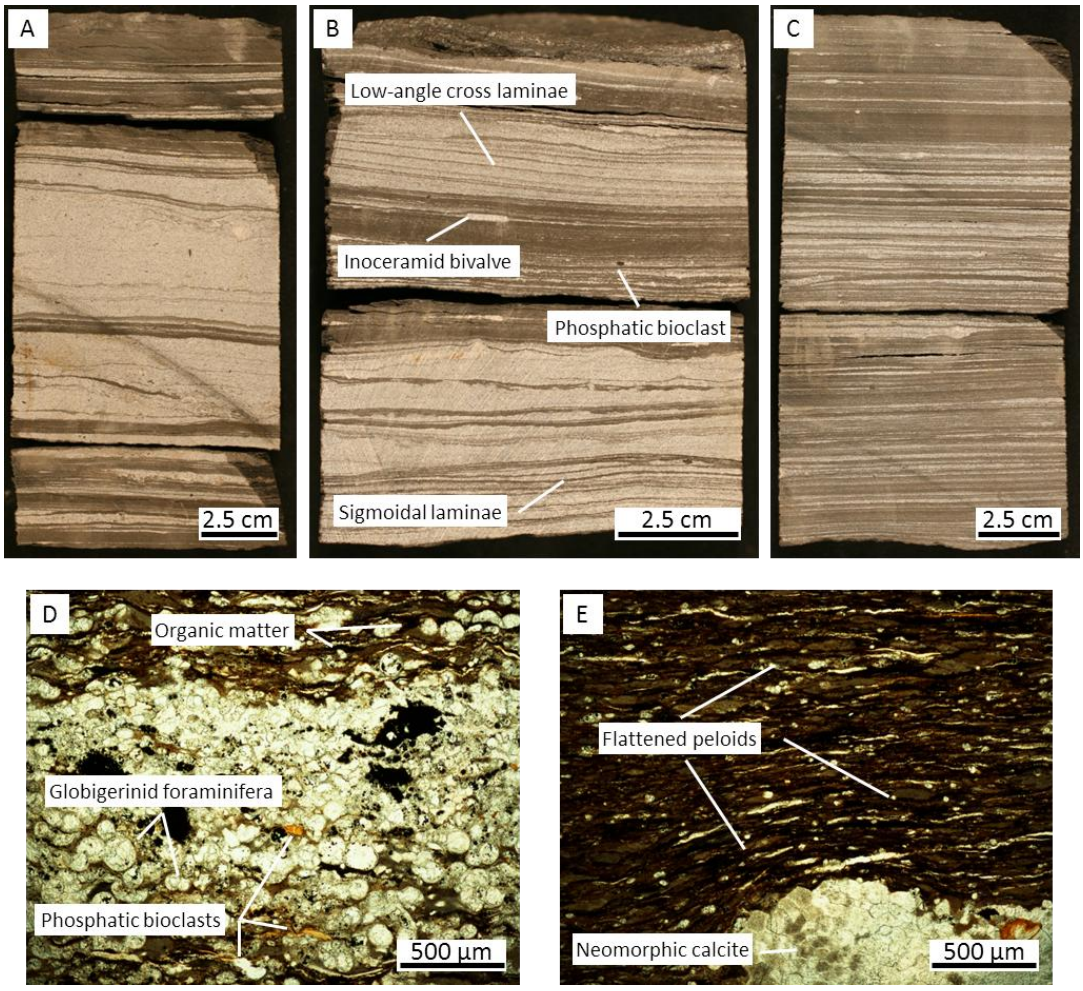

Figure 16: Photographs of laminated foraminiferal and peloidal packstone facies.
(A) Slab photo showing proximal, thick-bedded skeletal packstones exhibiting ripple and cross laminations, lower Eagle Ford, Hendershot #1, 4763.4'; (B) Medium-bedded packstone showing well-developed cross laminations and scour surfaces. Planar laminated peloidal packstone facies possess bedding parallel inoceramid bivalves. Skeletal laminations likely developed during higher-energy events, while organic-rich, planar laminated peloidal packstones represent a shift back to lower-energy sedimentation, core photo, lower Eagle Ford, Blumberg #1, 4213.0'; (C) Distal, thin-bedded skeletal packstone showing starved ripples and mm scale laminae, core photo, lower Eagle Ford, Hendershot #1, 4764.6'; (D) Photomicrograph illustrating irregular nature of the contact between coarser-grained, organic poor, skeletal packstone and finer-grained, organic-rich peloidal packstones, lower Eagle Ford, Hal #1, 2188.7'; (E) Photomicrograph showing loading structures in organic matter and peloids, forming around a skeletal packstone bed with pronounced diagenetic calcite development, lower Eagle Ford, Hal #1, 2188.7'.

matter is commonly restricted to interstratified peloidal packstones (Fig. 16). The remainder of the rock is composed of clay minerals (avg. 18%, range 3-31%) and quartz, plagioclase, and K-feldspar (avg. 13%, range 3-29%).

This facies is interpreted to represent episodic high-energy event deposition in above storm wave base depositional environments. Interstratified packstones developed distal to the San Marcos Arch predominately consist of planktonic foraminifera and inoceramid bivalves, the dominant biota found in the surrounding laminated calcareous foraminiferal mudrock facies. However, packstones proximal to the San Marcos Arch consist of planktonic foraminifera, inoceramid bivalves, echinoids, and oysters. The inclusion of biota more typically associated with oxygenated paleoenvironments and shallow water settings suggests transport between depositional environments. While these more oxygenated environments are not preserved in the rock record, they suggest the lateral proximity of well-oxygenated and anoxic environments during Eagle Ford deposition and transport between these environments during higher-energy event sedimentation. Proximal thickening of packstone beds suggests clay-sized matrix transport away from shallow settings during storm-generated return flow.

Post-depositional reworking by winnowing mud matrix and concentrating of grains that accumulated during pelagic settling. Structures indicative of traction transport, such as sigmoidal cross laminae (Fig. 16B), suggest potential transport as concentrated density flows. Sharp basal contacts of beds were likely generated during compaction forcing of early cemented calcareous grains into underlying sediments. Compaction structures are also observed in overlying mudrocks as they form around early cemented grains (Fig. 16). The presence loading structures indicates early diagenesis of calcareous packstone beds in comparison to surrounding organic-rich peloidal packstones.

Although the exact origin of peloids is currently unclear, relationships between peloid occurrence and bottom-current reworking suggest increased depositional energy contributed to peloid development. Potential processes include water column flocculation and synsedimentary reworking of micrite and clay matrix. Flügel (2009) characterized mud peloids as forming during synsedimentary and post-sedimentary reworking of mud and based their identification on poor sorting, wide variety in size, lack of burrowing (not fecal pellets), and repeated occurrence within specific stratigraphic profiles. Similar characteristics are seen in mixed mud and micrite peloids of the Eagle Ford, potentially indicating similar formational processes.

FACIES 5: MASSIVE TO BIOTURBATED KAOLINITIC CLAYSTONE

Remnants of volcanic ash deposits are common in subsurface Eagle Ford cores and outcrops from Del Rio to Dallas, Texas (Silver, 1963, Charvat, 1985, Surles, 1987, Donovan, 2010). Potential source areas recognized for Eagle Ford volcanics include Arkansas, West Texas, and the Western Interior Seaway (Charvat, 1985). Ash beds identified in the Eagle Ford show highly differentiated textural and mineralogical character from the surrounding mudrocks. Remnant ash deposits are also unique in that they serve as useful water chemistry indicators due to the strong role water chemistry plays in differentiating clay mineralogies within originally similar ash compositions.

Two distinct mineralogical compositions of marine deposited ash are commonly recognized (Potter et al., 2005). The first, typically attributed to open marine processes, involves the reaction of volcanic ash with saline solutions high in potassium. The resulting ash develops a mixed smectite-illite clay mineralogy and is called a bentonite (Potter et al., 2005). The second type of ash composition is commonly attributed to more

terrestrial environments, such as swamps or marshes. In these settings, ashes react in acidic environments and develop a kaolinite-rich clay mineralogy known as a tonstein (Potter et al., 2005).

Massive to bioturbated kaolinitic claystone facies represent diagenetically altered volcanic ash that were deposited in open marine settings yet developed a kaolinite-rich mineralogy indicative of diagenesis in acidic environments. XRD analyses show Eagle Ford volcanic ash consists predominately of clay minerals (avg. 91%, range 85-97%) with low quartz, plagioclase, and K-feldspar (avg. 9%, range 2-15%) and carbonate (avg. <1%). Clay minerals primarily consist of kaolinite (avg. 74%, range 63-84%) and illite (avg. 16%, range 2-25%). Pyrite, in the form of framboids, is present at 3%. While the composition of sampled ash beds is moderately consistent, the physical appearance of this facies is variable with two distinct expressions arising from the presence or lack of burrowing (Fig. 17).

The first type of volcanic ash is a sharp based, sharp topped, massively bedded, light green claystone (Fig. 17B, C). Bed thicknesses in studied cores range from 1-5 cm. This expression of the volcanic ash facies possesses high percentage of kaolinite contribution to the clay mineralogy and commonly lacks bioturbation. Current induced sedimentary structures are also lacking from this facies.

The second expression of volcanic ash is a sharp based, light green to grey, burrowed claystone that is gradational with overlying organic-rich mudrocks (Fig. 17A). Observed bed thicknesses of this claystone increase to 5-10+ cm. Bioturbation increases vertically through the ash bed, increasingly homogenizing the ash with overlying facies and generating varying mineralogical compositions (Fig. 17). Burrowing rarely persists much past the top of ash beds, marking a return to oxygen deficient conditions and a resulting lack in burrowing infauna.

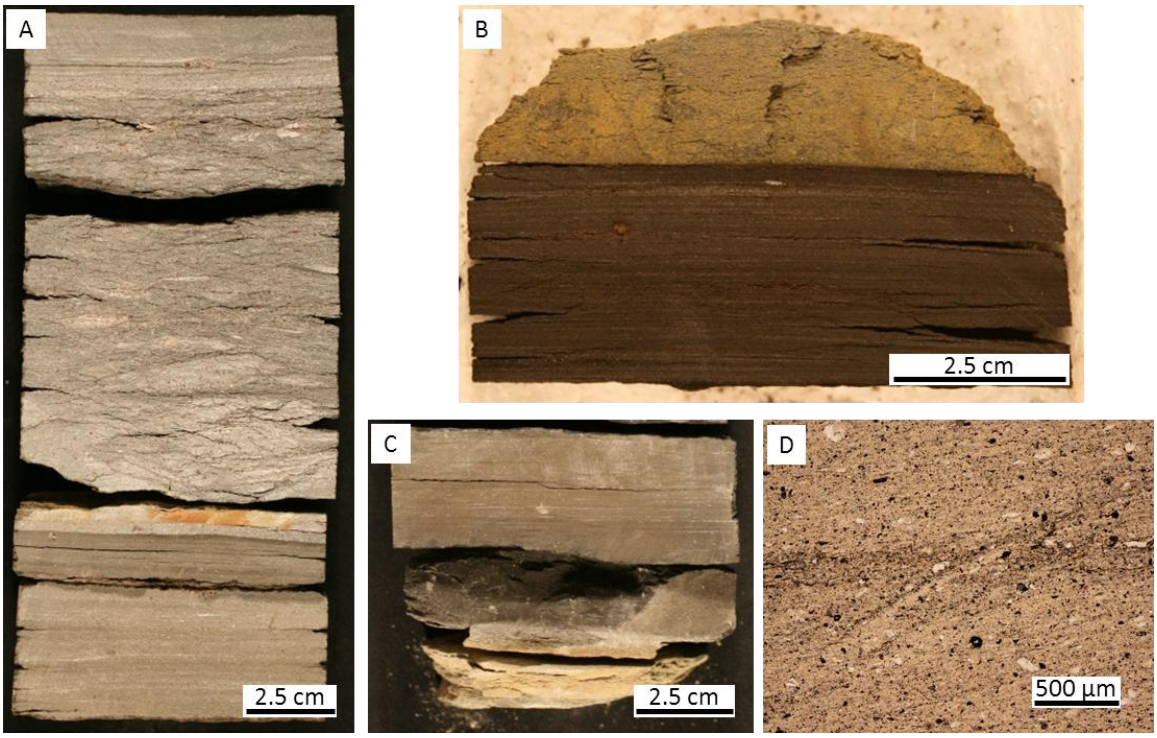

Figure 17: Photographs of massive to bioturbated kaolinitic claystone facies. (A) Burrowed and homogenized ash with sharp base and gradational top into overlying mudrock, core photo, lower Eagle Ford, Blumberg #1, 4196.5'; (B) Volcanic ash showing sharp basal contact with laminated calcareous foraminiferal mudrock, core photo, upper Eagle Ford, Hendershot #1, 4752.9'; (C) Volcanic ash showing sharp upper contact with laminated calcareous foraminiferal mudrock, core photo, lower Eagle Ford, Blumberg #1, 4213.7'; (D) Photomicrograph illustrating massive fabric, lack of calcareous skeletal component, lack of organic matter, and presence of sub-horizontal burrow trace, lower Eagle Ford, Mathews #1-1, 4651.7'.

Both types of volcanic ash are commonly found interstratified with laminated calcareous foraminiferal mudrocks (Fig. 17) in the lower and upper Eagle Ford. The most common stratigraphic occurrence of this facies is near the interpreted lower/upper Eagle Ford contact. Loutit et al. (1998) showed that volcanic ash beds show preferential preservation in condensed horizons due to low-energy and slow sediment accumulation rates. Dawson (2000) also recognized that while ash presence in the Eagle Ford is frequent, stratigraphic abundance varies by location. Eagle Ford cores examined in this study exhibit numerous ash beds, but currently appear uncorrelative between wells.

Massive to bioturbated kaolinitic claystone is interpreted to represent volcanic ash that underwent marine alteration on the seafloor in open marine, slightly acidic to acidic environments. The lack of skeletal allochems (carbonate content), detrital terrigenous material, and organic matter in distal, low-energy environments indicates that volcanic ash were likely deposited under increased depositional rates, preventing the pelagic and hemipelagic accumulations seen in other Eagle Ford facies. Evidence of high-energy transport in subaqueous environments resulting in massive bedded volcaniclastic deposits is well documented (Doronzo et al., 2010). Such high-energy events could potentially lead to mixing of the water column (Manville and Wilson, 2004) and development of short-lived reoxygenation events responsible for the burrowing seen in some ash facies that terminate rapidly with the deposition of overlying organic-rich mudrocks.

FACIES 6: LAMINATED WACKESTONE

The laminated wackestone facies is characterized by well-sorted clay-sized matrix with mm scale ripple laminations of globigerinid foraminifera, phosphatic bioclasts, disaggregated inoceramid bivalve shells, and peloids (Fig. 18). The color of this facies ranges from brown to medium grey (Fig. 18). Laminations exhibit undulatory, erosive

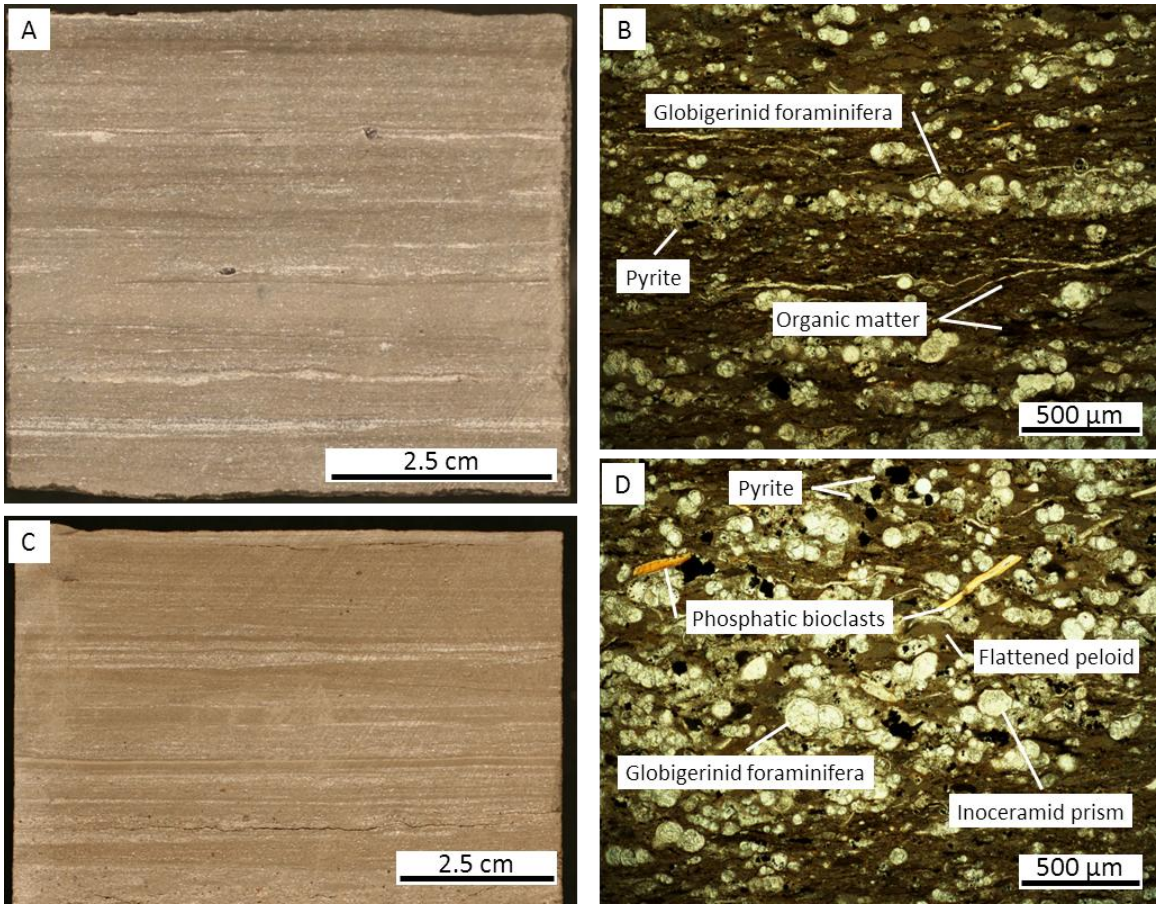

Figure 18: Photographs of laminated wackestone facies. (A) Grey, rippled calcareous mudrock of the upper Eagle Ford near the Maverick Basin, core photo, upper Eagle Ford, Gise #1, 7152.0'; (B) Photomicrograph illustrating wackestone matrix with thin, planar laminations of planktonic foraminifera. Concentrations of flattened peloids occur in close proximity to skeletal laminae, upper Eagle Ford, Shanklin #1, 2124.3'; (C) Brown, rippled calcareous mudrock of the upper Eagle Ford on San Marcos Arch, core photo, upper Eagle Ford, Shanklin #1, 2126.6'; (D) Photomicrograph of a skeletal ripple, consisting of planktonic foraminifera, inoceramid prisms, phosphatic fish bones and teeth, and peloids, with a scour surface into the underlying matrix, upper Eagle Ford, Shanklin #1, 2124.3'.

bases which appear to truncate up to several mm into underlying beds (Fig. 18). Phosphatic bioclasts and flattened peloids are occasionally present along laminae within the matrix, while coarser-grained laminations exhibit concentrations of phosphatic skeletal material and flattened peloids. Imbricate orientations of phosphatic bioclasts and peloids are indicative of current transport (Fig. 18).

Normalized XRD analysis shows this facies is composed of carbonate (avg. 66%, range 11-89%), clay minerals (avg. 19%, range 8-52%), and quartz, plagioclase, and K-feldspar (avg. 15%, range 4-37%). Carbonate is predominately found in the form micrite and coarser-grained globigerinid foraminifera, peloids, and locally abundant micritic intraclasts. Pyrite, in the form of framboids and larger crystals, is present at 2 %. Grain-rich laminations commonly lack organic matter; however, organic matter is commonly dispersed in the mud matrix as horizontal, laterally discontinuous streaks ranging from 50-150 μm in length. TOC values average 1.6 % (6 samples) and range from 1.0 and 2.5 %. Burrowing is commonly absent. However, in the transitional Eagle Ford of the Maverick Basin this facies is cyclically bedded with bioturbated lime wackestone facies and *Planolites* and *Chondrites* burrows occasionally penetrate the top few cm of laminated wackestone beds. Laminated wackestone facies also occur locally thickly bedded in upper Eagle Ford rocks on the San Marcos Arch.

Deposition of laminated wackestone facies occurred in subtidal, proximal depositional environments commonly susceptible to current reworking. Ripple laminations and starved ripples developed during concentration of coarse-grains due to active reworking and traction transport, commonly scouring into underlying finer-grained rock matrix (Fig. 18). Massive and weakly planar laminated globigerinid foraminifera in the rock matrix suggest low-energy sedimentation prevailed between higher-energy

events. Evidence of prolonged oxygen depletion seen in this facies includes low faunal diversity, low faunal abundance, lack of burrowing, and partial organic matter enrichment.

FACIES 7: DISRUPTED BEDDED FORAMINIFERAL PACKSTONE

Disrupted bedded foraminiferal packstone facies, consisting of two subfacies, are characterized by white to light grey colored, cm scale, discontinuous bedded and starved ripple laminae within a brown, mixed skeletal and mud matrix (Fig. 19). Coarser-grained laminae are predominately composed of moderately sorted 50-150 μm planktonic foraminifera tests with accessory, sub-parallel inoceramid bivalve prisms and phosphatic bioclasts (Fig. 19D). Massive, clay- to coarse-size matrix consists of well-abraded inoceramid bivalve shells with accessory textural components consisting of silt-to coarse-sized phosphatic bioclasts and planktonic foraminifera (Fig. 19C). Compaction generated laminae of sub-parallel organic matter (<1500 μm) commonly drape skeletal grains in the rock matrix (Fig. 19C).

Carbonate found in the rock matrix and skeletal debris combine to contribute an average content of 59% (range 51-67%). The organic-rich matrix (8.1%, 2 samples) consists of mixed clay minerals (avg. 29%, range 28-30%) and quartz, plagioclase, and K-feldspar (avg. 12%, range 5-19%). Pyrite (2 %) in the form of framboids, crystals, and nodules are commonly developed in the clay-sized matrix (Fig. 19). Bioturbation is absent from this facies.

The disrupted bedded foraminiferal packstone facies is found locally on the San Marcos Arch near the top of the upper Eagle Ford. Individual beds range from 0.5 to 5 ft in thickness and are commonly thinly interbedded with massive inoceramid packstone

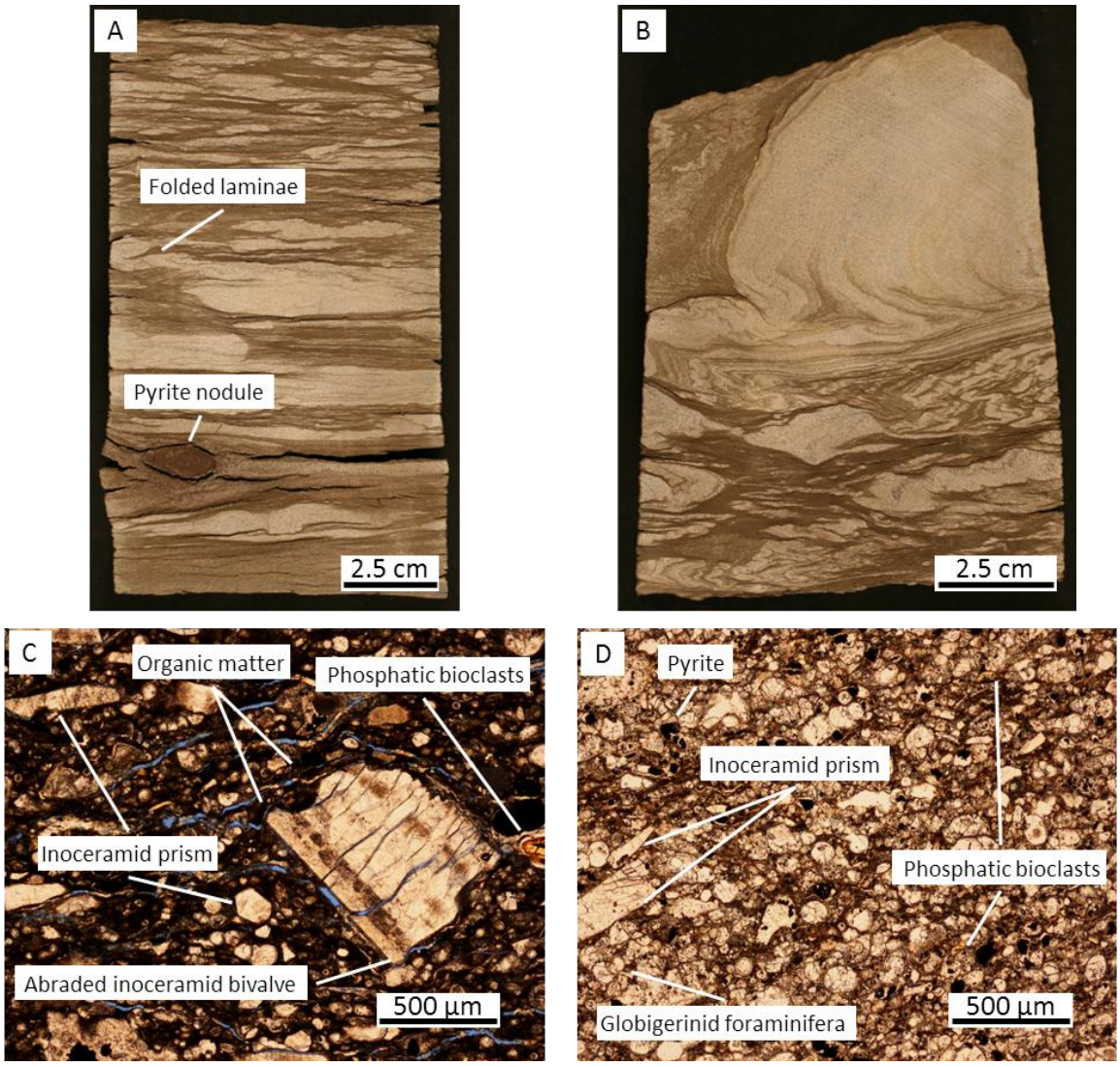

Figure 19: Photographs of disrupted bedded foraminiferal packstone facies. (A) Light-colored discontinuous laminae and starved ripples showing vertical compaction and horizontal compression related deformation within a brown matrix, core photo, upper Eagle Ford, Hendershot #1, 4735.3'; (B) Syndepositional slumping within coarser-grained subfacies, core photo, upper Eagle Ford, Hendershot #1, 4737.2'; (C) Photomicrograph showing abraded inoceramid bivalve shells and phosphatic bioclasts within organic-rich matrix, upper Eagle Ford, Hendershot #1, 4739.5'; (D) Photomicrograph illustrating silt- to coarse-grained nature of skeletal laminae, upper Eagle Ford, Shanklin #1, 2110.4'.

facies. Compaction related deformation and small-scale slumping/folding structures are apparent throughout (Fig. 19). The orientation of sub-horizontal inoceramid fragments, ostracods, and phosphatic bioclasts in both skeletal-rich laminae and the rock matrix indicate bottom-current reworking and transport. However, transported skeletal debris lack a well-developed orientation. High concentrations of organic matter and clay-sized mud in the rock matrix likely indicate episodic waning and waxing energy conditions, allowing accumulation of clay-sized matrix between higher-energy events.

Due to its limited expression, distinguishing the formational processes responsible for the distribution, sedimentological character, and high TOC of disrupted bedded foraminiferal packstone facies is difficult. Surles (1987) identified several outcrop locations surrounding the East Texas Basin that exhibited similarly high TOC values (>8%), representing the highest TOC's recognized in the Eagle Ford of the East Texas Basin. Surles attributed these proximal zones with surprisingly high TOC values to deposition within deltaic marginal embayments. Here, restricted conditions allowed increased organic matter preservation.

Although the disrupted bedding, slumping, and elevated TOC values can be attributed to deposition in near-shore environments such as marginal embayments; several characteristics of this facies indicate they likely developed in more distal depositional environments. One of the largest pieces of evidence that this facies is not deltaic in origin is the lack of titanium, a proxy for terrestrial sediment sourcing commonly recognized in XRF elemental analyses of Eagle Ford cores (Fig. 33). Also, the concentration of foraminifera and amount of abrasion seen in skeletal remains is not typical of restricted near-shore depositional environments. Disrupted bedded foraminiferal packstone more likely developed in open marine settings where episodic,

high-energy current reworking generated accumulation of coarser-grained laminae. Post depositional changes in slope and/or liquefaction likely produced down-slope transport of this facies, resulting in the slumped and folded character clearly identified in core.

FACIES 8: MASSIVE INOCERAMID PACKSTONE

The massive inoceramid packstone facies is characterized by brown, massively bedded, coarse-grained skeletal debris in a mixed micrite and clay mineral matrix (Fig. 20). Grains consist primarily of disaggregated inoceramid bivalve shells with accessory globigerinid foraminifera, echinoderms, and phosphatic bioclasts (Fig. 20). Inoceramid bivalve prisms constitute the largest and most abundant grains, ranging in size from 75-400 μm (Fig. 20C). Foraminifera and fragmented echinoids range in size from 50-200 μm. Foraminifera tests are calcite and pyrite filled, showing signs of early diagenesis through well-preserved test shape. Inoceramid prisms are horizontal to sub-horizontal and possess a fitted texture from mechanical compaction (Dawson, 1997). However, some intragranular porosity seems to have survived compaction (Fig. 20). Evidence of bioturbation is absent from this facies.

Normalized XRD analysis shows this facies possesses high carbonate content (70%) with clay minerals (25%) and accessory quartz, plagioclase, and K-feldspar (5%). Pyrite (<3 %) and apatite (<3 %) are additional matrix components. Organic matter occurs as small streaks commonly draping skeletal grains (Fig. 20C). The lone TOC sample collected from this facies measured 1.3 %. Limestone intraclasts found in the base of massive argillaceous packstone facies (Fig. 20) indicate early diagenesis of underlying beds preceding deposition of this facies. Intraclasts are elongate with the maximum axis in a bedding parallel orientation (Fig. 20A), likely developed during transport.

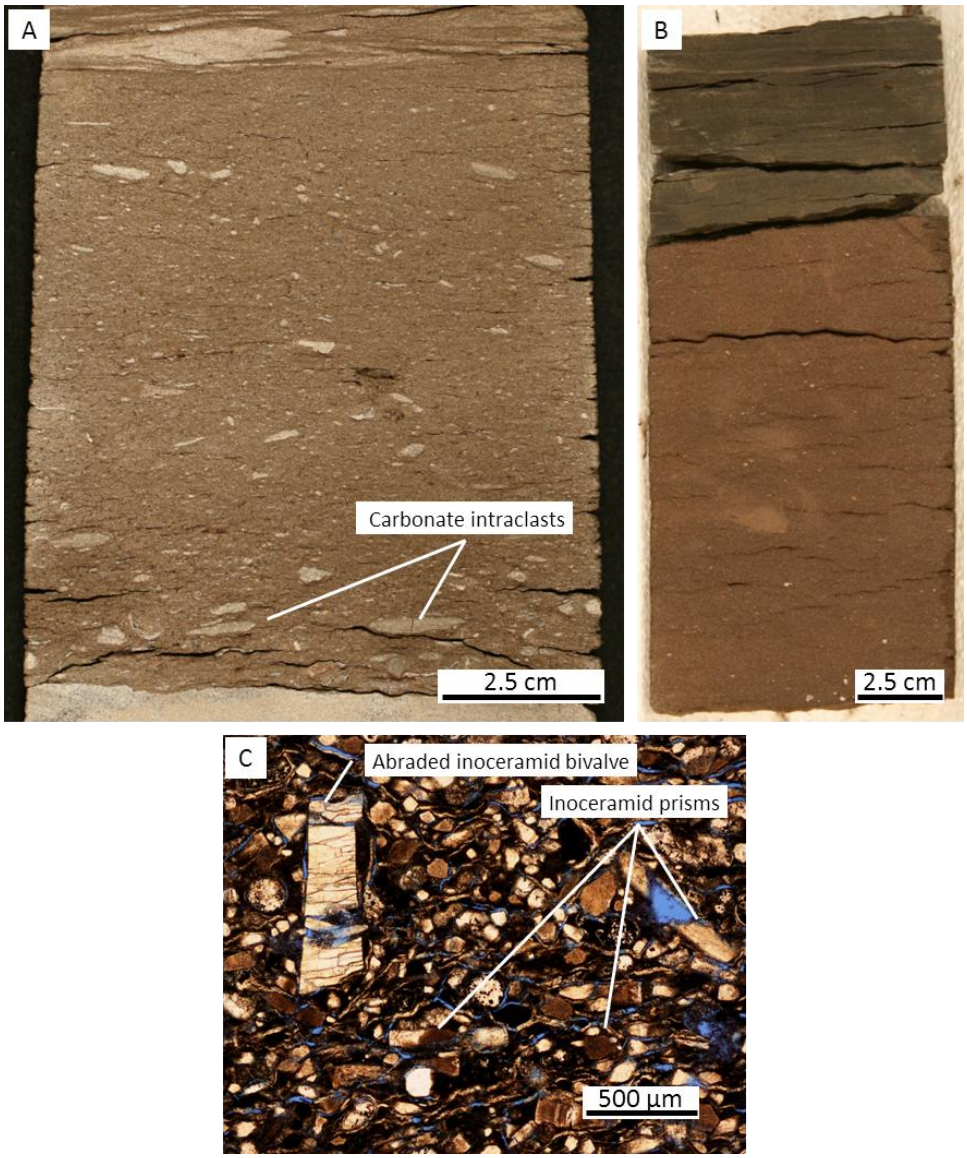

Figure 20: Photographs of massive inoceramid packstone facies. (A) Calcareous rip-up clasts within basal massive inoceramid packstone, sharply overlain by disrupted bedded foraminiferal packstone facies, core photo, upper Eagle Ford, Hendershot #1, 4738.9'; (B) Distal inoceramid packstone showing sharp upper contact with laminated calcareous foraminiferal mudrock facies, core photo, upper Eagle Ford, Hendershot #1, 4744.8'; (C) Photomicrograph illustrating grain-rich, transported fabric, upper Eagle Ford, Hendershot #1, 4745.5'.

Massive inoceramid packstone facies is found in upper Eagle Ford rocks along the axis of the San Marcos Arch. Stratigraphic abundance and, to a lesser degree, bed thickness show decreases off the arch toward the Stuart City reef margin. This facies is commonly sharply bounded by disrupted bedded foraminiferal packstone and laminated calcareous foraminiferal mudrock (Fig. 20). While found interbedded with both proximal (disrupted bedded foraminiferal packstone) and distal (laminated calcareous foraminiferal packstone) facies, the geographic extent of this facies is limited to the northeastern flank of the San Marcos Arch. Due to the nature of fabric texture, bounding contacts, and bed geometry, this facies is interpreted as a cohesive density flow as described by Mulder and Alexander (2001). Flows likely originated from more proximal, grain-rich, settings and were driven by gravity basinward into more distal facies associations.

FACIES 9: BIOTURBATED LIME WACKESTONE

The bioturbated lime wackestone facies is characterized by massive, highly bioturbated, micritic calcite matrix with planktonic foraminifera tests and inoceramid bivalve shells (Fig. 21A). Accessory skeletal material include calcispheres, echinoids, ostracods, and phosphatic bioclasts (Fig. 21B). Skeletal material commonly lack hydrodynamic sorting and appear to "float" in the rock matrix. Authigenic microspar to sparry calcite is locally abundant. XRD analysis show this facies possesses elevated carbonate at 90%, with only minor influx of quartz, plagioclase, and K-feldspar (7%) and clay (3%). This facies ranges in color from white to grey, relating to both clay and organic matter content. TOC values in bioturbated lime wackestone facies average 0.88% (2 samples). Intense burrowing and compaction commonly masks individual burrows; yet, *Zoophycos*, *Thalassinoides*, *Planolites*, and *Chondrites* traces are evident.

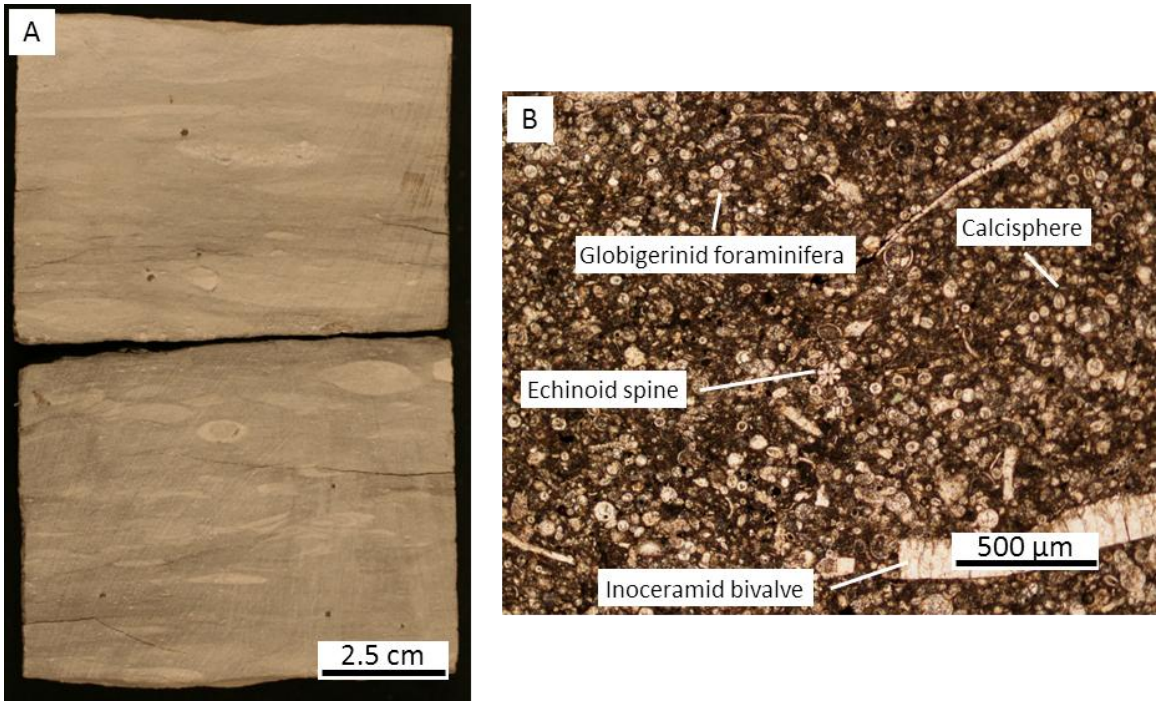

Figure 21: Photographs of bioturbated lime wackestone facies. (A) Light grey bioturbated lime wackestone showing intense bioturbation, core photo, upper Eagle Ford, Blumberg #1, 4180.4'; (B) Photomicrograph illustrating clay-sized matrix with silt-sized and coarser skeletal components including globigerinid foraminifera, inoceramid bivalves, echinoid spines, and calcispheres, lower Eagle Ford, Brechtel #1, 3311.5'.

Bioturbated lime wackestone facies is uncommon on the San Marcos Arch, where it occurs thinly bedded (< 4") in both lower and upper Eagle Ford rocks. However, in the Maverick Basin, this facies is widespread in the transitional Eagle Ford. Here, bioturbated lime wackestone facies are highly-cyclic bedded with laminated wackestone facies. High-energy event beds such as current-generated density flows and volcanic ash beds typical of both the lower and upper Eagle Ford are rare to absent in this facies. Sepkoski and Bambach (1979) showed that bioturbation increases on modern shelf environments quickly erase storm-generated sedimentary structures. Bioturbated lime wackestone facies of the transitional Eagle Ford in the Maverick Basin in some cases contain weak laminations generated during bottom-current reworking, but laminae are commonly absent due to homogenization during early bioturbation. Preservation of laminae appears partly due to early diagenetic calcite development.

The carbonate-rich mud matrix in this facies is believed to have accumulated mostly during pelagic settling of calcareous nannofossils, typically coccoliths, and planktonic foraminifera under low-energy, subtidal depositional environments. Oxygenated sea floor conditions led to intense bioturbation and homogenization of sediments during sedimentation.

EAGLE FORD SUBSURFACE STRATIGRAPHY

For this study, wireline logs calibrated from core investigation were used to identify and project Eagle Ford correlations through the subsurface of South Texas. Characteristic differences in mineralogy, fauna, facies assemblages, and organic carbon content as seen in core led to differentiation of previously recognized lower and upper Eagle Ford members (Grabowski, 1984, Hentz and Ruppel, 2010) into lower, upper, and transitional members of the Eagle Ford Formation (Fig. 22, 23). Characteristic wireline log response for the lower, upper, and transitional Eagle Ford make it possible to document the geographic extent, regional thickness trends, and stratigraphic relationships of the Eagle Ford in South Texas (Fig. 24).

LOWER EAGLE FORD DEPOSITIONAL SUCCESSION

Lower Eagle Ford rocks regionally overlie the Buda Limestone (Fig. 22, 23). This contact is marked by a sharp lithologic shift from highly-bioturbated, light to medium grey wackestones of the Buda to well-bedded, dark grey organic-rich mudrocks of the lower Eagle Ford. The distinct lithologic character shift at the Buda/Eagle Ford contact is interpreted as a widespread depositional hiatus recording the Mid-Cenomanian Unconformity (Addy and Buffler, 1984). This unconformity has been tied to lowering of global sea level and subaerial exposure of the shallow Buda platform beyond the shelf margin, while intrashelf basins such as the East Texas Basin and Maverick Basin experienced continued deposition (Salvador, 1991). Nondeposition and subaerial erosion likely characterize uppermost Buda rocks before initial Eagle Ford sedimentation began. On wireline logs, the Buda/Eagle Ford contact is recognizable by a sharp upward increase to higher gamma ray and sharp to gradational upward increase to higher resistivity response (Fig. 24).

Recognition of the lower Eagle Ford member is facilitated by characteristically high gamma ray values of the Eagle Ford Formation. Resistivity logs show an upward decreasing trend through the lower Eagle Ford, to the lower/upper Eagle Ford contact where the lowest resistivites of the Eagle Ford Formation are commonly observed.

The distribution of the lower Eagle Ford member covers the entirety of the study area (Fig. 22, 23). However, identified thicknesses vary considerably. On the San Marcos Arch, the lower Eagle Ford exhibits marked thinning. Preliminary wireline log correlations suggest thinning of basal lower Eagle Ford sediments onto the arch was primarily depositional (Fig. 22, 23). Moving from the San Marcos Arch, the lower Eagle Ford thickens to the southeast towards the Stuart City reef margin and to the southwest into the Maverick Basin. Approaching the Stuart City reef margin along the axis of the San Marcos Arch produces thickening of the lower Eagle Ford to 110 ft in De Witt County (Fig. 23). Similar thicknesses of 100-120 ft are found in the lower Eagle Ford of Frio and La Salle Counties along the margins of the Maverick Basin (Fig. 22). The thickest lower Eagle Ford succession is found in central Maverick County within the Maverick Basin, where the lower Eagle Ford member is commonly 175-200 ft thick and reaches maximum thicknesses of >200 ft (Hentz and Ruppel, 2010).

The lower Eagle Ford is overlain by the upper Eagle Ford over most of the study area (Fig. 22, 23). However, in the shallow Browne # 8 core on the northeast flank of the San Marcos Arch (Fig. 4), the entire Eagle Ford is 8 ft thick and bound by sharp lithologic contacts with bioturbated limestones of the underlying Buda Formation and the overlying Austin Formation. The thin Eagle Ford interval here appears related to lower Eagle Ford facies assemblages and suggests nondeposition or truncation of the upper Eagle Ford.

UPPER EAGLE FORD DEPOSITIONAL SUCCESSION

Dawson (1997) interpreted the contact between the upper and lower Eagle Ford in outcrops as associated with an unconformity stemming from a second-order maximum flood and shift in depositional style from transgressive systems tract lower Eagle Ford to highstand systems tract upper Eagle Ford (Dawson, 1997). On logs, this contact is recognized by a sharp upward decrease to lower gamma ray and shift to increasing resistivity (Fig. 22, 23). In core, the lithologic expression of this contact varies and often proves difficult to distinguish, requiring wireline logs to facilitate consistent recognition.

The wireline log signature of the upper Eagle Ford is characterized by lower maximum gamma ray values than the lower Eagle Ford. In the upper Eagle Ford, gamma ray values typically range from 45-60 API units with sparse, thin beds reaching 120 API units (Hentz and Ruppel, 2010). Upper Eagle Ford rocks also commonly manifest upward increasing resistivity trends beginning at the lower/upper Eagle Ford contact. On the San Marcos Arch, the top of the upper Eagle Ford is marked by a sharp increase on the resistivity log (Fig. 22, 23).

Like the lower Eagle Ford, the upper Eagle Ford is thinnest on the San Marcos Arch and thickens toward the Stuart City reef margin and into the Maverick Basin. Proximal to the Stuart City reef margin in De Witt County, the upper Eagle Ford thickens to 115 ft (Fig. 23). However, highly variable upper Eagle Ford thicknesses are recognized proximal to the shelf edge. From the San Marcos Arch to the southwest, the upper Eagle Ford maintains consistent thickness (< 45 ft) to near the margin of the Maverick Basin, where thickness increases markedly (Fig. 22). The thickest upper Eagle Ford rocks are found in north-central Maverick County with common thicknesses of 250-300 ft and maximum thicknesses of >300 ft.

Historically, thickness trends of the upper Eagle Ford have been attributed to the variable nature of the upper Eagle Ford-Austin contact (Brown & Pierce, 1962, Montgomery, 1991). In outcrops on the San Marcos Arch, Turonian age upper Eagle Ford rocks are unconformably overlain by Coniacian Austin (Jiang, 1989, Liro, 1994, and Dawson, 1997). Upper Turonian and lower Coniacian rocks are missing in this area due to non-deposition and/or truncation (Surles, 1987). However, several authors (Montgomery, 1991, Hentz and Ruppel, 2010, Phelps, 2011) have interpreted the upper Eagle Ford of the Maverick Basin to be gradational with the overlying Austin (Fig. 22, 23). When compared to the lower Eagle Ford, the upper Eagle Ford shows increased rates of thinning onto the San Marcos Arch. While the possibility of depositional thinning onto the lower accommodation San Marcos Arch is not contested, internal markers within the upper Eagle Ford also suggest truncation of upper-most upper Eagle Ford beds begins near the margins of the Maverick Basin and increases in magnitude toward the San Marcos Arch (Fig. 22, 23).

Regionally, the upper bounding contact of the upper Eagle Ford is highly variable. Over most of the study area, the upper Eagle Ford possesses a sharp lithologic contact with the overlying Austin Formation (Fig. 22, 23). In the Maverick Basin, the transitional Eagle Ford member overlies the upper Eagle Ford (Fig. 22).

TRANSITIONAL AUSTIN-EAGLE FORD DEPOSITIONAL SUCCESSION

The transitional Eagle Ford in the subsurface of South Texas overlies the upper Eagle Ford (Fig. 23). The contact is recognizable by a sharp lithologic shift from dark grey, organic-rich, calcareous mudrocks of the upper Eagle Ford to light and dark colored, cyclic-bedded wackestones of the transitional Eagle Ford. Light colored beds of

the transitional Eagle Ford are characterized by common bioturbation and locally abundant neomorphic spar (Fig. 25). Occasionally, faint and discontinuous laminae are preserved in bioturbated lime wackestone facies. The dark beds, laminated wackestone facies, lack significant bioturbation and preserve bedding structures indicative of bottom-current reworking and transport (Fig. 25).

On logs, the upper/transitional Eagle Ford contact is identifiable by a sharp upward increase in gamma ray followed by a highly irregular gamma ray with API values similar to or slightly lower than those seen in the upper Eagle Ford (Fig. 25). A second, high gamma ray spike is characteristic in the lower transitional Eagle Ford (Fig. 22, 24). Trends of upward-increasing resistivity in the upper Eagle Ford become more uniform near the top of the upper Eagle Ford (Fig. 24)

Unlike the lower and upper Eagle Ford, the transitional Eagle Ford shows restricted development to distal depositional environments surrounding the Maverick Basin. Here, observed thicknesses of 90-125 ft are common (Fig. 22). Approaching the San Marcos Arch, the transitional Eagle Ford thins and undergoes a distinct character change to bioturbated, organic-lean facies of the Austin Formation (Fig. 22).

Highly cyclic laminated wackestone facies decrease in abundance vertically through the transitional Eagle Ford as bioturbated lime wackestone facies become increasing prominent. At the stratigraphic contact with the overlying Austin Formation, the cyclic nature of transitional Eagle Ford facies disappears. Laminated wackestone facies occur sporadically and thinly bedded through the Austin Formation, but lack the cyclicity seen in the transitional Eagle Ford member. As such, the transitional Eagle Ford is interpreted to be a gradational transition between anoxic, organic-rich upper Eagle Ford and oxic, organic-lean Austin rocks (Fig. 22, 25).

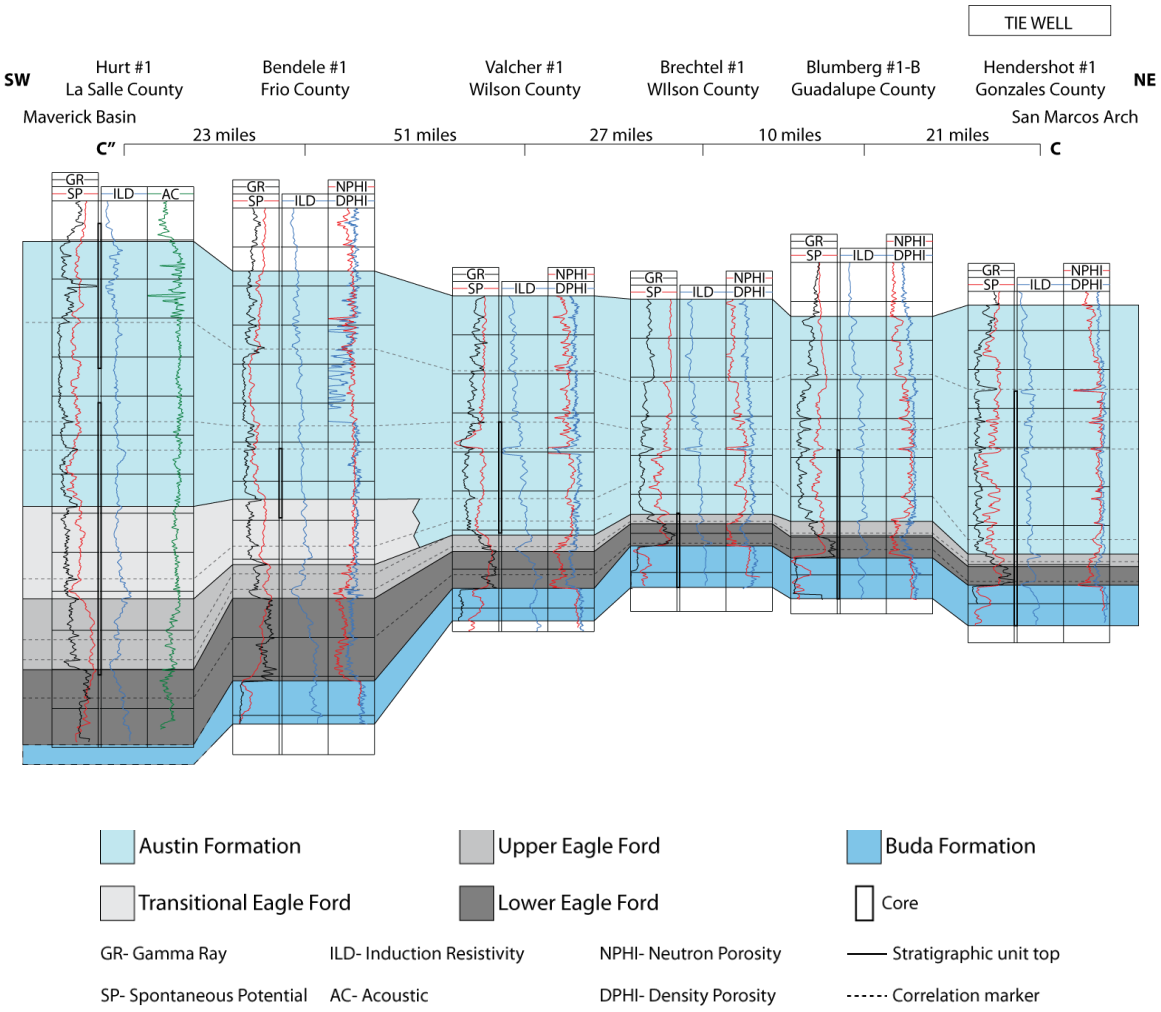

Figure 22: Southwest-Northeast cross section (C-C") showing lower, upper, and transitional Eagle Ford members in the San Marcos Arch to Maverick Basin area. Increased accommodation off of the San Marcos Arch to the southwest caused thickening of the lower and upper Eagle Ford and the development of the transitional Eagle Ford. Line of section shown in Figure 4. Datum: Marker bed within Austin Formation.

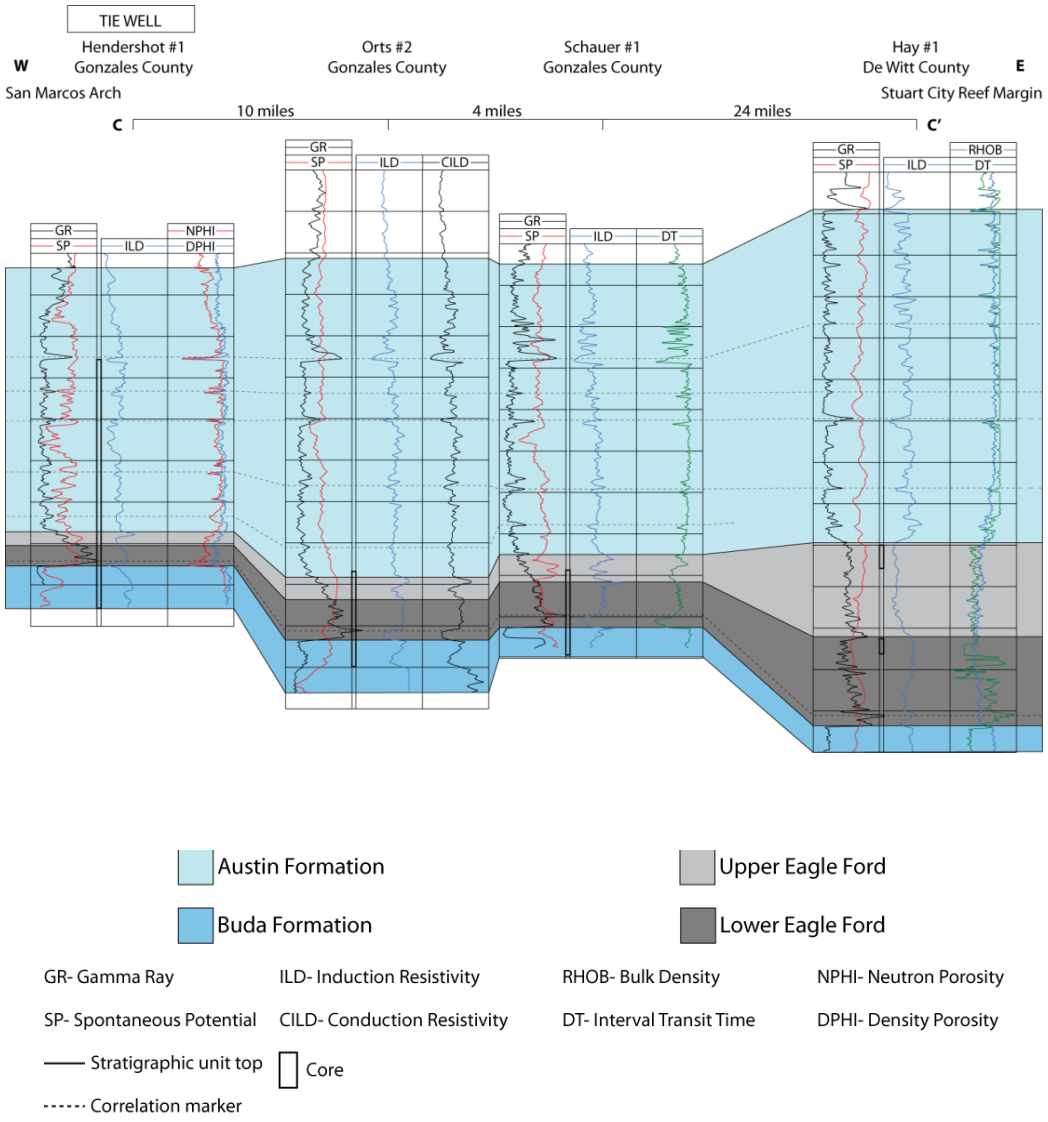

Figure 23: West–East cross section (C-C') showing thicknesses and bounding contacts of lower and upper Eagle Ford members in the San Marcos Arch to Stuart City reef margin area. Line of section shown in Figure 4. Datum: Marker bed within Austin Formation.

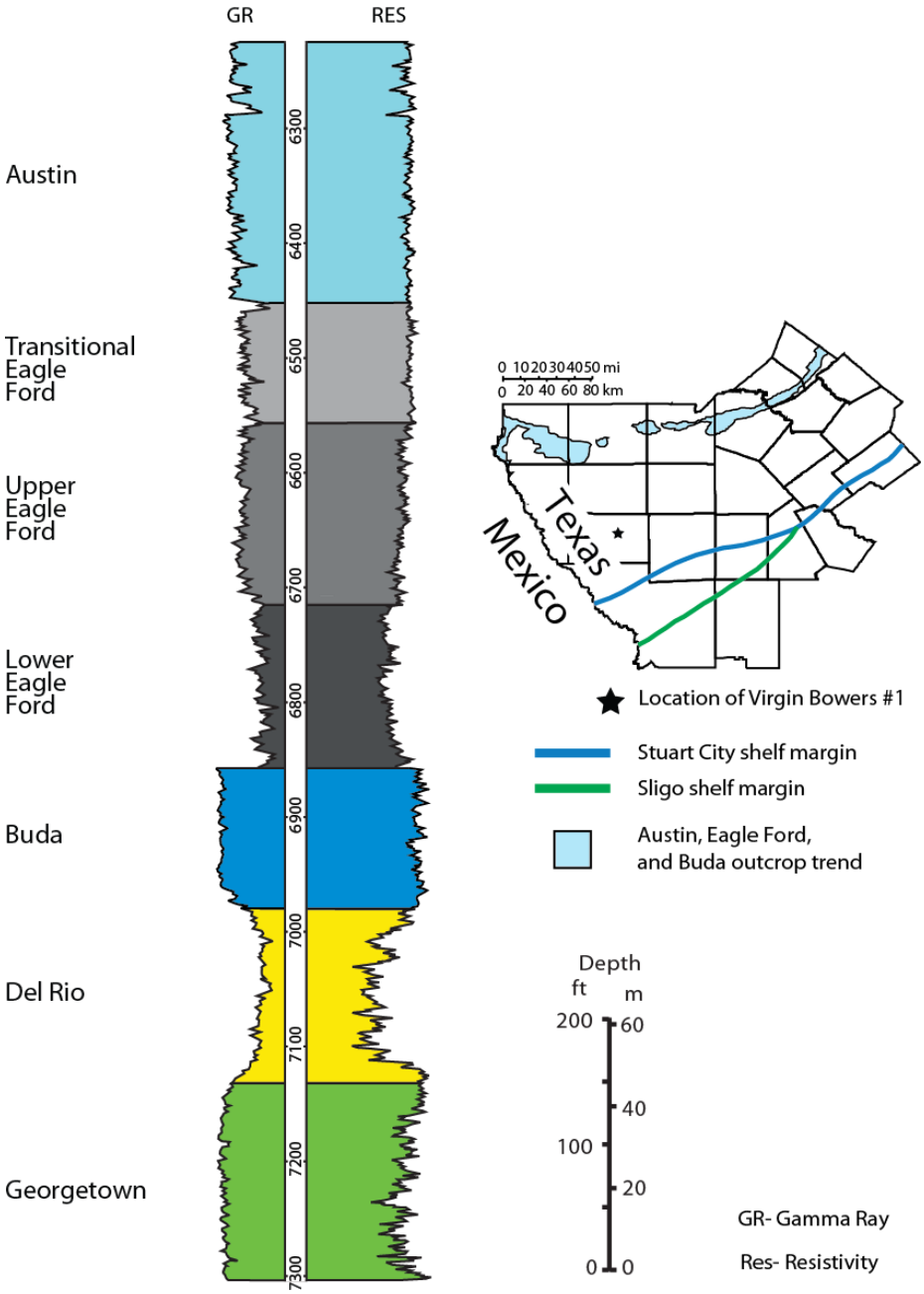

Figure 24: Typical gamma ray and resistivity response for Early to Late Cretaceous carbonates and mudrocks in South Texas. Lower, upper, and transitional Eagle Ford members possess characteristic log responses facilitating identification and correlation through the subsurface of South Texas. Vertical well depths are shown in ft. Virgin Bowers #1, Dimmit County, Texas. Location of the study area is shown in Figure 3. Modified after Hentz and Ruppel (2010).

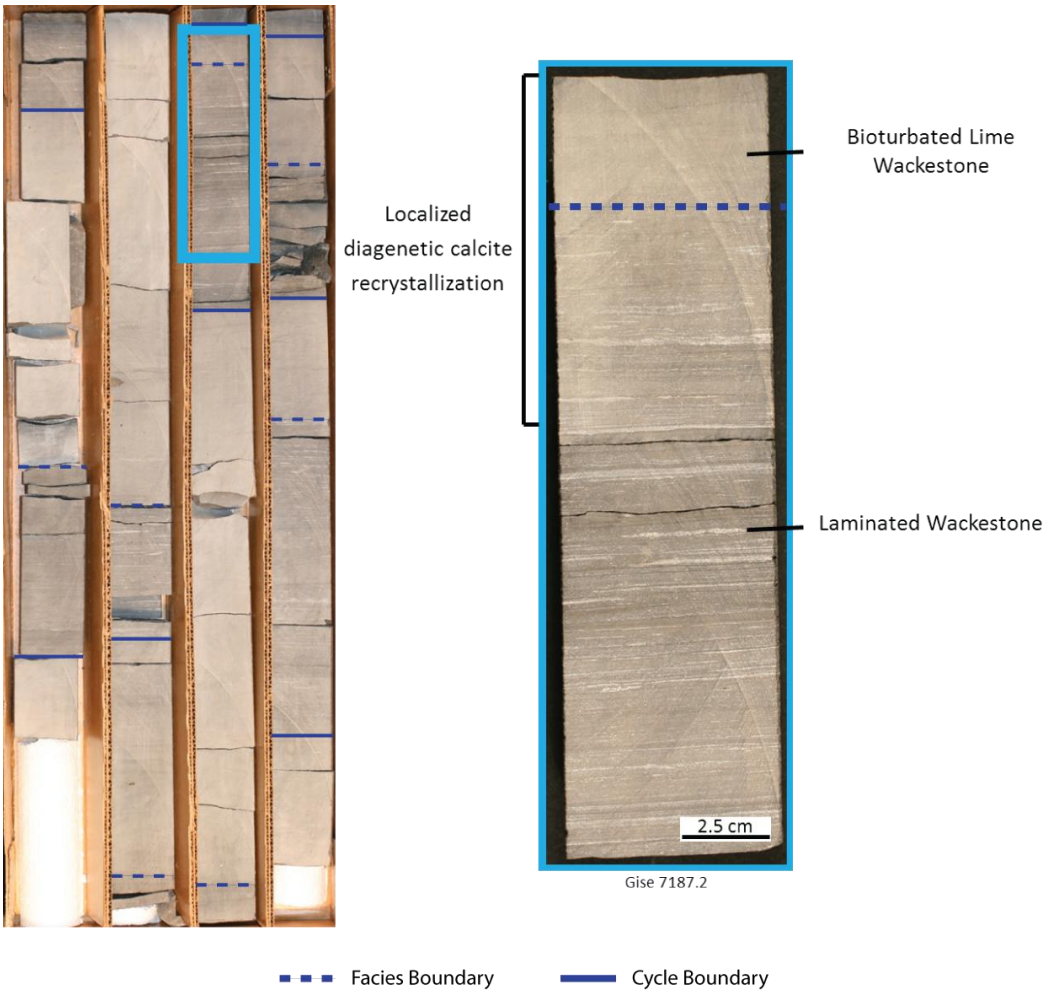

Figure 25: Photographs of **t**ransitional Eagle Ford facies association. Transitional Eagle Ford facies consist of highly-cyclic bioturbated lime wackestone (cycle top) and laminated wackestone (cycle base) facies. Microspar/pseudospar calcite is locally developed, generating a gradational appearance between facies, core photo, Gise #1, 7181.1-7193.0'.

DIAGENESIS AND STABLE ISOTOPE GEOCHEMISTRY

The Eagle Ford Formation in the subsurface of South Texas exhibits evidence of localized to widespread diagenesis, commonly resulting in the formation of microspar/pseudospar calcite and pyrite. Relationships between these diagenetic products and surrounding strata suggest early recrystallization and/or cementation occurred in the shallow subsurface before substantial compaction occurred. Documenting diagenetic products in mudrocks is not only important because they act as key indicators as to conditions existing near the sediment-water interface at the time of deposition; but also because of their potential effects on source and reservoir character of the Eagle Ford.

MICROSPAR/PSEUDOSPAR CALCITE

Microspar/pseudospar calcite is characterized by light grey, silt-sized calcite matrix with individual crystals commonly ranging from 5-50 μm. In the Eagle Ford, microspar/pseudospar is found almost exclusively associated with early diagenetic concretions. Relationships between organic-rich, black shale successions and concretions are well documented (Weeks, 1953, Siegel et al., 1987, Lash and Blood, 2004, Loucks and Ruppel, 2007). However, the size, shape, mineralogical and chemical compositions, and formational processes behind concretion development vary considerably (Coleman, 1993, Handford, 1986). Confusion surrounding concretions often arise from differences in opinion as to what constitutes a concretion and the processes involved in their formation. Several common forms of concretions have been described in shale successions; these include oblate ellipsoids (Lash and Blood, 2004), elliptical to spherical, hard, typically calcareous masses with sharp contacts, commonly nucleating around calcareous fossil debris (Potter, 2005), irregularly formed (Gary et al., 1977), and

laterally extensive beds (Coleman, 1993). Due to the inability to accurately constrain the dimensions of microspar/pseudospar concretions from core studies, concretions are defined in this study as rock fabric consisting of a "mass or aggregate of mineral matter" (Gary et al., 1977) exhibiting distinct compositional variability from surrounding rocks.

In concretions, normalized XRD analyses show high volumes of calcite (avg. 84%, range 71-92%) with accessory quartz, plagioclase, and K-feldspar (avg. 8%) and clay minerals (avg. 8%). Sedimentary structures within concretions vary between massive, planar laminated, ripple laminated, and occasionally low-angle cross laminated (Fig. 26). Evidence for early diagenesis comes from the identification of pre-compaction lithification of bedding structures within microspar/pseudospar fabrics in comparison to surrounding mudrock facies (Fig. 26). The upper and lower bounding surfaces of microspar/pseudospar concretions are commonly horizontal, but occasionally preserve the ellipsoidal shape developed at their lateral margins (Fig. 26A). At these margins, laminae passing into laminated calcareous foraminiferal mudrock facies show that concretions experienced 3-4 times less compaction than surrounding mudrocks (Fig. 26A). TOC values are lower than surrounding mudrocks with an average of 1.2% (7 samples), likely due in part to early lithification preventing concentration of organic matter present in surrounding organic-rich mudrock facies.

Other forms of calcite cements and partially recrystallized fabrics are also recognized in the Eagle Ford. Calcite cements appear to be concentrated in the skeletal-rich laminae of several facies; particularly well-developed in laminated foraminiferal and peloidal packstone and disrupted bedded foraminiferal packstone facies (Fig 16, 19). Recrystallization of depositional facies is especially common in the transitional Eagle Ford. Here, boundaries between laminated wackestone and bioturbated lime wackestone

facies commonly show formation of recrystallized calcite (Fig. 26D). However, the original depositional texture of these rocks is preserved.

Microspar/pseudospar concretions differ from other examples of authigenic calcite development in the level of recrystallization/cementation and formation of distinct aggregate bodies with well-defined bed boundaries. During early concretion development, unlithified matrix was reshaped and fitted between calcite crystals. Comparison of thin sections from weakly developed concretions show irregular shaped neomorphic spar patchily developed and "floating" within organic-rich mudrock matrix (Fig. 26F). Highly-recrystallized concretionary bodies commonly exhibit a crystalline matrix with small remnants of dark grey concentrations of quartz, clay, and organic matter visible between individual crystals (Fig. 26E). Near uniform crystal distribution, with only limited decreases in the abundance of crystals approaching concretion edges, generates sharp contacts with under- and overlying laminated calcareous foraminiferal mudrocks. Observed heights of microspar/pseudospar concretions vary from 1-36", but are most commonly 6-10".

Microspar/pseudospar calcite in the form of a crystalline matrix often exhibits a hypidiotopic inequigranular crystallization fabric. Curved interfaces between crystals and large crystals in association with smaller crystals are diagnostic features of neomorphic microspar/pseudospar (Fig. 26) (Flügel, 2009). Textural changes associated with grain diminution, replacement of larger crystals with smaller, matrix uniform calcite crystals, mask the original fabric of highly-recrystallized concretionary beds. Evidence of grain diminution is recognized in the recrystallization of individual skeletal tests and fragments (Fig. 26E). In highly recrystallized concretionary fabrics, calcite mineralized (common) to open (less common) fractures are evident, signifying the lone Eagle Ford fabric where macro-fractures are readily apparent (Fig. 26C).

Microspar/pseudospar concretions represent the lone identified fabric in the Eagle Ford that cannot be clearly related to specific depositional processes. Destruction of primary depositional character makes distinction of physical sedimentation and diagenetic processes difficult. Dawson (1997) recognized higher abundances of concretionary limestones within organic-rich transgressive Eagle Ford rocks of East Texas. In the subsurface of South Texas, core investigation during this study has shown that microspar/pseudospar concretions are also most common in the lower Eagle Ford. Facies commonly associated with concretion development include laminated calcareous foraminiferal mudrock, laminated foraminiferal and peloidal packstone, and infrequently in massive argillaceous mudrock. Each of these facies is interpreted to have been deposited in low energy, oxygen-depleted environments associated with the accumulation of organic-rich sediment. Associations between facies and concretions allows establishment of preliminary relationships between depositional environment and concretion formation.

Figure 26: (Following page) Photographs of Microspar/Pseudospar Calcite. (A) Slab photo showing nodular concretion with contacts cutting across bedding planes within laminated calcareous foraminiferal mudrock facies. Well preserved planar laminations indicate increased compaction within mudrock facies when compared to concretionary fabrics, lower Eagle Ford, Krause #1, 9996.8'; (B) Slab photo with planar laminations and starved ripples preserved in recrystallized microspar/pseudospar facies, lower Eagle Ford, Schauer #1, 8110.0'; (C) Massive bedded concretionary fabric with mineralized and open vertical fractures. Macro-fractures are generally lacking from Eagle Ford mudrocks, but calcite mineralized (common) and open (rare) fractures are found within concretions, core photo, lower Eagle Ford, Mathews #1, 4650.1'; (D) Slab photo showing diagenetic recrystallization at the contact of laminated wackestone and bioturbated lime wackestone facies, transitional Eagle Ford, Hurt #1, 7033.4'; (E) Photomicrograph illustrating microspar fabric, with calcite filled planktic foraminifera showing evidence of aggrading neomorphism, lower Eagle Ford, Hendershot #1, 4763.0'; (F) Photomicrograph showing weakly developed neomorphic pseudospar in organic-rich mudrock matrix, upper Eagle Ford, Leppard #1-H, 13553.0'.

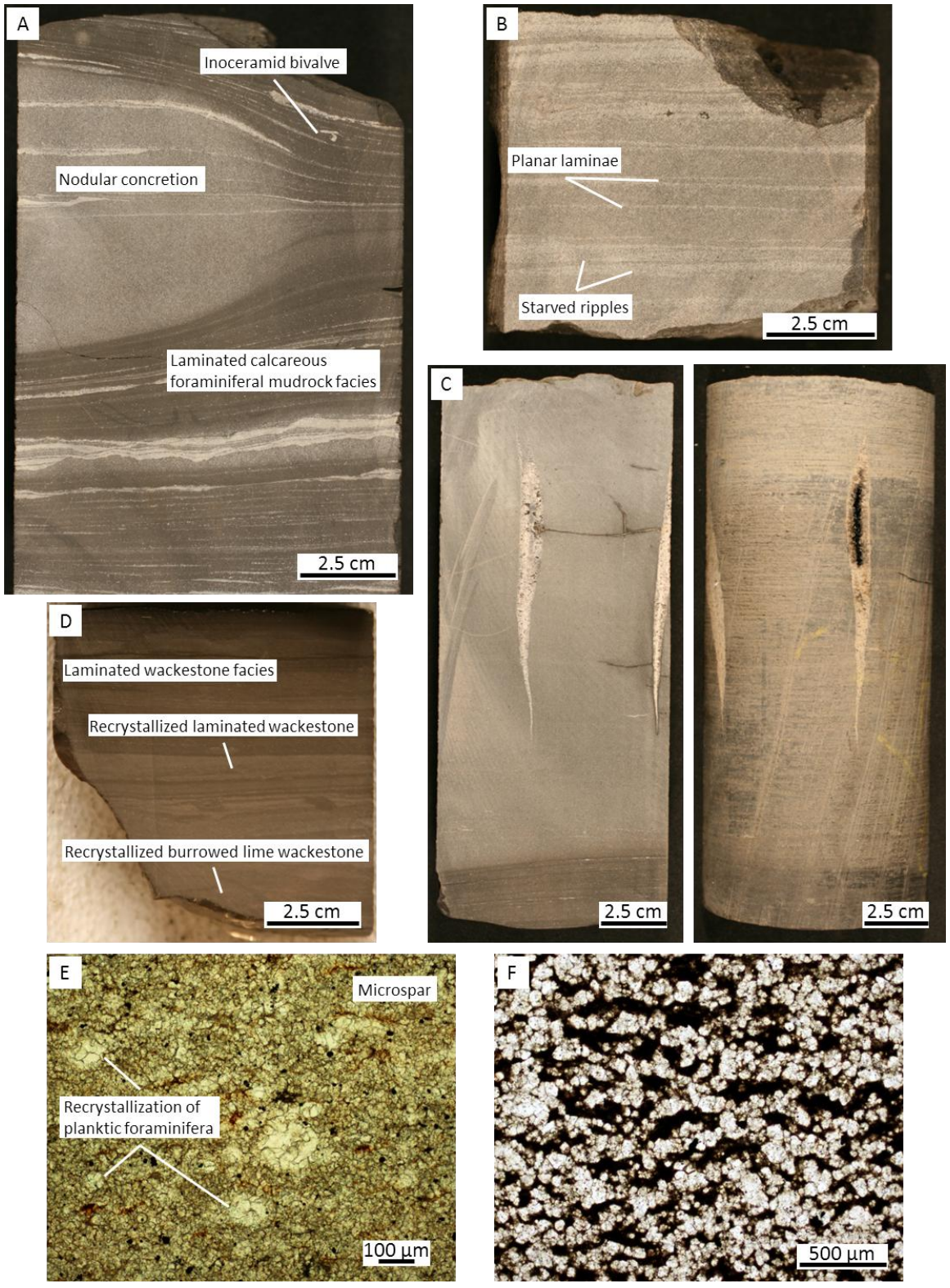
A
Inoceramid bivalve
Nodular concretion
Laminated calcareous foraminiferal mudrock facies
2.5 cm
B
Planar laminae
Starved ripples
2.5 cm
C
2.5 cm
2.5 cm
D
Laminated wackestone facies
Recrystallized laminated wackestone
Recrystallized burrowed lime wackestone
2.5 cm
E
Microspar
Recrystallization of planktic foraminifera
100 µm
F
500 µm

STABLE ISOTOPES AND CONCRETION DIAGENESIS

Whereas outcrop, core, and thin section analyses are useful in determining geometry, sedimentary structures, and grain types; stable isotope analyses hold the potential to document diagenetic processes involved during concretion development (Curtis et al., 1972, Irwin et al., 1977). Evidence of concretionary fabrics in argillaceous formations (Hudson, 1977) and more specifically organic-rich sediments deposited surrounding the Cenomanian/Turonian boundary is well established (Ludvigson et al., 1994). Determining the diagenetic history of concretionary fabrics is important because it helps unlock conditions present near the sediment-water interface during organic-rich mudrock deposition. Characteristic $\delta^{13}C$ isotope values are produced in response to varying microbial processes, potentially allowing recognition of processes involved and estimating relative depth of concretion formation (Fig. 27). Microbial processes are in turn dictated by water oxygenation and sedimentation rates, which together act to control the depths and rates at which organic matter decay occurs below the sediment-water interface (Potter et al., 2005, Allan and Wiggins, 1993, and Wignall, 1994).

At the sediment-water interface, diffusion of oxygen into mud pore space from overlying oxygenated water columns occurs (Fig. 27) (Potter et al., 2005). Aside from the effect of burrowing infauna, increased burial produces increasingly dysoxic and eventually anoxic pore fluids. Oxygen depletion results from reactions between decaying organic matter and oxygen that generates hydrogen and bicarbonate, with bicarbonate commonly precipitating as calcite during shallow burial (Potter et al., 2005). As dissolved oxygen disappears, sulfate becomes the new oxygen source for microbial activity (Fig. 27) (Potter et al., 2005). The reaction of sulfate and organic matter produces bicarbonate ($2HCO^{-}_{3}$) and H_2S (Allan and Wiggins, 1993). Available iron reacts with H_2S and forms pyrite (Fig. 27). Pyrite can take the form of single crystals,

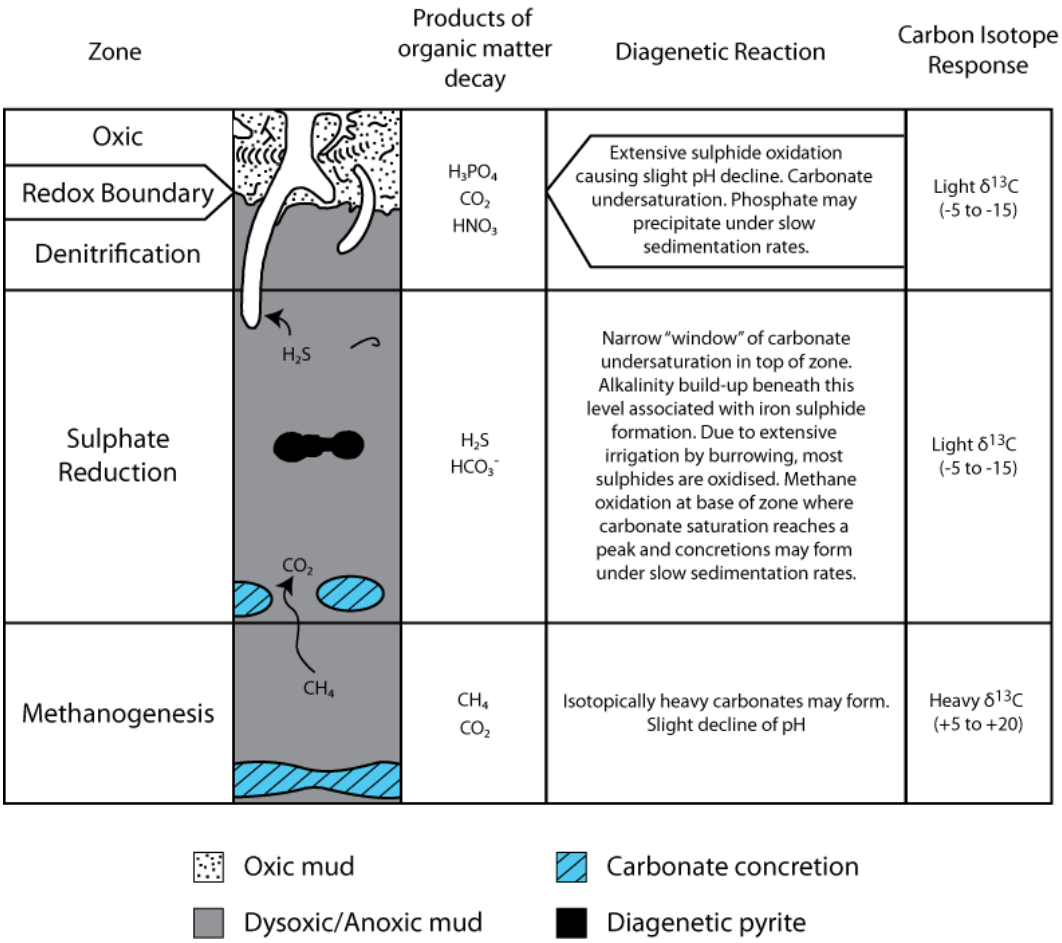

Figure 27: Chemical reaction pathways of organic matter oxidation resulting in the generation of diagenetic calcite and associated $\delta^{13}C$ response. Modified after Allan and Wiggins (1993) and Wignall (1994).

framboids, or concretions. After sulfate is exhausted, bacteria begin to produce methane by carbonate reduction in a process referred to as microbial methanogenesis. Within the methanogenic zone, organic matter is broken down into methane and CO_2 (Fig. 27). Carbonate saturation is maximized near the base of the sulphate reduction zone where methane diffusing from the underlying methanogenic zone is oxidized into CO_2 (Wignall, 1994).

In more anoxic/euxinic environments, abundant H_2S prevents inhabitation by burrowing infauna and sulfate reducers drive primary microbial reactions with organic matter. In these environments, pyrite is a common diagenetic product (Fig. 27). Excess iron for carbonate minerals such as siderite is absent, resulting in mainly calcite formation. The process of methanogenesis is also more significant in anoxic/euxinic settings due to the lack of oxygen-efficient organisms, thus preserving more organic matter to undergo methanogenesis (Potter et al., 2005).

Aside from diagenetic oxidation of organic matter, physical depositional processes also serve as potential sources for development of concretionary fabrics. Sea water saturated in marine carbonate may also generate sufficient CaCO3 needed for calcite recrystallization and concretion formation. Handford (1986) showed that laterally extensive limestone beds of the Fayetteville Shale possess $\delta^{13}C$ values typical of ocean water (+1.0 ‰ PDB). These deposits were likely generated during storm winnowing and suspension of carbonate from shallow-water environments that were transported distally and settled to the sea-floor. However, the Fayetteville Shale also possesses limestones exhibiting depleted $\delta^{13}C$ values indicative of carbon origination from anaerobic oxidization of organic-rich mud (-13.7 ‰ PDB).

Eagle Ford concretions commonly exhibit both enriched (2.17 ‰ PDB, n=5) and depleted (-1.81 ‰ PDB, n=11) $\delta^{13}C$ values when compared to surrounding Eagle Ford mudrocks (0.54 ‰ PDB, n=256) and bounding platform carbonates (1.25 ‰ PDB, n=150) (Fig. 28, 29). Anoxic depositional settings of the Eagle Ford (Charvat et al., 1981) likely led to organic matter bypass of the oxic zone and primary degradation within the sulfate reduction zone, leading to increased organic matter preservation and depleted $\delta^{13}C$ values (Fig. 28, 29). Continued burial and decreasing oxygen likely allowed further microbial processes to differentiate carbon isotope character, resulting in the formation of $\delta^{13}C$ enriched concretions involving the process of methanogenesis (Fig. 28).

A small number of measured Eagle Ford concretions show values that lack depletion or enrichment of $\delta^{13}C$ (-0.01 ‰ PDB, n=2) (Fig. 30). These suggest carbonate saturation likely originated through physical processes, while the remainder of Eagle Ford concretions shows at least partial contributions of carbonate from organic sources.

$\delta^{13}C$ plots in the Eagle Ford show highly variable character (Fig. 29). Peaks recording depleted values on the $\delta^{13}C$ curve relate directly to the presence of concretions and show the significant influence of diagenesis on $\delta^{13}C$ curve response. Because such $\delta^{13}C$ data are commonly used in correlations as a proxy for global-sea water conditions, care must be taken to carefully distinguish diagenetic isotope values before such data are used in regional and global stratigraphic correlations.

IRON SULPHIDE PRECIPITATION

Reduction processes involved in the development of calcite concretions in the Eagle Ford also lead to the formation of abundant diagenetic pyrite. In the sulphate reduction zone (Fig. 27), concentrated pyrite formation occurs from pseudomorphing of greigite framboids and/or from the direct reaction of Fe^{2+} with H_2S (Wignall, 1994).

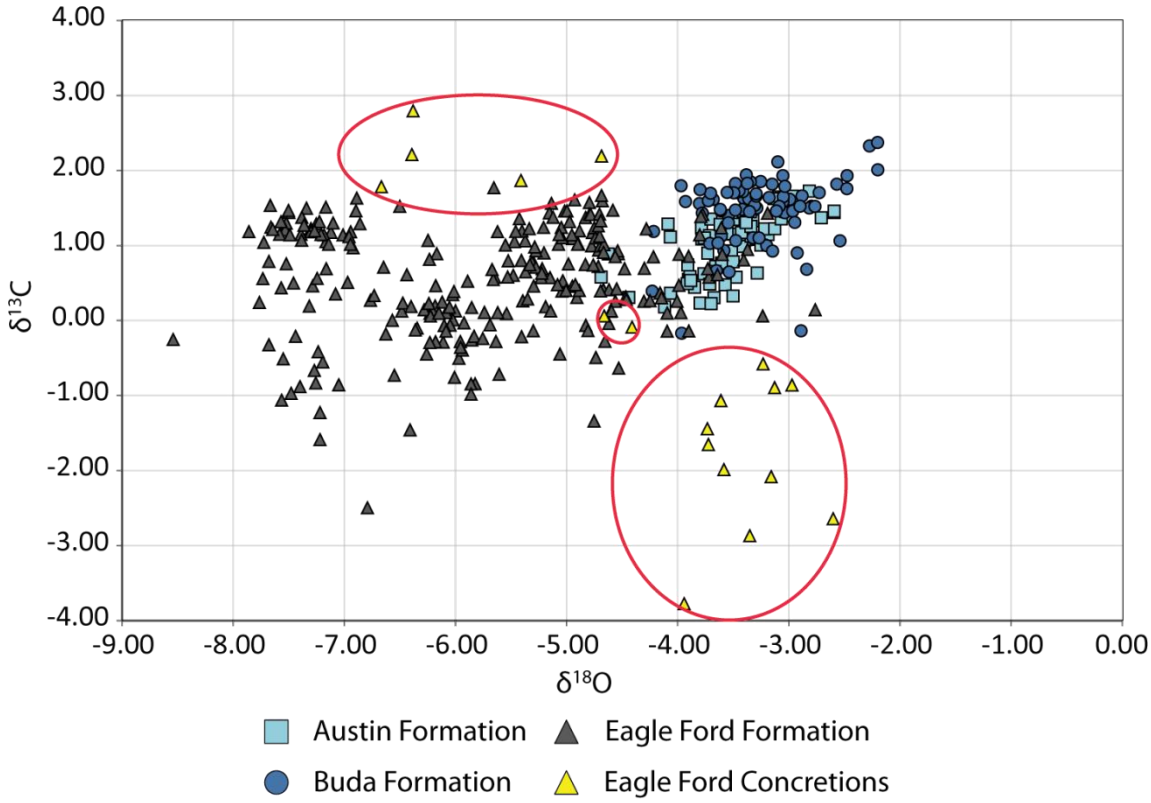

Figure 28: Plot of stable isotope values for the Eagle Ford and surrounding platform carbonates. Within the Eagle Ford, concretionary fabrics commonly show depletion or enrichment of $\delta^{13}C$, resulting from differentiated microbial pathways at and below the sediment-water interface.

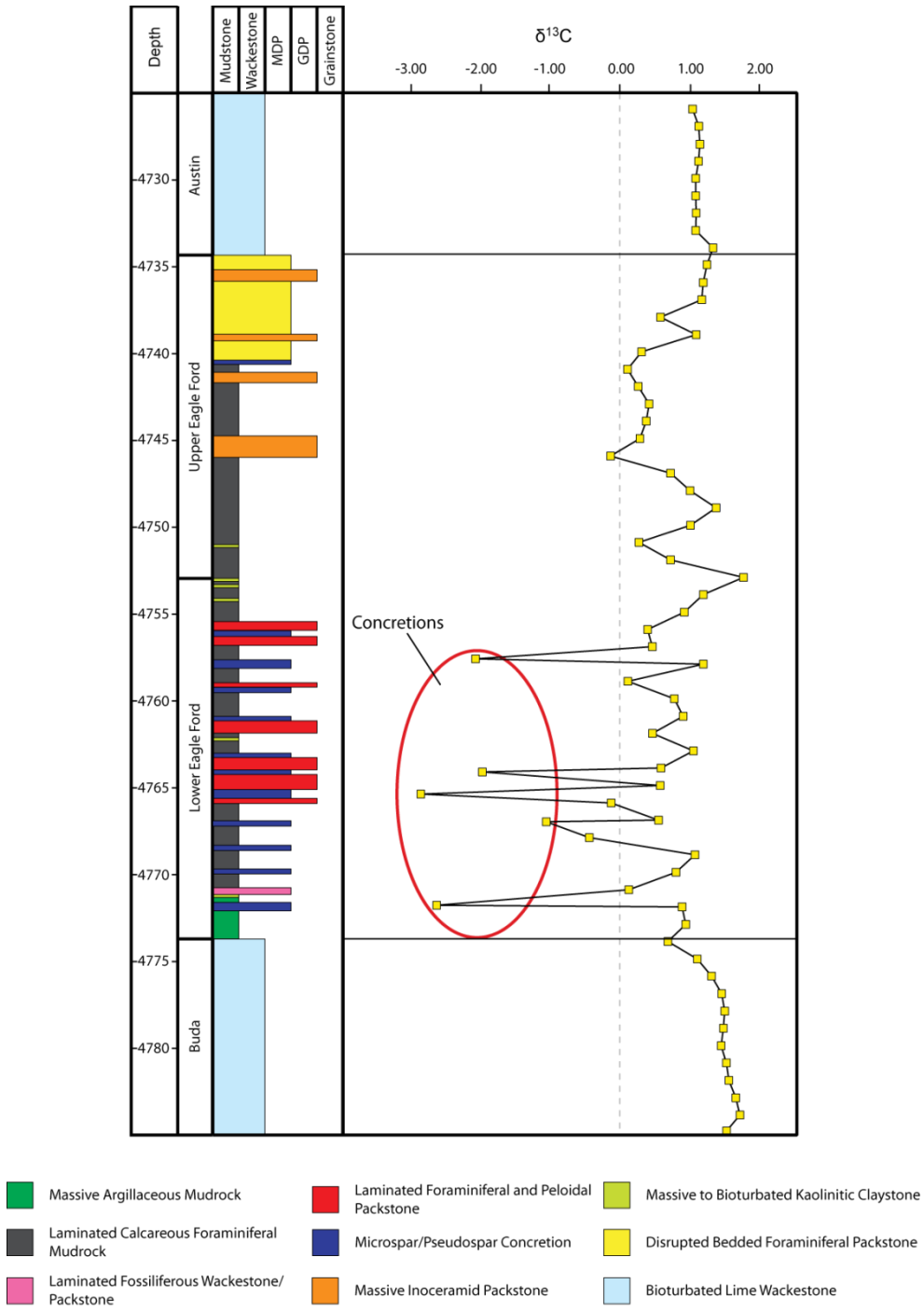

Figure 29: Typical plot of $\delta^{13}C$ in the Buda, Eagle Ford, and Austin Formations showing $\delta^{13}C$ variability, relating to early diagenesis and concretion development. C.J. Hendershot #1.

Common expressions of pyrite in the Eagle Ford include silt-sized, disseminated framboids (Fig. 30). The large size of many Eagle Ford framboids suggests nucleation and the redox boundary were persistent below the sediment-water interface. In more euxinic settings than recognized in the Eagle Ford, the redox boundary expands vertically into the water column and generates smaller (<5 μm) pyrite framboids (Wignall and Newton, 1998). Larger framboid aggregates, crystals of euhedral pyrite, nodules, and pyritization of calcareous skeletal material represent other common diagenetic pyrite expressions (Fig. 30).

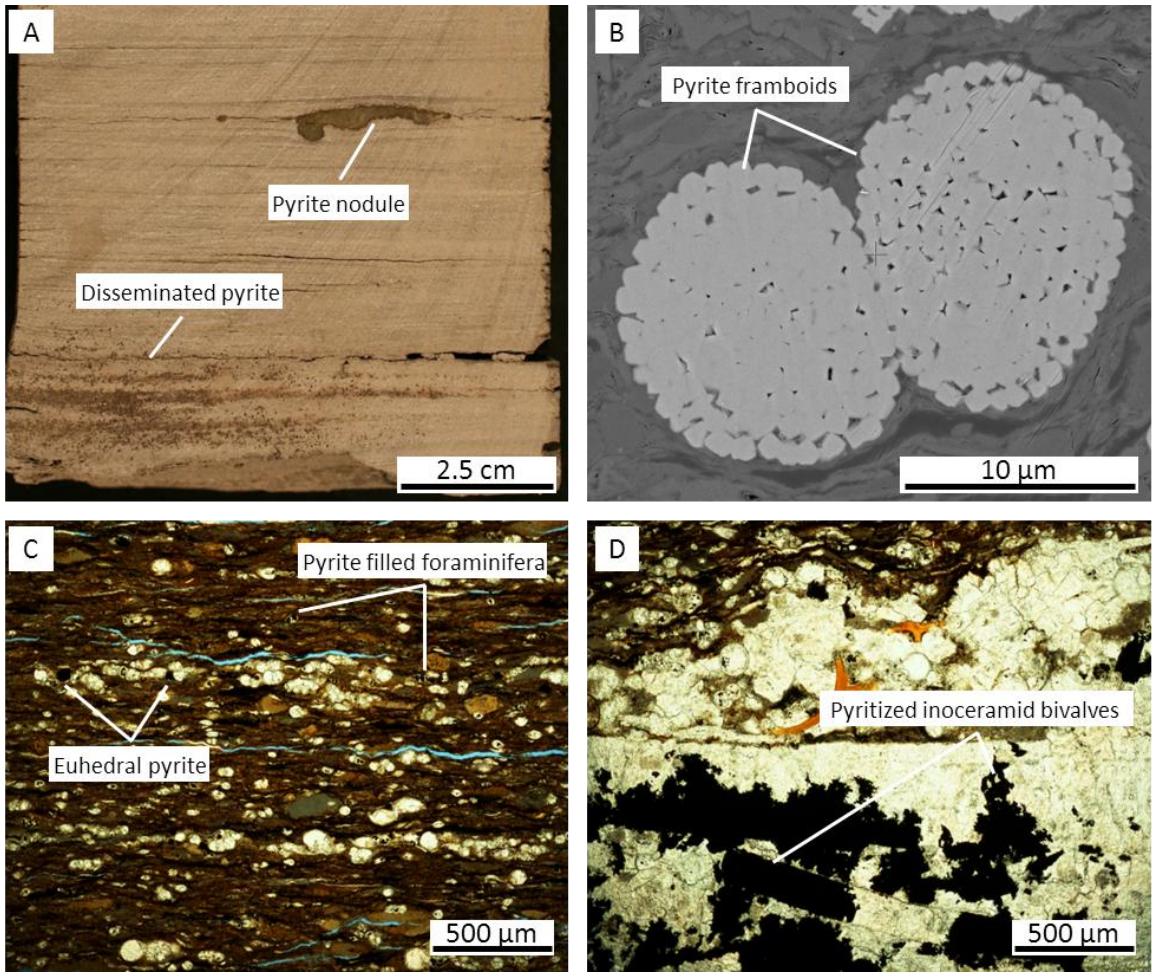

Figure 30: Photographs of Eagle Ford diagenetic pyrite. (A) Disseminated and nodular pyrite are common in Eagle Ford facies, here shown in laminated wackestone facies, core photo, upper Eagle Ford, Shanklin #1, 2122.6'; (B) Pair of pyrite framboids in a mixed clay and micrite matrix, scanning electron microscope photograph of a core chip, lower Eagle Ford, Brechtel #1, 3313.0'; (C) Photomicrograph of euhedral and pyrite filled foraminifera, lower Eagle Ford, Blumberg #1, 4215.5'; (D) Photomicrograph of partially pyritized inoceramid bivalve shells, lower Eagle Ford, Browne #8, 2188.7'.

GEOGRAPHIC AND STRATIGRAPHIC TRENDS IN ROCK PROPERTIES

The fine-grained nature of Eagle Ford mudrocks necessitated the use of XRD and XRF analyses for identification of mineralogical and elemental proportions, respectively. Coarser grains, including pyrite, phosphatic bioclasts, calcareous skeletal material, and quartz grains are identifiable in thin-section. Comparison of X-ray and visual analyses of the Eagle Ford reveal both geographically and stratigraphically varied compositions. However, partitioning of varied rock compositions identify trends relating to depositional setting and form characteristic log signatures facilitating their recognition away from cored intervals. The distribution and type of organic matter in the Eagle Ford Formation in South Texas also show trends relating to depositional environment and sediment delivery process.

MINERALOGY

Elevated carbonate content distinguishes Eagle Ford mudrocks from other successful resource plays, including the Barnett, Haynesville, and Bossier Shales, currently being explored in Texas. Carbonate content varies widely in measured Eagle Ford samples (92) from 9-90%, but averages 56%. Minimal contributions of carbonate minerals such as dolomite (<6%), ankerite (<6%), and siderite (<2%) leave calcite as the dominant carbonate mineral expression in the Eagle Ford. Calcite is believed to have originated primarily from pelagic marine fauna sourced in the overlying oxygenated water column. In addition, proximal benthic communities show episodic to persistent calcite contribution. The distribution of calcite in the mudrock matrix commonly exists as clay-sized disaggregated coccospheres and as larger, individual skeletal remains of

pelagic (primary) and benthic (secondary) fauna. Ternary diagrams showing normalized relative proportions of clay, carbonate, and silicate minerals help identify mineralogical trends in the Eagle Ford (Fig. 31, 32).

The lower Eagle Ford depositional succession displays the most diverse mineralogical character in the Eagle Ford (Fig. 31). The close proximity of competing sediment sources, commonly including terrigenous derived siliciclastics and marine carbonate, explain this variability. Geographically, well-developed clay- and quartz-rich mineral assemblages are recognized in proximity to the San Marcos Arch. These rocks show low-order trends of decreasing quartz and increasing calcite laterally from the arch and stratigraphically upward into the lower Eagle Ford. Progressive increases in calcite into the lower Eagle Ford likely originated from continued accommodation increases and the formation of increasingly distal environments to terrigenous sources. Development of abundant microspar/pseudospar concretionary fabrics in the lower Eagle Ford result in locally high (>80%) calcite mineralogies (Fig. 31, 32). However, the inclusion of altered volcanic ash beds (massive to bioturbated kaolinitic claystone facies) in combination with basal massive argillaceous mudrock facies combine to skew the lower Eagle Ford trend away from the overall calcareous nature (average 51%, 44 samples) of these rocks (Fig. 31, 32).

The mineralogical character of the upper Eagle Ford originates from facies development over a wide range of depositional energies and environments showing variable oxygenation conditions. On the San Marcos Arch, the upper Eagle Ford shows a variety of facies developed under episodic to event-driven high-energy conditions. These facies are texturally diverse, yet maintain an elevated calcareous nature (Fig. 32). A geographic trend of decreasing carbonate in the upper Eagle Ford is seen moving away from coarser-grained deposition on the San Marcos Arch toward the finer-grained

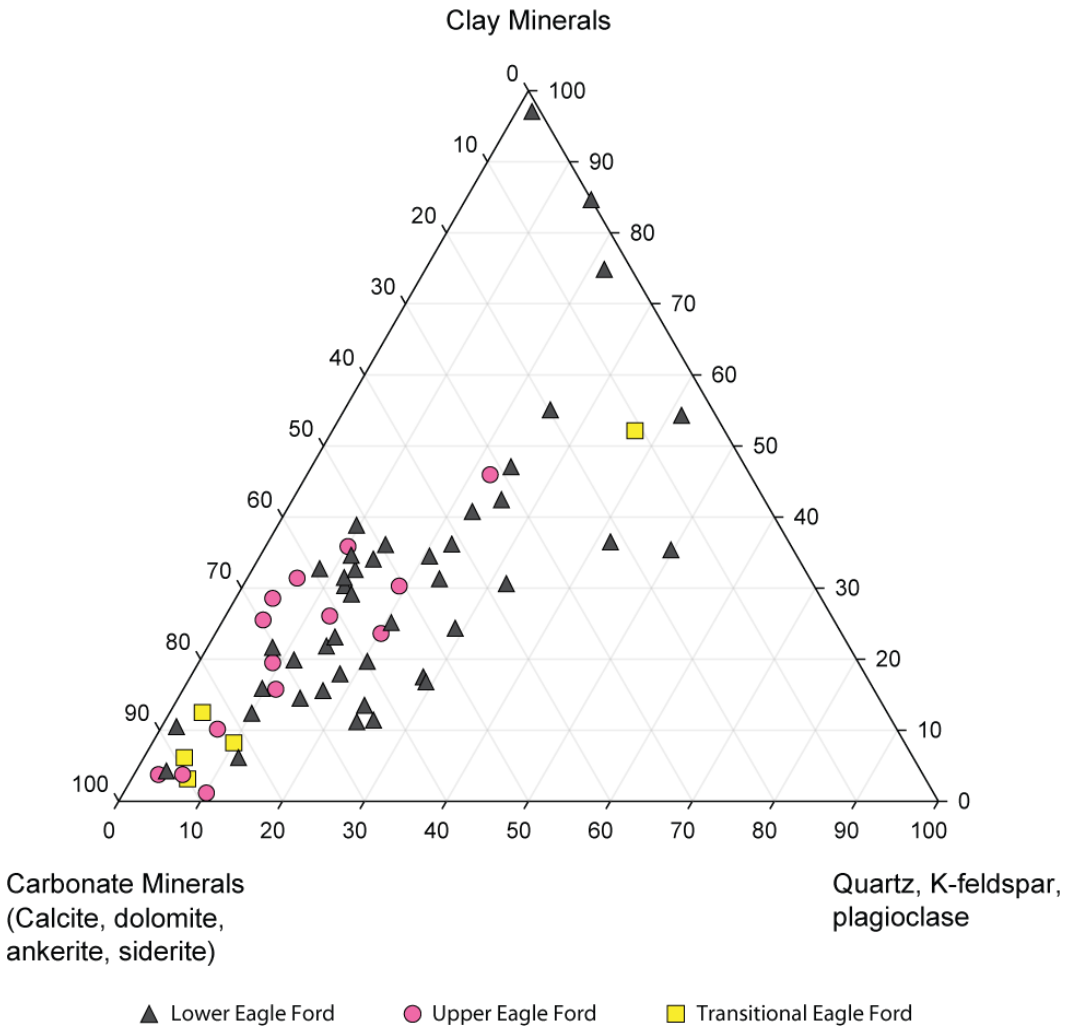

Figure 31: Ternary plot of mineralogy by stratigraphic unit. Eagle Ford members show widespread enrichment of carbonate. Noticeable decreases in mineralogical variability occur between the lower, upper, and transitional Eagle Ford, respectively.

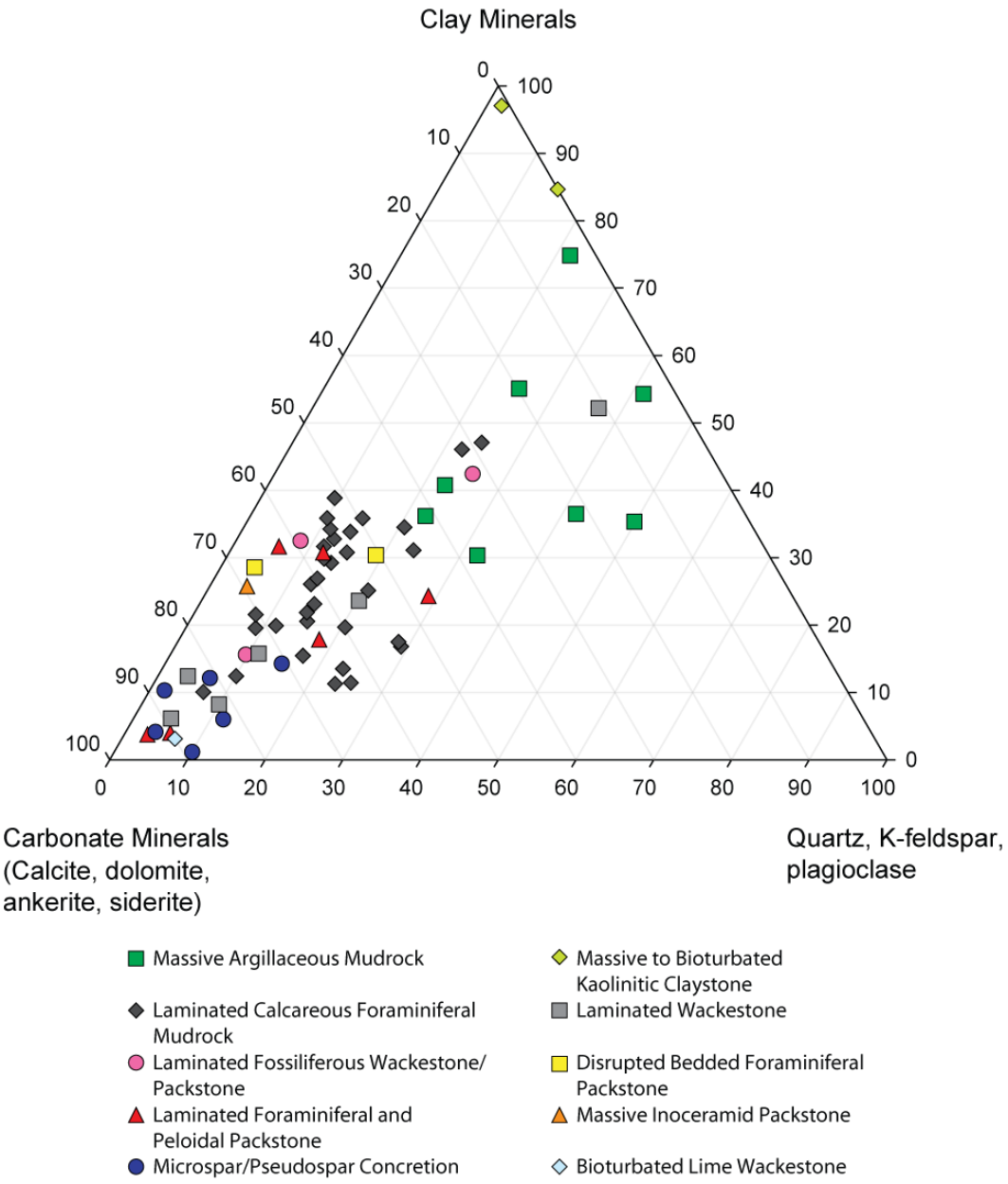

Figure 32: Ternary plot of mineralogy by facies. Within the Eagle Ford, identified facies consist of both argillaceous and calcareous mudrocks. However, calcite rich mineralogies dominate the Eagle Ford.

deposits of the Maverick Basin and Stuart City reef margin (Fig. 32). However, development of microspar/pseudospar concretions continued to generate beds with concentrated calcite in the distal upper Eagle Ford. The upper Eagle Ford exhibits higher carbonate content (67%, 15 samples) and lower mineralogical heterogeneity over the lower Eagle Ford.

The transitional Eagle Ford member appears to be geographically restricted to the Maverick Basin and surrounding areas. These distal depositional environments led to nearly uniform mineralogical character of transitional Eagle Ford facies, commonly showing high calcite content (87%, 4 samples) with low levels of siliceous minerals (Fig. 31). However, occasional thin beds of clay and quartz minerals with low carbonate (12%, 1 sample) are present within the transitional Eagle Ford (Fig. 31). Rocks exhibiting elevated silica appear lithologically similar to surrounding facies and likely represent small, isolated zones within larger facies designations. Local diagenetic calcite recrystallization within transitional Eagle Ford facies further elevates carbonate values, but the amount of recrystallization is far less significant than in lower and upper Eagle Ford depositional successions.

Comparison of Eagle Ford members reveal stratigraphic trends relating to shifting sediment sources, delivery processes, and depositional environments during deposition of the Eagle Ford. One of the more noticeable trends is that as calcite increases, mineralogical variability progressively decreases through the lower and upper Eagle Ford and into the transitional Eagle Ford (Fig. 31). The abundance of terrigenous siliciclastic material was highest during early transgressive deposition of the lower Eagle Ford and diminished through time. Regressive deposition of upper and transitional Eagle Ford members fails to show similar levels of siliciclastic input, suggesting a shift to carbonate

sourced depositional environments. Trends between depositional texture and carbonate content indicate lower-energy, finer-grained intervals possess lower carbonate. The most calcareous Eagle Ford rocks are commonly microspar/pseudospar concretions, which decrease in abundance from the lower, upper, and transitional Eagle Ford, respectively.

XRF CHEMISTRY

In unconventional shale resources, hand-held XRF scanners are emerging as useful chemostratigraphic tools utilized during development of stratigraphic correlations and identification of potential organic-rich zones through recognition of redox sensitive trace elements. XRF analyses are also useful when coupled with mineralogical data in relating systematic elemental variability to facies and depositional setting. Elemental chemistry plots were produced for several Eagle Ford wells in order to identify characteristic differences and relate these to sediment source and proximity (Fig. 33, 34, 35). For each plot, Ca (calcium) and Ti (titanium) and Si (silicon) curves were generated and compared with vertical facies distributions.

Dominant calcitic mineralogies of Eagle Ford carbonates allow Ca plots to model the contribution of marine carbonate in Eagle Ford rocks. Ti, along with Al (aluminum) and Fe (iron), serve as common proxies for terrigenous sediment supply (Brughmans, 2004, Narayana et al., 2009). As was shown in the section on diagenesis, Fe in the Eagle Ford is commonly concentrated in early diagenetic products including framboids and pyritization of calcareous skeletal material. These diagenetic products likely do not preserve an original depositional signal. Ti and Al values vary by two orders of magnitude; yet, closely exhibit a covariant relationship. Ti was chosen over Al due to higher instrumental calibration confidence. The inversely covariant relationship of Ca

and Ti speaks to the dominant interplay between competing marine carbonate and terrigenous siliciclastic sediment sources during Eagle Ford time. Si plots also act as proxy for silica-rich terrigenous quartz, clays, and feldspars; but, also reflect silica originating from biota in the water column.

The C.J. Hendershot #1 Eagle Ford core proximal to the San Marcos Arch in Gonzales County shows three XRF packages that are relatable to facies distributions. The first package consists of a cyclic Ca, Ti, and Si response with upward increasing Ca and upward decreasing Ti and Si (Fig. 33 package A). The base of the first package shows the highest Ti in the Eagle Ford resting on top of the Buda Limestone (Fig. 33 package A). This high Ti zone is related to massive argillaceous mudrock facies. Above this high Ti interval, Ca, Ti, and Si response are highly-cyclic and relate to the thinly-bedded distribution of laminated calcareous foraminiferal mudrock, laminated fossiliferous wackestone/packstone, laminated foraminiferal and peloidal packstone, and microspar/pseudospar concretions. Internal variability within facies also accounts for the cyclic nature of elemental curves. Decreasing Ti and Si coupled with increasing Ca indicate decreasing terrigenous contribution through time.

Low facies diversity within the second package leads to a less cyclic Ca, Ti, and Si response. However, upward increasing Ti and Si coupled with upward decreasing Ca are seen within the laminated calcareous foraminiferal mudrock facies. This suggests increased terrigenous influx through time to the upper Eagle Ford in depositional environments surrounding the San Marcos Arch.

The third package shows high Ca with low Ti and Si. A sharp increase in Ca at the base of this package corresponds to the drastic facies shift from laminated calcareous foraminiferal mudrock to disrupted bedded foraminiferal packstone and massive

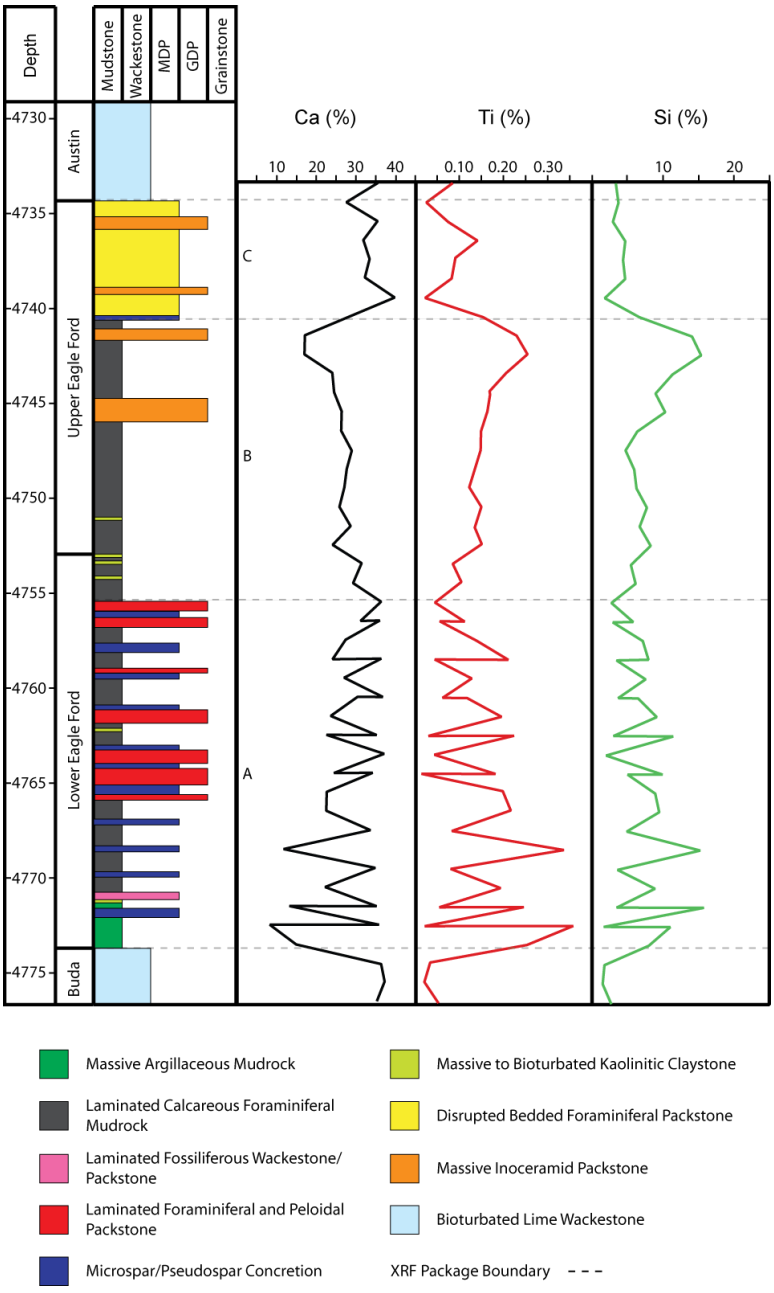

Figure 33: Relationships between Ca, Ti, and Si elemental abundance relate to depositional environment and dominant facies distributions in the proximal lower and upper Eagle Ford. Letters denote XRF packages. Plots based on 1 ft sample spacing. C.J. Hendershot #1.

inoceramid packstones. These facies have been interpreted to result from higher-energy, event sedimentation which would explain the sharp shift in the nature of the elemental chemistry of these rocks.

The J.A. Leppard #1-H distal Eagle Ford core near the Stuart City reef margin in Bee County consists of two distinct XRF packages that correspond with the lower and upper Eagle Ford. The lower Eagle Ford exhibits a highly cyclic yet overall consistent Ca, Ti, and Si response (Fig. 34 package A). Within this interval, zones showing the highest Ca commonly relate to individual beds or zones containing microspar/pseudospar concretions (Fig. 34). Laminated calcareous foraminiferal mudrock facies also exhibit elemental cyclicity (Fig. 34 package A). It is important to note that the high Ti values seen in the basal Eagle Ford of proximal wells are absent in this distal depositional setting (Fig. 33 package A, 34 package A), indicating the terrigenous source active during early Eagle Ford deposition did not actively transport sediment to the more distal shelf margin.

The upper Eagle Ford is also highly cyclic but shows increased amplitude and increased Ti and Si. Unlike the more proximal C.J. Hendershot #1 Eagle Ford core, Ti values in the distal upper Eagle Ford increase rapidly and are highly variable (Fig. 33 package B & C, 34 package B). Corresponding Ti and Si trends suggest that Si originated dominantly from terrigenous sources. Direct relationships between proximally and distally deposited Eagle Ford are difficult do to the thinned nature of the upper Eagle Ford in this distal well.

The L. Hurt #1 Eagle Ford core in La Salle County near the margin of the Maverick Basin shows two distinct XRF packages that correspond to the distal upper and transitional Eagle Ford (Fig. 35). The upper Eagle Ford package displays highly cyclic

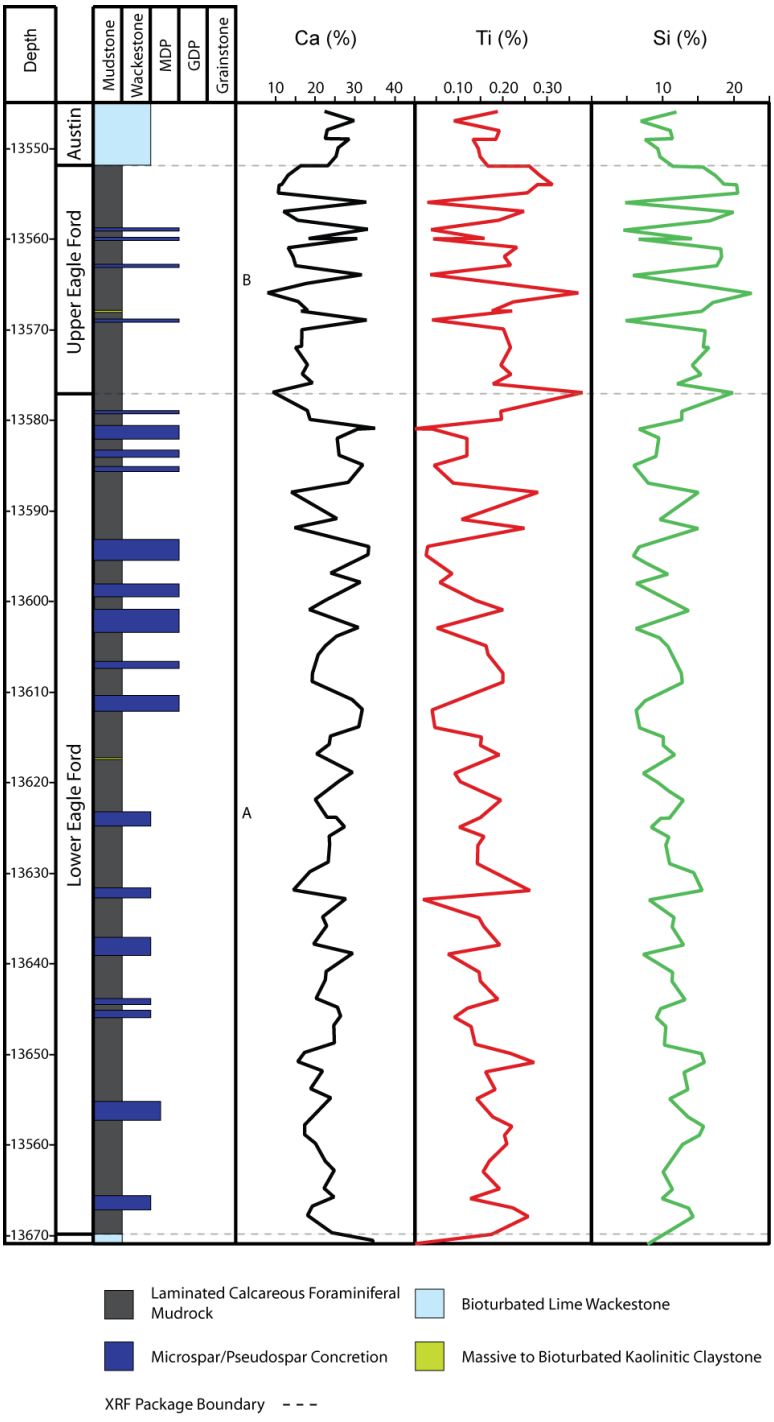

Figure 34: Relationships between Ca, Ti, and Si elemental abundance relate to depositional environment and dominant facies distributions in the distal lower and upper Eagle Ford. Letters denote XRF packages. Plots based on 1 ft sample spacing, J.A. Leppard #1-H.

Ca, Ti, and Si values. The variable elemental nature of this interval is related to interbedded laminated fossiliferous wackestone/packstone facies, laminated foraminiferal and peloidal packstone facies, and abundant microspar/pseudospar concretions (Fig. 35 package A). Elemental cyclicity is also observed within in laminated calcareous foraminiferal mudrock facies (Fig. 35 package A). Vertical facies changes coupled with trends of higher and lower Ti (Fig. 35 package A) show a potential shift in terrigenous flux during upper Eagle Ford deposition in South Texas. Increased Si and separation from the Ti curve at the top of the upper Eagle Ford suggests additional silica sourced from non-terrigenous environments. This trend may suggest increased contribution of biogenic silica.

The second, transitional Eagle Ford package consists of high Ca with low, cyclic Ti and Si values (Fig. 35 package B). The sharp decrease in Ti and Si coupled with increased Ca indicates a marked decrease in terrigenous siliciclastic input during the transitional Eagle Ford (Fig. 35 package B). However, small and isolated Ti zones show sharp increases in terrigenous influx. The cyclic nature of Ti and Si values appear related to the cyclic nature of laminated wackestone and bioturbated lime wackestone facies. The absence of equivalent facies on the San Marcos Arch makes interpreting sediment source location for the transitional Eagle Ford difficult. Currently, it is unclear whether terrigenous sediments were continually sourced from the north or if another source emerged during transitional Eagle Ford deposition.

Due to the large distances between these cores and potential unconformities within and bounding the Eagle Ford, direct chemostratigraphic correlation from the elemental chemistry is not possible. Recognition of distinct geographic and stratigraphic trends do suggest that comparison of more genetically related depositional settings may

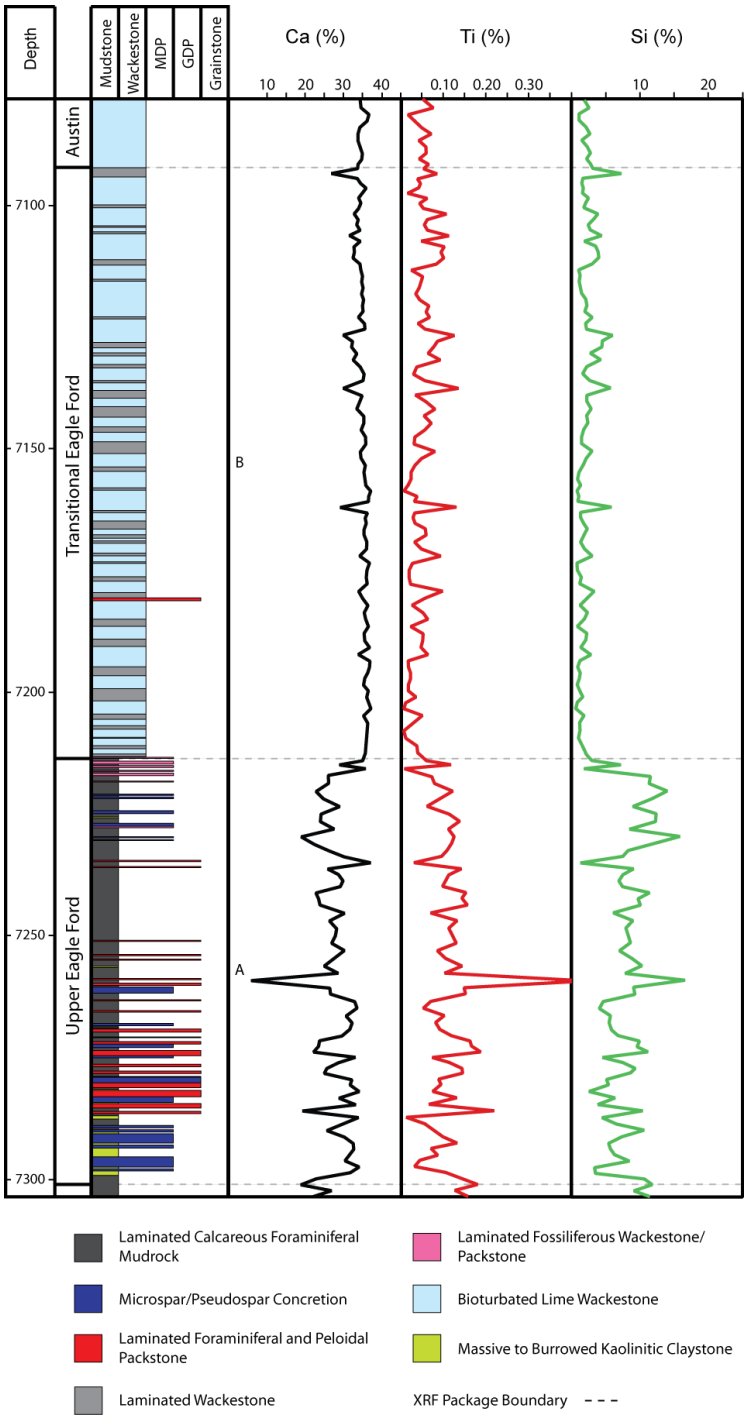

Figure 35: Relationships between Ca, Ti, and Si elemental abundance relate to depositional environment and dominant facies distributions in the distal upper and transitional Eagle Ford. Letters denote XRF packages. Plots based on 1 ft sample spacing. L. Hurt #1.

Allow these correlations to be established. XRF plots correlate well with both Eagle Ford member designations and facies picks, offering additional support for previous interpretations. In addition, comparison of cores with XRF elemental analyses offer valuable information on sediment source and proximity not always identifiable by core or mineralogical data alone.

WIRELINE LOG CHARACTER OF EAGLE FORD FACIES

As established in the discussion on regional Eagle Ford stratigraphy (Fig. 11, 12) and Eagle Ford subsurface stratigraphy (Fig. 22, 23), high gamma ray response allows distinction of the Eagle Ford from under- and over-lying platform carbonates. Additionally, variable gamma ray response facilitates recognition of three lithologically distinct members within the Eagle Ford. The lower, upper, and transitional Eagle Ford members developed as a function of the interplay between competing sediment sources, which include terrigenous siliciclastic, marine carbonate, diagenetic, organic, and volcanic sources.

Detailed core to log calibrations of the Eagle Ford show that gamma ray, resistivity, and neutron density logs exhibit systematic variability relating to and allowing recognition of variable elemental, mineralogical, and organic carbon character. Whereas gamma ray, resistivity, and neutron density logs allow division of the Eagle Ford into lower, upper, and transitional members; gamma ray and neutron density logs correlate well with facies trends and XRF plots, indicating the driving relationships between depositional environment and elemental abundance with log character.

Proximal to the San Marcos Arch, the C.J. Hendershot #1 core, gamma ray logs define a sharp basal contact of the Eagle Ford the Buda Formation and a gradational upper contact with the Austin Formation (Fig. 36). The lower Eagle Ford commonly

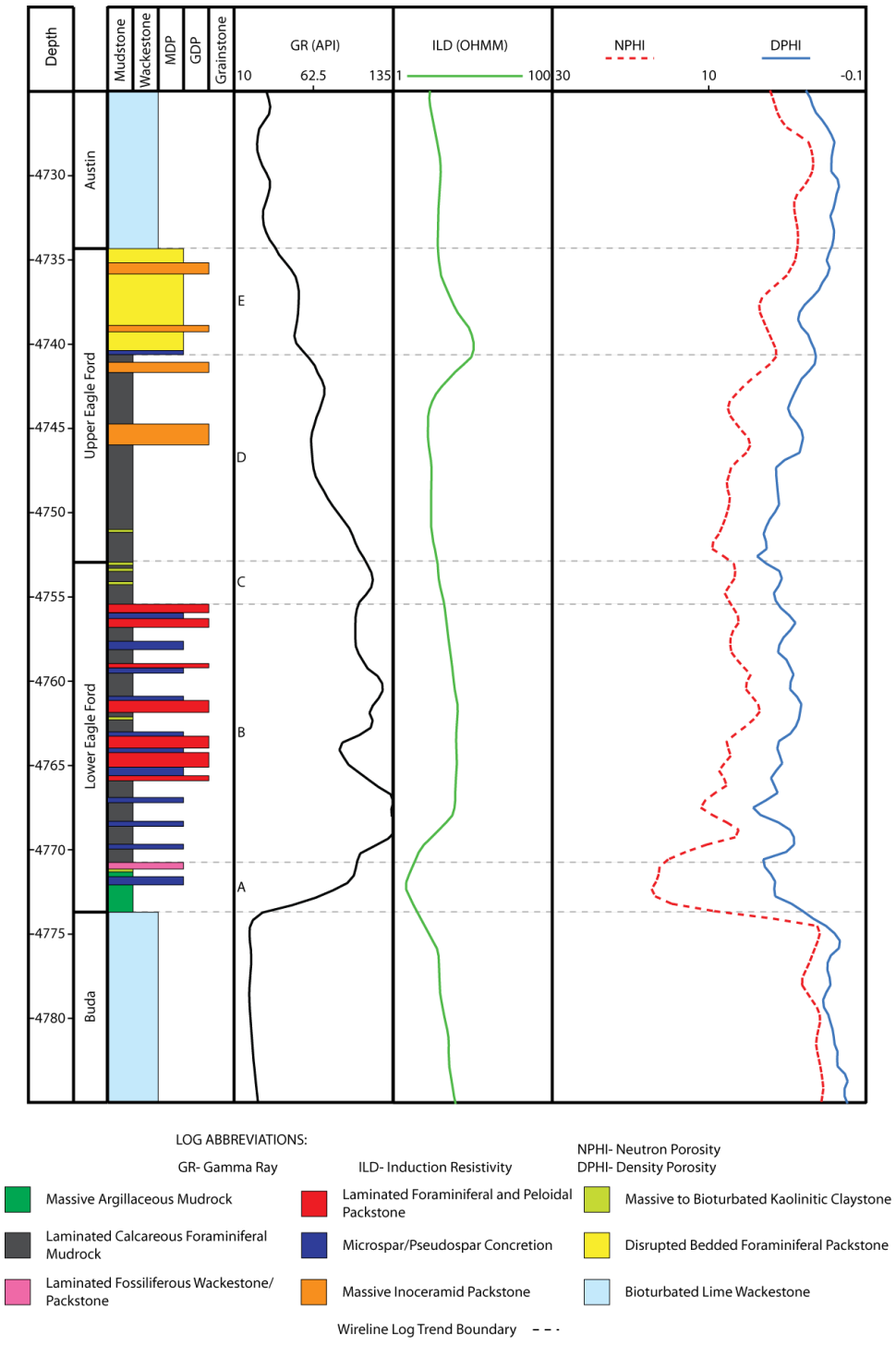

Figure 36: Facies and log character of lower and upper Eagle Ford mudrocks on the San Marcos Arch. Letters denote wireline log trend packages. C.J. Hendershot #1.

shows the highest gamma response (Fig. 36 package A, B, & C) and is overlain by the lower gamma ray upper Eagle Ford (Fig. 36 package D & E). At the base of the lower Eagle Ford, the massive argillaceous mudrock facies forms a thick succession that possesses characteristic high gamma and high neutron density log response (Fig 36 package A). Comparison between neutron density logs and XRF elemental chemistry plots show that increasing neutron porosity as well as increasing separation of neutron and density porosity logs correlates with increasing Ti and Si (Fig. 33, 36).

Laminated calcareous foraminiferal wackestone facies possess high gamma ray values and constitute much of the lower Eagle Ford (Fig. 36 package B). Perturbations in gamma ray response appear to correlate with packages of thinly bedded laminated foraminiferal and peloidal packstone facies and/or microspar/pseudospar concretions (Fig. 36 package B). Massive to bioturbated kaolinitic claystone facies increase the gamma response surrounding the lower/upper Eagle Ford contact (Fig. 36 package C).

Laminated calcareous foraminiferal mudrock facies continue as the dominant facies in the upper Eagle Ford. However, the upper Eagle Ford commonly exhibits lower gamma ray values (Fig. 36 package D) due to increased silica (Fig. 33) and lower preservation of organic matter. The contact of the upper Eagle Ford with the Austin is poorly defined by the gamma ray log (Fig. 36 package E). The ambiguous character of this contact likely developed due to the highly calcareous nature of disrupted bedded foraminiferal packstone facies in the upper Eagle Ford and bioturbated lime wackestone facies in the Austin. The low Ti content of these disrupted bedded foraminiferal packstone facies is also indicated by lower neutron and density porosity values (Fig. 33, 36).

Proximal to the Stuart City reef margin, the J.A. Leppard #1-H core, the Eagle Ford shows high gamma ray values compared to its lower and upper bounding platform

carbonates (Fig. 37 package A & B). Facies diversity is lower in this area; yet, logs show variability relating to cyclic alternations between depositional and diagenetic facies and elemental variability within depositional facies (Fig. 34, 37). Here, the lower Eagle Ford consists predominately of laminated calcareous foraminiferal mudrock facies with intermittent microspar/pseudospar concretions. The gamma ray exhibits a consistent trend through the lower Eagle Ford and is highly cyclic with the lowest gamma values commonly correlative to individual or packages of microspar/pseudospar concretions. Cyclicity in the gamma ray shows a relationship with Ti and Si values (Fig. 34, 37). The upper Eagle Ford of this distal shelf locality shows a reversal in gamma trend from the proximal San Marcos Arch example (Fig. 36, 37). Higher gamma response at the top of the J.A. Leppard well (Fig. 37 package B) originates from increased terrigenous influx (Fig. 34, 37) and decreased preservation of organic matter.

Near the Maverick Basin, the L. Hurt #1 core, the base of the upper Eagle Ford contact is marked by a low gamma spike that correlates to abundant microspar/pseudospar concretion development (Fig. 38 package A). Above this interval, the upper Eagle Ford exhibits a cyclic, intermediate gamma ray trend relating to laminated foraminiferal and peloidal packstone and microspar/pseudospar concretion beds within laminated calcareous foraminiferal mudrock facies (Fig. 38 package B). Internal variation within laminated calcareous foraminiferal mudrock facies also contributes to cyclic gamma response (Fig. 38 package B). The transitional Eagle Ford is characterized by a highly-cyclic gamma ray response generated in relation to cyclic bedded laminated wackestone and bioturbated lime wackestone facies. Highly-cyclic stratification, closely related calcite-rich mineralogies, and abundant localized diagenesis prevent recognition of one-to-one relationships between gamma ray logs and facies.

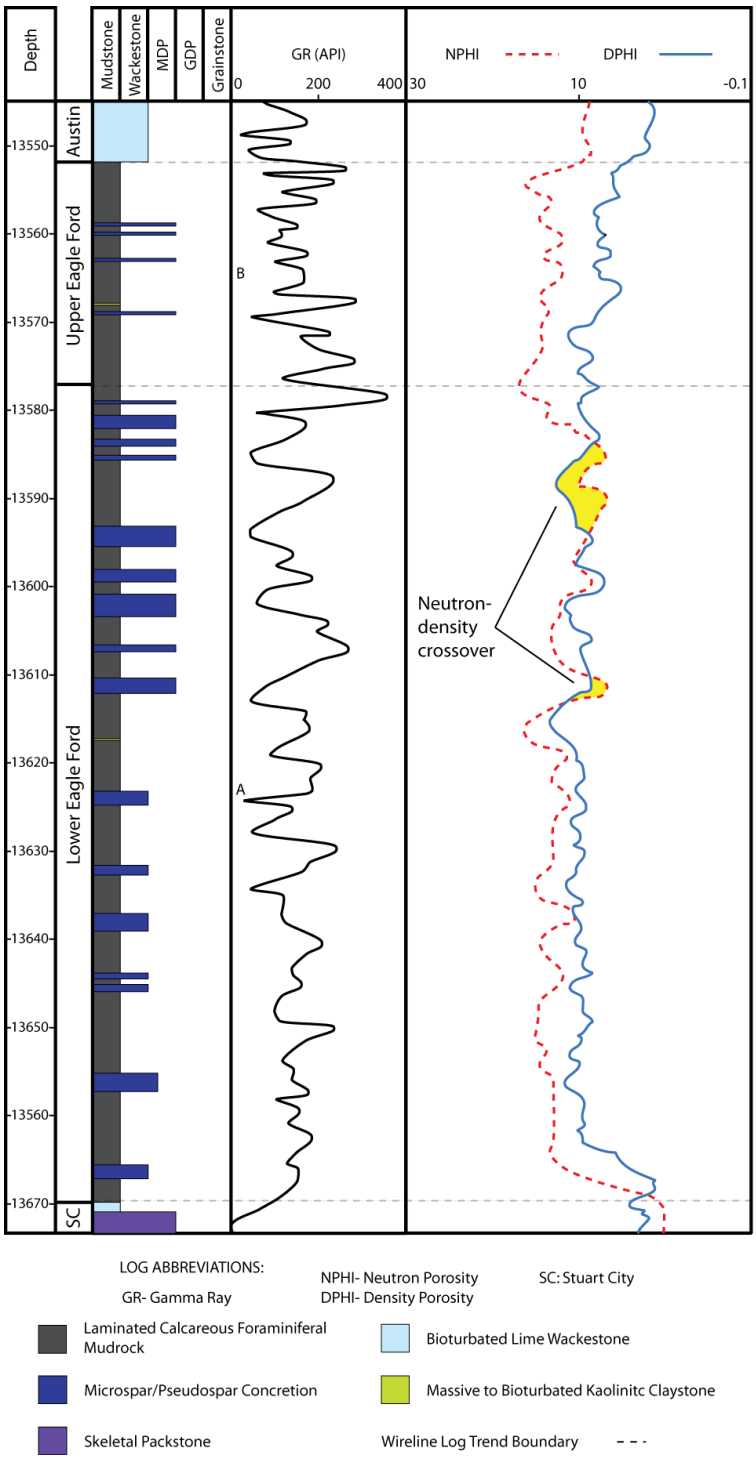

Figure 37: Facies and log character of lower and upper Eagle Ford mudrocks near the Stuart City Shelf Margin. Gamma ray plot based on 1 ft sample spacing. Letters denote wireline log trend packages. J.A. Leppard #1-H.

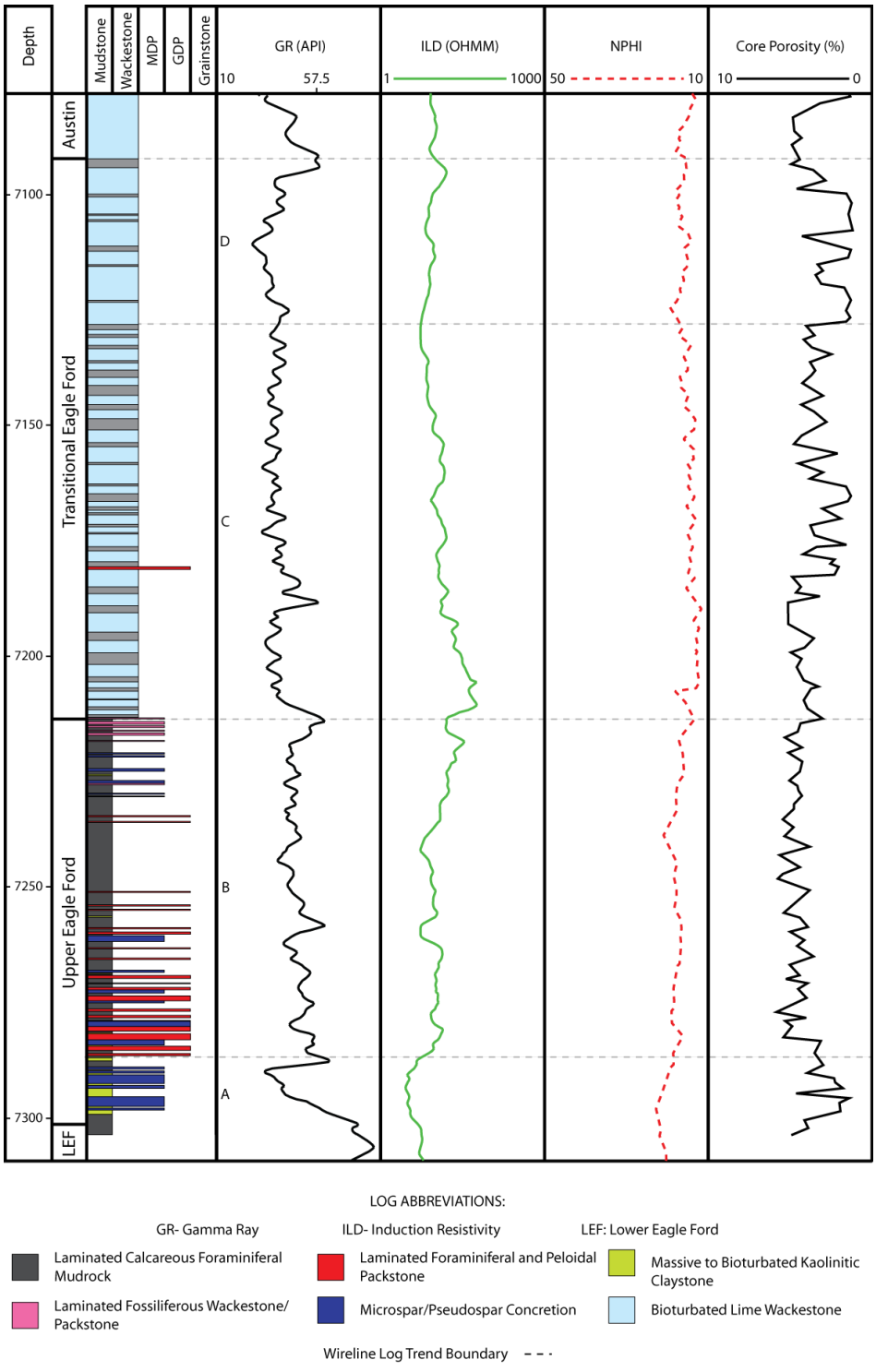

Figure 38: Facies and log character of upper and transitional Eagle Ford mudrocks of the Maverick Basin. Letters denote wireline log trend packages. L. Hurt #1.

However, comparison of the lower (Fig. 38 package C) and upper transitional Eagle Ford (Fig. 38 package D) shows that laminated wackestones generate a higher gamma ray trend. It is also important to note that the gamma ray log and core porosity analyses appear covariant; lower gamma ray values commonly align with lower porosity values.

The Eagle Ford consists of three distinct members that developed under varying depositional conditions and possess characteristic log response. Identification of individual facies within members is made difficult by the thinly bedded nature, multiple facies in close proximity to one another, and heterogeneous lithologic nature of fine-grained rock matrix. Due to these factors, individual facies show multiple log expressions and multiple facies appear with similar log expression. These factors combine to make wireline log recognition of lithologic trends in the Eagle Ford difficult. However, identification of relative shelfal and stratigraphic position allows comparison to established trends in Eagle Ford lithology and facies.

TOTAL ORGANIC CARBON

The Eagle Ford is a proven source rock (Robinson, 1997) showing elevated organic matter content, with TOC values ranging up to 11.8% (120 samples). Trends in TOC values identify both large- and small-scale depositional controls on organic matter abundance and preservation (Fig. 39, 40). The lower Eagle Ford depositional succession consistently shows the highest organic matter content with an average of 5.1% (52 samples) (Fig. 39). Two distinct TOC trends are apparent due to the interplay between terrigenous siliciclastic and marine carbonate sources (Fig. 40). Massive argillaceous mudrock facies (5.1% TOC, 8 samples) show increasing TOC with increasing carbonate content while the remainder of the calcareous Eagle Ford mudrocks (5.0% TOC, 55 samples) show established trends of decreasing TOC with increasing carbonate (Fig. 40).

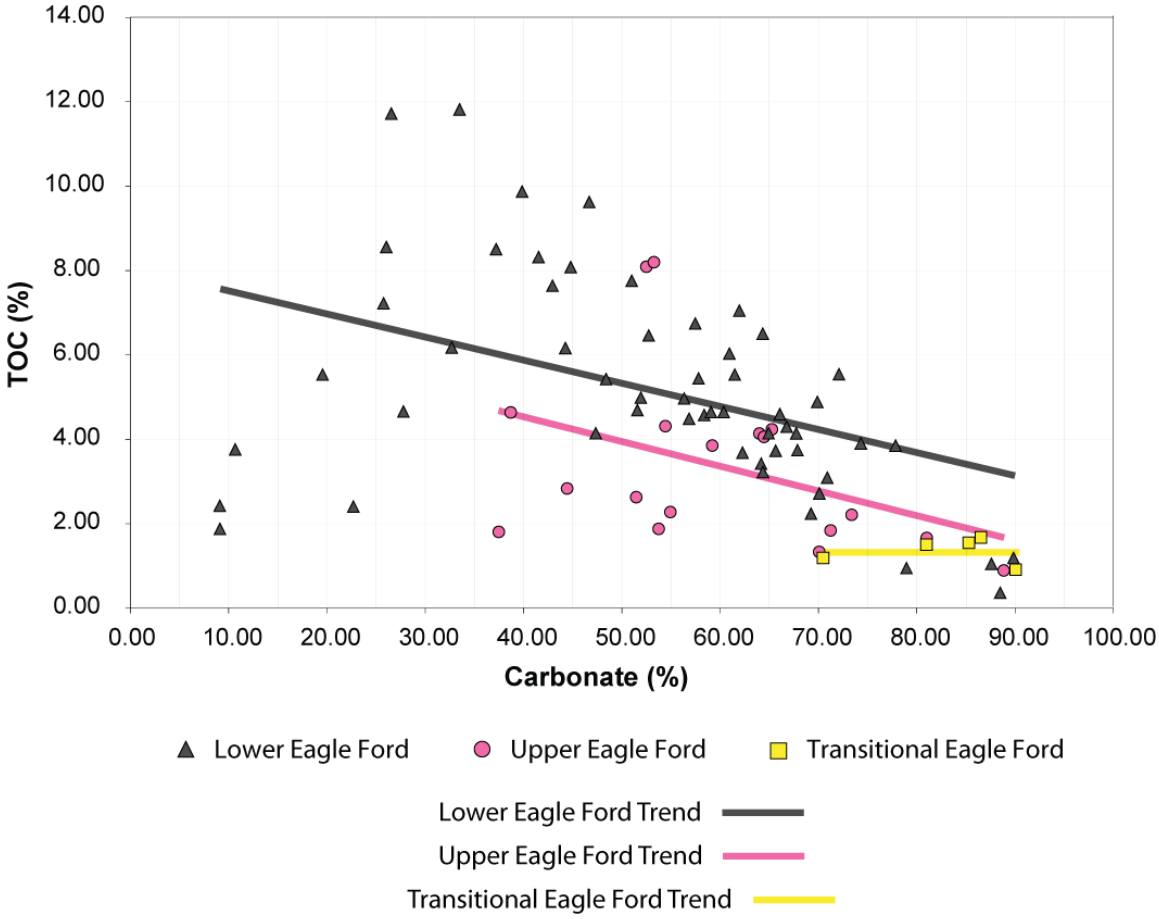

Figure 39: Eagle Ford members show progressive decreases in TOC and increases in carbonate content between the lower, upper, and transitional Eagle Ford, respectively.

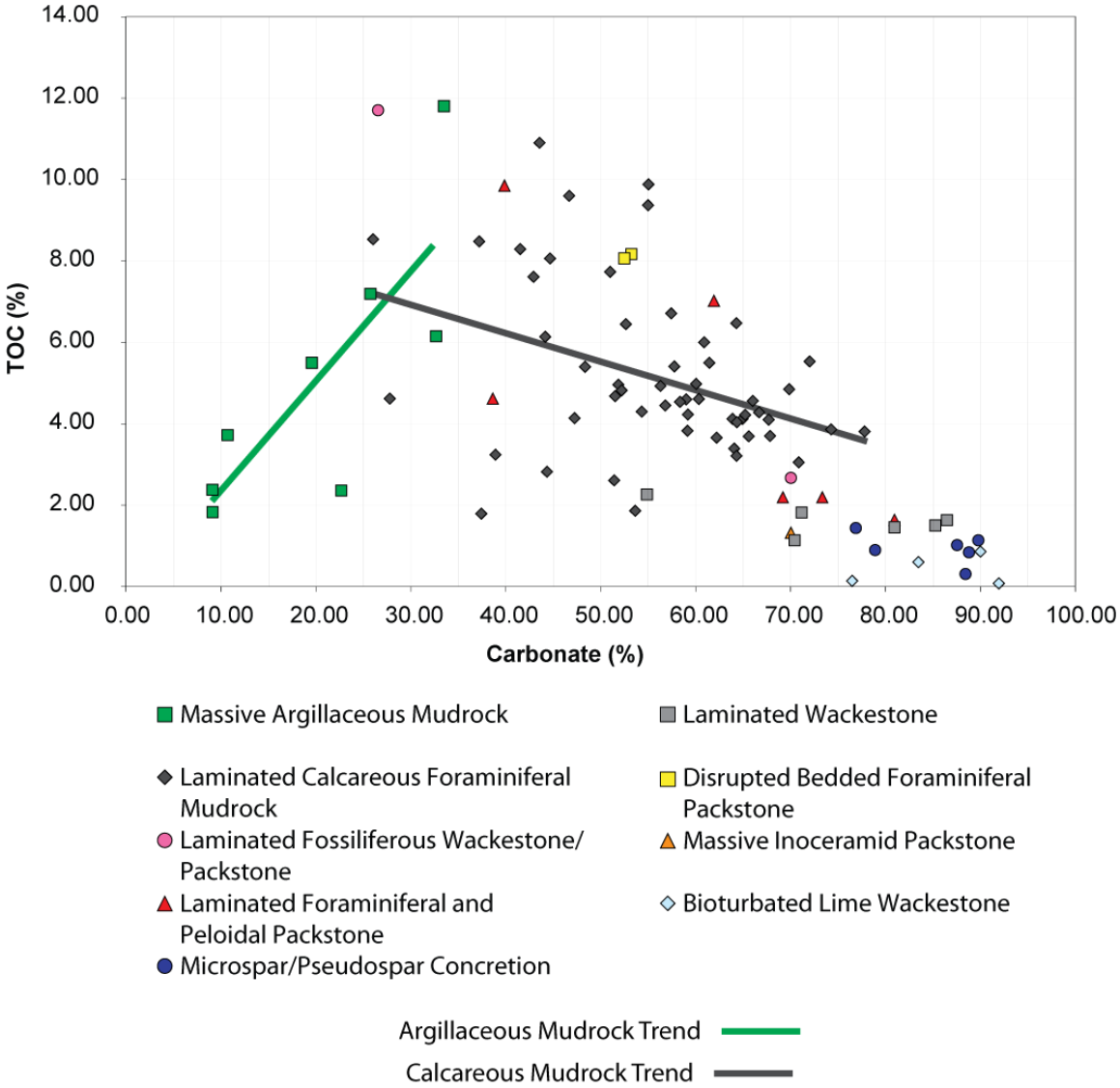

Figure 40: Within Eagle Ford facies, distinct TOC trends are evident between carbonate content and preserved TOC values. These trends relate to both sediment source and proximity. No TOC values were measured in massive to bioturbated kaolinitic claystone facies.

Upward decreases in TOC from the upper Eagle Ford (average 3.2 %, 18 samples) to the transitional Eagle Ford (average 1.3 %, 5 samples) are associated with increasing depositional energy and bioturbation (Fig. 39). The lack of well-established depositional timelines and highly variable thermal maturities in the Eagle Ford prevents time equivalent TOC comparisons across the shelf. However, clear proximal to distal trends of increasing TOC exist in both Eagle Ford and the transitional Austin-Eagle Ford depositional succession.

Comparison of Eagle Ford facies with TOC analyses show TOC preservation is consistent with prolonged water anoxia and low depositional energies. Sedimentological characteristics typical of increasing anoxic bottom conditions commonly include decreased benthic diversity and size, absence of benthic fauna, decreasing burrow size, and eventually the termination of burrowing resulting in well-preserved sediment laminations (Wignall, 1994). Other indicators of anoxia include the formation of authigenic pyrite, increasing ratios of pelagic to benthic fossils, and general dark rock color (Charvat and Grayson, 1981). While organic richness is not always determinable in Eagle Ford rocks based on color alone, the remainder of these controls as anoxia indicators and eventual organic matter preservation are evident in Eagle Ford facies. Fine-grained mudrocks of the Eagle Ford contain higher TOCs (average 5%, 76 samples) while coarser fabrics show lower TOCs (average 3.05%, 26 samples). The proximity of source rocks with coarser-grained packstone fabrics potentially extends the storage capability and transmissibility of hydrocarbons within organic-rich zones.

ORGANIC MATTER TYPE

The high oil-generative potential of Eagle Ford source rocks was established by by Robinson (1997) who conducted visual kerogen analysis of Eagle Ford outcrops near

Austin and Waco, Texas and a core from the East Texas Basin. In these outcrops (Tmax 404-433) and core (Tmax 430-446), kerogen macerals including fluorescent amorphinite (primary) and exinite (secondary) generated 50-85% oil-prone kerogen (Robinson, 1997). Robinson (1997) also noted that the richest intervals of 80-85% oil- prone kerogen were concentrated in the transgressive lower Eagle Ford. Dawson (2010) further characterized Eagle Ford organic matter character in East Texas by showing the association of oil-prone organic matter with lower Eagle Ford deposits and gas-prone organic matter with upper Eagle Ford deposits.

Little published work exists on Eagle Ford organic matter from the subsurface of South Texas. For this study, Hydrogen Index vs. Tmax plots were constructed to help distinguish the character of organic matter in sampled Eagle Ford cores. Sampling efforts concentrated on both immature and thermally mature samples. Immature samples provide more reliable indicators of the original organic matter type before maturation related alteration. Thermally mature samples provide insight into the current generating potential of the Eagle Ford Formation.

Immature (<435 Tmax, 0.50 %Ro) organic matter samples from lower and upper members of the Eagle Ford Formation of South Texas plot as possessing a highly oil-prone generative potential (Fig. 41). A single sample from the lower Eagle Ford depositional succession displayed lower hydrogen index values, typical of mixed oil/gas generating organic matter (Fig. 41). Comparison of oil generative potential by members of the subsurface Eagle Ford Formation shows that variability is due predominately to level of thermal maturation (Fig. 41). No immature transitional Eagle Ford samples were collected and therefore organic matter type could not be characterized.

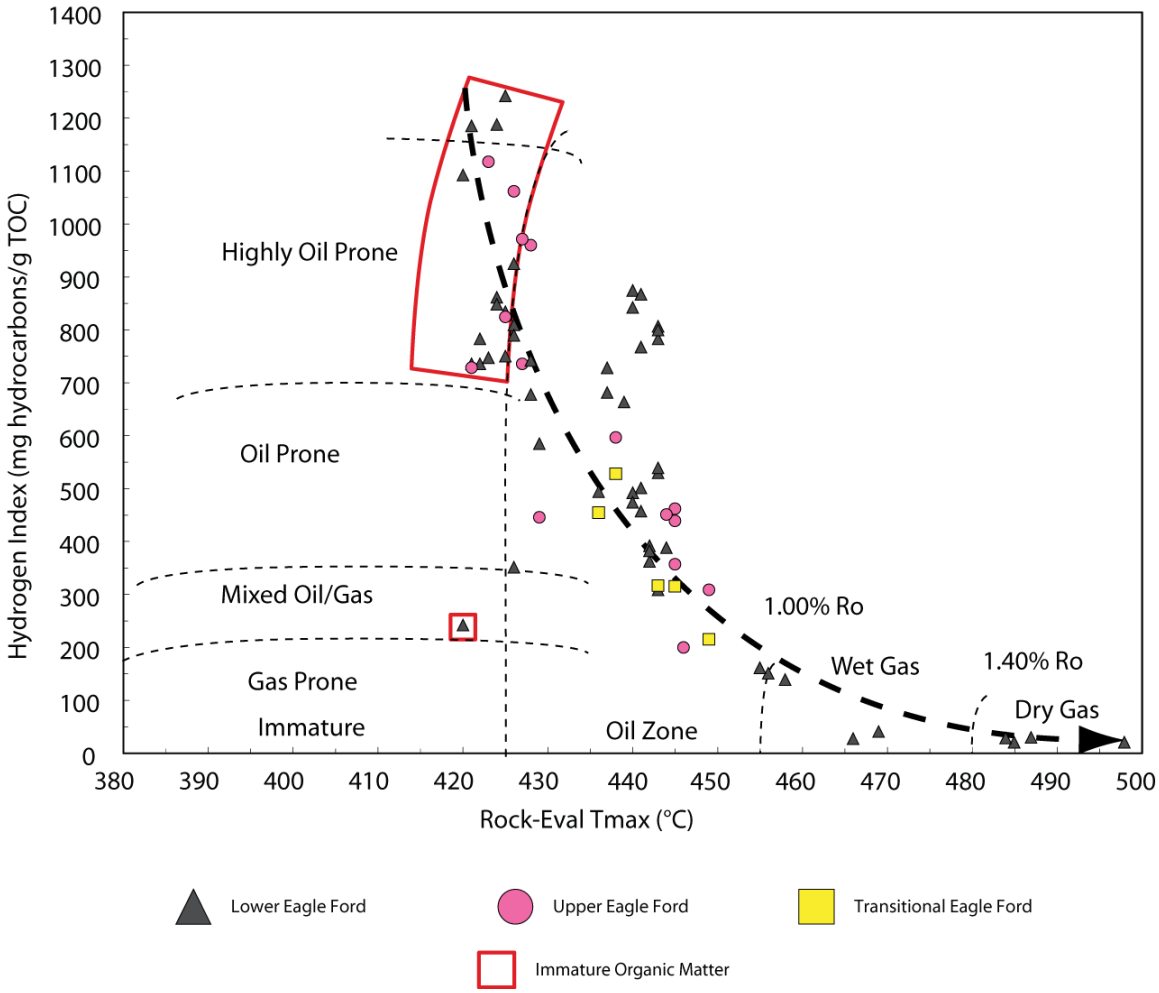

Figure 41: Organic matter in the Eagle Ford Formation commonly shows high oil-generative potential (based on hydrogen index). The dashed black line follows the progression from oil generation to subsequent wet gas and dry gas generation due to increasing thermal maturity.

FACIES ARCHITECTURE AND DEPOSITIONAL MODELS

Analysis of lateral and vertical variations in Eagle Ford facies distributions helps define trends that correspond to depositional and geochemical conditions on the flooded Comanche Shelf. Facies defined in this study typically represent open marine, mud-rich depositional environments ranging from above storm wave base, winnowed, concentrated, and transported coarse-grained skeletal sediment to below storm wave base, fine-grained, planar laminated sediment.

Processes inferred from low-energy mudrock sedimentation include hemipelagic settling of terrigenous clay- to silt- sized quartz, plagioclase, K-feldspar, and clay minerals. Pelagic settling of planktonic globigerinid foraminifera, calcareous nanoplankton, phosphatic bioclasts, and organic matter from an overlying, oxygenated water column also contributed considerable sediment to Eagle Ford mudrocks.

Eagle Ford facies also show strong evidence of bottom-current winnowing, cohesive and non-cohesive density flows, and dilute turbidity flows. Sedimentary structures indicative of these processes include planar and ripple laminations (Fig. 14, 18), starved ripples (Fig. 16, 19), low-angle cross bedding (Fig. 16), scour surfaces (Fig. 18, 20) and transported skeletal debris (Fig. 15, 18, 19, 20). Many of these higher-energy processes were episodic; this resulted in fine-grained, lower-energy sediments accumulating in close proximity to coarser-grained skeletal sediments. Similarly, higher-energy event sedimentation was not limited only to proximal depositional environments; resedimentation of entrained sediment extended into distal depositional environments.

Well-developed trends in geographic distribution, stratigraphic abundance, and relative thickness of both fine-grained, low-energy and coarser-grained, higher-energy Eagle Ford facies allow recognition of depositional relationships between proximally and

distally developed facies. Based on these criteria, lateral and vertical facies relationships were defined from core-calibrated wireline logs (Fig. 42, 43). Due to issues regarding the thinly bedded nature of massive to bioturbated kaolinitic claystone facies and microspar /pseudospar concretions, these were not included in these cross sections. A review of the stratigraphic and geographic occurrence of massive to bioturbated claystone and microspar/pseudospar concretions accompanies their previous descriptions and can be seen for each core in Appendix A.

The San Marcos Arch and Maverick Basin acted as regional structural controls on the development of depositional profiles and were largely responsible for observed variability in the geographic distribution of facies. Facies on the San Marcos Arch show increased variability and concentration of coarser-grained, calcite-rich facies (Fig. 42, 43). Distal environments, including the Maverick Basin (Fig. 42) and the Stuart City reef margin (Fig. 43) show decreased facies variability.

Beginning on the San Marcos Arch, basal Eagle Ford rocks consist of massive argillaceous mudrock facies. These rock exists as a thin (< 10ft), continuous unit that extends along the axis of the San Marcos Arch toward the Stuart City reef margin (Fig. 43). Extending from the San Marcos Arch to the southwest, massive argillaceous mudrock facies thicken to approximately 20-25 ft, but undergo a lithology change before reaching the Maverick Basin area (Fig. 42). Laminated calcareous foraminiferal mudrock facies were deposited as a distal equivalent to massive argillaceous mudrock facies and show increased thickening into the Maverick Basin (Fig. 42).

Above this initial terrigenous depositional phase, the remainder of the lower and upper Eagle Ford predominately consist of laminated calcareous foraminiferal mudrock facies and laminated foraminiferal and peloidal packstone facies (Fig. 42, 43). The laminated calcareous foraminiferal mudrock facies are the most abundant facies in the

Eagle Ford and are commonly present in the Maverick Basin, but are less prevalent on the San Marcos Arch (Fig. 42, 43) Laminated foraminiferal and peloidal packstone facies occur thinly bedded within laminated calcareous foraminiferal mudrock facies. These facies have been grouped (Fig. 42, 43) to better define the geographic extent and thicknesses of higher-energy depositional phases during the Eagle Ford. Trends of alternating laminated calcareous foraminiferal mudrock and laminated foraminiferal and peloidal packstone facies likely relate to changing accommodation on the platform.

On the San Marcos Arch, the upper Eagle Ford commonly consists of thickly bedded (<15 ft) laminated wackestone facies (Fig. 42, 43). Disrupted bedded foraminiferal packstone facies and massive inoceramid packstone facies also occur thinly bedded (<5 ft) but fail to extend distally beyond the San Marcos Arch area (Fig. 42, 43). The transitional Eagle Ford is present near the Maverick Basin in the subsurface of South Texas. Transitional Eagle Ford rocks overlie low-energy laminated calcareous foraminiferal mudrock facies of the upper Eagle Ford. Transitional Eagle Ford facies have been grouped due to the current inability to accurately interpret correlative relationships between cycles.

In order to better distinguish the character and distribution of Eagle Ford facies, identified facies relationships were analyzed and combined into idealized depositional models (Fig. 44). Process based models are useful in explaining observed sedimentological features and stratigraphic relationships while generating the ability to predict the distribution of hydrocarbon source and reservoir character. Models were constructed from observed and interpreted facies relationships from cores and wireline logs. Future biostratigraphic work and additional subsurface data will further constrain Eagle Ford facies architecture and allow formation of higher resolution depositional models.

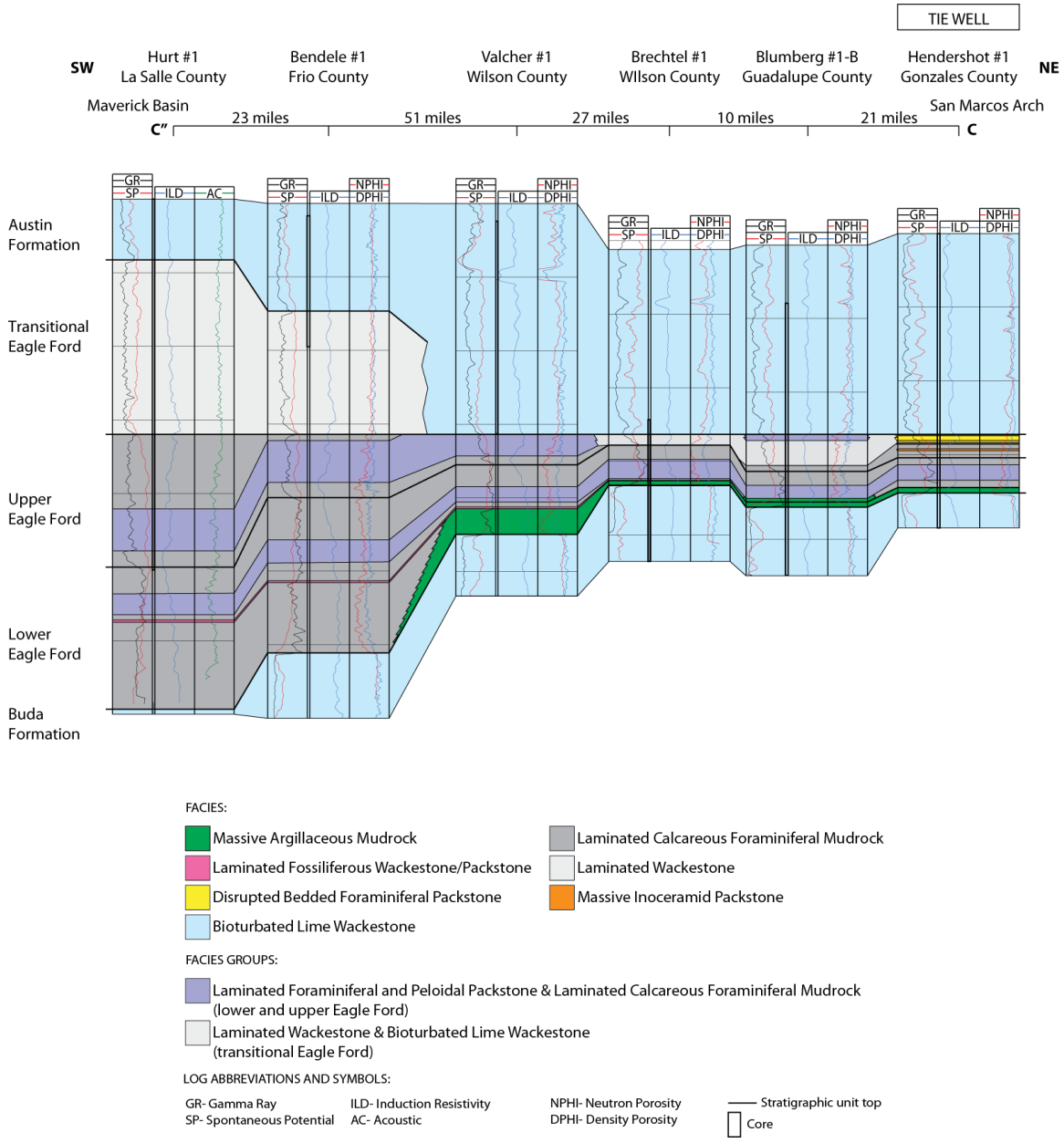

Figure 42: Southwest-Northeast Cross Section (C-C") depicting facies architecture in the Eagle Ford along an approximate strike section from the San Marcos Arch to the Maverick Basin area. Constructed from 6 cores and associated wireline logs. Line of section shown in Figure 4. Datum: Top upper Eagle Ford.

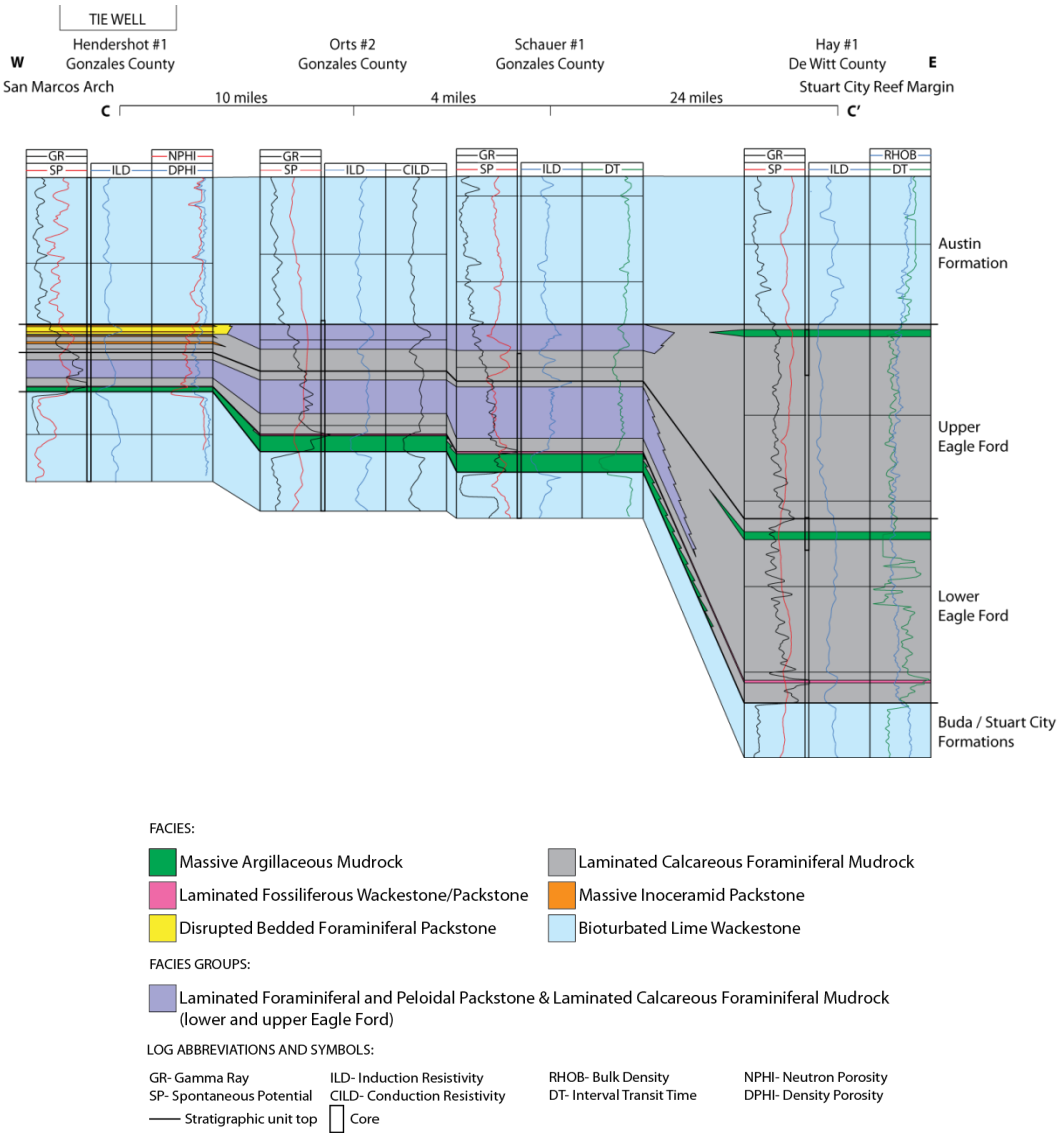

Figure 43: West–East Cross Section (C-C') depicting facies architecture in the Eagle Ford along an approximate dip section from the San Marcos Arch to the Stuart City reef margin area. Constructed from 4 cores and associated wireline logs. Line of section shown in Figure 4. Datum: Top upper Eagle Ford.

LOWER EAGLE FORD DEPOSITIONAL SUCCESSION

Early Eagle Ford sedimentation along the San Marcos Arch was dominated by point-sourced terrigenous siliciclastics; with dominant expressions including clay and quartz minerals with accessory plagioclase and K-feldspar (Fig. 44A). The resulting rocks, massive argillaceous mudrock facies, are interpreted to record deposition of the most proximal terrigenous Eagle Ford sediments in the subsurface of South Texas.

Basal Eagle Ford massive argillaceous mudrocks facies show trends of decreasing silt-sized quartz away from the San Marcos Arch. Proximal to distal trends of increasing TOC are also evident. Distal equivalents of these rocks consist of laminated calcareous foraminiferal mudrock facies (Fig. 44A). Sediment sources for the laminated calcareous foraminiferal mudrock facies predominately include coccoliths and planktonic foraminifera that were sourced from the overlying, oxygenated water column. These rocks show decreased volumes of terrigenous siliciclastic minerals. As a result, carbonate increases while terrigenous silica decreases away from the San Marcos Arch during early deposition of the lower Eagle Ford (Fig. 44A).

Sedimentary structures, including massive to fine-laminae of silt-sized globigerinid foraminifera, likely developed in below storm wave base depositional environments. Lack of burrowing, high pyrite content, and elevated TOC values (avg. >5%) indicate anoxic conditions persisted during early Eagle Ford deposition.

UPPER EAGLE FORD DEPOSITIONAL SUCCESSION

The upper Eagle Ford depositional succession shows greater lithologic variability than the lower Eagle Ford (Fig. 44B). Low-energy, anoxic conditions prevalent during lower Eagle Ford deposition persisted in distal settings; while more proximal depositional environments like those on the San Marcos Arch show coarser-grained deposition

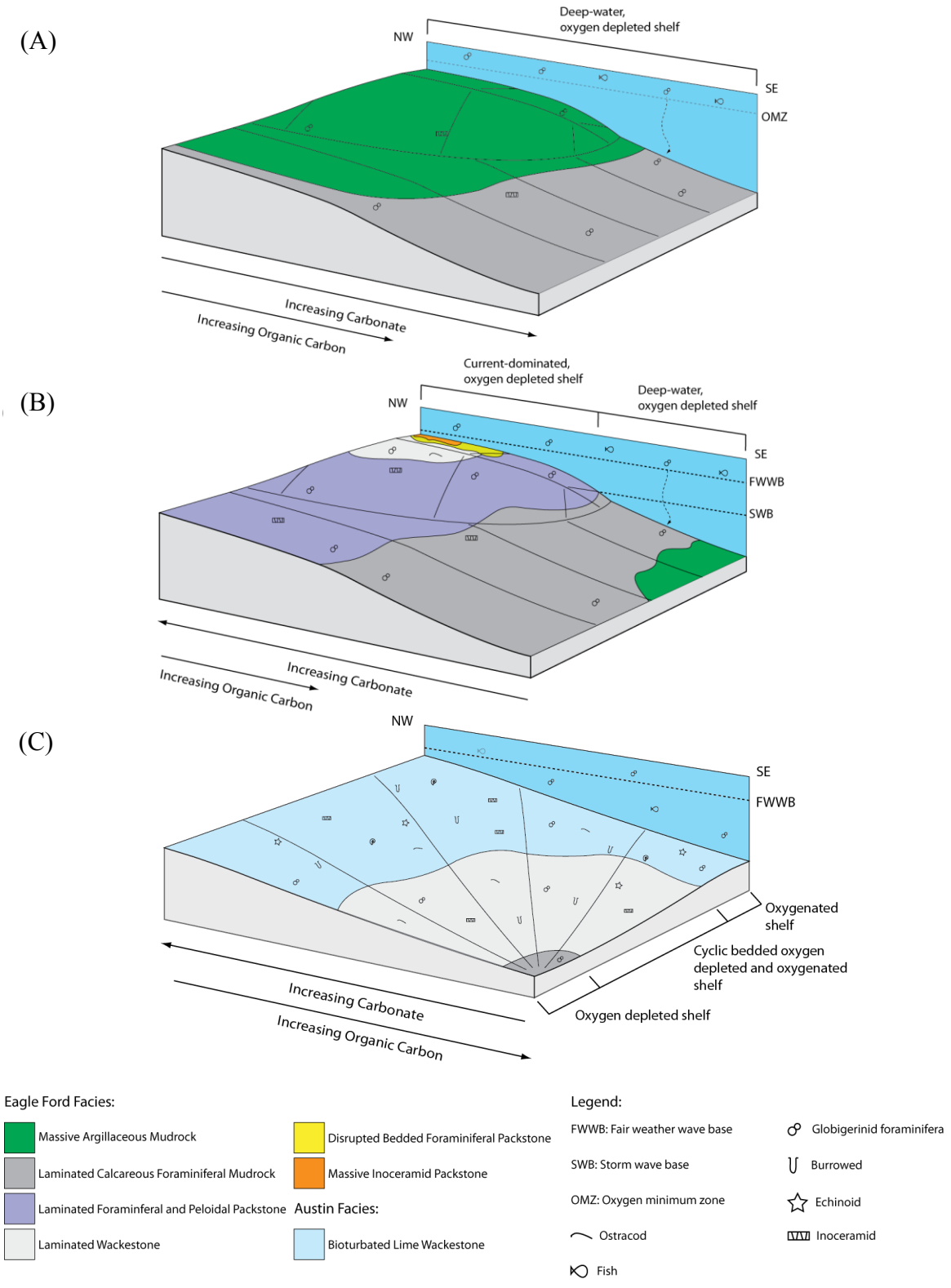
(A)
Deep-water,
oxygen depleted shelf
NW
SE
OMZ
Increasing Carbonate
Increasing Organic Carbon
(B)
Current-dominated,
oxygen depleted shelf
Deep-water,
oxygen depleted shelf
NW
SE
FWWB
SWB
Increasing Carbonate
Increasing Organic Carbon
(C)
NW
SE
FWWB
Oxygenated
shelf
Cyclic bedded oxygen
depleted and oxygenated
shelf
Oxygen depleted shelf
Increasing Carbonate
Increasing Organic Carbon
Eagle Ford Facies:
Massive Argillaceous Mudrock
Laminated Calcareous Foraminiferal Mudrock
Laminated Foraminferal and Peloidal Packstone
Laminated Wackestone
Disrupted Bedded Foraminiferal Packstone
Massive Inoceramid Packstone
Austin Facies:
Bioturbated Lime Wackestone
Legend:
FWWB: Fair weather wave base
SWB: Storm wave base
OMZ: Oxygen minimum zone
Ostracod
Fish
Globigerinid foraminifera
Burrowed
Echinoid
Inoceramid

Figure 44: (Previous page) (A) Depositional setting and facies patterns during the lower Eagle Ford, San Marcos Arch area. (B) Depositional setting and facies patterns during the upper Eagle Ford, San Marcos Arch area. (C) Depositional setting and facies patterns during transitional Austin-Eagle Ford, eastern Maverick Basin area. Proximal oxygenation of the water column led to increased bioturbation, while continued basinal restriction generated organic-rich mudrocks of the transitional Eagle Ford.

beginning in the upper Eagle Ford (Fig. 42, 44B). Proximal facies deposited on the San Marcos Arch exhibit elevated calcite and exhibit more diverse faunal assemblages than elsewhere in the upper Eagle Ford. These fauna lived in more proximal, oxygenated environments and were subsequently transported by storm-generated events. Facies associated with proximal deposition on the San Marcos Arch include laminated wackestone, disrupted bedded foraminiferal packstone, and massive inoceramid packstone (Fig. 44B). Concentrated skeletal material, ripple and cross laminations, and rip-up clasts within these facies show evidence of episodic to persistent bottom-current reworking and transport (Fig. 18, 19, 20).

Burrowing is uncommon in the upper Eagle Ford, even in proximal depositional environments on the San Marcos Arch. While TOC values are locally similar to the lower Eagle Ford, the majority of the upper Eagle Ford possesses lower TOC (Fig. 39). The highest, most consistent TOC values are found predominately in distal, low-energy depositional settings.

Distally, upper Eagle Ford rocks show evidence of a well-defined storm wave base, marked by a proximal to distal transition from laminated foraminiferal and peloidal packstone facies to laminated calcareous foraminiferal mudrock facies (Fig. 44B). Higher levels of winnowing and bed amalgamation in laminated foraminiferal and peloidal packstone facies of proximal depositional environments indicate strong relationships between increasing bottom-currents and decreasing water depth. In the most

distal shelfal settings, the laminated calcareous foraminiferal mudrock facies is dominant. Marine carbonate and resedimentation of storm entrained sediment from more proximal environments commonly act as sediment sources in distal depositional environments. Carbonate content is higher in the upper Eagle Ford than in the lower Eagle Ford, resulting from an overall decrease in terrigenous influx and concentration during higher-energy depositional processes. However, massive argillaceous mudrock facies are locally common in distal upper Eagle Ford rocks; these deposits are likely the result of siliciclastic influx from the north

TRANSITIONAL AUSTIN-EAGLE FORD DEPOSITIONAL SUCCESSION

The transitional Austin-Eagle Ford depositional succession overlies the upper Eagle Ford and marks a return to oxygenated depositional conditions across much of the shelf (Fig. 42). Widespread oxygenation of the water column led to increased diversity and habitation of benthic fauna, increased bioturbation, increased sedimentation rates (Phelps, 2011), and decreased organic matter preservation. As a result, accumulation of well-laminated organic-rich upper Eagle Ford mudrocks shifted to deposition of highly bioturbated, light to medium gray, calcisphere-, echinoid-, and foraminiferal-bearing wackestones (Siemers, 1978) of the Austin Formation in depositional environments proximal to the San Marcos Arch (Fig. 44C).

Transitional Eagle Ford facies developed in distal depositional environments surrounding the Maverick Basin and consist of highly-cyclic laminated wackestone (Fig. 18) and bioturbated lime wackestone facies (Fig. 21). The cyclic nature of laminated wackestone facies (cycle base) and bioturbated lime wackestone facies (cycle top) suggest that distal environments of the transitional Austin-Eagle Ford depositional succession were subjected to recurrent variations in water column oxygenation. Shifts

from oxygenated to anoxic conditions likely occurred rapidly, developing sharp bounding contacts at the base of laminated facies (Fig. 25). The upper contact of laminated facies is commonly sharp, but occasionally appears gradational due to the formation of diagenetic microspar/pseudospar calcite (Fig. 25). Evidence of calcite recrystallization is much stronger in bioturbated facies.

Continuous to discontinuous laminae exhibiting scoured bases are evident in both facies and indicate accumulation in depositional environments commonly subjected to current reworking. Oxygenation events permitted access to burrowing infauna, which typically destroyed laminae in bioturbated lime wackestone facies. The higher degree of burrowing in these rocks probably also account for lower levels of TOC than in the laminated facies. An overall trend of increasing oxygenation upward is manifested by the upward thickening of bioturbated beds in relation to diminishing thickness and occurrence of laminated, organic-rich beds. These rocks represent a distal equivalent to typical Austin facies.

SUMMARY AND CONCLUSIONS

Nine facies showing systematic variability in spatial distribution were characterized and related to varying depositional processes and geochemical environments on the flooded Comanche Shelf, these include:

1) Massive Argillaceous Mudrock
2) Laminated Calcareous Foraminiferal Mudrock
3) Laminated Fossiliferous Wackestone/Packstone
4) Laminated Foraminiferal and Peloidal Packstone
5) Massive to Bioturbated Kaolinitic Claystone
6) Laminated Wackestone
7) Disrupted Bedded Foraminiferal Packstone
8) Massive Inoceramid Packstone
9) Bioturbated Lime Wackestone

The most abundant facies in the Eagle Ford consist of fine-grained, laminated calcareous foraminiferal mudrocks. This facies is composed of a mixed calcite (avg. 54 %) and clay (avg. 25 %) matrix enriched with organic matter (avg. 5.0 % TOC) and developed in below storm wave base depositional environments. Millimeter scale pelagic foraminifera laminations developed from waning density flows and act as an indicator of water anoxia. Formation of abundant diagenetic pyrite and microspar/pseudospar concretions also indicate anoxic environments persisted near the sediment-water interface during deposition.

Laminated foraminiferal and peloidal packstone facies were deposited as proximal equivalents to laminated calcareous foraminiferal mudrock facies. These rocks consist of two subfacies. These include light grey, ripple and low angle cross laminated

skeletal limestones interbedded with dark grey, organic-rich (avg. 4.6% TOC) peloidal packstones. Individual skeletal beds are commonly thin (< 5mm) but reach thickness up to 15 cm proximal to the San Marcos Arch. Evidence of early calcite cementation is evident in skeletal laminations. XRD analysis shows high carbonate (avg. 69 %) and low clay (avg. 18 %) contribution to the rock matrix. Together, laminated calcareous foraminiferal mudrock facies and laminated foraminiferal and peloidal mudrock facies constitute the primary reservoir for the Eagle Ford in the subsurface of South Texas.

The Eagle Ford can be subdivided into lower, upper, and transitional members that represent three regionally extensive stratigraphic units possessing unique rock properties and characteristic source and reservoir potential. Core studies show that key rock properties originated in unique depositional environments with variable sediment source and distribution, diagenesis, and water column chemistry.

Lower Eagle Ford rocks along the San Marcos Arch show accumulation of clay- (avg. 45 %) and quartz-rich (avg. 32 %), organic-rich (avg. 5.1 %) massive argillaceous mudrock facies. These rocks record sedimentation of the most proximal terrigenous siliciclastics in the Eagle Ford Formation. Distal equivalents to these rocks consist of laminated calcareous foraminiferal mudrock facies and were sourced predominately from the overlying, oxygenated water column. The terrigenous character of the lower Eagle Ford also decreases stratigraphically upward. These rocks commonly show episodic early diagenetic recrystallization of calcite. Lower Eagle Ford facies show the most diverse mineralogical character (avg. 51 % carbonate), highest TOC (avg. 5.1%), and thickest accumulation across the study area.

Upper Eagle Ford rocks show development of increased facies variability and accumulation of coarser-grained sediment than seen in the lower Eagle Ford. On the San

Marcos Arch, transported skeletal sediments resulted in facies with well-developed laminations to massive beds with rip-up clasts. These facies originated from higher-energy depositional processes during the upper Eagle Ford and represent more proximal depositional environments than were present during lower Eagle Ford deposition. In distal environments, lower and upper Eagle Ford facies appear lithologically similar; however, a shift away from terrigenous sourced sediment in upper Eagle Ford commonly leads to increased carbonate content (avg. 67 %). TOC is also lower in the upper Eagle Ford (avg. 3.2 %).

The transitional Austin/Eagle Ford depositional succession is marked by an increase in water oxygenation and decrease in organic matter preservation across much of the shelf. Evidence of water column oxygenation includes increased benthic fossil abundance and diversity, increased bioturbation, and decreased organic matter preservation. The transitional Eagle Ford member developed distally to foraminiferal lime wackestones of the Austin Formation and shows increased TOC (avg. 1.3 %). In the transitional Eagle Ford member, highly–cyclic laminated wackestone (cycle base) and bioturbated wackestone facies (cycle top) suggest recurrent variation in geochemical conditions in distal depositional environments.

Characterization of facies and stratigraphic architecture contribute understanding to the development of the emerging Eagle Ford unconventional resource play. Distinct, predictable variation between proximal and distal rock attributes for lower and upper Eagle Ford and transitional Austin-Eagle Ford depositional successions allow prediction into the distribution of hydrocarbon source and reservoir character.

Appendix A: Eagle Ford Core Descriptions

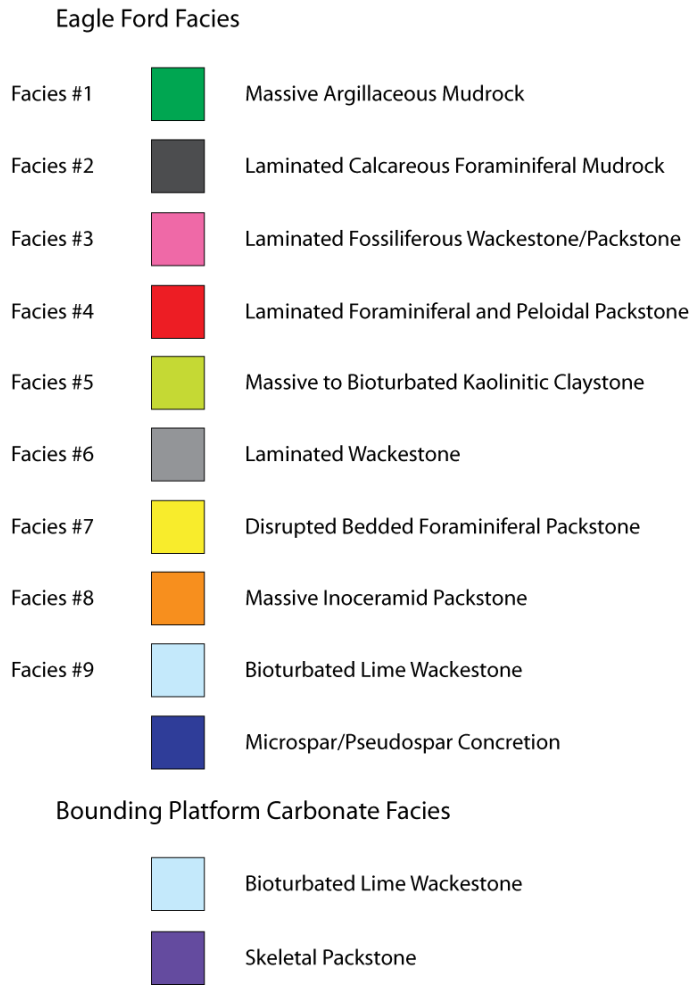

Stratigraphic Interval Abbreviations:

LEF- Lower Eagle Ford

UEF- Upper Eagle Ford

EF Tran. - Transitional Eagle Ford

SC- Stuart City Formation

BUD- Buda Formation

AUS- Austin Formation

Sample No.	Operator	Lease Name	API	County	Latitude	Longitude
1	Shell Oil Co.	Roessler, A.E. #1-R	42025301480000	Bee	28.6184	97.9794
2	Getty Oil Co.	Hurt, Lloyd #1	42283303050000	La Salle	28.6163	-99.3402
3	Steve Gose	Hassett #3	42507304400000*	Zavala	28.6556	-99.8597
4	Tesoro Petroleum	Hendershot, Clare J. #1	42177302180000	Gonzales	29.5613	-97.5838
5	Prarie Producing Co.	Brechtel, Wayne #1	42493302080000	Wilson	29.3616	-98.0226
6	Tesoro Petroleum	Calvert, J.H. #1	42163307280000	Frio	28.8086	-99.2952
7	Magnolia Oil Co.	Proctor, G.W. #23	42055033040000	Caldwell	29.7235	-97.7224
8	Goodrich Oil Co.	Shanklin, W.R. #1A	42187015980000	Guadalupe	29.6802	-97.7517
9	Prarie Producing Co.	Blumberg, Jane W. #1-B	42187305320000	Guadalupe	29.3798	-97.8627
10	Zavala Energy, Inc.	Mathews, J.L. #1-1	42507319640000	Zavala	28.9050	-99.9058
11	Shell Oil Co.	Hay, E.D. #1	42123303590000	De Witt	29.0592	-97.4846
12	Standard Oil of Texas	Dilworth, Mrs Mary J. #1	42311012590000	McMullen	28.4128	-98.5970
13	Geological Research Corp.	Schauers, F.T. etal #1	42177303940000	Gonzales	29.3978	-97.4919
14	Tesoro Petroleum	Valcher, Emma #1	42493302300000	Wilson	29.0241	-98.2397
15	Shell Oil Co.	Leppard, J.A. #1-H	42025303890000	Bee	28.5984	-98.0289
16	Pinnacle Rylt & Op Co.	Gise, Lawrence #1	42127328780000	Dimmit	28.5559	-99.4185
17	Beard-Schefts (Mim Oil Co.)	Hal, Browne #8	42055017810000	Caldwell	29.8229	-97.6047
18	Transocean Oil, Inc.	Orts, H.P. #2	42177302030000	Gonzales	29.4530	-97.4718
19	Prarie Producing Co.	Bendele. Spettel #1	42163306230000	Frio	28.6470	-98.9589
20	Shell Oil Co.	Krause, A.L. estate #2	42283302740000	La Salle	28.1758	-99.3838
21	Brazos Oil & Gas Co.	Person, Otha D. #1	42255001410000	Karnes	29.0238	-97.8713
22	Superior Oil Co.	Blackwell, R.F. etal #1	42123302790000	De Witt	29.0728	-97.3768
23	Seaboard & Hamon	Szalwinski, J.J. #1	42255007450000	Karnes	28.9947	-98.0049
24	Wellington Oil of Del	Chittim, J.M. #1	42323003230000	Maverick	28.8547	-100.2896
25	Rutherford Oil Corp.	Triple Bar Ranch #1	42283302250000	La Salle	28.0906	-99.2646
26	Shell Oil Co.	Pawelek, Ben A. #1-A	42255305980000	Karnes	29.0246	-97.8790
27	Quintana Petroleum Corp.	Halff, H.A. etal #1	42163305910000	Frio	28.8864	-99.2887

* Nearby well (Hassett #2)

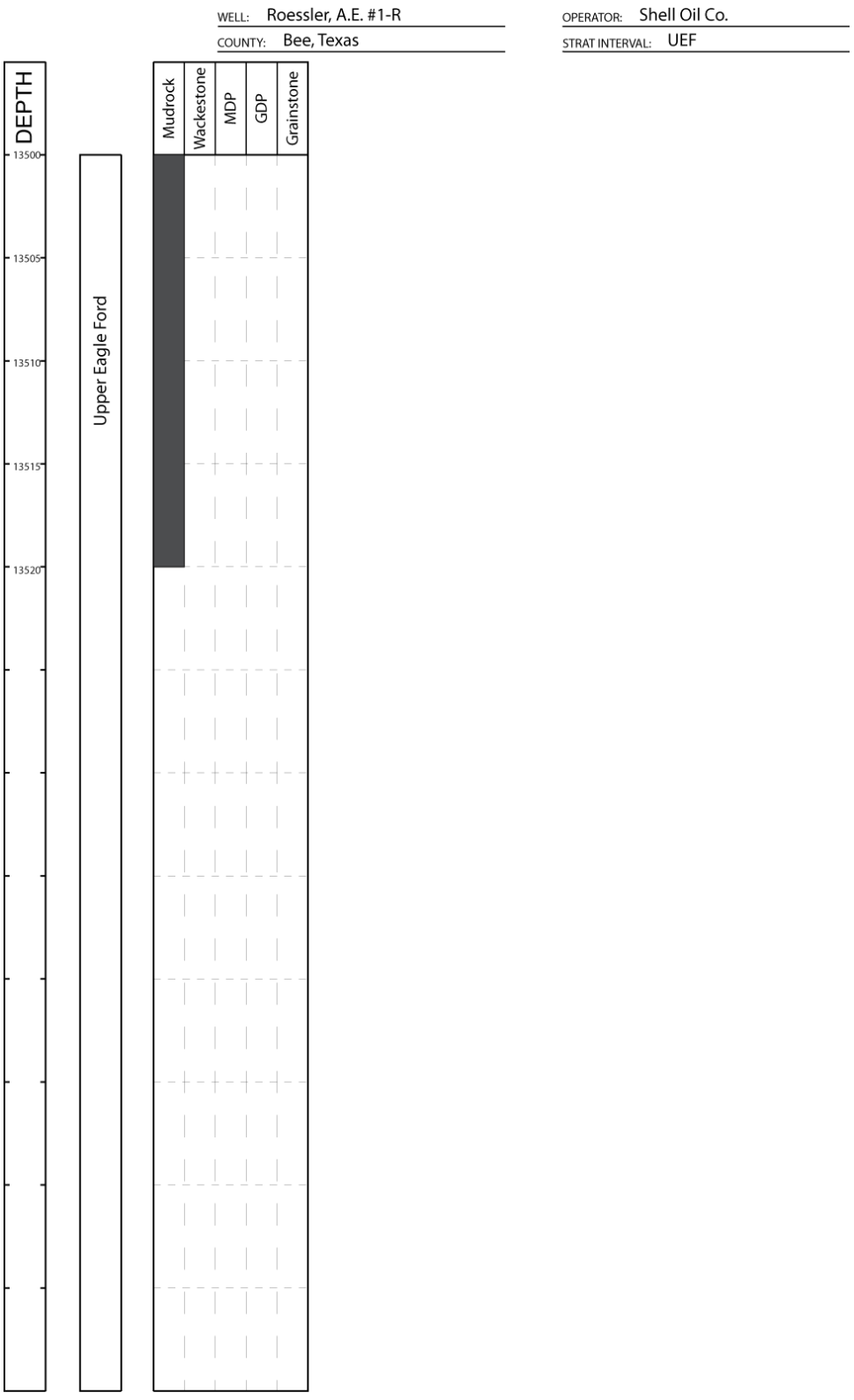
WELL: Roessler, A.E. #1-R
COUNTY: Bee, Texas
OPERATOR: Shell Oil Co.
STRAT INTERVAL: UEF
DEPTH
13500
13505
13510
13515
13520
Upper Eagle Ford
Mudrock
Wackestone
MDP
GDP
Grainstone

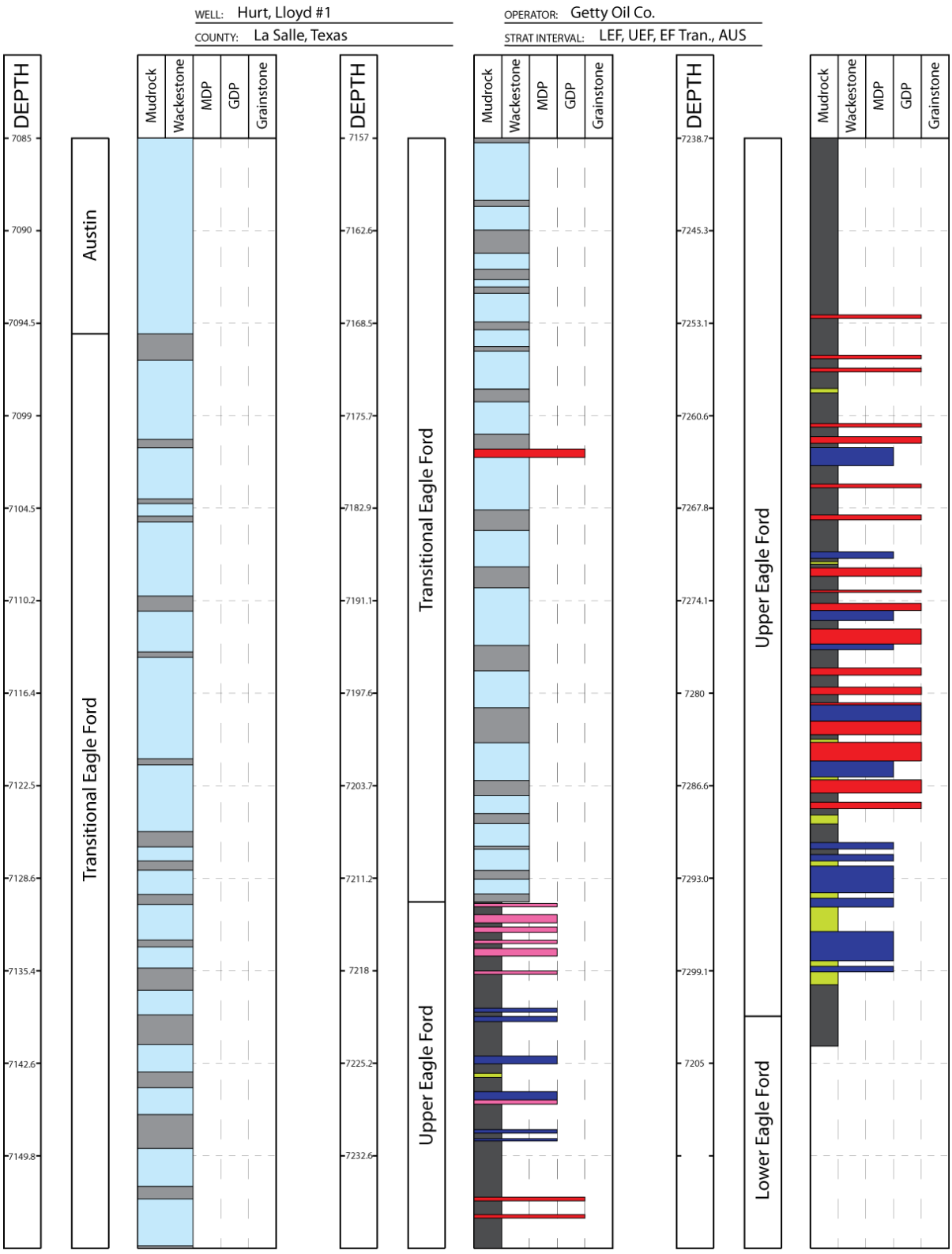
WELL: Hurt, Lloyd #1
COUNTY: La Salle, Texas
OPERATOR: Getty Oil Co.
STRAT INTERVAL: LEF, UEF, EF Tran., AUS
DEPTH
7085
7090
7094.5
7099
7104.5
7110.2
7116.4
7122.5
7128.6
7135.4
7142.6
7149.8
Austin
Transitional Eagle Ford
Mudrock
Wackestone
MDP
GDP
Grainstone
DEPTH
7157
7162.6
7168.5
7175.7
7182.9
7191.1
7197.6
7203.7
7211.2
7218
7225.2
7232.6
Transitional Eagle Ford
Upper Eagle Ford
Mudrock
Wackestone
MDP
GDP
Grainstone
DEPTH
7238.7
7245.3
7253.1
7260.6
7267.8
7274.1
7280
7286.6
7293.0
7299.1
7205
Upper Eagle Ford
Lower Eagle Ford
Mudrock
Wackestone
MDP
GDP
Grainstone

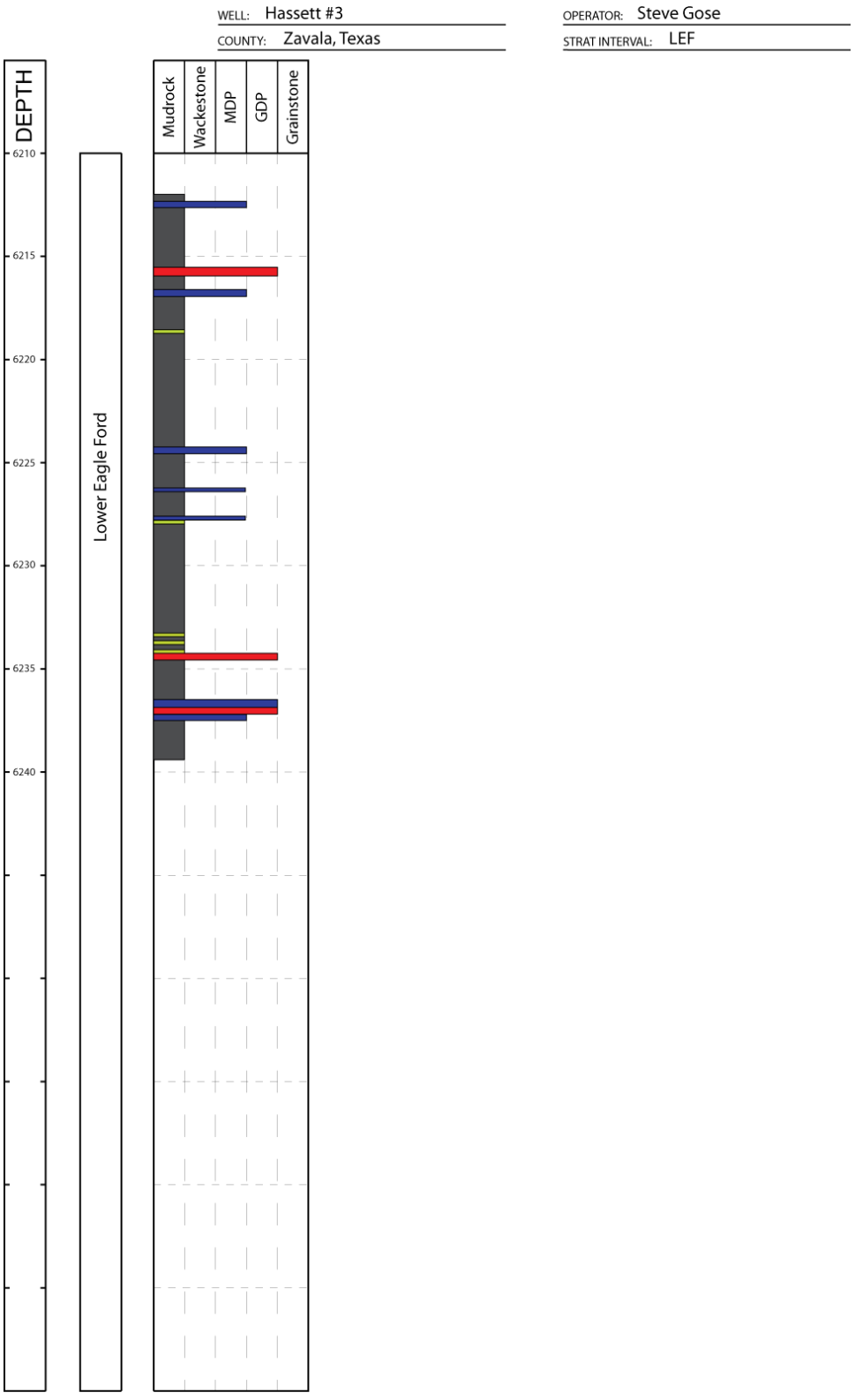
WELL: Hassett #3
COUNTY: Zavala, Texas
OPERATOR: Steve Gose
STRAT INTERVAL: LEF
DEPTH
6210
6215
6220
6225
6230
6235
6240
Lower Eagle Ford
Mudrock
Wackestone
MDP
GDP
Grainstone

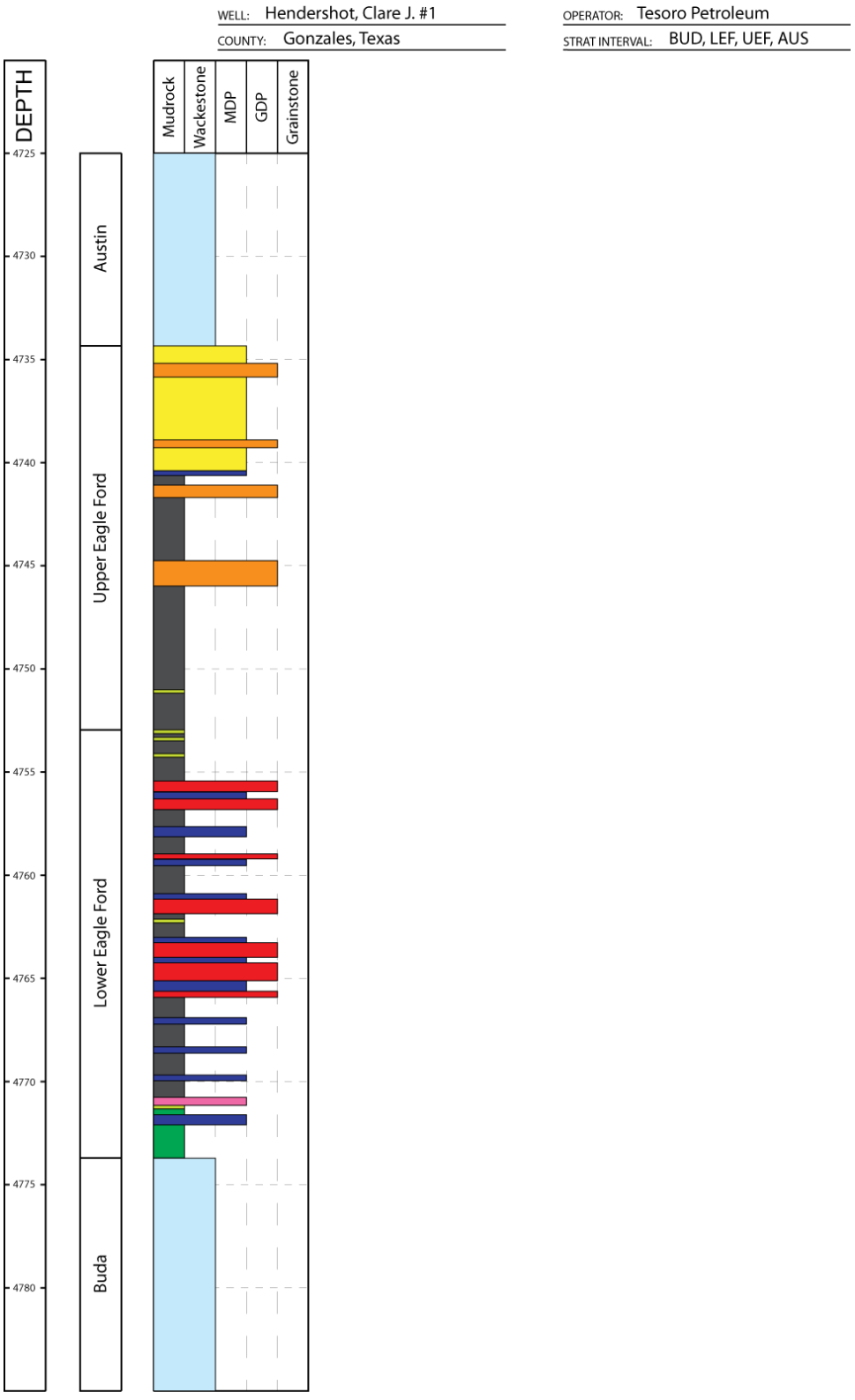
WELL: Hendershot, Clare J. #1
COUNTY: Gonzales, Texas
OPERATOR: Tesoro Petroleum
STRAT INTERVAL: BUD, LEF, UEF, AUS
DEPTH
4725
4730
4735
4740
4745
4750
4755
4760
4765
4770
4775
4780
Austin
Upper Eagle Ford
Lower Eagle Ford
Buda
Mudrock
Wackestone
MDP
GDP
Grainstone

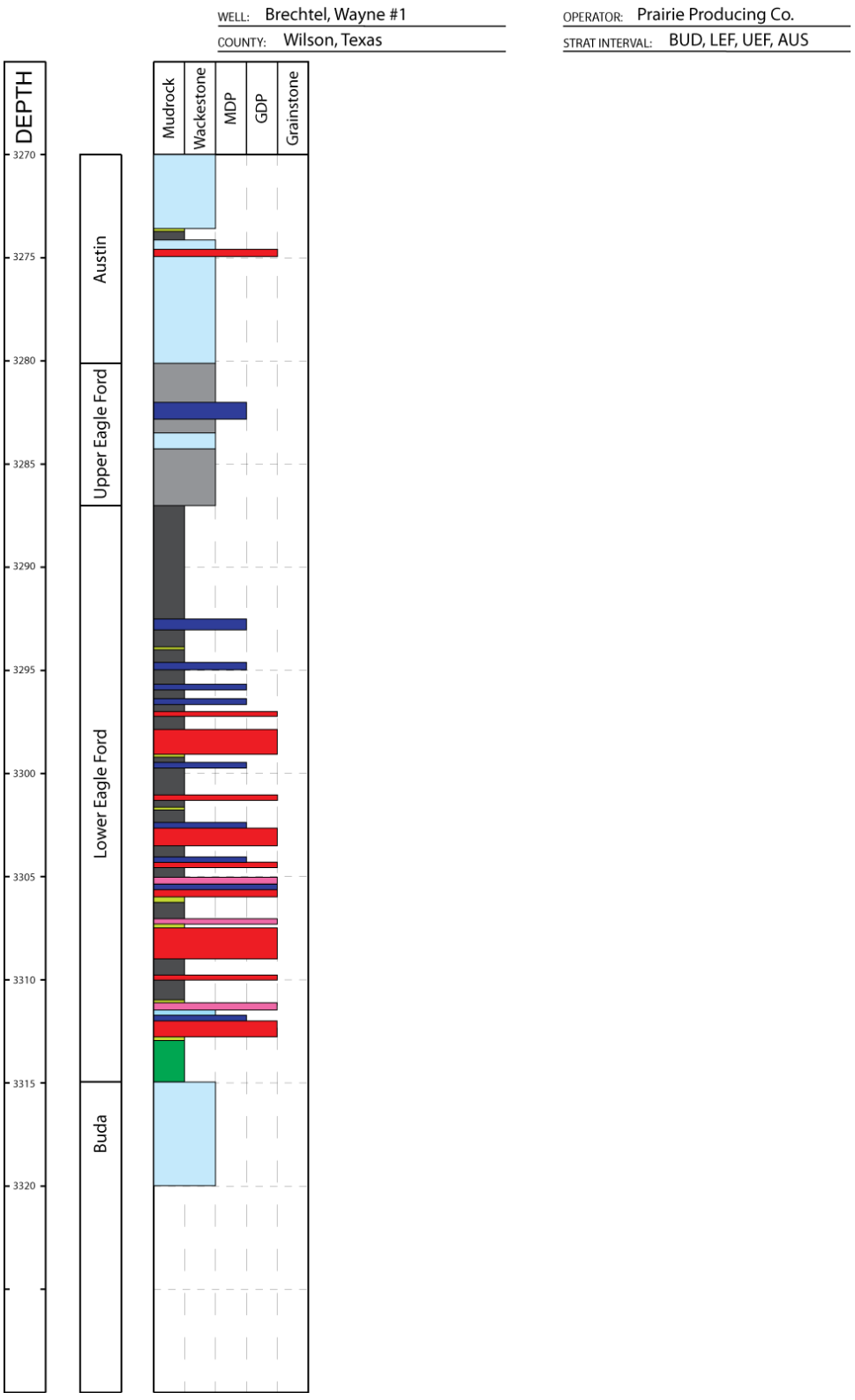
WELL: Brechtel, Wayne #1
COUNTY: Wilson, Texas
OPERATOR: Prairie Producing Co.
STRAT INTERVAL: BUD, LEF, UEF, AUS
DEPTH
3270
3275
3280
3285
3290
3295
3300
3305
3310
3315
3320
Austin
Upper Eagle Ford
Lower Eagle Ford
Buda
Mudrock
Wackestone
MDP
GDP
Grainstone

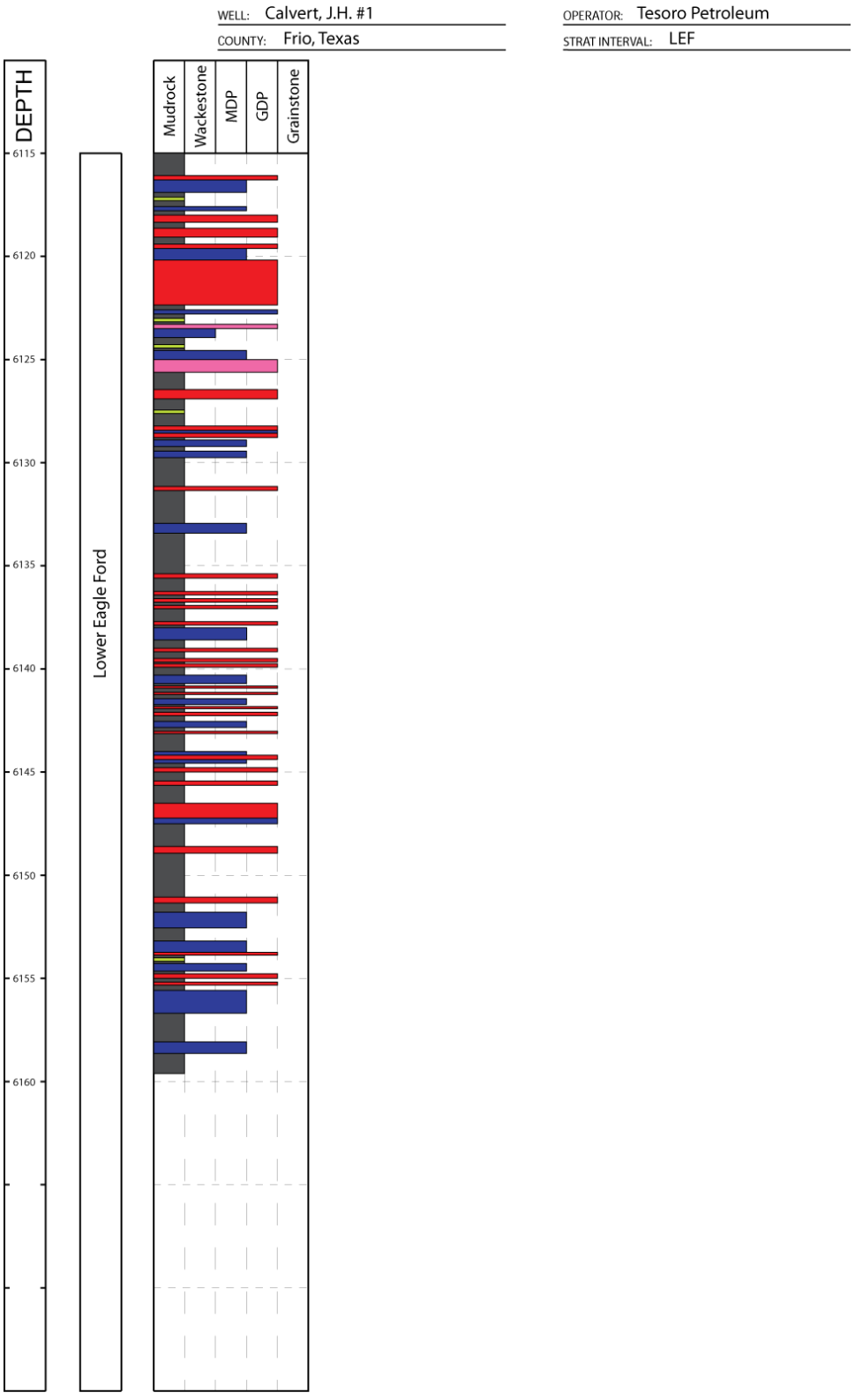
WELL: Calvert, J.H. #1
COUNTY: Frio, Texas
OPERATOR: Tesoro Petroleum
STRAT INTERVAL: LEF
DEPTH
6115
6120
6125
6130
6135
6140
6145
6150
6155
6160
Lower Eagle Ford
Mudrock
Wackestone
MDP
GDP
Grainstone

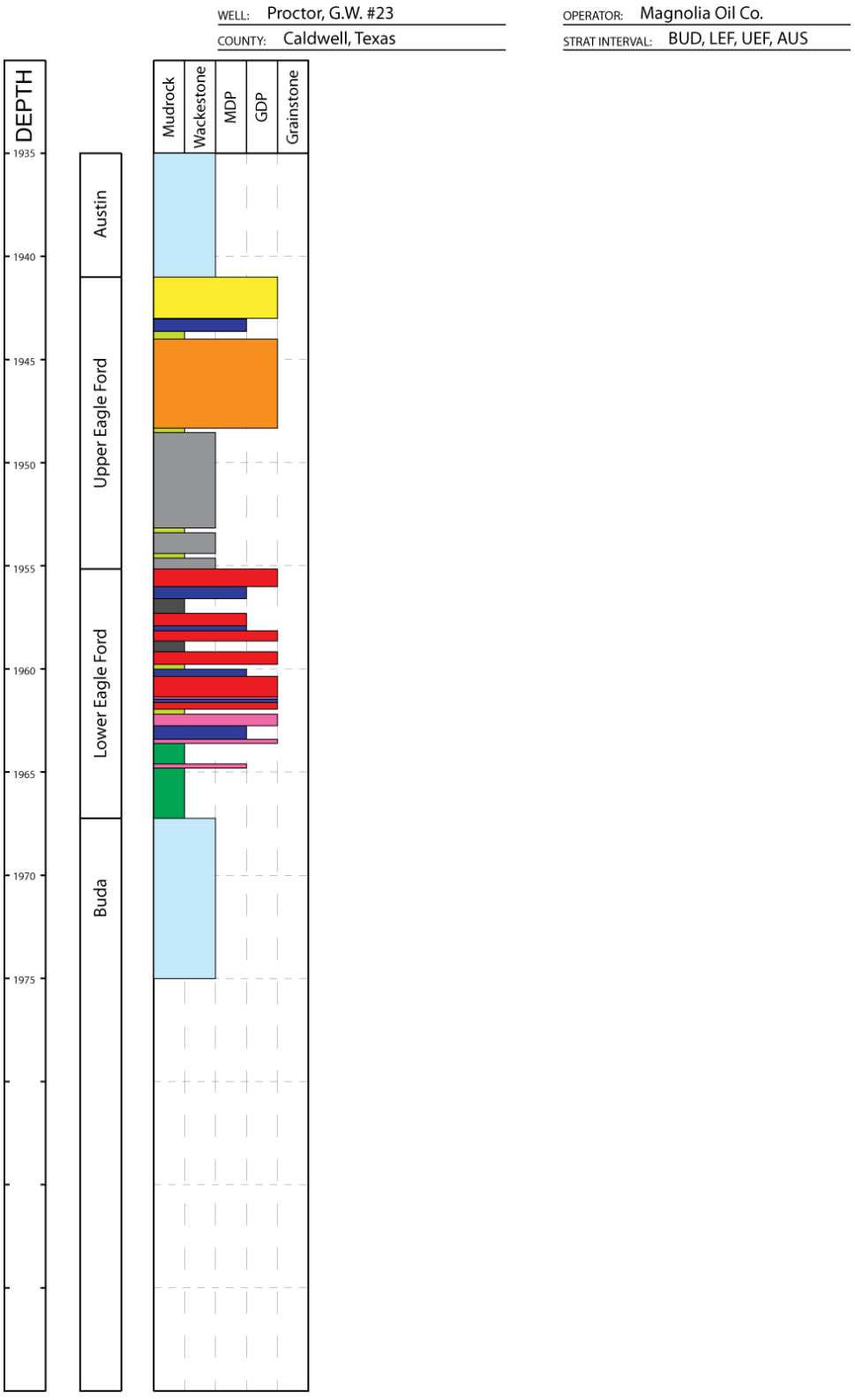
WELL: Proctor, G.W. #23
COUNTY: Caldwell, Texas
OPERATOR: Magnolia Oil Co.
STRAT INTERVAL: BUD, LEF, UEF, AUS
DEPTH
1935
1940
1945
1950
1955
1960
1965
1970
1975
Austin
Upper Eagle Ford
Lower Eagle Ford
Buda
Mudrock
Wackestone
MDP
GDP
Grainstone

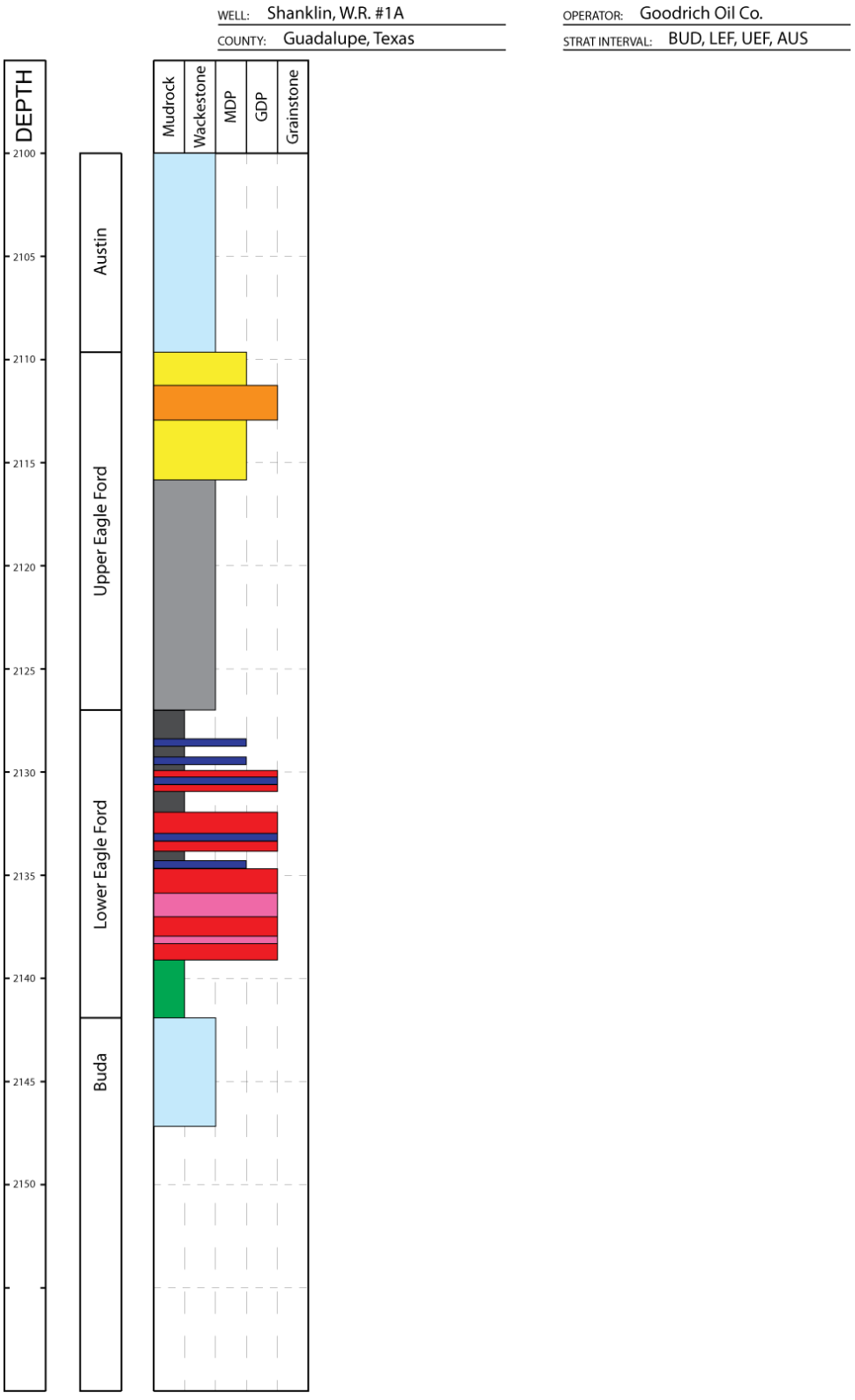
WELL: Shanklin, W.R. #1A
COUNTY: Guadalupe, Texas
OPERATOR: Goodrich Oil Co.
STRAT INTERVAL: BUD, LEF, UEF, AUS
DEPTH
2100
2105
2110
2115
2120
2125
2130
2135
2140
2145
2150
Austin
Upper Eagle Ford
Lower Eagle Ford
Buda
Mudrock
Wackestone
MDP
GDP
Grainstone

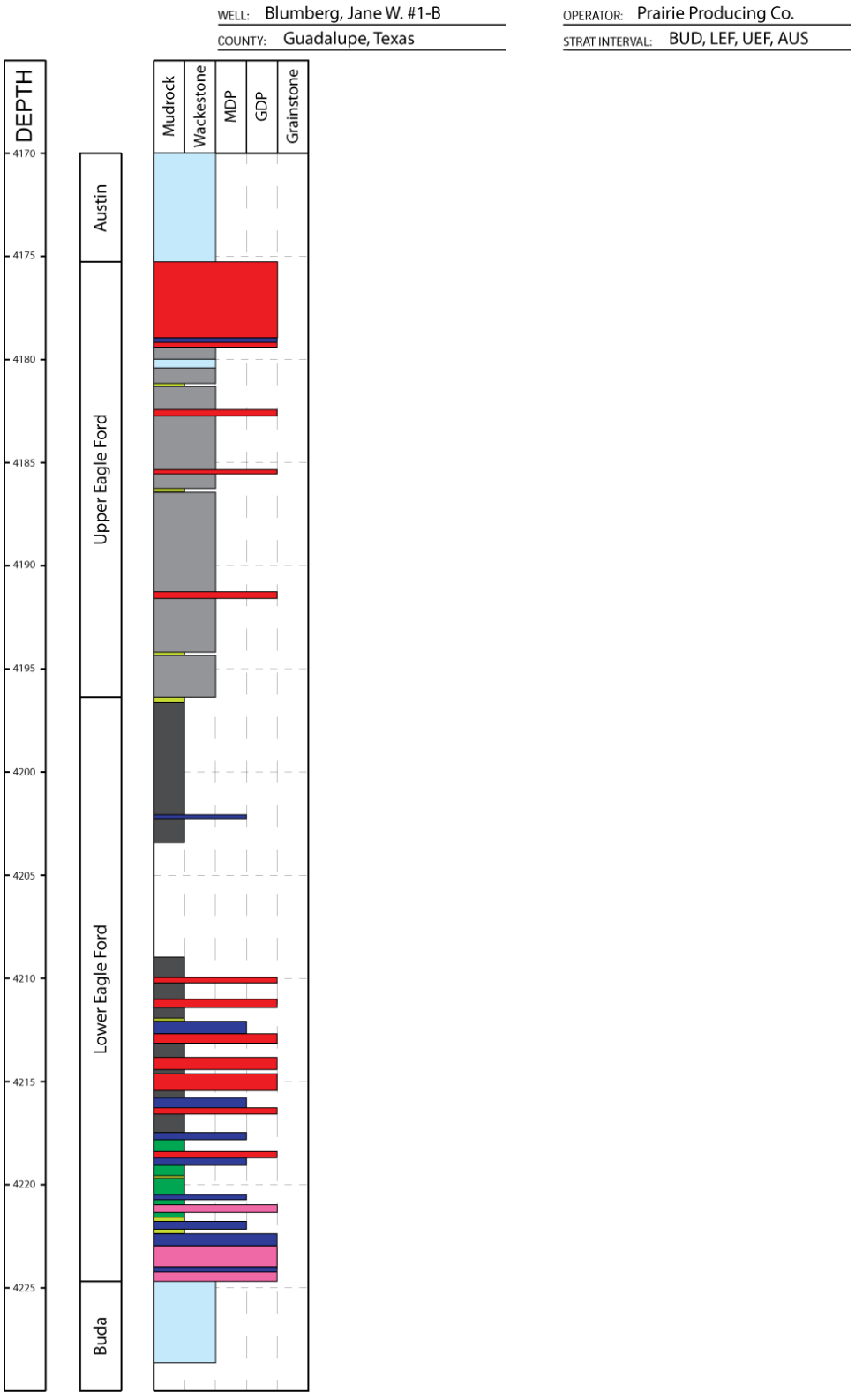
WELL: Blumberg, Jane W. #1-B
COUNTY: Guadalupe, Texas
OPERATOR: Prairie Producing Co.
STRAT INTERVAL: BUD, LEF, UEF, AUS
DEPTH
4170
4175
4180
4185
4190
4195
4200
4205
4210
4215
4220
4225
Austin
Upper Eagle Ford
Lower Eagle Ford
Buda
Mudrock
Wackestone
MDP
GDP
Grainstone

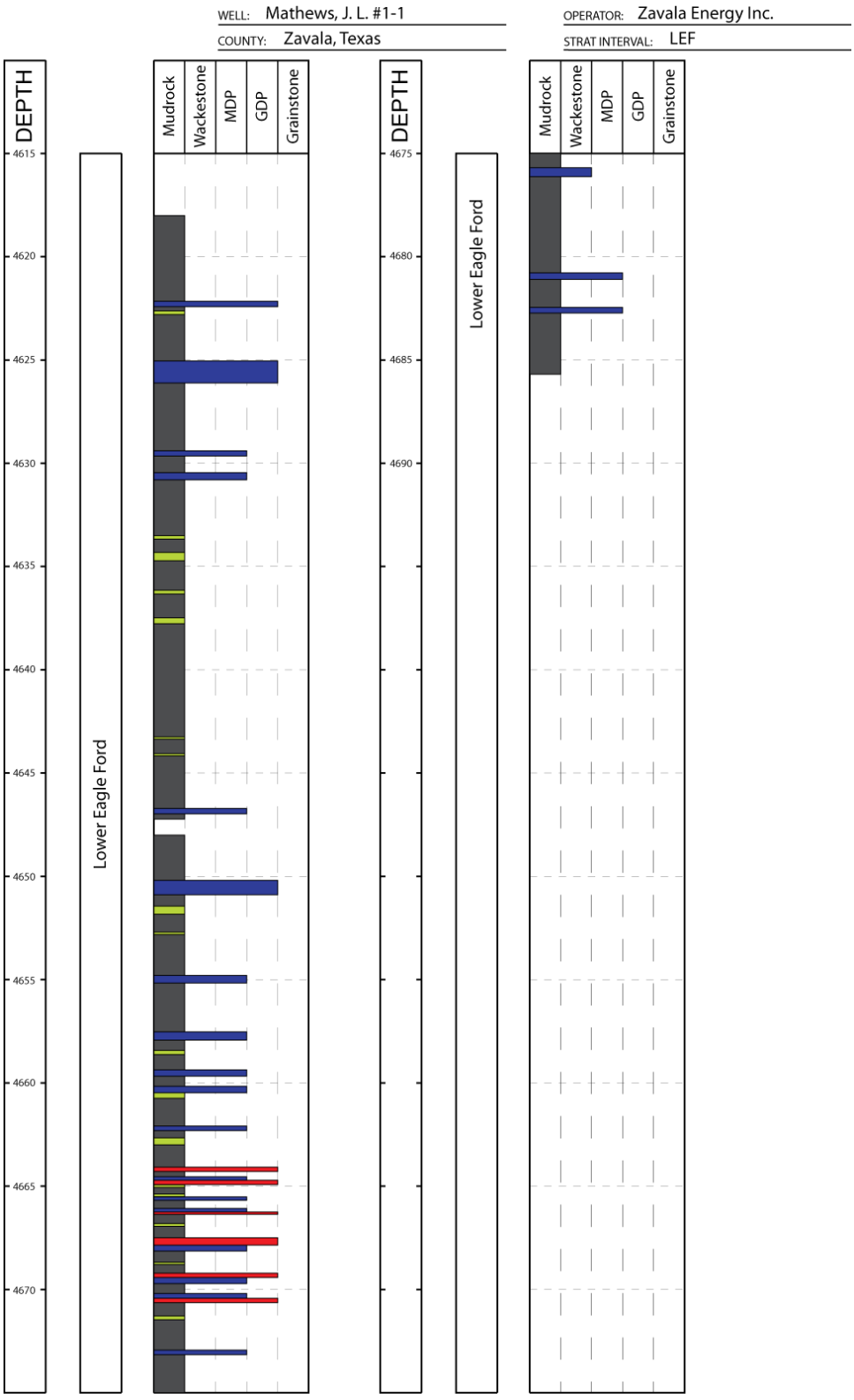
WELL: Mathews, J. L. #1-1
COUNTY: Zavala, Texas
OPERATOR: Zavala Energy Inc.
STRAT INTERVAL: LEF
DEPTH
4615
4620
4625
4630
4635
4640
4645
4650
4655
4660
4665
4670
Lower Eagle Ford
Mudrock
Wackestone
MDP
GDP
Grainstone
DEPTH
4675
4680
4685
4690
Lower Eagle Ford
Mudrock
Wackestone
MDP
GDP
Grainstone

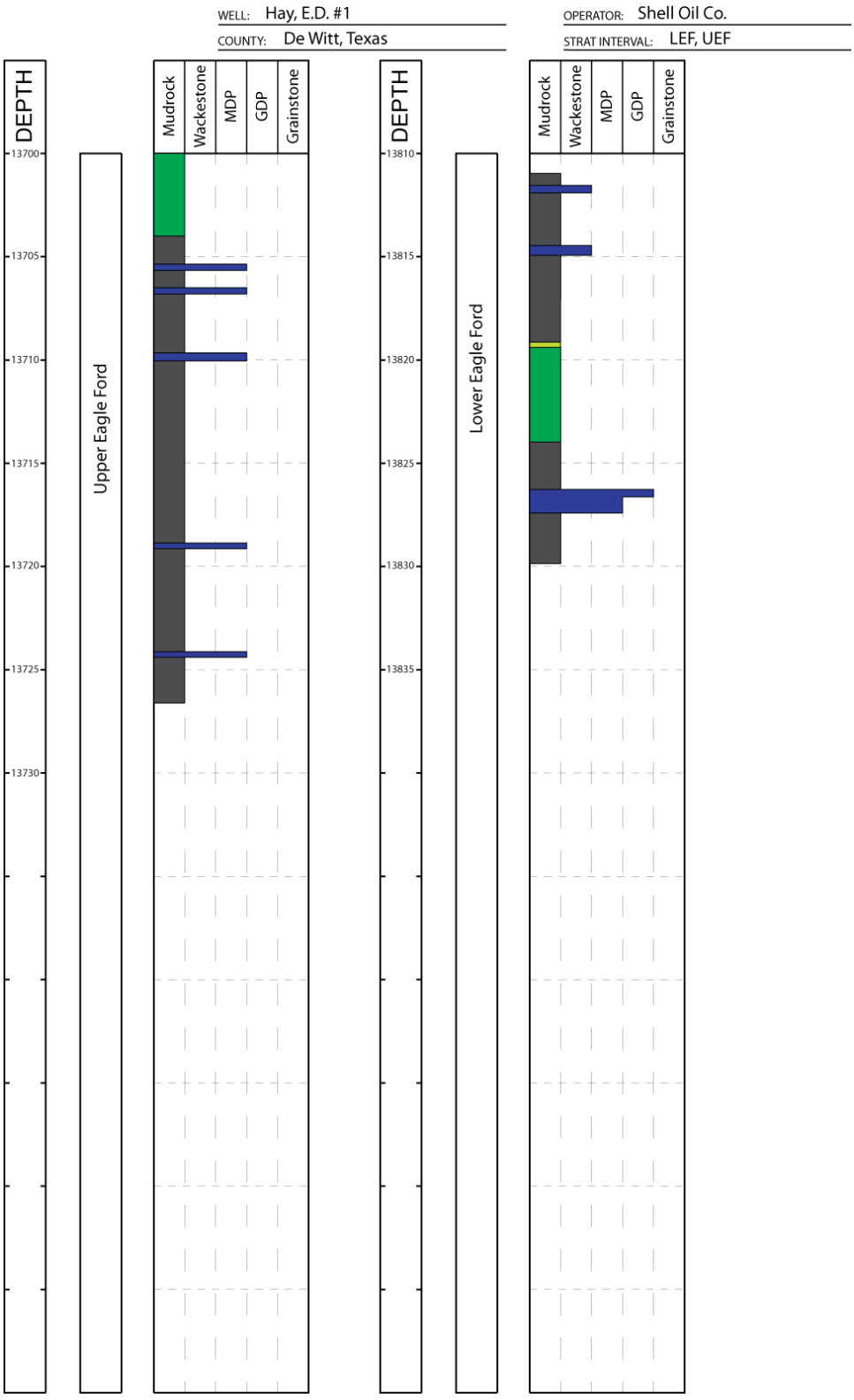
WELL: Hay, E.D. #1
COUNTY: De Witt, Texas
OPERATOR: Shell Oil Co.
STRAT INTERVAL: LEF, UEF
DEPTH
13700
13705
13710
13715
13720
13725
13730
Upper Eagle Ford
Mudrock
Wackestone
MDP
GDP
Grainstone
DEPTH
13810
13815
13820
13825
13830
13835
Lower Eagle Ford
Mudrock
Wackestone
MDP
GDP
Grainstone

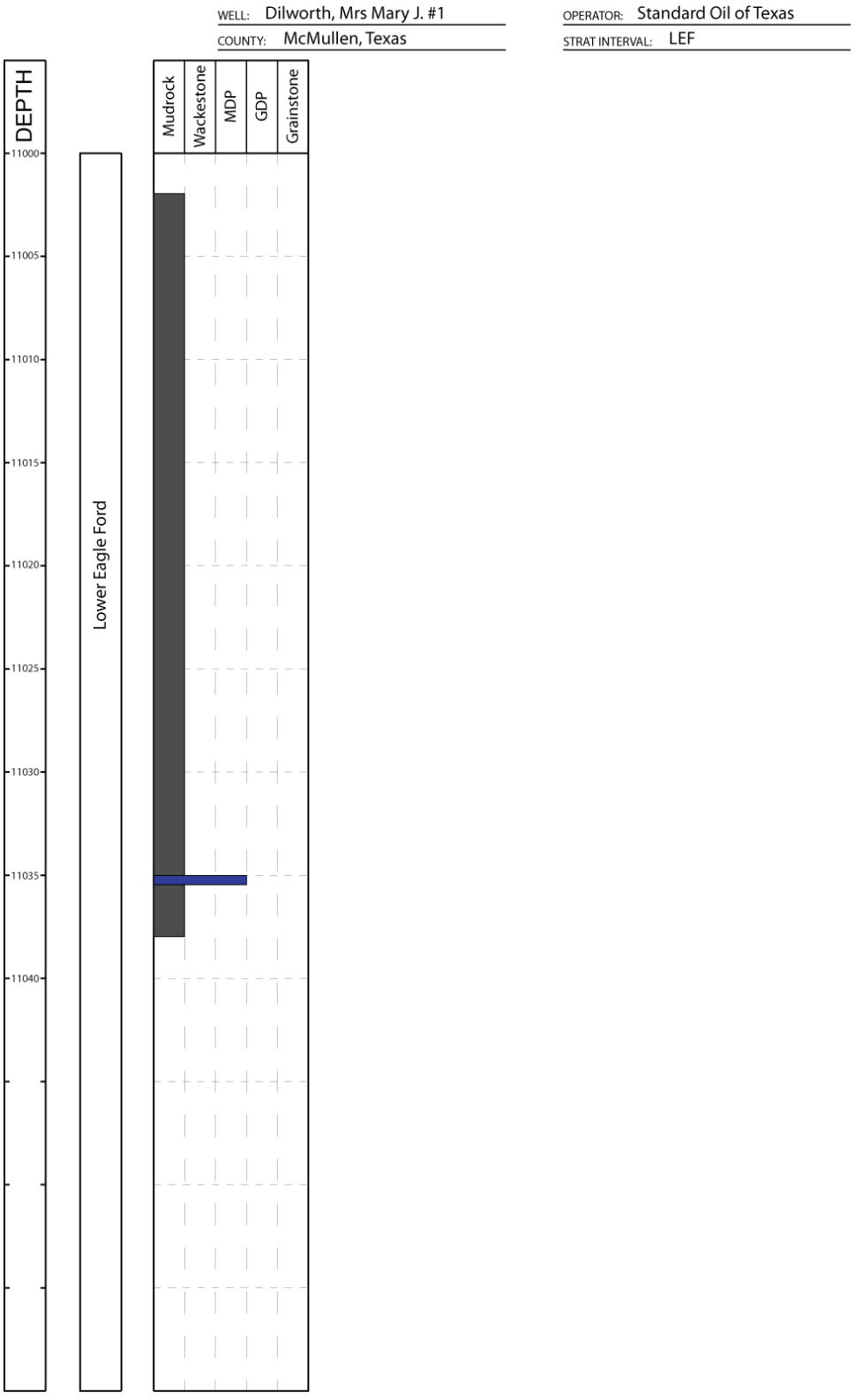
WELL: Dilworth, Mrs Mary J. #1
COUNTY: McMullen, Texas
OPERATOR: Standard Oil of Texas
STRAT INTERVAL: LEF
DEPTH
11000
11005
11010
11015
11020
11025
11030
11035
11040
Lower Eagle Ford
Mudrock
Wackestone
MDP
GDP
Grainstone

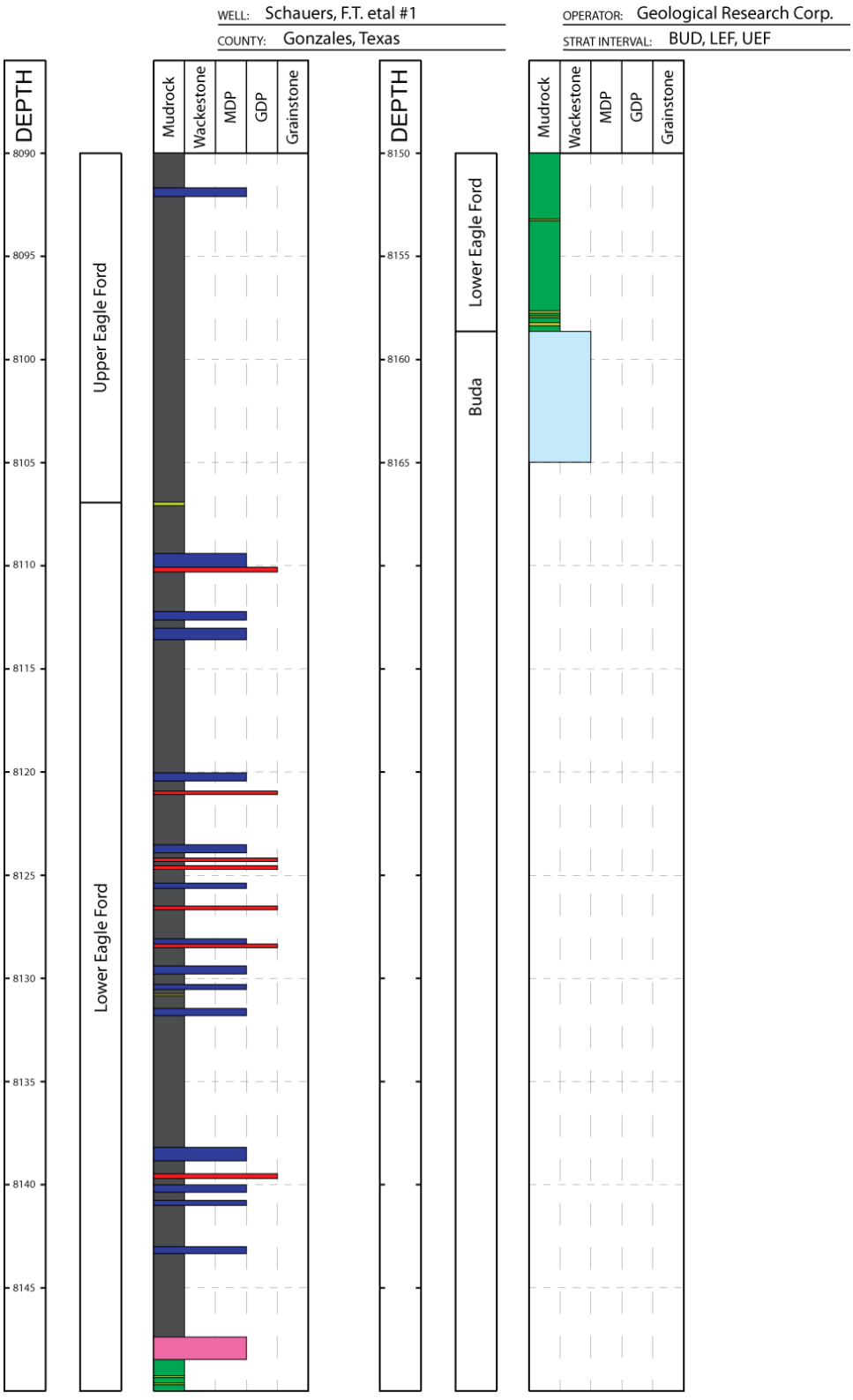
WELL: Schauers, F.T. etal #1
COUNTY: Gonzales, Texas
OPERATOR: Geological Research Corp.
STRAT INTERVAL: BUD, LEF, UEF
DEPTH
8090
8095
8100
8105
8110
8115
8120
8125
8130
8135
8140
8145
Upper Eagle Ford
Lower Eagle Ford
Mudrock
Wackestone
MDP
GDP
Grainstone
DEPTH
8150
8155
8160
8165
Lower Eagle Ford
Buda
Mudrock
Wackestone
MDP
GDP
Grainstone

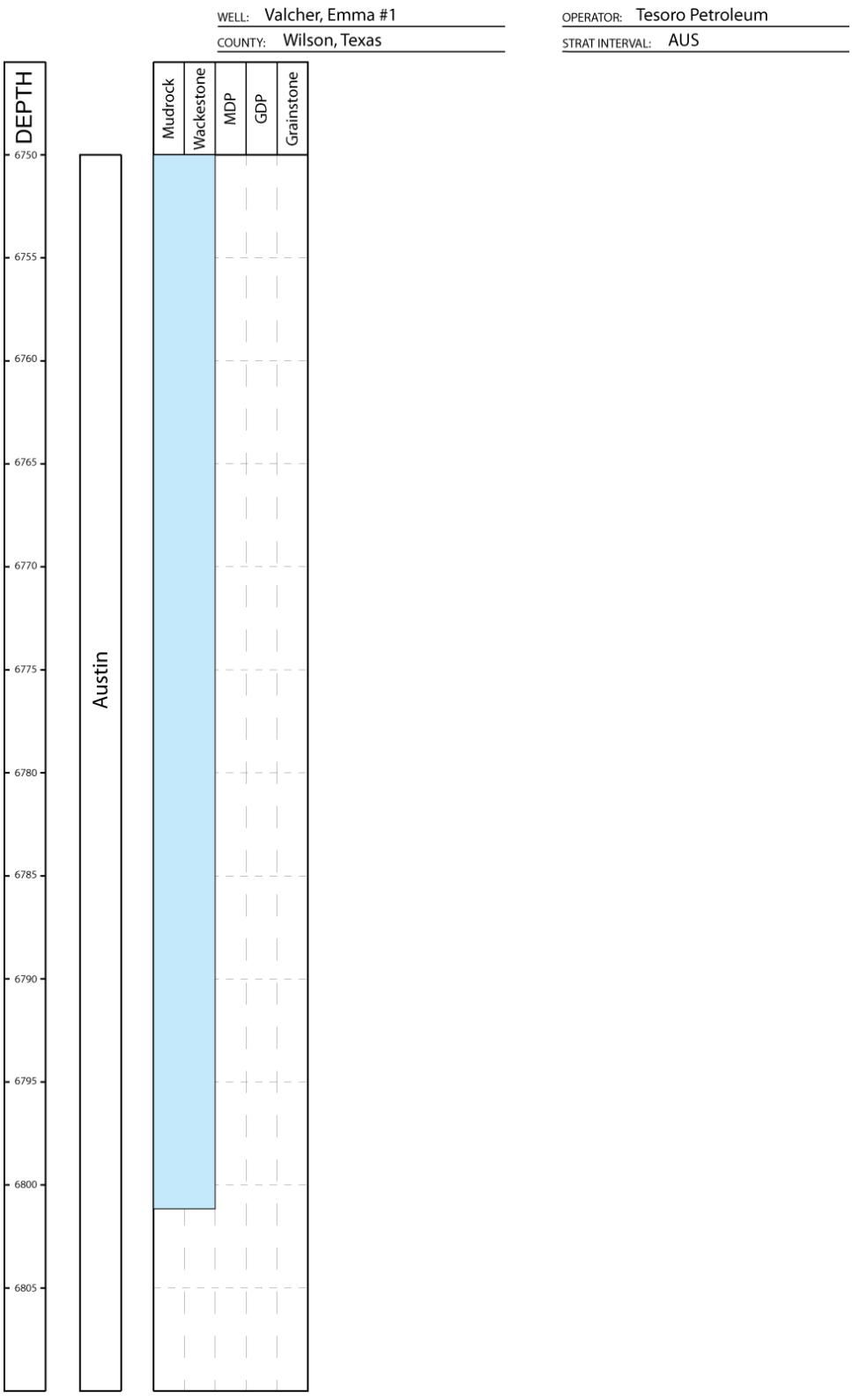
WELL: Valcher, Emma #1
COUNTY: Wilson, Texas
OPERATOR: Tesoro Petroleum
STRAT INTERVAL: AUS
DEPTH
6750
6755
6760
6765
6770
6775
6780
6785
6790
6795
6800
6805
Austin
Mudrock
Wackestone
MDP
GDP
Grainstone

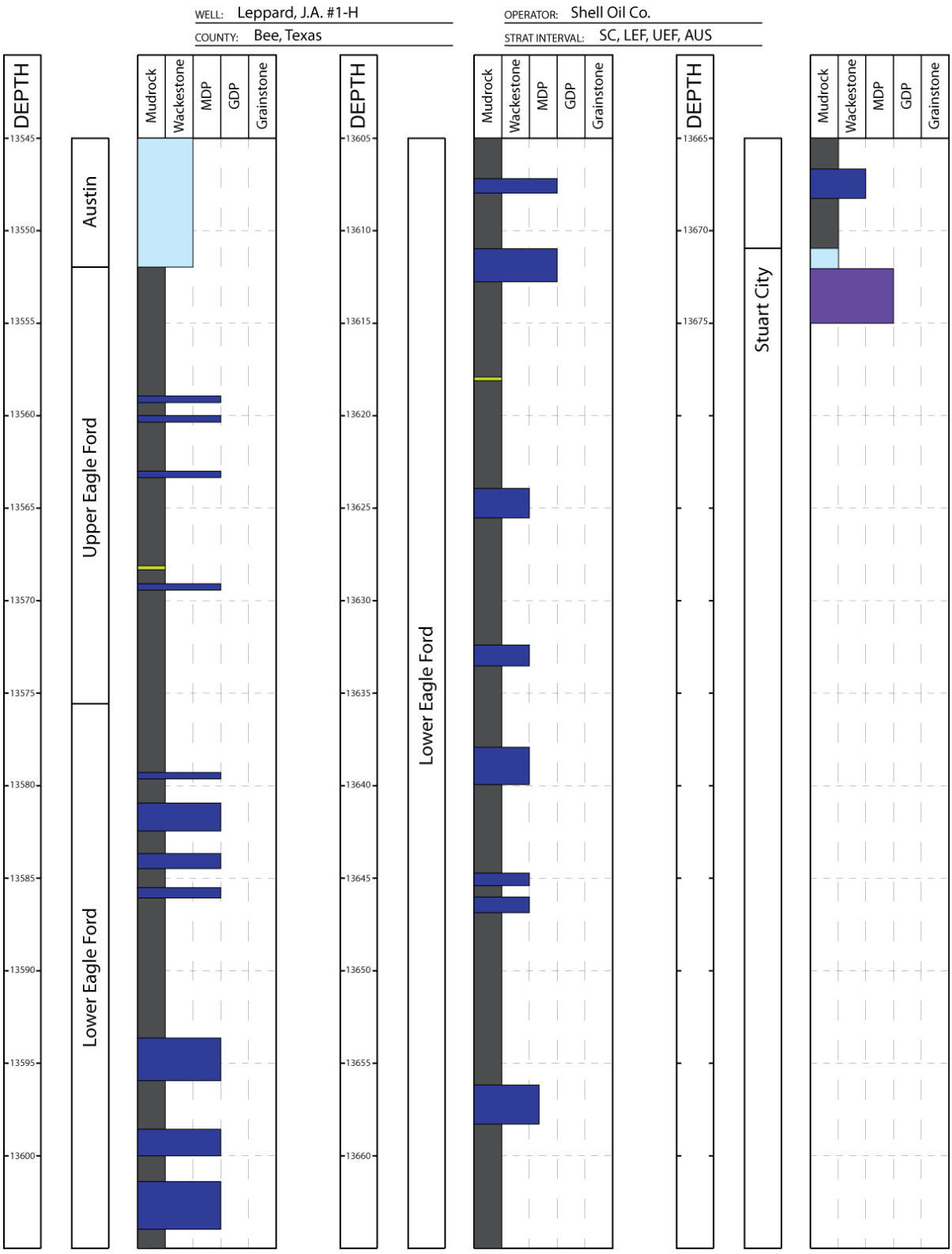
WELL: Leppard, J.A. #1-H
COUNTY: Bee, Texas
OPERATOR: Shell Oil Co.
STRAT INTERVAL: SC, LEF, UEF, AUS
DEPTH
13545
13550
13555
13560
13565
13570
13575
13580
13585
13590
13595
13600
Austin
Upper Eagle Ford
Lower Eagle Ford
Mudrock
Wackestone
MDP
GDP
Grainstone
DEPTH
13605
13610
13615
13620
13625
13630
13635
13640
13645
13650
13655
13660
Lower Eagle Ford
Mudrock
Wackestone
MDP
GDP
Grainstone
DEPTH
13665
13670
13675
Stuart City
Mudrock
Wackestone
MDP
GDP
Grainstone

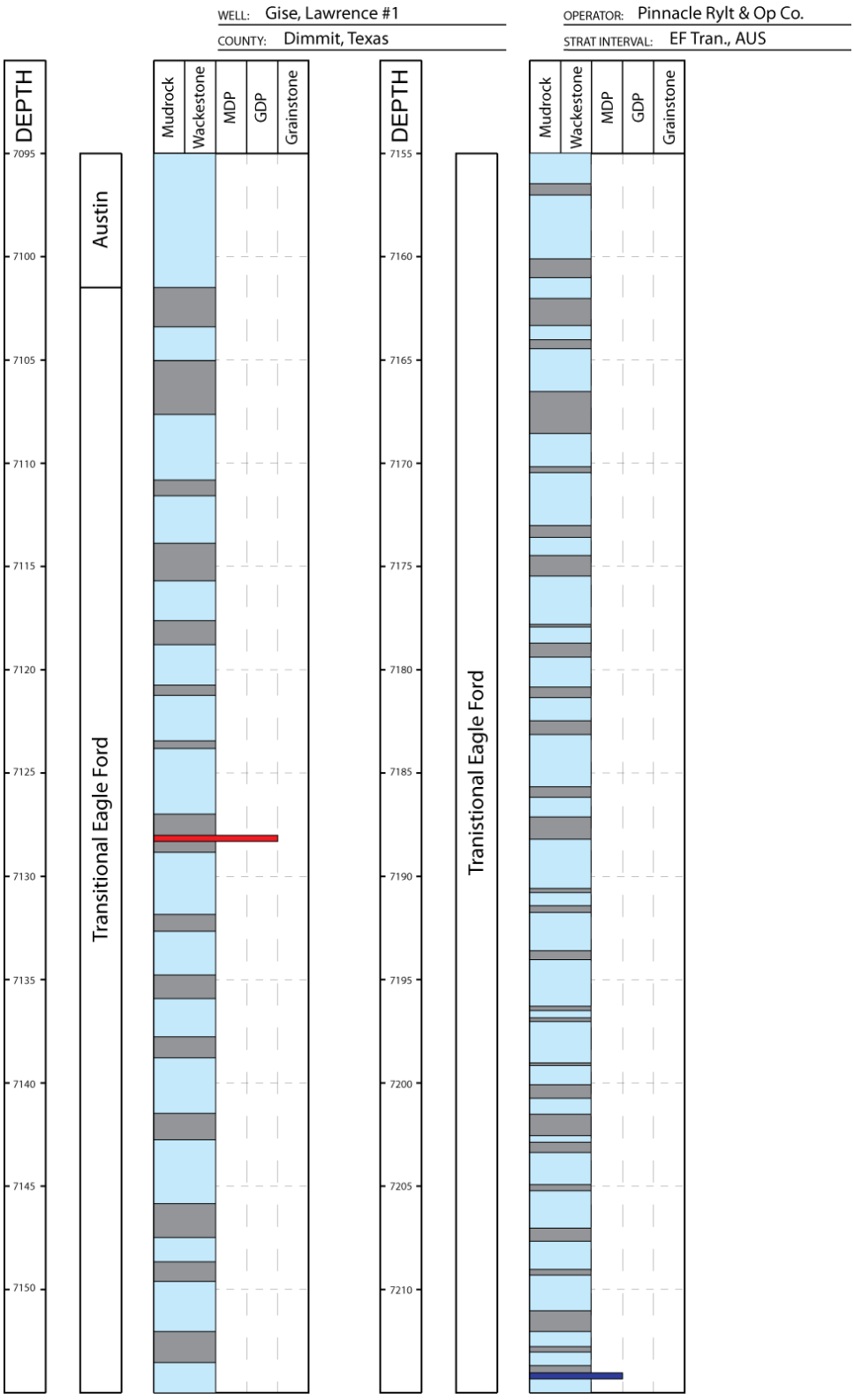
WELL: Gise, Lawrence #1
COUNTY: Dimmit, Texas
OPERATOR: Pinnacle Rylt & Op Co.
STRAT INTERVAL: EF Tran., AUS
DEPTH
7095
7100
7105
7110
7115
7120
7125
7130
7135
7140
7145
7150
Austin
Transitional Eagle Ford
Mudrock
Wackestone
MDP
GDP
Grainstone
DEPTH
7155
7160
7165
7170
7175
7180
7185
7190
7195
7200
7205
7210
Tranistional Eagle Ford
Mudrock
Wackestone
MDP
GDP
Grainstone

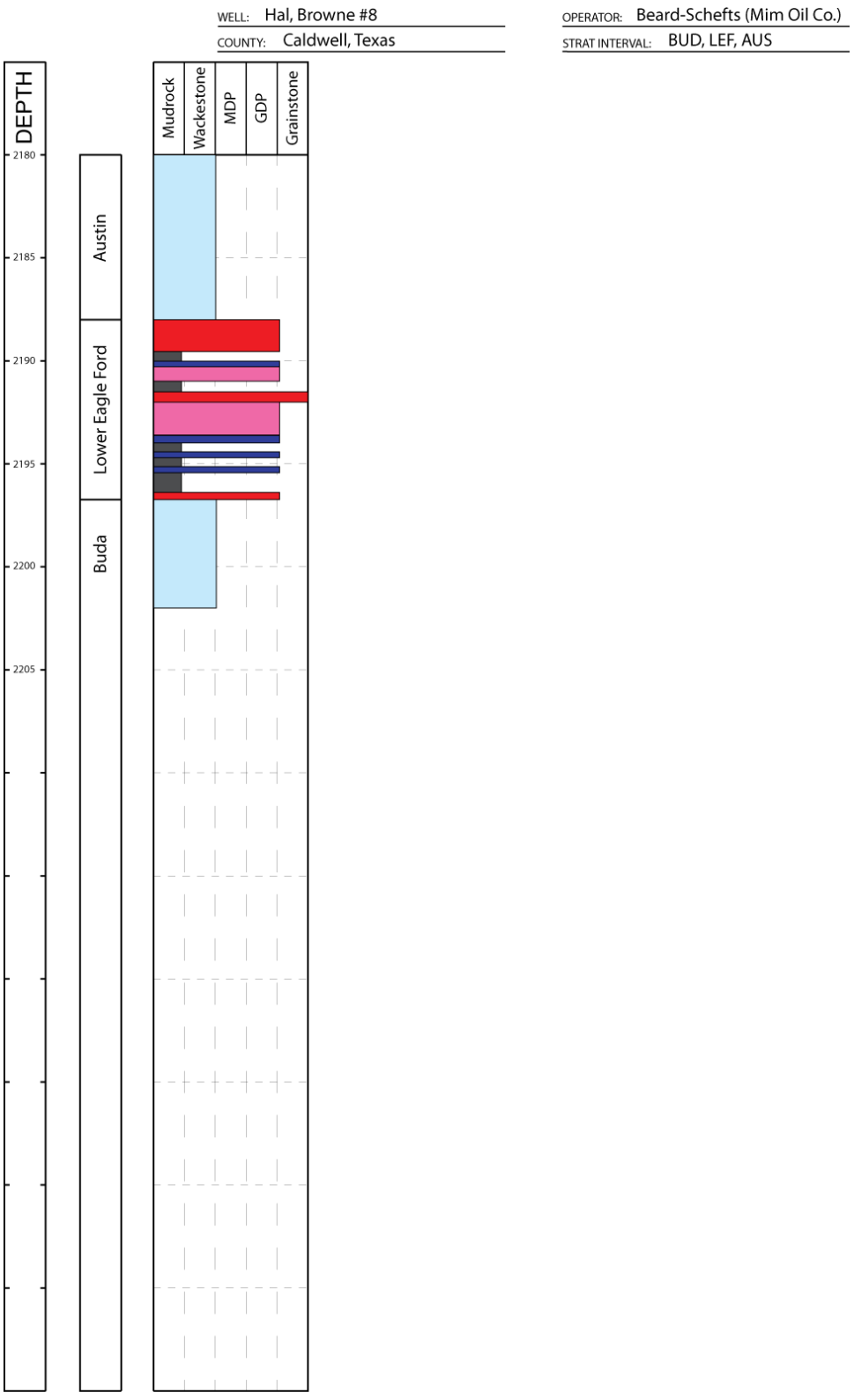
WELL: Hal, Browne #8
COUNTY: Caldwell, Texas
OPERATOR: Beard-Schefts (Mim Oil Co.)
STRAT INTERVAL: BUD, LEF, AUS
DEPTH
2180
2185
2190
2195
2200
2205
Austin
Lower Eagle Ford
Buda
Mudrock
Wackestone
MDP
GDP
Grainstone

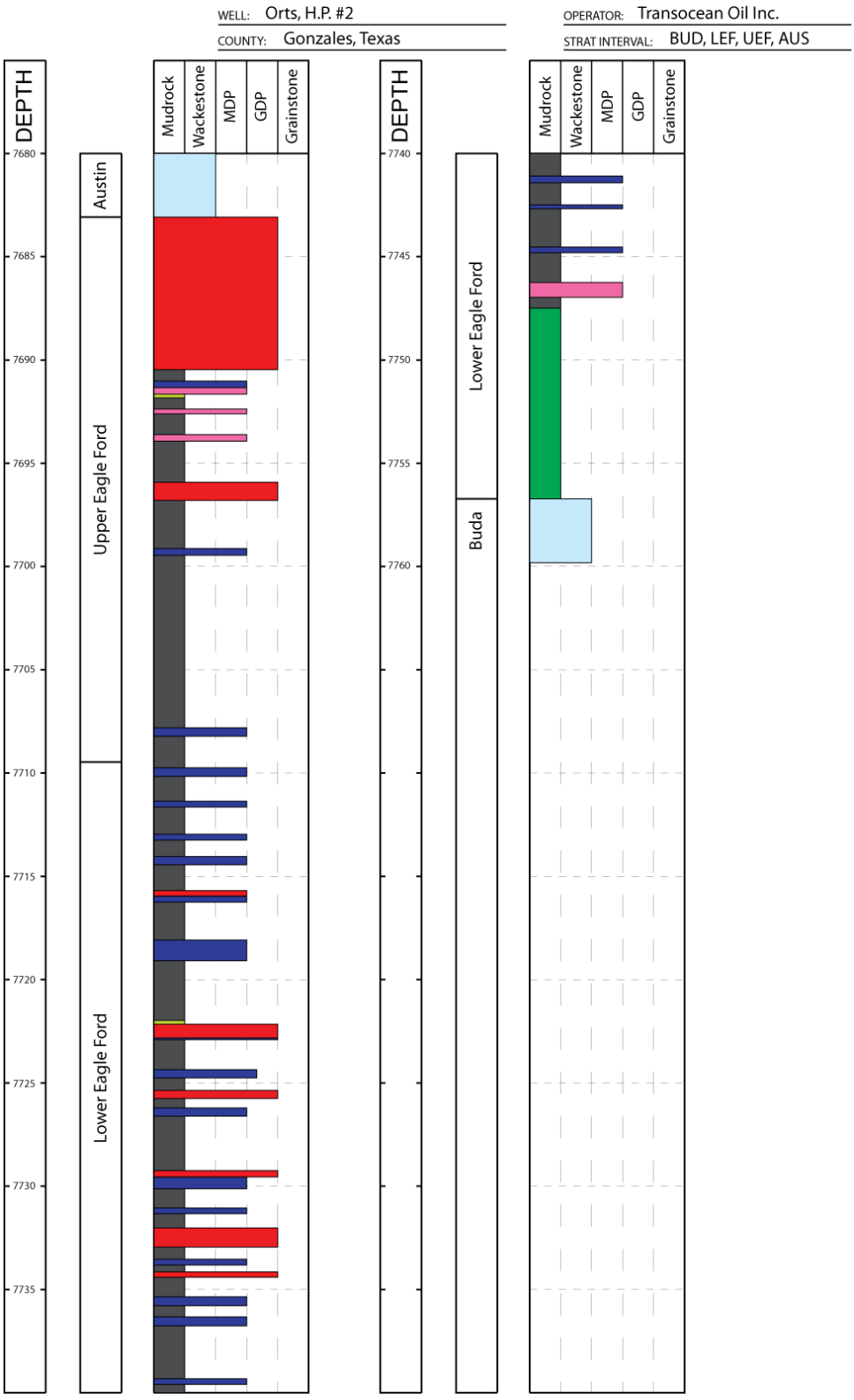
WELL: Orts, H.P. #2
COUNTY: Gonzales, Texas
OPERATOR: Transocean Oil Inc.
STRAT INTERVAL: BUD, LEF, UEF, AUS
DEPTH
7680
7685
7690
7695
7700
7705
7710
7715
7720
7725
7730
7735
Austin
Upper Eagle Ford
Lower Eagle Ford
Mudrock
Wackestone
MDP
GDP
Grainstone
DEPTH
7740
7745
7750
7755
7760
Lower Eagle Ford
Buda
Mudrock
Wackestone
MDP
GDP
Grainstone

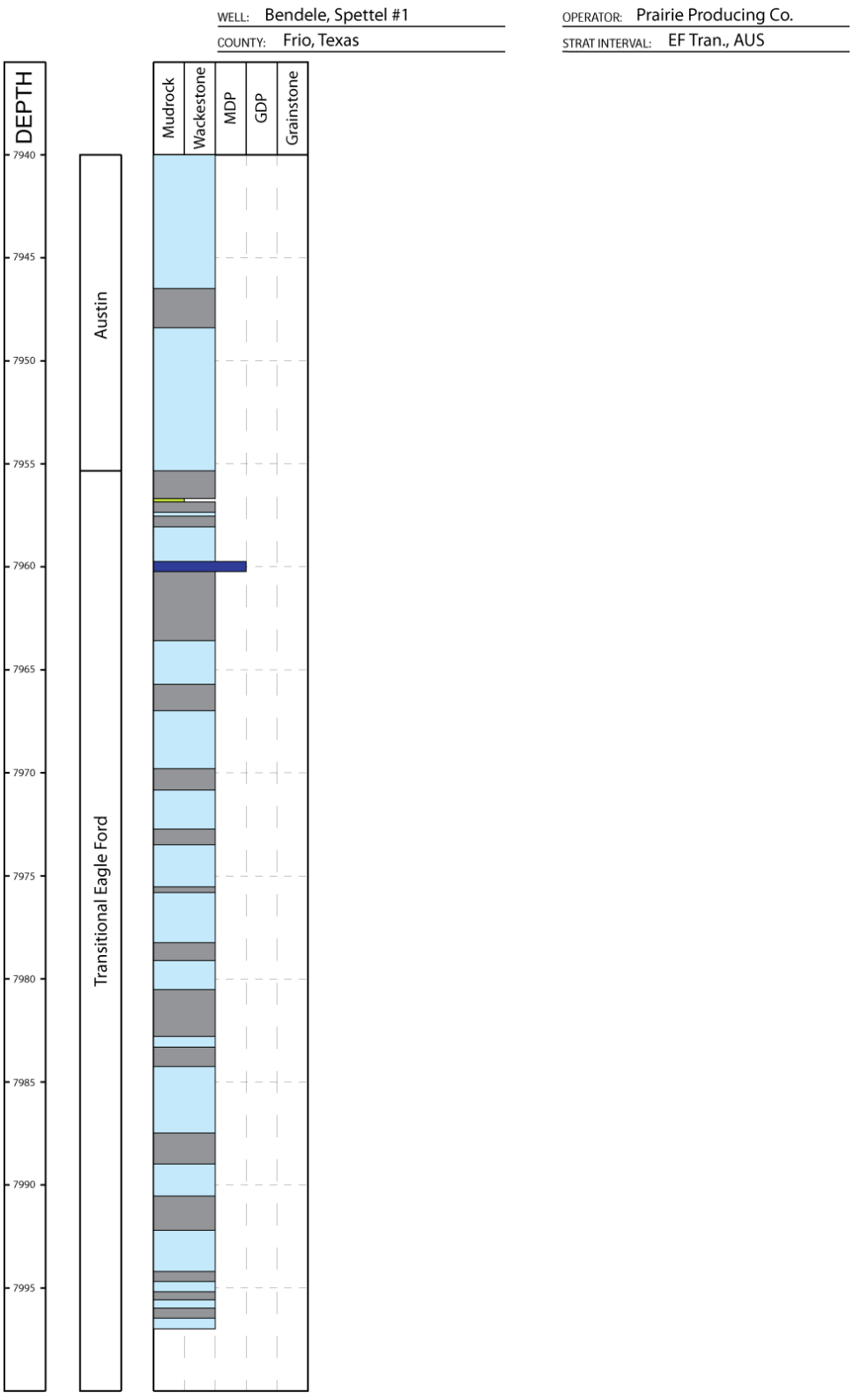
WELL: Bendele, Spettel #1
COUNTY: Frio, Texas
OPERATOR: Prairie Producing Co.
STRAT INTERVAL: EF Tran., AUS
DEPTH
7940
7945
7950
7955
7960
7965
7970
7975
7980
7985
7990
7995
Austin
Transitional Eagle Ford
Mudrock
Wackestone
MDP
GDP
Grainstone

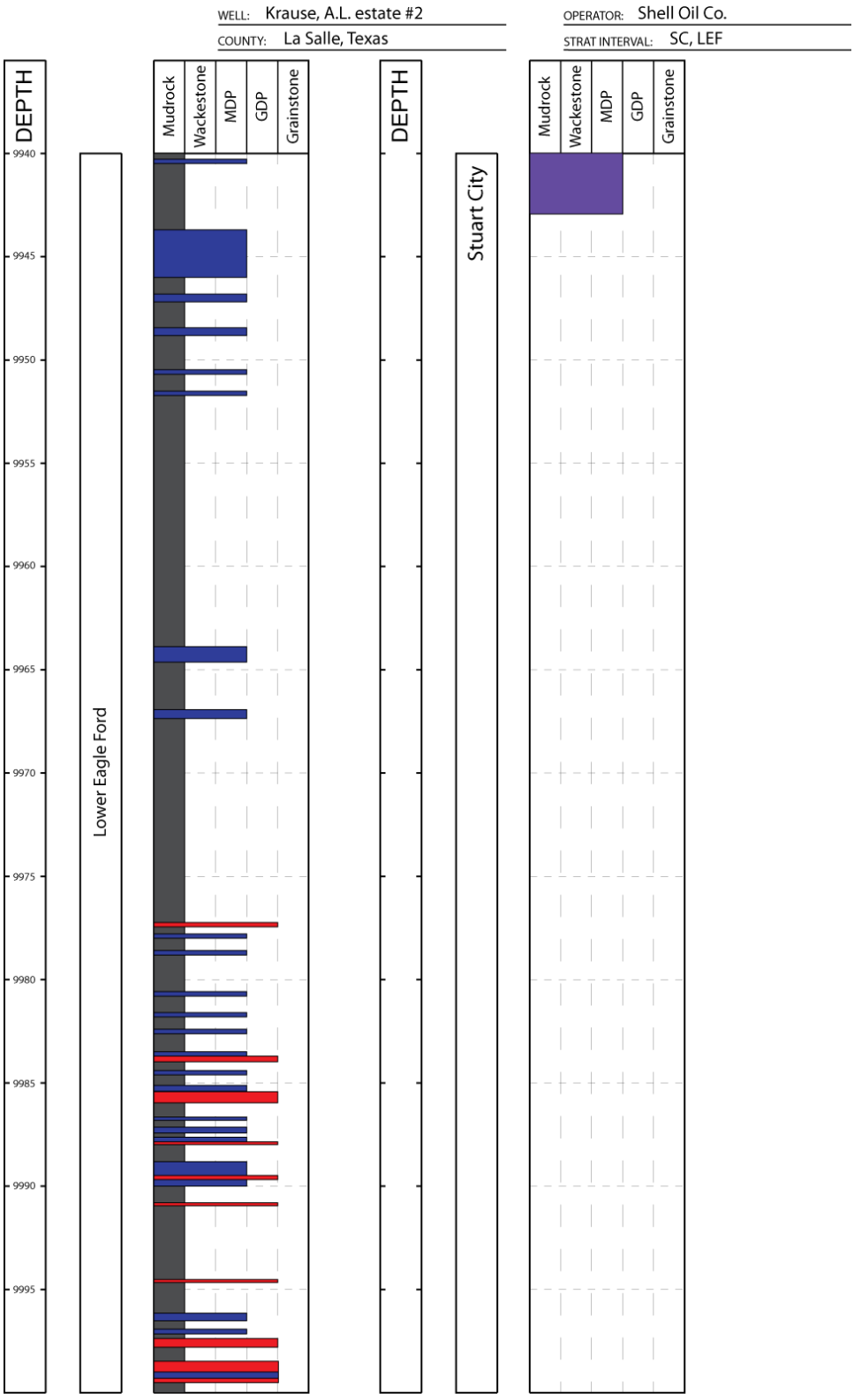
WELL: Krause, A.L. estate #2
COUNTY: La Salle, Texas
OPERATOR: Shell Oil Co.
STRAT INTERVAL: SC, LEF
DEPTH
9940
9945
9950
9955
9960
9965
9970
9975
9980
9985
9990
9995
Lower Eagle Ford
Mudrock
Wackestone
MDP
GDP
Grainstone
DEPTH
Stuart City
Mudrock
Wackestone
MDP
GDP
Grainstone

Appendix B: TOC, Rock EVAL, and Thermal Maturity Data

Total Organic Carbon & Rock Eval Abbreviations:

Percent Carbonate (wt %)

Leco TOC (wt % HC)

Rock-Eval S1 (mg HC/g)

Rock-Eval S2 (mg HC/g)

Rock Eval S3 (mg CO2/g)

Tmax (°C)

Calculated %RO (RE-Tmax)

Hydrogen Index (S2 x 100/TOC)

Oxygen Index (S3 x100/TOC)

S2/S3 Conc. (mg HC/mg CO2)

S1/TOC Norm. Oil Content

Production Index (S1/(S1+S2))

Roessler, A.E. #1-R												
Depth (ft)	% Carbonate	Leco TOC	Rock-Eval S1	Rock-Eval S2	Rock-Eval S3	TMAX	Calculated %RO	Hydrogen Index	Oxygen Index	S2/S3	S1/TOC	Production Index
13502.0	65.23	4.22	0.16	0.60	0.11	547	2.69	14	3	5	4	0.21
13511.0	63.90	4.12	0.51	0.58	0.18	543	2.61	14	4	3	12	0.47
13519.7	64.36	4.04	0.08	0.44	0.10	545	2.65	11	2	4	2	0.15

Hassett #3												
Depth (ft)	% Carbonate	Leco TOC	Rock-Eval S1	Rock-Eval S2	Rock-Eval S3	TMAX	Calculated %RO	Hydrogen Index	Oxygen Index	S2/S3	S1/TOC	Production Index
6212.8	59.00	4.60	5.84	17.84	0.16	444	0.83	388	3	112	127	0.25
6214.0	52.65	6.45	8.51	23.31	0.20	442	0.80	361	3	117	132	0.27
6220.4	57.77	5.41	9.63	20.70	0.17	442	0.80	383	3	122	178	0.32
6225.4	60.91	6.00	10.45	23.52	0.22	442	0.80	392	4	107	174	0.31
6230.2	72.03	5.53	7.25	25.07	0.23	444	0.83	453	4	109	131	0.22
6239.0	64.93	4.12	7.00	15.53	0.22	442	0.80	377	5	71	170	0.31

Hendershot, Clare J. #1												
Depth (ft)	% Carbonate	Leco TOC	Rock-Eval S1	Rock-Eval S2	Rock-Eval S3	TMAX	Calculated %RO	Hydrogen Index	Oxygen Index	S2/S3	S1/TOC	Production Index
4741.0	44.36	2.82	0.59	20.75	0.69	427		736	24	30	21	0.03
4745.0	70.04	1.32	0.13	5.88	0.55	429	0.56	445	42	11	10	0.02
4758.0	26.05	8.53	1.81	63.22	1.00	428		741	12	63	21	0.03
4771.0	41.53	8.29	2.87	65.37	0.83	426		789	10	79	35	0.04
4773.7	9.14	1.83	0.46	4.44	0.38	420		243	21	12	25	0.09

Brechtel, Wayne #1												
Depth (ft)	% Carbonate	Leco TOC	Rock-Eval S1	Rock-Eval S2	Rock-Eval S3	TMAX	Calculated %RO	Hydrogen Index	Oxygen Index	S2/S3	S1/TOC	Production Index
3274.1	54.34	4.30	1.80	47.97	0.22	423	0.45	1,116	5	218	42	0.04
3289.7	67.71	4.10	1.39	48.51	0.25	421	0.42	1,183	6	194	34	0.03
3291.3	69.85	4.85	1.60	52.91	0.33	420	0.40	1,091	7	160	33	0.03
3309.3	77.81	3.81	2.58	45.19	0.24	424	0.47	1,186	6	188	68	0.05
3314.0	32.68	6.15	4.81	76.24	0.23	425	0.49	1,240	4	331	78	0.06

Calvert, J.H. #1												
Depth (ft)	% Carbonate	Leco TOC	Rock-Eval S1	Rock-Eval S2	Rock-Eval S3	TMAX	Calculated %RO	Hydrogen Index	Oxygen Index	S2/S3	S1/TOC	Production Index
6115.1	56.81	4.45	4.73	23.56	0.34	443	0.81	529	8	69	106	0.17
6117.4	27.79	4.62	3.90	24.93	0.32	443	0.81	540	7	78	84	0.14
6129.1	61.45	5.50	10.26	46.26	0.30	440	0.76	841	5	154	187	0.18
6135.6	42.94	7.61	9.06	58.32	0.22	441	0.78	766	3	265	119	0.13
6141.1	61.93	7.02	8.98	61.29	0.19	440	0.76	873	3	323	128	0.13
6145.7	46.68	9.60	9.13	76.65	0.20	443	0.81	798	2	383	95	0.11
6147.0	39.86	9.85	10.46	76.86	0.13	443	0.81	780	1	591	106	0.12
6155.0	57.44	6.71	8.81	54.13	0.12	443	0.81	807	2	451	131	0.14
6158.7	51.00	7.73	9.50	66.95	0.14	441	0.78	866	2	478	123	0.12

Proctor, G.W. #23												
Depth (ft)	% Carbonate	Leco TOC	Rock-Eval S1	Rock-Eval S2	Rock-Eval S3	TMAX	Calculated %RO	Hydrogen Index	Oxygen Index	S2/S3	S1/TOC	Production Index
1942.5	53.24	8.17	13.21	86.60	0.68	426	0.51	1,060	8	127	162	0.13
1961.8	70.05	2.67	3.71	19.62	0.35	422	0.44	735	13	56	139	0.16
1961.8A	88.43	0.31	0.32	1.09	0.20	426	0.51	352	65	5	103	0.23
1967.2	19.59	5.50	3.65	50.81	0.58	426	0.51	924	11	88	66	0.07

Shanklin, W.R. #1A												
Depth (ft)	% Carbonate	Leco TOC	Rock-Eval S1	Rock-Eval S2	Rock-Eval S3	TMAX	Calculated %RO	Hydrogen Index	Oxygen Index	S2/S3	S1/TOC	Production Index
2110.4	52.49	8.06	14.43	78.17	0.86	427	0.53	970	11	91	179	0.16
2124.3	71.17	1.82	1.44	14.99	0.37	425	0.49	824	20	41	79	0.09

2128.3	64.30	6.47	17.42	54.82	0.58	424	0.47	847	9	95	269	0.24
2132.4	69.20	2.19	9.55	16.36	0.28	423	0.45	747	13	58	436	0.37
2139.9	10.71	3.72	3.66	32.00	0.42	424	0.47	860	11	76	98	0.10

Blumberg, Jane W. #1-B												
Depth (ft)	% Carbonate	Leco TOC	Rock-Eval S1	Rock-Eval S2	Rock-Eval S3	TMAX	Calculated %RO	Hydrogen Index	Oxygen Index	S2/S3	S1/TOC	Production Index
4147.5	76.50	0.14	0.03	0.08	0.20	426	0.51	57	143	0	21	0.27
4177.4	38.65	4.62	1.37	44.26	0.47	428	0.54	958	10	94	30	0.03
4192.4	54.88	2.26	0.67	16.44	0.43	421	0.42	727	19	38	30	0.04
4212.3	78.92	0.90	0.27	5.26	0.28	429	0.56	584	31	19	30	0.05
4215.7	37.20	8.48	3.40	68.54	0.50	426	0.51	808	6	137	40	0.05
4218.4	33.50	11.80	4.54	88.47	0.44	425	0.49	750	4	201	38	0.05
4221.4	25.76	7.19	1.84	59.55	0.35	425	0.49	828	5	170	26	0.03
4224.5	26.55	11.70	3.08	91.50	0.63	422	0.44	782	5	145	26	0.03
4244.5	91.94	0.08	0.02	0.05	0.12	337	-1.09	63	150	0	25	0.29

Mathews, J.L. #1-1												
Depth (ft)	% Carbonate	Leco TOC	Rock-Eval S1	Rock-Eval S2	Rock-Eval S3	TMAX	Calculated %RO	Hydrogen Index	Oxygen Index	S2/S3	S1/TOC	Production Index
4619.0	51.53	4.68	4.87	31.05	0.27	439	0.74	663	6	115	104	0.14
4647.0	87.55	1.02	1.25	5.04	0.18	436	0.69	494	18	28	123	0.20
4662.0	66.7	4.28	6.24	31.16	0.31	437	0.71	728	7	101	146	0.17
4681.4	44.67	8.06	13.35	54.85	0.31	437	0.71	681	4	177	166	0.20

Hay, E.D. #1												
Depth (ft)	% Carbonate	Leco TOC	Rock-Eval S1	Rock-Eval S2	Rock-Eval S3	TMAX	Calculated %RO	Hydrogen Index	Oxygen Index	S2/S3	S1/TOC	Production Index
13823.9	44.17	6.14	1.41	1.75	0.15	466	1.23	29	2	12	23	0.45
13824.4	67.84	3.70	1.47	1.52	0.17	469	1.28	41	5	9	40	0.49

Dilworth, Mrs Mary J. #1												
Depth (ft)	% Carbonate	Leco TOC	Rock-Eval S1	Rock-Eval S2	Rock-Eval S3	TMAX	Calculated %RO	Hydrogen Index	Oxygen Index	S2/S3	S1/TOC	Production Index
11002.3	64.08	3.39	3.87	5.49	0.37	455	1.03	162	11	15	114	0.41
11020.5	62.21	3.66	3.57	5.56	0.35	456	1.05	152	10	16	98	0.39
11034.5	51.87	4.96	3.52	6.95	0.41	458	1.08	140	8	17	71	0.34

Schauers, F.T. etal #1												
Depth (ft)	% Carbonate	Leco TOC	Rock-Eval S1	Rock-Eval S2	Rock-Eval S3	TMAX	Calculated %RO	Hydrogen Index	Oxygen Index	S2/S3	S1/TOC	Production Index
8096.0	51.42	2.61	3.30	15.56	0.11	438	0.72	596	4	141	126	0.17
8109.4	65.61	3.69	2.40	18.15	0.13	440	0.76	492	4	140	65	0.12
8122.4	64.32	3.21	2.33	15.17	0.20	440	0.76	473	6	76	73	0.13
8140.3	70.87	3.05	1.90	13.94	0.13	441	0.78	457	4	107	62	0.12
8143.1	89.79	1.14	0.50	3.52	0.11	443	0.81	309	10	32	44	0.12
8157.4	22.70	2.36	2.08	11.83	0.20	441	0.78	501	8	59	88	0.15

Leppard, J.A. #1-H												
Depth (ft)	% Carbonate	Leco TOC	Rock-Eval S1	Rock-Eval S2	Rock-Eval S3	TMAX	Calculated %RO	Hydrogen Index	Oxygen Index	S2/S3	S1/TOC	Production Index
13556.9		2.80	0.28	0.49	0.24	506	1.95	18	9	2	10	0.36
13561.2		2.71	0.13	0.23	0.24	509	2.00	8	9	1	5	0.36
13568.0		2.27	0.08	0.33	0.20	526	2.31	15	9	2	3	0.19
13573.9		2.98	0.08	0.29	0.21	514	2.09	10	7	1	3	0.21
13580.4		5.14	0.15	0.47	0.26	530	2.38	9	5	2	3	0.24
13583.8		2.55	0.21	0.32	0.19	533	2.43	13	7	2	8	0.40
13587.6		4.42	0.26	0.66	0.22	528	2.34	15	5	3	6	0.29
13592.0		4.30	0.17	0.50	0.26	525	2.29	12	6	2	4	0.25
13608.0		5.01	0.22	0.70	0.26	533	2.43	14	5	3	4	0.24
13616.9		5.21	0.20	0.67	0.38	530	2.38	13	7	2	4	0.23
13630.9		4.49	0.29	0.73	0.22	527	2.33	16	5	3	6	0.28

13636.5		4.44	0.15	0.57	0.27	529	2.36	13	6	2	3	0.21
13651.0		4.34	0.21	0.30	0.39	512	2.06	7	9	1	5	0.42
13660.2		4.50	0.15	0.43	0.23	521	2.22	10	5	2	3	0.26
13666.8		4.46	0.21	0.57	0.21	526	2.31	13	5	3	5	0.27
13671.0		0.90	0.07	0.08	0.26	473	1.34	9	29	0	8	0.47

Gise, Lawrence #1

Depth (ft)	% Carbonate	Leco TOC	Rock-Eval S1	Rock-Eval S2	Rock-Eval S3	TMAX	Calculated %RO	Hydrogen Index	Oxygen Index	S2/S3	S1/TOC	Production Index
7181.4	86.48	1.63	2.39	5.16	0.21	443	0.81	317	13	25	147	0.32
7191.6	85.24	1.50	1.29	3.24	0.22	449	0.92	216	15	15	86	0.28

Hal, Browne #8

Depth (ft)	% Carbonate	Leco TOC	Rock-Eval S1	Rock-Eval S2	Rock-Eval S3	TMAX	Calculated %RO	Hydrogen Index	Oxygen Index	S2/S3	S1/TOC	Production Index
2189.8	66.04	4.56	3.34	30.89	0.95	428	0.54	677	21	33	73	0.10
2195.0	74.27	3.86	2.33	28.24	0.79	421	0.42	732	20	36	60	0.08

Orts, H.P. #2

Depth (ft)	% Carbonate	Leco TOC	Rock-Eval S1	Rock-Eval S2	Rock-Eval S3	TMAX	Calculated %RO	Hydrogen Index	Oxygen Index	S2/S3	S1/TOC	Production Index
7689.8	80.96	1.64	0.48	7.20	0.26	445	0.85	439	16	28	29	0.06
7696.3	73.34	2.19	0.60	10.13	0.30	445	0.85	463	14	34	27	0.06
7711.5	88.79	0.84	0.41	3.00	0.23	445	0.85	357	27	13	49	0.12
7712.8	59.15	3.83	2.32	17.26	0.47	444	0.83	451	12	37	61	0.12
7744.0	48.35	5.40	1.49	23.51	0.47	445	0.85	435	9	50	28	0.06
7753.6	9.12	2.38	1.29	10.53	0.43	444	0.83	442	18	24	54	0.11

Bendele, Spettel #1

Depth (ft)	% Carbonate	Leco TOC	Rock-Eval S1	Rock-Eval S2	Rock-Eval S3	TMAX	Calculated %RO	Hydrogen Index	Oxygen Index	S2/S3	S1/TOC	Production Index
7987.5	80.95	1.46	2.16	7.71	0.19	438	0.72	528	13	41	148	0.22
7996.5	90.01	0.86	2.85	3.91	0.18	436	0.69	455	21	22	331	0.42

Krause, A.L. estate #2

Depth (ft)	% Carbonate	Leco TOC	Rock-Eval S1	Rock-Eval S2	Rock-Eval S3	TMAX	Calculated %RO	Hydrogen Index	Oxygen Index	S2/S3	S1/TOC	Production Index
9940.6	56.32	4.93	1.30	1.53	0.17	487	1.61	31	3	9	26	0.46
9961.6	60.33	4.61	1.29	1.44	0.15	484	1.55	31	3	10	28	0.47
9980.8	58.36	4.54	0.79	1.02	0.15	485	1.57	22	3	7	17	0.44
9997.6	47.25	4.14	0.33	0.90	0.15	498	1.80	22	4	6	8	0.27

Person, Otha D. #1

Depth (ft)	% Carbonate	Leco TOC	Rock-Eval S1	Rock-Eval S2	Rock-Eval S3	TMAX	Calculated %RO	Hydrogen Index	Oxygen Index	S2/S3	S1/TOC	Production Index
10350.0		1.27	0.43	2.23	1.9	435		176	150		34	0.16
10410.0		1.1	0.29	2.12	0.6	441	0.87	193	55		26	0.12
10470.0		0.81	0.13	1.13	0.53	439		139	65		16	0.10

Blackwell, R.F. etal #1

Depth (ft)	% Carbonate	Leco TOC	Rock-Eval S1	Rock-Eval S2	Rock-Eval S3	TMAX	Calculated %RO	Hydrogen Index	Oxygen Index	S2/S3	S1/TOC	Production Index
14060.0		0.99	0.09	0.35	0.45	459	1.36	35	45		9	0.20
14240.0		0.82	0.09	0.56	0.65	452		68	79		11	0.14
14270.0		0.66	0.05	0.48	0.67	452		72	101		8	0.09
14330.0		0.76	0.07	0.51	0.72	453		67	95		9	0.12
14360.0		0.72	0.07	0.51	0.64	448		71	89		9	0.12
14420.0		0.77	0.03	0.48	0.6	448	1.28	62	78		4	0.06

Szalwinski, J.J. #1

Depth (ft)	% Carbonate	Leco TOC	Rock-Eval S1	Rock-Eval S2	Rock-Eval S3	TMAX	Calculated %RO	Hydrogen Index	Oxygen Index	S2/S3	S1/TOC	Production Index
9982.0	76.89	1.44	1.51	3.24	0.33	445	0.85	225	23	10	105	0.32

10077.0	59.20	4.23	7.38	10.76	0.30	445	0.85	254	7	36	174	0.41
10155.0	60.06	4.98	5.53	13.95	0.35	443	0.81	280	7	40	111	0.28

Chittim, J.M. #1												
Depth (ft)	% Carbonate	Leco TOC	Rock-Eval S1	Rock-Eval S2	Rock-Eval S3	TMAX	Calculated %RO	Hydrogen Index	Oxygen Index	S2/S3	S1/TOC	Production Index
2414.0	78.81	2.71	1.67	21.29	0.28	438	0.72	786	10	76	62	0.07
2450.0	48.38	6.65	3.81	36.45	0.48	437	0.71	548	7	76	57	0.09
2514.0	26.11	2.72	1.22	17.13	0.37	436	0.69	630	14	46	45	0.07

Triple Bar Ranch #1												
Depth (ft)	% Carbonate	Leco TOC	Rock-Eval S1	Rock-Eval S2	Rock-Eval S3	TMAX	Calculated %RO	Hydrogen Index	Oxygen Index	S2/S3	S1/TOC	Production Index
10780.0		1	0.04	0.5	1.72	425	1.32	50	172		4	0.07
10870.0		1.07	0.04	0.47	1.68	427		44	157		4	0.08

Pawelek, Ben A. #1-A												
Depth (ft)	% Carbonate	Leco TOC	Rock-Eval S1	Rock-Eval S2	Rock-Eval S3	TMAX	Calculated %RO	Hydrogen Index	Oxygen Index	S2/S3	S1/TOC	Production Index
10240.0		0.75										
10300.0		0.53	0.02	0.37	0.34	441	1.2552	70	64		4	0.05
10390.0		0.71	0.04	0.86	0.31	447		121	44		6	0.04

Halff, H.A. etal #1												
Depth (ft)	% Carbonate	Leco TOC	Rock-Eval S1	Rock-Eval S2	Rock-Eval S3	TMAX	Calculated %RO	Hydrogen Index	Oxygen Index	S2/S3	S1/TOC	Production Index
6122.5	83.48	0.60	0.24	1.78	0.24	438	0.72	297	40	7	40	0.12
6408.0	38.93	3.24	4.69	21.95	0.30	442	0.80	677	9	73	145	0.18
6422.6	55.03	9.88	11.31	76.06	0.39	439	0.74	770	4	195	114	0.13
6433.5	43.55	10.90	16.35	86.35	0.33	440	0.76	792	3	262	150	0.16
6455.8	55.00	9.37	14.30	79.33	0.23	439	0.74	847	2	345	153	0.15
6459.5	52.22	4.82	8.66	44.58	0.16	438	0.72	925	3	279	180	0.16

Appendix C: XRD & XRF Data

XRD Symbols:

(+) present but below 1% level

XRD

Hendershot, Clare J. #1															
Depth	Quartz	Plagioclase	K-Feldspar	Calcite	Dolomite	Ankerite	Siderite	Rutile	Gypsum	Pyrite	Apatite	Illite+Mica	I/S Mixed-layer	Kaolinite	Chlorite
4741.0	20		2	31						2		20	10	15	
4745.5	4			55					8	2	3	12	3	5	
4773.7	22			40						3		15	10	10	

Calvert, J.H. #1															
Depth	Quartz	Plagioclase	K-Feldspar	Calcite	Dolomite	Ankerite	Siderite	Rutile	Gypsum	Pyrite	Apatite	Illite+Mica	I/S Mixed-layer	Kaolinite	Chlorite
6115.1	20	3		58	4			+		2	+	5	3	5	
6117.4	17	7		26	2			+		2	+	30	6	10	
6129.1	25			62				+		2	+	4	2	5	
6135.6	25	3		50	3			+		2	+	5	2	10	
6141.1	18			60	3			+		2	+	5	3	9	
6145.7	25	3		48	4			+		4	+	4	2	10	
6147.0	25	3		39	4		2	+		4	+	10	5	8	
6155.0	20			58				+		3	+	3	6	10	
6158.7	20			48	4			+		4	+	7	5	12	

Proctor, G.W. #23															
Depth	Quartz	Plagioclase	K-Feldspar	Calcite	Dolomite	Ankerite	Siderite	Rutile	Gypsum	Pyrite	Apatite	Illite+Mica	I/S Mixed-layer	Kaolinite	Chlorite
1942.5	4			58		1			3	2	3	10	5	10	
1961.8	4		2	40		2			5	3	3	12	3	8	
1961.8A	2			80		6				2		5	2	3	
1967.2	20			3					7	2		45	13	10	

Shanklin, W.R. #1A															
Depth	Quartz	Plagioclase	K-Feldspar	Calcite	Dolomite	Ankerite	Siderite	Rutile	Gypsum	Pyrite	Apatite	Illite+Mica	I/S Mixed-layer	Kaolinite	Chlorite
2110.4	15		1	37		5			5	2		10	5	10	
2124.3	10		1	69	1				2	2		5	5	5	
2128.3	10		1	45					20	1		8	5	10	
2132.4	10		2	53	2				2	2		10	5	14	
2139.9	40			4					2	2		20	17	15	

Blumberg, Jane W. #1-B															
Depth	Quartz	Plagioclase	K-Feldspar	Calcite	Dolomite	Ankerite	Siderite	Rutile	Gypsum	Pyrite	Apatite	Illite+Mica	I/S Mixed-layer	Kaolinite	Chlorite
4177.4	5			50					6	3	3	15	5	5	
4192.4	17		3	55				+		2	+	5	6	12	
4212.3	10			70										5	
4215.7	10			76				+		2	+	2		10	
4218.4	20		2	35				+		3	1	15	10	14	
4221.4	23			18				+	3	5	1	10	10	30	
4224.5	20			25				1	14	5	2	5	3	25	

Mathews, J.L. #1-1															
Depth	Quartz	Plagioclase	K-Feldspar	Calcite	Dolomite	Ankerite	Siderite	Rutile	Gypsum	Pyrite	Apatite	Illite+Mica	I/S Mixed-layer	Kaolinite	Chlorite
4619.0	14			50	1					2		18	10		5
4647.0	15			69	1					1		9	5		
4651.7	2			1						2		8	7	80	
4655.4	15									3		20	10	52	

4662.0	23			64						2		6	5		
4681.4	20			43						4		15	10	8	

Hay, E.D. #1															
Depth	Quartz	Plagioclase	K-Feldspar	Calcite	Dolomite	Ankerite	Siderite	Rutile	Gypsum	Pyrite	Apatite	Illite+Mica	I/S Mixed-layer	Kaolinite	Chlorite
13705.0	8	1		70						2		10	6		3
13820.0	28	3		32	4				1	3		10	17		2
13823.9	20	3		44						3		10	10		10
13824.4	15	2		66						2		7	6		2

Dilworth, Mrs Mary J. #1															
Depth	Quartz	Plagioclase	K-Feldspar	Calcite	Dolomite	Ankerite	Siderite	Rutile	Gypsum	Pyrite	Apatite	Illite+Mica	I/S Mixed-layer	Kaolinite	Chlorite
11002.3	10	2		52						3	2	15	10	6	
11020.5	10			59						2	2	8	3	6	
11034.5	10			48						3		15	5	10	

Schauers, F.T. etal #1															
Depth	Quartz	Plagioclase	K-Feldspar	Calcite	Dolomite	Ankerite	Siderite	Rutile	Gypsum	Pyrite	Apatite	Illite+Mica	I/S Mixed-layer	Kaolinite	Chlorite
8143.1	4			92								3	1		

Leppard, J.A. #1-H															
Depth	Quartz	Plagioclase	K-Feldspar	Calcite	Dolomite	Ankerite	Siderite	Rutile	Gypsum	Pyrite	Apatite	Illite+Mica	I/S Mixed-layer	Kaolinite	Chlorite
13539.0	10	3		36					3	3		10	20	10	5
13564.0	10			53						2		10	15	10	
13578.0	12	2		47						3	2	14	20		
13666.0	10	2		54					1	3	2	10	13	5	

Gise, Lawrence #1															
Depth	Quartz	Plagioclase	K-Feldspar	Calcite	Dolomite	Ankerite	Siderite	Rutile	Gypsum	Pyrite	Apatite	Illite+Mica	I/S Mixed-layer	Kaolinite	Chlorite
7181.4	34	2	1	11								15	14	13	10
7191.6	3	2		89								4	2		

Hal, Browne #8															
Depth	Quartz	Plagioclase	K-Feldspar	Calcite	Dolomite	Ankerite	Siderite	Rutile	Gypsum	Pyrite	Apatite	Illite+Mica	I/S Mixed-layer	Kaolinite	Chlorite
2191.7	5		2	1					4	3		3	2	80	
2195.0	6		2	69					1	1		10	6	5	

Orts, H.P. #2															
Depth	Quartz	Plagioclase	K-Feldspar	Calcite	Dolomite	Ankerite	Siderite	Rutile	Gypsum	Pyrite	Apatite	Illite+Mica	I/S Mixed-layer	Kaolinite	Chlorite
7689.8	3			85						2		3			
7696.3	5			75					4	4	1	3			
7711.5	10			87								1			
7712.8	2	3		58						5	2	2		5	
7744.0	8	1	1	44						5	1	10		5	
7746.3	6	1		53						3	1	5		6	
7748.8	26		1	8					2	4		5		14	
7753.6	22		1	12						5		10		10	

Bendele, Spettel #1															
Depth	Quartz	Plagioclase	K-Feldspar	Calcite	Dolomite	Ankerite	Siderite	Rutile	Gypsum	Pyrite	Apatite	Illite+Mica	I/S Mixed-layer	Kaolinite	Chlorite
7987.5	10			81						1		5	3		
7996.5	6	1		90						+		2	1		

Krause, A.L. estate #2															
Depth	Quartz	Plagioclase	K-Feldspar	Calcite	Dolomite	Ankerite	Siderite	Rutile	Gypsum	Pyrite	Apatite	Illite+Mica	I/S Mixed-layer	Kaolinite	Chlorite
9940.6	10	1		52						2	1	14	5	10	
9961.6	12	1		54						2	1	10	5	5	
9980.8	10			48						3		20	5	5	

9997.6	9			48						4		20	6	10	

Szalwinski, J.J. #1															
Depth	Quartz	Plagioclase	K-Feldspar	Calcite	Dolomite	Ankerite	Siderite	Rutile	Gypsum	Pyrite	Apatite	Illite+Mica	I/S Mixed-layer	Kaolinite	Chlorite
9982.0	5	2		81						+		7	5		
10077.0	13	2		53						2		20	10		
10155.0	13			58						3		10	5	11	

Chittim, J.M. #1															
Depth	Quartz	Plagioclase	K-Feldspar	Calcite	Dolomite	Ankerite	Siderite	Rutile	Gypsum	Pyrite	Apatite	Illite+Mica	I/S Mixed-layer	Kaolinite	Chlorite
2414.0	20	2		47	2				1	2		10	5	11	
2450.0	15			61	2					2		5	5	10	
2514.0	15	2		27	2				2	2		10	5	35	

XRF Major Elements

Hendershot, Clare J. #1													
Depth	SiO2	Al2O3	Fe2O3 (%)	Na2O	MgO	P2O5	K2O	CaO	TiO2	MnO	S	C	Sum*
4741.0	42.88	13.05	2.35	0.78	1.42	0.10	2.55	17.21	0.58	0.01	0.91		81.84
4745.5	5.33	4.25	2.96	0.32	0.6	1.33	1.05	31.74	0.32	0.03	2.94	7.99	58.86
4773.7	38.11	10.03	2.82	0.55	1.24	0.22	2.45	23.89	0.44	0.05	1.37		81.17

Calvert, J.H. #1													
Depth	SiO2	Al2O3	Fe2O3 (%)	Na2O	MgO	P2O5	K2O	CaO	TiO2	MnO	S	C	Sum*
6115.1	33.32	4.54	1.69	0.38	0.73	0.12	0.58	34.55	0.23	0.02	1.07		77.23
6117.4	43.13	14.52	2.13	0.83	1.23	0.09	2.19	16.01	0.44	0.01	1.25		81.82
6129.1	29.30	4.19	1.69	0.21	0.69	0.16	0.63	34.65	0.21	0.02	1.16		72.91
6135.6	34.07	6.63	2.33	0.32	0.78	0.33	0.89	29.75	0.29	0.02	1.58		76.98
6141.1	26.27	4.09	1.87	0.23	0.69	0.21	0.59	35.74	0.19	0.02	1.54		71.41
6145.7	33.26	6.86	3.04	0.38	0.85	0.31	1.17	26.59	0.32	0.02	2.33		75.12
6147.0	38.14	7.70	3.54	0.40	0.88	0.38	1.35	22.93	0.36	0.02	2.69		78.38
6155.0	30.94	6.04	1.74	0.21	0.72	0.25	0.89	33.29	0.27	0.02	1.30		75.67
6158.7	32.97	7.31	2.55	0.26	0.81	0.22	1.16	28.86	0.34	0.02	1.91		76.40

Proctor, G.W. #23													
Depth	SiO2	Al2O3	Fe2O3 (%)	Na2O	MgO	P2O5	K2O	CaO	TiO2	MnO	S	C	Sum*
1942.5	7.63	4.51	1.69	0.21	0.47	1.01	1.19	34.68	0.33	0.03	1.20	13.30	66.25
1961.8	9.46	6.64	3.01	0.21	0.8	0.99	3.38	25.18	0.36	0.02	2.99	11.27	64.31
1961.8A	5.22	2.27	2.22	0.14	1.95	0.49	0.52	48.37	0.08	0.05	0.99	10.52	72.82
1967.2	49.94	19.34	4.49	0.36	0.9	0.25	2.31	4.82	0.56	0.05	2.66	6.00	91.68

Shanklin, W.R. #1A													
Depth	SiO2	Al2O3	Fe2O3 (%)	Na2O	MgO	P2O5	K2O	CaO	TiO2	MnO	S	C	Sum*
2110.4	25.23	7.94	3.56	0.25	1.26	1.84	2.19	22.06	0.4	0.04	2.43	12.58	79.78
2124.3	15.90	3.60	1.69	<0.2	<0.6	0.15	1.04	39.52	<0.08	0.02	1.24	10.27	73.43
2128.3	18.45	4.87	1.94	<0.2	<0.6	0.24	2.70	32.03	0.11	0.02	8.43	13.27	82.06
2132.4	21.76	5.63	1.50	<0.2	<0.6	0.22	2.54	31.22	0.11	0.02	1.61	11.98	76.58
2139.9	58.99	15.41	3.57	0.21	0.74	0.22	2.17	2.72	0.60	0.02	2.01	4.49	91.15

Blumberg, Jane W. #1-B													
Depth	SiO2	Al2O3	Fe2O3 (%)	Na2O	MgO	P2O5	K2O	CaO	TiO2	MnO	S	C	Sum*
4177.4	14.03	8.77	2.7	0.26	0.58	1.11	1.01	29.91	0.36	0.03	3.17	9.61	71.54
4192.4	30.38	7.83	2.28	0.34	0.83	0.09	2.41	31.15	0.34	0.02	1.20		76.85
4212.3	12.48	1.88	0.9	0.18	0.34	0.07	<0.05	38.95	0.29	0.02	0.22	10.80	66.13
4215.7	19.95	3.87	1.44	0.09	0.61	0.21	0.63	42.86	0.12	0.02	1.28		71.09
4218.4	36.60	9.70	3.82	0.28	1.03	0.33	2.81	20.80	0.43	0.02	3.79		79.61
4221.4	44.64	17.93	4.09	0.37	1.20	0.38	2.53	11.89	0.65	0.02	3.12		86.82
4224.5	40.86	17.41	6.47	0.33	1.08	0.97	2.42	8.28	0.98	0.04	6.26		85.10

Mathews, J.L. #1-1													
Depth	SiO2	Al2O3	Fe2O3 (%)	Na2O	MgO	P2O5	K2O	CaO	TiO2	MnO	S	C	Sum*
4619.0	31.11	5.61	1.26	0.18	0.40	0.17	1.58	29.07	0.16	0.01	0.91	11.54	81.99
4647.0	21.79	2.91	0.82	0.06	0.09	0.14	0.54	38.83	0.04	0.02	0.64	0.29	66.15
4651.7	39.21	30.78	2.05	0.27	0.00	0.12	1.02	0.44	0.67	0.01	1.28	0.31	76.16
4655.4	48.89	34.3	2.12	0.39	0.3	0.17	1.33	0.69	0.62	0.01	1.41	0.05	90.28
4662.0	25.94	2.78	0.89	0.07	0.05	0.18	0.33	35.98	0.03	0.01	0.87	12.10	79.22
4681.4	31.85	6.75	2.19	0.13	0.25	0.19	1.50	24.11	0.22	0.01	2.24	13.63	83.07

Hay, E.D. #1													
Depth	SiO2	Al2O3	Fe2O3 (%)	Na2O	MgO	P2O5	K2O	CaO	TiO2	MnO	S	C	Sum*
13823.9	35.22	9.39	2.78	0.39	0.86	0.11	1.57	25.32	0.42	0.01	1.67		77.74
13824.4	24.79	5.87	1.43	0.32	0.73	0.31	0.97	37.40	0.28	0.02	0.84		72.94

Dilworth, Mrs Mary J. #1													
Depth	SiO2	Al2O3	Fe2O3 (%)	Na2O	MgO	P2O5	K2O	CaO	TiO2	MnO	S	C	Sum*
11002.3	24.94	7.06	1.63	0.39	0.44	0.63	0.93	29.22	0.35	<0.01	1.41	10.22	77.22
11020.5	21.17	4.57	1.3	0.3	0.42	0.67	0.52	33.07	0.33	0.01	1.00	11.12	74.48
11034.5	30.54	8	1.83	0.28	0.5	0.32	1.13	26.98	0.39	0.01	1.66	10.88	82.52

Schauers, F.T. etal #1													
Depth	SiO2	Al2O3	Fe2O3 (%)	Na2O	MgO	P2O5	K2O	CaO	TiO2	MnO	S	C	Sum*
8143.1	7.24	1.61	0.57	<0.2	0.16	0.13	<0.3	53.87	<0.08	0.01	0.09	12.02	75.69

Gise, Lawrence #1													
Depth	SiO2	Al2O3	Fe2O3 (%)	Na2O	MgO	P2O5	K2O	CaO	TiO2	MnO	S	C	Sum*
7181.4	48.69	16.00	4.50	0.50	1.73	0.13	2.34	6.32	0.58	0.01	1.72	3.92	86.45
7191.6	7.45	2.22	0.55	0.14	0.66	0.11	0.44	49.85	0.08	0.01	0.23	11.33	73.07

Hal, Browne #8													
Depth	SiO2	Al2O3	Fe2O3 (%)	Na2O	MgO	P2O5	K2O	CaO	TiO2	MnO	S	C	Sum*
2191.7	35.54	28.31	4.96	<0.2	<0.6	0.18	0.73	0.44	0.74	0.01	3.28	0.15	74.34
2195.0	15.17	3.01	1.51	<0.2	<0.6	0.40	1.70	39.06	<0.08	0.02	0.89	11.99	73.75

Orts, H.P. #2													
Depth	SiO2	Al2O3	Fe2O3 (%)	Na2O	MgO	P2O5	K2O	CaO	TiO2	MnO	S	C	Sum*
7689.8	9.31	2.48	1.64	0.07	0.72	0.26	0.57	48.87	0.09	0.04	0.79	11.18	76.02
7696.3	11.57	4.16	3.75	0.13	0.77	0.6	0.9	43.45	0.12	0.02	2.87	9.93	78.27
7711.5	11.77	0.79	0.25	0.04	0.6	0.03	0.16	48.08	0.06	0.02	0.06	11.26	73.12
7712.8	4.09	6.87	2.09	0.51	0.41	0.76	0.56	32.47	0.35	<0.01	2.21	11.04	61.36
7744.0	16.14	9.37	2.2	0.33	0.85	0.34	2.11	24.67	0.43	0.01	1.92	11.00	69.37
7746.3	11.57	6.85	1.6	0.37	0.59	0.36	1.24	29.54	0.34	0.01	1.42	8.17	62.06
7748.8	56.95	19.95	3.93	0.5	1.17	0.17	3.07	4.41	0.69	0.01	2.69	2.94	96.48
7753.6	53.85	19.22	3.7	0.46	1.11	0.15	3.02	6.8	0.64	0.02	2.62	4.29	95.88

Bendele, Spettel #1													
Depth	SiO2	Al2O3	Fe2O3 (%)	Na2O	MgO	P2O5	K2O	CaO	TiO2	MnO	S	C	Sum*
7987.5	13.83	3.22	1.07	0.21	0.83	0.12	0.84	45.45	0.15	0.03	0.46		66.21
7996.5	9.21	1.37	0.38	0.11	0.62	0.07	0.31	50.37	0.05	0.03	0.16		62.66

Krause, A.L. estate #2													
Depth	SiO2	Al2O3	Fe2O3 (%)	Na2O	MgO	P2O5	K2O	CaO	TiO2	MnO	S	C	Sum*
9,940.60	27.34	4.92	1.37	0.29	0.41	0.3	0.82	29.77	0.33	<0.01	1.06	11.60	78.21
9,961.60	24.27	5.82	1.36	0.32	0.5	0.38	0.8	30.11	0.34	<0.01	1.05	11.45	76.40
9,980.80	30.38	7.27	1.73	0.25	0.43	0.25	1.1	26.95	0.36	<0.01	1.52	10.84	81.08
9,997.60	28.09	9.06	1.96	0.22	0.43	0.21	1.28	26.81	0.38	<0.01	1.80	9.94	80.18

Szalwinski, J.J. #1													
Depth	SiO2	Al2O3	Fe2O3 (%)	Na2O	MgO	P2O5	K2O	CaO	TiO2	MnO	S	C	Sum*
9982.0	11.44	3.16	0.95	0.38	0.56	0.47	0.64	45.35	0.05	0.03	0.10	10.81	73.93
10077.0	24.54	6.03	1.44	0.36	0.57	0.16	1.69	29.97	0.16	0.01	1.07	11.15	77.15
10155.0	22.88	5.27	1.60	0.19	0.25	0.27	1.30	32.20	0.14	0.01	1.67	12.35	78.12

Chittim, J.M. #1													
Depth	SiO2	Al2O3	Fe2O3 (%)	Na2O	MgO	P2O5	K2O	CaO	TiO2	MnO	S	C	Sum*
2414.0	30.70	5.37	1.73	0.47	<0.6	0.21	0.49	27.55	0.14	0.01	1.78	12.74	81.18
2450.0	25.83	3.44	1.09	0.26	<0.6	0.29	0.30	34.29	0.05	0.01	0.94	13.78	80.27
2514.0	33.23	14.07	2.41	0.62	0.74	0.12	0.75	16.35	0.27	0.02	2.13	7.50	78.20

XRF Trace Elements

Hendershot, Clare J. #1																		
Depth	Ba	Co	Cr	Cu	La	Mo	Nb	Ni	Pb	Rb	Sr	Th	U	V	Y	Zn	Zr	% Sulfer
4741.0	106	<5	101	37	69	9	10	38	10	169	400	36	6	189	26	101	119	1.11
4745.5	92	<5	44	16	123	7	7	14	6	156	520	38	19	54	16	58	88	4.99
4773.7	129	<5	102	12	79	5	10	22	8	163	389	35	4	187	26	94	93	1.69

Calvert, J.H. #1																		
Depth	Ba	Co	Cr	Cu	La	Mo	Nb	Ni	Pb	Rb	Sr	Th	U	V	Y	Zn	Zr	% Sulfer
6115.1	92	<5	52	32	90	29	5	54	9	115	541	34	13	204	26	99	90	1.39
6117.4	92	<5	78	31	76	49	6	54	12	151	338	40	7	431	26	149	110	1.53
6129.1	92	<5	68	39	89	32	<5	48	9	115	496	34	9	169	26	110	82	1.59
6135.6	92	<5	82	50	89	35	5	57	9	126	486	36	10	186	26	97	93	2.05
6141.1	92	<5	74	53	89	35	<5	66	9	115	589	34	9	215	26	117	92	2.15
6145.7	92	<5	89	75	85	115	<5	115	9	141	432	36	16	262	26	117	86	3.10
6147.0	92	<5	114	114	93	195	<5	196	9	149	425	37	23	396	26	151	93	3.44
6155.0	92	<5	79	41	79	30	5	52	9	134	524	36	9	272	26	99	93	1.72
6158.7	92	<5	94	73	86	66	<5	105	9	142	522	36	12	395	26	166	108	2.50

Proctor, G.W. #23																		
Depth	Ba	Co	Cr	Cu	La	Mo	Nb	Ni	Pb	Rb	Sr	Th	U	V	Y	Zn	Zr	% Sulfer
1942.5	92	<5	41	<10	112	10	6	26	7	162	308	40	22	61	16	51	82	1.81
1961.8	92	<5	43	20	115	31	8	80	7	172	261	41	30	192	24	144	82	4.65
1961.8A	92	<5	21	<10	122	5	7	<14	6	146	217	38	28	60	18	60	82	1.36
1967.2	153	10	105	<10	98	15	10	29	8	288	184	55	21	179	34	119	91	2.90

Shanklin, W.R. #1A																		
Depth	Ba	Co	Cr	Cu	La	Mo	Nb	Ni	Pb	Rb	Sr	Th	U	V	Y	Zn	Zr	% Sulfer
2110.4	92	<5	60	<10	104	13	8	23	8	188	223	44	22	75	24	51	82	3.05
2124.3	92	<5	36	<10	103	3	5	<20	<8	128	349	37	11	74	<15	54	82	1.69
2128.3	92	<5	53	12	102	32	5	57	8	151	298	40	17	198	15	117	82	10.27
2132.4	92	<5	43	<10	97	20	6	26	8	154	320	41	16	120	<15	53	82	2.10
2139.9	174	9	94	<10	85	17	11	<20	9	294	188	57	12	155	35	60	88	2.21

Blumberg, Jane W. #1-B																		
Depth	Ba	Co	Cr	Cu	La	Mo	Nb	Ni	Pb	Rb	Sr	Th	U	V	Y	Zn	Zr	% Sulfer
4177.4	92	<5	35	<10	117	6	6	17	7	161	290	40	17	63	20	77	82	4.43
4192.4	92	<5	55	<10	79	3	6	<14	8	122	357	31	5	88	26	65	82	1.56
4212.3	92	<5	28	<10	110	7	5	<14	7	149	183	39	21	61	10	55	82	0.33
4215.7	92	<5	40	<10	84	14	5	20	8	94	240	29	9	100	26	66	82	1.80
4218.4	92	<5	173	68	74	64	8	95	10	153	233	34	13	436	26	154	82	4.76
4221.4	92	7	146	16	64	44	12	37	13	178	162	40	17	307	26	83	109	3.59
4224.5	92	15	181	84	72	48	14	105	10	190	195	37	23	383	26	56	124	7.36

Mathews, J.L. #1-1																		
Depth	Ba	Co	Cr	Cu	La	Mo	Nb	Ni	Pb	Rb	Sr	Th	U	V	Y	Zn	Zr	% Sulfer
4619.0	92	<5	76	38	97	22	6	39	8	160	658	41	13	266	15	97	136	1.11
4647.0	92	<5	48	21	98	20	5	27	8	132	621	38	11	187	8	64	89	0.97
4651.7	92	6	45	<10	79	22	<5	9	16	241	126	65	<1.1	213	28	84	138	1.68
4655.4	92	6	41	<10	83	25	5	<14	14	250	126	64	12	278	24	88	82	1.56
4662.0	513	<5	21	26	99	14	7	31	9	132	710	39	15	141	9	111	164	1.10
4681.4	92	<5	93	47	92	44	5	60	9	159	430	42	14	310	16	104	86	2.70

Hay, E.D. #1																		
Depth	Ba	Co	Cr	Cu	La	Mo	Nb	Ni	Pb	Rb	Sr	Th	U	V	Y	Zn	Zr	% Sulfer
13823.9	97	<5	102	54	83	42	7	79	9	150	496	37	10	324	26	128	111	2.15

13824.4	97	<5	67	23	86	8	5	17	8	123	581	34	5	90	26	69	105	1.15

Dilworth, Mrs Mary J. #1																		
Depth	Ba	Co	Cr	Cu	La	Mo	Nb	Ni	Pb	Rb	Sr	Th	U	V	Y	Zn	Zr	% Sulfer
11002.3	92	<5	53	11	110	14	7	17	7	174	448	42	22	62	21	70	99	1.83
11020.5	92	<5	52	<10	113	10	6	14	7	165	426	41	21	60	16	65	82	1.34
11034.5	117	<5	79	28	108	17	8	29	7	186	511	44	22	87	21	83	113	2.01

Schauers, F.T. etal #1																		
Depth	Ba	Co	Cr	Cu	La	Mo	Nb	Ni	Pb	Rb	Sr	Th	U	V	Y	Zn	Zr	% Sulfer
8143.1	92	<5	30	<10	96	6	<5	<20	<8	120	347	36	10	54	<15	51	82	0.12

Gise, Lawrence #1																		
Depth	Ba	Co	Cr	Cu	La	Mo	Nb	Ni	Pb	Rb	Sr	Th	U	V	Y	Zn	Zr	% Sulfer
7181.4	239	10	96	<10	95	18	10	33	8	243	272	48	10	235	32	101	140	1.99
7191.6	92	<5	31	27	116	<1.5	9	<14	7	151	882	39	20	79	9	125	140	0.31

Hal, Browne #8																		
Depth	Ba	Co	Cr	Cu	La	Mo	Nb	Ni	Pb	Rb	Sr	Th	U	V	Y	Zn	Zr	% Sulfer
2191.7	92	12	46	<10	85	25	<5	<20	14	147	126	50	<1	263	<15	741	86	
2195.0	92	<5	37	<10	107	17	6	47	<8	131	379	37	18	132	<15	67	82	

Orts, H.P. #2																		
Depth	Ba	Co	Cr	Cu	La	Mo	Nb	Ni	Pb	Rb	Sr	Th	U	V	Y	Zn	Zr	% Sulfer
7689.8	92	<5	27	<10	123	<1.5	6	<14	6	143	482	37	17	38	12	51	82	1.04
7696.3	92	<5	40	25	134	13	6	135	5	144	454	35	20	57	15	195	82	3.67
7711.5	92	<5	25	<10	119	4	5	<14	6	143	270	37	22	67	9	52	82	0.08
7712.8	92	<5	47	26	116	31	6	81	7	156	493	40	22	195	17	173	102	3.60
7744.0	92	<5	75	43	104	43	8	46	6	204	373	44	23	300	25	118	100	2.77
7746.3	92	<5	59	45	179	6	23	55	6	188	796	40	73	150	6	97	237	2.29
7748.8	199	8	77	<10	102	14	12	29	6	301	231	53	21	207	34	101	129	2.79
7753.6	186	7	79	<10	101	14	11	30	6	291	237	52	20	229	35	87	129	2.73

Bendele, Spettel #1																		
Depth	Ba	Co	Cr	Cu	La	Mo	Nb	Ni	Pb	Rb	Sr	Th	U	V	Y	Zn	Zr	% Sulfer
7987.5	92	<5	46	31	87	<1.5	7	16	8	93	859	28	3	84	26	77	124	0.69
7996.5	92	<5	28	20	87	<1.5	6	<14	8	84	861	28	<1.5	52	26	52	112	0.26

Krause, A.L. estate #2																		
Depth	Ba	Co	Cr	Cu	La	Mo	Nb	Ni	Pb	Rb	Sr	Th	U	V	Y	Zn	Zr	% Sulfer
9,940.60	92	<5	63	35	108	36	5	42	8	175	489	43	23	244	16	102	87	1.36
9,961.60	92	<5	61	21	109	20	6	25	8	171	445	43	22	138	16	86	82	1.37
9,980.80	92	<5	69	33	111	50	6	60	7	180	403	43	24	379	20	134	99	1.87
9,997.60	96	<5	53	30	109	48	6	50	7	179	307	43	25	312	19	105	83	2.24

Szalwinski, J.J. #1																		
Depth	Ba	Co	Cr	Cu	La	Mo	Nb	Ni	Pb	Rb	Sr	Th	U	V	Y	Zn	Zr	% Sulfer
9982.0	215	<5	38	50	103	<1	10	<15	8	124	1346	37	3	59	<15	51	246	0.14
10077.0	92	<5	83	22	93	21	6	25	8	154	467	40	11	203	14	84	84	1.39
10155.0	92	<5	89	28	99	28	5	35	8	152	436	40	13	121	16	89	82	2.14

Chittim, J.M. #1																		
Depth	Ba	Co	Cr	Cu	La	Mo	Nb	Ni	Pb	Rb	Sr	Th	U	V	Y	Zn	Zr	% Sulfer
2414.0	92	<5	81	70	94	68	5	69	9	164	612	44	19	391	16	139	140	2.19
2450.0	92	<5	77	58	107	118	<5	79	8	153	759	41	25	494	<15	148	137	1.17
2514.0	92	<5	58	15	98	57	<5	39	9	178	396	46	13	334	22	108	115	2.72

Hand-held XRF Scanner, Major Elements

Data courtesy of Robert Nirkirk and Harold Rowe, University of Texas at Arlington

Core	Depth (ft)	Ca	Ti	Si
Hendershot, Clare J. #1	4734	35.3332	0.0820	3.3909
Hendershot, Clare J. #1	4735	27.7132	0.0252	3.7288
Hendershot, Clare J. #1	4736	35.2560	0.0723	2.9538
Hendershot, Clare J. #1	4737	31.9962	0.1380	4.7052
Hendershot, Clare J. #1	4738	33.2490	0.0900	4.3797
Hendershot, Clare J. #1	4739	32.3527	0.0793	4.6868
Hendershot, Clare J. #1	4740	39.5810	0.0225	1.8093
Hendershot, Clare J. #1	4741	27.6954	0.1518	6.7228
Hendershot, Clare J. #1	4742	17.2490	0.2290	14.0500
Hendershot, Clare J. #1	4743	17.1466	0.2516	15.3601
Hendershot, Clare J. #1	4744	23.8661	0.2026	11.3230
Hendershot, Clare J. #1	4745	24.6470	0.1677	8.9098
Hendershot, Clare J. #1	4746	26.2213	0.1634	10.3091
Hendershot, Clare J. #1	4747	26.4096	0.1463	6.4063
Hendershot, Clare J. #1	4748	28.7857	0.1454	4.7457
Hendershot, Clare J. #1	4749	27.5040	0.1316	5.9338
Hendershot, Clare J. #1	4750	27.2118	0.1221	6.2483
Hendershot, Clare J. #1	4751	25.9568	0.1470	7.7347
Hendershot, Clare J. #1	4752	28.6937	0.1344	6.7218
Hendershot, Clare J. #1	4753	24.2536	0.1483	8.2736
Hendershot, Clare J. #1	4754	31.2433	0.0850	5.4637
Hendershot, Clare J. #1	4755	29.3909	0.1021	6.1828
Hendershot, Clare J. #1	4756	36.1561	0.0447	2.7425
Hendershot, Clare J. #1	4757	31.2868	0.1091	5.8755
Hendershot, Clare J. #1	4757	35.8247	0.0555	2.8935
Hendershot, Clare J. #1	4758	27.2379	0.1374	7.1513
Hendershot, Clare J. #1	4759	24.2251	0.2081	8.0545
Hendershot, Clare J. #1	4759	36.1862	0.0443	3.4154
Hendershot, Clare J. #1	4760	27.1501	0.1251	7.6461
Hendershot, Clare J. #1	4761	36.5817	0.0619	3.6370
Hendershot, Clare J. #1	4761	30.2597	0.1155	6.5222
Hendershot, Clare J. #1	4762	23.7690	0.1928	9.1114
Hendershot, Clare J. #1	4763	35.0293	0.0299	2.9986
Hendershot, Clare J. #1	4763	22.6974	0.2209	11.4394
Hendershot, Clare J. #1	4764	36.9174	0.0433	1.9484
Hendershot, Clare J. #1	4765	24.5714	0.1790	9.9613
Hendershot, Clare J. #1	4765	34.0311	0.0142	4.9595
Hendershot, Clare J. #1	4766	22.7621	0.1969	8.8871
Hendershot, Clare J. #1	4767	22.6435	0.2141	9.4460
Hendershot, Clare J. #1	4768	33.6267	0.0830	4.8285
Hendershot, Clare J. #1	4769	11.8862	0.3342	15.2563
Hendershot, Clare J. #1	4770	34.6903	0.0803	3.5448
Hendershot, Clare J. #1	4771	22.3490	0.1905	8.9654
Hendershot, Clare J. #1	4772	35.0063	0.0545	3.4558
Hendershot, Clare J. #1	4772	13.3550	0.2431	15.7449
Hendershot, Clare J. #1	4773	35.7977	0.0215	1.6587
Hendershot, Clare J. #1	4773	8.4210	0.3550	11.0644
Hendershot, Clare J. #1	4774	14.7909	0.2518	7.9682
Hendershot, Clare J. #1	4775	36.4470	0.0326	1.7371
Hendershot, Clare J. #1	4776	37.3974	0.0205	1.5373
Hendershot, Clare J. #1	4777	35.3864	0.0498	2.6571

Core	Depth (ft)	Ca	Ti	Si
Hurt, Lloyd #1	7079	34.0336	0.0596	1.9401
Hurt, Lloyd #1	7080	34.2121	0.0784	2.5975
Hurt, Lloyd #1	7081	36.3231	0.0160	1.0102
Hurt, Lloyd #1	7083	35.7467	0.0328	1.0557
Hurt, Lloyd #1	7084	33.7946	0.0498	2.0615
Hurt, Lloyd #1	7085	33.4175	0.0737	2.6737
Hurt, Lloyd #1	7087	33.3772	0.0422	1.3752
Hurt, Lloyd #1	7088	34.0097	0.0600	2.2558
Hurt, Lloyd #1	7089	34.5352	0.0609	2.7274
Hurt, Lloyd #1	7091	34.4321	0.0430	2.0740
Hurt, Lloyd #1	7092	33.3525	0.0674	2.7273
Hurt, Lloyd #1	7093	33.5059	0.0537	3.0711
Hurt, Lloyd #1	7094	26.4270	0.0875	7.2757
Hurt, Lloyd #1	7095	33.1990	0.0388	1.5910
Hurt, Lloyd #1	7096	34.0872	0.0473	1.4806
Hurt, Lloyd #1	7097	35.5206	0.0425	1.6873
Hurt, Lloyd #1	7098	34.4244	0.0153	1.5151
Hurt, Lloyd #1	7099	33.5608	0.0638	2.5165
Hurt, Lloyd #1	7100	34.2005	0.0436	2.0491
Hurt, Lloyd #1	7101	33.5548	0.0539	1.6719
Hurt, Lloyd #1	7102	32.2479	0.1100	3.8749
Hurt, Lloyd #1	7103	33.6442	0.0628	3.2364
Hurt, Lloyd #1	7104	32.8946	0.0545	2.3001
Hurt, Lloyd #1	7105	34.0567	0.0637	2.7118
Hurt, Lloyd #1	7106	31.1094	0.1161	4.3859
Hurt, Lloyd #1	7107	34.0890	0.0488	1.7817
Hurt, Lloyd #1	7108	32.1366	0.1056	3.5045
Hurt, Lloyd #1	7110	32.5429	0.0964	3.8534
Hurt, Lloyd #1	7111	31.9093	0.1044	4.0640
Hurt, Lloyd #1	7112	33.8659	0.0845	2.9854
Hurt, Lloyd #1	7113	34.1008	0.0241	0.8962
Hurt, Lloyd #1	7115	34.5817	0.0535	1.2288
Hurt, Lloyd #1	7116	34.3487	0.0486	1.0867
Hurt, Lloyd #1	7117	34.6502	0.0431	1.2260
Hurt, Lloyd #1	7118	34.3499	0.0352	1.4247
Hurt, Lloyd #1	7119	34.9205	0.0447	2.0845
Hurt, Lloyd #1	7121	34.5817	0.0675	2.2239
Hurt, Lloyd #1	7122	34.7489	0.0607	1.8750
Hurt, Lloyd #1	7123	33.3637	0.0700	3.0576
Hurt, Lloyd #1	7124	35.0922	0.0402	2.0052
Hurt, Lloyd #1	7126	35.4075	0.0577	2.1465
Hurt, Lloyd #1	7127	29.4621	0.1292	5.9915
Hurt, Lloyd #1	7128	32.0185	0.0875	4.4814
Hurt, Lloyd #1	7129	31.7511	0.0777	4.3975
Hurt, Lloyd #1	7130	33.2654	0.0643	2.6507
Hurt, Lloyd #1	7132	31.9958	0.0954	4.2680
Hurt, Lloyd #1	7133	33.9847	0.0375	2.1550
Hurt, Lloyd #1	7135	35.0743	0.0286	1.5026
Hurt, Lloyd #1	7136	34.7315	0.0579	2.6159
Hurt, Lloyd #1	7138	29.5076	0.1390	5.7024
Hurt, Lloyd #1	7139	34.6253	0.0343	2.0859
Hurt, Lloyd #1	7140	33.8741	0.0604	2.1881
Hurt, Lloyd #1	7142	32.9169	0.0829	2.9221
Hurt, Lloyd #1	7143	34.9189	0.0547	2.1922
Hurt, Lloyd #1	7145	34.9381	0.0743	2.3553
Hurt, Lloyd #1	7146	34.0367	0.0566	1.7148

Hurt, Lloyd #1	7148	35.3833	0.0322	1.4109
Hurt, Lloyd #1	7149	35.4880	0.0308	1.4020
Hurt, Lloyd #1	7151	33.8108	0.0824	3.0263
Hurt, Lloyd #1	7152	34.2321	0.0493	2.1216
Hurt, Lloyd #1	7153	35.3254	0.0331	1.6545
Hurt, Lloyd #1	7155	34.9551	0.0241	1.0230
Hurt, Lloyd #1	7156	35.2887	0.0242	0.7930
Hurt, Lloyd #1	7158	35.4773	0.0166	1.2980
Hurt, Lloyd #1	7159	36.9265	0.0062	0.7523
Hurt, Lloyd #1	7160	36.1859	0.0402	1.0202
Hurt, Lloyd #1	7161	36.1336	0.0312	0.7772
Hurt, Lloyd #1	7162	28.7213	0.1338	5.8277
Hurt, Lloyd #1	7163	35.9854	0.0321	1.2326
Hurt, Lloyd #1	7164	35.2288	0.0288	1.2877
Hurt, Lloyd #1	7165	35.6450	0.0336	1.7201
Hurt, Lloyd #1	7166	35.0148	0.0593	2.3546
Hurt, Lloyd #1	7168	35.0207	0.0610	1.7650
Hurt, Lloyd #1	7169	35.6841	0.0315	1.1658
Hurt, Lloyd #1	7171	35.6731	0.0489	1.8931
Hurt, Lloyd #1	7172	33.7444	0.0963	3.0385
Hurt, Lloyd #1	7174	36.4285	0.0267	0.6913
Hurt, Lloyd #1	7175	35.7707	0.0197	0.7823
Hurt, Lloyd #1	7176	35.5595	0.0194	1.4040
Hurt, Lloyd #1	7178	36.0076	0.0222	1.0568
Hurt, Lloyd #1	7179	33.4310	0.1007	3.3188
Hurt, Lloyd #1	7181	34.6593	0.0574	2.1964
Hurt, Lloyd #1	7182	36.1812	0.0260	1.1281
Hurt, Lloyd #1	7184	34.9925	0.0527	2.3838
Hurt, Lloyd #1	7185	35.4507	0.0659	1.8222
Hurt, Lloyd #1	7187	36.1230	0.0225	0.7412
Hurt, Lloyd #1	7188	34.9882	0.0531	2.2180
Hurt, Lloyd #1	7189	35.1106	0.0524	1.9993
Hurt, Lloyd #1	7191	36.5669	0.0475	1.2258
Hurt, Lloyd #1	7192	33.3897	0.0657	2.8443
Hurt, Lloyd #1	7194	36.5154	0.0167	1.1695
Hurt, Lloyd #1	7195	36.4279	0.0182	0.8333
Hurt, Lloyd #1	7196	35.9436	0.0230	1.2375
Hurt, Lloyd #1	7197	35.1295	0.0231	1.0757
Hurt, Lloyd #1	7199	34.8140	0.0177	0.8152
Hurt, Lloyd #1	7200	36.1517	0.0175	1.1887
Hurt, Lloyd #1	7201	35.6574	0.0372	1.6328
Hurt, Lloyd #1	7202	36.3716	0.0101	0.7957
Hurt, Lloyd #1	7203	36.9378	0.0064	0.5248
Hurt, Lloyd #1	7205	34.6962	0.0522	1.8657
Hurt, Lloyd #1	7206	35.9459	0.0310	1.1309
Hurt, Lloyd #1	7208	35.7203	0.0050	1.1780
Hurt, Lloyd #1	7209	35.5832	0.0110	1.0047
Hurt, Lloyd #1	7211	35.5194	0.0378	1.4654
Hurt, Lloyd #1	7213	35.3201	0.0400	2.0710
Hurt, Lloyd #1	7214	34.6409	0.0614	2.9037
Hurt, Lloyd #1	7215	28.5228	0.1210	7.1774
Hurt, Lloyd #1	7216	35.4293	0.0079	1.7703
Hurt, Lloyd #1	7217	25.5581	0.0741	11.6083
Hurt, Lloyd #1	7219	25.7513	0.0799	11.3040
Hurt, Lloyd #1	7220	22.3456	0.1256	14.0013
Hurt, Lloyd #1	7222	24.3076	0.0947	11.7413
Hurt, Lloyd #1	7223	28.6943	0.0621	8.9033

Hurt, Lloyd #1	7225	23.7528	0.1159	12.3883
Hurt, Lloyd #1	7227	23.5314	0.1423	12.2955
Hurt, Lloyd #1	7228	27.2604	0.1133	8.4264
Hurt, Lloyd #1	7230	18.5343	0.1283	15.8508
Hurt, Lloyd #1	7231	21.9398	0.1220	11.9992
Hurt, Lloyd #1	7233	25.9321	0.1100	8.2589
Hurt, Lloyd #1	7234	29.7730	0.0975	7.4180
Hurt, Lloyd #1	7235	36.7610	0.0308	1.2363
Hurt, Lloyd #1	7236	25.4404	0.1464	9.0767
Hurt, Lloyd #1	7238	28.3389	0.1148	7.4733
Hurt, Lloyd #1	7239	29.4846	0.1079	6.8706
Hurt, Lloyd #1	7240	28.8464	0.0994	7.3986
Hurt, Lloyd #1	7241	22.2890	0.1579	11.4073
Hurt, Lloyd #1	7242	23.1118	0.1455	9.6129
Hurt, Lloyd #1	7244	23.2314	0.1611	10.1160
Hurt, Lloyd #1	7245	29.9516	0.0709	6.0266
Hurt, Lloyd #1	7247	25.8419	0.1360	8.9846
Hurt, Lloyd #1	7248	28.0351	0.1138	7.9215
Hurt, Lloyd #1	7250	27.4716	0.1238	8.2915
Hurt, Lloyd #1	7252	26.3740	0.1347	8.6901
Hurt, Lloyd #1	7253	29.9629	0.0868	6.9130
Hurt, Lloyd #1	7255	27.3123	0.1069	8.7815
Hurt, Lloyd #1	7256	24.4788	0.1479	10.3125
Hurt, Lloyd #1	7258	28.3046	0.1049	7.7733
Hurt, Lloyd #1	7259	5.4529	0.4495	16.5847
Hurt, Lloyd #1	7261	26.2352	0.1513	9.0225
Hurt, Lloyd #1	7262	26.0146	0.1571	9.1885
Hurt, Lloyd #1	7264	32.6082	0.0712	4.5388
Hurt, Lloyd #1	7265	33.3164	0.0529	3.9302
Hurt, Lloyd #1	7266	30.1831	0.1052	5.6703
Hurt, Lloyd #1	7268	32.0736	0.0822	5.4653
Hurt, Lloyd #1	7269	31.2440	0.0941	5.7609
Hurt, Lloyd #1	7271	29.1446	0.1209	6.7408
Hurt, Lloyd #1	7272	23.2672	0.1667	9.9754
Hurt, Lloyd #1	7273	23.0337	0.1706	9.4707
Hurt, Lloyd #1	7274	21.7085	0.1930	11.1609
Hurt, Lloyd #1	7275	32.7907	0.0748	4.4633
Hurt, Lloyd #1	7276	28.1763	0.1162	7.4500
Hurt, Lloyd #1	7277	25.2578	0.1468	9.3469
Hurt, Lloyd #1	7278	24.4910	0.1488	8.5478
Hurt, Lloyd #1	7279	31.9355	0.0898	5.0091
Hurt, Lloyd #1	7281	31.1655	0.0980	5.4577
Hurt, Lloyd #1	7282	33.8125	0.0758	2.4796
Hurt, Lloyd #1	7283	28.4012	0.1350	6.3670
Hurt, Lloyd #1	7285	32.8768	0.0672	3.7835
Hurt, Lloyd #1	7286	18.8916	0.2255	10.3810
Hurt, Lloyd #1	7287	33.5868	0.0120	4.3957
Hurt, Lloyd #1	7289	29.8165	0.0576	6.5356
Hurt, Lloyd #1	7290	25.2360	0.0807	10.6186
Hurt, Lloyd #1	7291	29.8248	0.1016	7.2393
Hurt, Lloyd #1	7293	32.0889	0.1358	5.2961
Hurt, Lloyd #1	7294	32.3752	0.0717	5.6422
Hurt, Lloyd #1	7295	31.1736	0.0894	6.2603
Hurt, Lloyd #1	7296	29.8883	0.0441	8.4617
Hurt, Lloyd #1	7298	33.8108	0.0318	3.2334
Hurt, Lloyd #1	7299	31.4240	0.1059	3.4259
Hurt, Lloyd #1	7300	22.5441	0.1476	10.6832

Hurt, Lloyd #1	7301	18.4536	0.1855	11.8222
Hurt, Lloyd #1	7302	26.5420	0.1295	8.8608
Hurt, Lloyd #1	7304	22.0066	0.1596	11.2749

Core	Depth (ft)	Ca	Ti	Si
Leppard, J.A. #1-H	13546	22.5586	0.1858	11.7822
Leppard, J.A. #1-H	13547	29.7459	0.0906	6.9053
Leppard, J.A. #1-H	13548	22.7631	0.1928	11.1769
Leppard, J.A. #1-H	13549	22.2733	0.1850	11.5199
Leppard, J.A. #1-H	13549	28.5052	0.1324	7.5160
Leppard, J.A. #1-H	13550	25.7466	0.1446	9.3537
Leppard, J.A. #1-H	13551	25.1279	0.1496	9.7191
Leppard, J.A. #1-H	13552	23.0175	0.1661	11.4818
Leppard, J.A. #1-H	13552	16.2571	0.2586	15.6851
Leppard, J.A. #1-H	13553	12.9735	0.2811	17.5341
Leppard, J.A. #1-H	13554	11.3748	0.3088	18.6984
Leppard, J.A. #1-H	13554	10.6295	0.2762	20.6595
Leppard, J.A. #1-H	13555	10.3534	0.2531	20.7466
Leppard, J.A. #1-H	13556	32.7750	0.0320	4.7486
Leppard, J.A. #1-H	13557	11.8679	0.2466	20.0446
Leppard, J.A. #1-H	13558	15.4869	0.1907	16.6291
Leppard, J.A. #1-H	13559	33.1873	0.0399	4.4983
Leppard, J.A. #1-H	13560	18.2188	0.1588	14.1640
Leppard, J.A. #1-H	13560	30.4720	0.0448	6.6380
Leppard, J.A. #1-H	13561	12.9856	0.2316	18.3714
Leppard, J.A. #1-H	13562	14.3481	0.2018	18.3390
Leppard, J.A. #1-H	13563	14.9734	0.2175	17.6496
Leppard, J.A. #1-H	13564	31.6084	0.0381	5.8348
Leppard, J.A. #1-H	13565	17.5409	0.1806	15.7709
Leppard, J.A. #1-H	13566	7.8836	0.3676	22.6039
Leppard, J.A. #1-H	13567	15.7560	0.2230	17.0480
Leppard, J.A. #1-H	13568	18.0303	0.1752	15.3382
Leppard, J.A. #1-H	13568	16.3234	0.2204	16.0390
Leppard, J.A. #1-H	13569	32.8984	0.0423	4.8247
Leppard, J.A. #1-H	13570	16.3458	0.2013	16.1024
Leppard, J.A. #1-H	13572	16.6600	0.2156	15.6497
Leppard, J.A. #1-H	13572	14.8682	0.2175	16.6311
Leppard, J.A. #1-H	13574	18.1328	0.1940	14.0858
Leppard, J.A. #1-H	13575	16.5007	0.2184	15.5080
Leppard, J.A. #1-H	13576	19.2578	0.1773	12.0477
Leppard, J.A. #1-H	13577	9.2080	0.3769	19.9667
Leppard, J.A. #1-H	13579	17.9009	0.1934	12.7366
Leppard, J.A. #1-H	13580	18.4994	0.1982	12.7805
Leppard, J.A. #1-H	13581	34.9966	0.0066	6.3384
Leppard, J.A. #1-H	13581	30.8796	0.0420	6.6165
Leppard, J.A. #1-H	13582	25.2805	0.1215	9.5441
Leppard, J.A. #1-H	13584	25.8400	0.1201	9.1010
Leppard, J.A. #1-H	13585	31.9922	0.0459	5.8837
Leppard, J.A. #1-H	13587	28.2189	0.0898	8.0432
Leppard, J.A. #1-H	13588	13.8301	0.2778	15.1151
Leppard, J.A. #1-H	13591	25.3934	0.1077	9.5874
Leppard, J.A. #1-H	13592	14.6981	0.2476	15.0715
Leppard, J.A. #1-H	13594	33.5438	0.0309	6.6380
Leppard, J.A. #1-H	13595	33.2328	0.0269	5.8013
Leppard, J.A. #1-H	13597	23.7326	0.0875	10.8320
Leppard, J.A. #1-H	13598	31.3483	0.0587	6.2687

Leppard, J.A. #1-H	13600	22.3483	0.1403	11.3073
Leppard, J.A. #1-H	13601	18.3568	0.2005	13.7367
Leppard, J.A. #1-H	13603	30.8354	0.0526	6.2168
Leppard, J.A. #1-H	13604	25.2808	0.1138	9.5322
Leppard, J.A. #1-H	13605	22.5406	0.1627	10.7726
Leppard, J.A. #1-H	13606	20.6918	0.1670	11.3828
Leppard, J.A. #1-H	13608	19.2120	0.2002	12.7221
Leppard, J.A. #1-H	13609	18.9034	0.1994	12.8040
Leppard, J.A. #1-H	13611	29.2780	0.0956	7.5418
Leppard, J.A. #1-H	13612	31.9732	0.0408	6.2653
Leppard, J.A. #1-H	13614	30.9203	0.0478	6.8129
Leppard, J.A. #1-H	13615	23.7025	0.1534	10.1433
Leppard, J.A. #1-H	13616	23.4581	0.1481	10.1286
Leppard, J.A. #1-H	13617	20.1731	0.1919	11.8099
Leppard, J.A. #1-H	13619	29.3773	0.0918	7.2418
Leppard, J.A. #1-H	13620	25.8166	0.1053	9.2758
Leppard, J.A. #1-H	13621	22.8324	0.1459	11.0064
Leppard, J.A. #1-H	13622	19.7614	0.1958	13.0275
Leppard, J.A. #1-H	13624	22.8761	0.1488	10.9982
Leppard, J.A. #1-H	13624	25.1832	0.1482	9.6709
Leppard, J.A. #1-H	13625	27.4029	0.1023	8.3325
Leppard, J.A. #1-H	13626	23.2275	0.1588	11.0309
Leppard, J.A. #1-H	13627	23.5173	0.1441	10.5020
Leppard, J.A. #1-H	13629	23.1366	0.1424	10.9916
Leppard, J.A. #1-H	13630	18.5763	0.1811	14.4587
Leppard, J.A. #1-H	13632	14.3100	0.2602	15.6799
Leppard, J.A. #1-H	13633	27.6855	0.0222	8.0843
Leppard, J.A. #1-H	13635	21.6029	0.1463	11.6778
Leppard, J.A. #1-H	13636	22.9522	0.1577	11.3878
Leppard, J.A. #1-H	13638	19.3683	0.1936	13.0523
Leppard, J.A. #1-H	13639	29.4162	0.0774	7.2670
Leppard, J.A. #1-H	13641	22.6181	0.1493	11.4653
Leppard, J.A. #1-H	13642	22.3986	0.1492	11.3417
Leppard, J.A. #1-H	13644	19.9741	0.1891	13.2878
Leppard, J.A. #1-H	13645	25.6201	0.1200	9.7058
Leppard, J.A. #1-H	13646	26.4979	0.0911	9.0351
Leppard, J.A. #1-H	13647	24.5348	0.1293	10.4747
Leppard, J.A. #1-H	13649	24.9159	0.1382	10.2424
Leppard, J.A. #1-H	13650	17.1740	0.2157	15.5589
Leppard, J.A. #1-H	13651	15.3797	0.2694	15.9012
Leppard, J.A. #1-H	13652	21.8564	0.1601	12.9332
Leppard, J.A. #1-H	13654	18.5853	0.1836	13.6955
Leppard, J.A. #1-H	13655	23.9362	0.1406	10.9439
Leppard, J.A. #1-H	13657	19.7498	0.1775	13.6415
Leppard, J.A. #1-H	13658	17.2751	0.2207	15.9158
Leppard, J.A. #1-H	13659	16.9207	0.2018	15.1709
Leppard, J.A. #1-H	13660	20.0133	0.2101	12.8399
Leppard, J.A. #1-H	13662	22.5610	0.1673	10.9859
Leppard, J.A. #1-H	13663	24.8692	0.1542	9.9606
Leppard, J.A. #1-H	13665	21.9617	0.1930	11.5254
Leppard, J.A. #1-H	13666	24.7027	0.1268	9.8864
Leppard, J.A. #1-H	13667	19.0138	0.2218	13.7056
Leppard, J.A. #1-H	13668	17.8061	0.2567	14.4278
Leppard, J.A. #1-H	13670	24.1356	0.1731	10.0415
Leppard, J.A. #1-H	13671	34.4052	0.0000	7.8413
Leppard, J.A. #1-H	13673	34.4841	0.0000	8.0107
Leppard, J.A. #1-H	13677	34.8536	0.0011	7.8442

Appendix D: Stable Isotope Data

Blumberg #1-B					
Core	Depth (ft)	Formation	$\delta^{13}C$ PDB	$\delta^{18}O$ PDB	%TIC
Blumberg #1-B	4138	Austin	1.16	-3.55	10.419
Blumberg #1-B	4139	Austin	1.01	-3.25	10.945
Blumberg #1-B	4140	Austin	1.17	-3.43	10.073
Blumberg #1-B	4141	Austin	1.39	-3.02	9.819
Blumberg #1-B	4142	Austin	1.25	-3.37	10.263
Blumberg #1-B	4143	Austin	1.12	-3.34	9.354
Blumberg #1-B	4144	Austin	0.78	-3.50	8.873
Blumberg #1-B	4145	Austin	0.93	-3.51	10.693
Blumberg #1-B	4146	Austin	1.22	-3.22	9.479
Blumberg #1-B	4147	Austin	1.17	-3.39	8.007
Blumberg #1-B	4148	Austin	1.45	-3.35	8.628
Blumberg #1-B	4149	Austin	1.15	-3.52	9.066
Blumberg #1-B	4150	Austin	1.29	-4.09	10.725
Blumberg #1-B	4151	Austin	0.90	-3.73	9.662
Blumberg #1-B	4152	Austin	1.10	-3.76	10.775
Blumberg #1-B	4153	Austin	0.65	-3.66	9.738
Blumberg #1-B	4154	Austin	0.63	-3.28	10.497
Blumberg #1-B	4155	Austin	0.33	-3.50	10.489
Blumberg #1-B	4156	Austin	0.48	-3.57	10.322
Blumberg #1-B	4157	Austin	0.22	-3.70	10.937
Blumberg #1-B	4158	Austin	0.58	-3.47	9.971
Blumberg #1-B	4159	Austin	0.18	-4.12	10.719
Blumberg #1-B	4160	Austin	0.49	-3.71	10.793
Blumberg #1-B	4161	Austin	0.23	-3.80	10.608
Blumberg #1-B	4162	Austin	0.77	-3.61	11.231
Blumberg #1-B	4163	Austin	0.53	-3.88	9.895
Blumberg #1-B	4164	Austin	1.11	-4.07	9.473
Blumberg #1-B	4165	Austin	0.74	-3.60	9.904
Blumberg #1-B	4166	Austin	1.15	-3.19	8.090
Blumberg #1-B	4167	Austin	0.49	-3.91	9.135
Blumberg #1-B	4168	Austin	0.72	-3.66	10.100
Blumberg #1-B	4169	Austin	0.62	-3.76	9.198
Blumberg #1-B	4170	Austin	0.36	-4.06	9.288
Blumberg #1-B	4171	Austin	0.59	-3.89	10.070
Blumberg #1-B	4172	Austin	0.44	-3.85	9.926
Blumberg #1-B	4173	Austin	0.55	-3.90	10.276
Blumberg #1-B	4174	Austin	0.31	-3.67	10.223
Blumberg #1-B	4175	Austin	0.74	-3.91	9.935
Blumberg #1-B	4176	Eagle Ford	0.85	-4.56	5.499
Blumberg #1-B	4177	Eagle Ford	0.85	-4.22	4.611
Blumberg #1-B	4179	Eagle Ford	0.26	-4.00	8.836
Blumberg #1-B	4180	Eagle Ford	-0.04	-4.62	3.242
Blumberg #1-B	4181	Eagle Ford	0.13	-4.60	8.142
Blumberg #1-B	4182	Eagle Ford	0.75	-5.33	6.250
Blumberg #1-B	4183	Eagle Ford	0.48	-5.08	6.496
Blumberg #1-B	4184	Eagle Ford	0.39	-4.69	7.457
Blumberg #1-B	4185	Eagle Ford	0.68	-5.67	5.800
Blumberg #1-B	4186	Eagle Ford	1.02	-4.90	7.114

Blumberg #1-B	4187	Eagle Ford	0.98	-5.29	6.288
Blumberg #1-B	4188	Eagle Ford	0.75	-4.98	7.592
Blumberg #1-B	4189	Eagle Ford	1.19	-5.46	6.232
Blumberg #1-B	4190	Eagle Ford	1.24	-5.21	5.856
Blumberg #1-B	4191	Eagle Ford	1.12	-4.70	5.593
Blumberg #1-B	4192	Eagle Ford	1.24	-5.05	5.882
Blumberg #1-B	4193	Eagle Ford	1.10	-4.74	6.183
Blumberg #1-B	4194	Eagle Ford	0.91	-4.67	7.270
Blumberg #1-B	4195	Eagle Ford	0.93	-4.54	7.603
Blumberg #1-B	4196	Eagle Ford	0.74	-4.76	7.701
Blumberg #1-B	4197	Eagle Ford	0.42	-4.55	8.641
Blumberg #1-B	4198	Eagle Ford	0.40	-5.00	7.807
Blumberg #1-B	4199	Eagle Ford	1.10	-5.04	7.346
Blumberg #1-B	4200	Eagle Ford	0.63	-5.22	7.596
Blumberg #1-B	4201	Eagle Ford	1.23	-4.75	8.574
Blumberg #1-B	4202	Eagle Ford	0.75	-4.83	7.960
Blumberg #1-B	4202.1	Eagle Ford Concretion	-1.65	-3.72	10.666
Blumberg #1-B	4203	Eagle Ford	1.14	-4.95	7.541
Blumberg #1-B	4209	Eagle Ford	0.89	-4.53	5.690
Blumberg #1-B	4210	Eagle Ford	1.02	-5.07	7.872
Blumberg #1-B	4211	Eagle Ford	1.22	-5.34	5.384
Blumberg #1-B	4212	Eagle Ford	0.48	-4.92	5.858
Blumberg #1-B	4212.3	Eagle Ford Concretion	-1.44	-3.73	9.632
Blumberg #1-B	4213	Eagle Ford	0.40	-4.88	4.824
Blumberg #1-B	4214	Eagle Ford	0.31	-4.91	3.643
Blumberg #1-B	4215	Eagle Ford	-0.14	-3.90	6.320
Blumberg #1-B	4216	Eagle Ford	0.69	-4.48	4.953
Blumberg #1-B	4217	Eagle Ford	0.13	-5.14	4.985
Blumberg #1-B	4218	Eagle Ford	0.53	-5.03	6.104
Blumberg #1-B	4219	Eagle Ford	0.57	-5.23	5.056
Blumberg #1-B	4220	Eagle Ford	1.02	-4.89	4.688
Blumberg #1-B	4221	Eagle Ford	0.70	-4.30	7.041
Blumberg #1-B	4222	Eagle Ford	1.36	-5.42	1.461
Blumberg #1-B	4222.4	Eagle Ford Concretion	-0.90	-3.13	8.259
Blumberg #1-B	4223	Eagle Ford	1.01	-4.66	4.683
Blumberg #1-B	4224	Eagle Ford	0.14	-2.76	9.186
Blumberg #1-B	4225	Buda	1.06	-2.54	11.251
Blumberg #1-B	4226	Buda	1.10	-3.27	11.271
Blumberg #1-B	4227	Buda	1.52	-2.76	11.287
Blumberg #1-B	4228	Buda	1.52	-2.90	11.286
Blumberg #1-B	4229	Buda	1.66	-2.88	11.192

Hendershot #1					
Core	Depth (ft)	Formation	$\delta^{13}C$ PDB	$\delta^{18}O$ PDB	%TIC
Hendershot #1	4711	Austin	1.66	-2.97	9.9158
Hendershot #1	4712	Austin	1.63	-2.99	9.3924
Hendershot #1	4713	Austin	1.65	-2.91	10.2599
Hendershot #1	4714	Austin	1.72	-2.81	9.1933
Hendershot #1	4715	Austin	1.62	-3.13	10.0319
Hendershot #1	4716	Austin	1.65	-3.00	9.8428

Hendershot #1	4717	Austin	1.61	-2.95	9.5576
Hendershot #1	4718	Austin	1.65	-3.09	8.9957
Hendershot #1	4719	Austin	1.55	-3.35	9.3168
Hendershot #1	4720	Austin	1.50	-3.06	9.4195
Hendershot #1	4721	Austin	1.46	-3.41	10.2885
Hendershot #1	4722	Austin	1.44	-3.45	9.8676
Hendershot #1	4723	Austin	0.99	-3.42	11.1137
Hendershot #1	4724	Austin	1.35	-3.70	10.1767
Hendershot #1	4725	Austin	1.34	-3.50	9.2696
Hendershot #1	4726	Austin	1.04	-3.40	10.9033
Hendershot #1	4727	Austin	1.12	-3.44	10.7988
Hendershot #1	4728	Austin	1.14	-3.47	10.4602
Hendershot #1	4729	Austin	1.13	-3.71	9.7208
Hendershot #1	4730	Austin	1.08	-3.37	9.6449
Hendershot #1	4731	Austin	1.08	-3.35	9.7081
Hendershot #1	4732	Austin	1.09	-3.78	10.6693
Hendershot #1	4733	Austin	1.08	-3.39	10.1174
Hendershot #1	4734	Austin	1.33	-3.32	9.8604
Hendershot #1	4735	Austin	1.24	-3.78	9.9005
Hendershot #1	4736	Eagle Ford	1.19	-4.88	7.5439
Hendershot #1	4737	Eagle Ford	1.17	-4.77	7.1702
Hendershot #1	4738	Eagle Ford	0.58	-3.72	10.3810
Hendershot #1	4739	Eagle Ford	1.09	-4.95	7.6512
Hendershot #1	4740	Eagle Ford	0.30	-4.15	9.8036
Hendershot #1	4741	Eagle Ford	0.10	-4.09	6.9063
Hendershot #1	4742	Eagle Ford	0.25	-4.56	4.7623
Hendershot #1	4743	Eagle Ford	0.41	-4.62	4.5884
Hendershot #1	4744	Eagle Ford	0.37	-4.16	5.9672
Hendershot #1	4745	Eagle Ford	0.28	-4.46	5.1209
Hendershot #1	4746	Eagle Ford	-0.14	-4.09	6.2592
Hendershot #1	4747	Eagle Ford	0.72	-4.71	7.3966
Hendershot #1	4748	Eagle Ford	0.99	-4.70	7.8664
Hendershot #1	4749	Eagle Ford	1.37	-4.83	6.7181
Hendershot #1	4750	Eagle Ford	1.00	-4.77	6.8485
Hendershot #1	4751	Eagle Ford	0.26	-4.25	8.4804
Hendershot #1	4752	Eagle Ford	0.71	-5.27	7.8293
Hendershot #1	4753	Eagle Ford	1.77	-5.65	4.6651
Hendershot #1	4754	Eagle Ford	1.18	-5.62	8.4825
Hendershot #1	4755	Eagle Ford	0.93	-5.28	7.4120
Hendershot #1	4756	Eagle Ford	0.39	-5.04	7.1726
Hendershot #1	4757	Eagle Ford	0.46	-4.95	6.6370
Hendershot #1	4757.7	Eagle Ford Concretion	-2.08	-3.16	9.9687
Hendershot #1	4758	Eagle Ford	1.19	-5.40	6.3617
Hendershot #1	4759	Eagle Ford	0.11	-3.97	6.1332
Hendershot #1	4760	Eagle Ford	0.77	-5.31	6.1334
Hendershot #1	4761	Eagle Ford	0.90	-5.20	6.2064
Hendershot #1	4762	Eagle Ford	0.46	-5.29	6.0564
Hendershot #1	4763	Eagle Ford	1.05	-5.47	5.9441
Hendershot #1	4764	Eagle Ford	0.58	-5.53	3.7748
Hendershot #1	4764.2	Eagle Ford Concretion	-1.99	-3.58	10.3588
Hendershot #1	4765	Eagle Ford	0.57	-5.15	6.0720

Hendershot #1	4765.5	Eagle Ford Concretion	-2.87	-3.35	10.1911
Hendershot #1	4766	Eagle Ford	-0.14	-4.81	6.0163
Hendershot #1	4767	Eagle Ford	0.54	-5.66	5.6415
Hendershot #1	4767.1	Eagle Ford Concretion	-1.07	-3.61	9.6848
Hendershot #1	4768	Eagle Ford	-0.45	-5.06	8.1686
Hendershot #1	4769	Eagle Ford	1.07	-6.25	3.2480
Hendershot #1	4770	Eagle Ford	0.80	-5.52	4.6807
Hendershot #1	4771	Eagle Ford	0.12	-4.60	6.9265
Hendershot #1	4771.9	Eagle Ford Concretion	-2.64	-2.60	11.1380
Hendershot #1	4772	Eagle Ford	0.88	-3.99	0.4745
Hendershot #1	4773	Eagle Ford	0.94	-4.71	0.0455
Hendershot #1	4774	Buda	0.68	-2.84	11.1751
Hendershot #1	4775	Buda	1.10	-3.32	11.1946
Hendershot #1	4776	Buda	1.31	-2.95	11.3737
Hendershot #1	4777	Buda	1.46	-2.96	11.1166
Hendershot #1	4778	Buda	1.50	-2.82	11.4183
Hendershot #1	4779	Buda	1.47	-3.48	11.5467
Hendershot #1	4780	Buda	1.45	-3.35	11.4631
Hendershot #1	4781	Buda	1.52	-3.09	11.2993
Hendershot #1	4782	Buda	1.56	-3.80	11.2163
Hendershot #1	4783	Buda	1.65	-3.05	11.1338
Hendershot #1	4784	Buda	1.72	-3.41	11.3618
Hendershot #1	4785	Buda	1.52	-2.79	11.1436
Hendershot #1	4786	Buda	1.59	-3.05	10.9258
Hendershot #1	4787	Buda	1.66	-3.29	10.9217
Hendershot #1	4788	Buda	1.53	-3.31	10.8424
Hendershot #1	4789	Buda	1.62	-3.36	9.8839

Mathews #1-1					
Core	**Depth (ft)**	**Formation**	**$\delta^{13}C$ PDB**	**$\delta^{18}O$ PDB**	**%TIC**
Mathews #1-1	4618	Eagle Ford	1.52	-6.50	3.805
Mathews #1-1	4619	Eagle Ford	0.97	-6.92	6.993
Mathews #1-1	4620	Eagle Ford	1.29	-6.86	6.210
Mathews #1-1	4621	Eagle Ford	1.14	-7.01	6.898
Mathews #1-1	4622	Eagle Ford	1.18	-7.12	7.249
Mathews #1-1	4623	Eagle Ford	1.50	-7.34	7.142
Mathews #1-1	4624	Eagle Ford	1.18	-6.94	8.122
Mathews #1-1	4625	Eagle Ford	1.12	-6.96	6.755
Mathews #1-1	4625.5	Eagle Ford Concretion	2.21	-6.39	10.589
Mathews #1-1	4626	Eagle Ford	1.51	-7.17	6.328
Mathews #1-1	4627	Eagle Ford	1.05	-7.16	7.587
Mathews #1-1	4628	Eagle Ford	1.14	-7.18	8.184
Mathews #1-1	4629	Eagle Ford	1.22	-7.54	7.891
Mathews #1-1	4630	Eagle Ford	1.63	-6.89	6.162
Mathews #1-1	4631	Eagle Ford	1.44	-7.50	8.101
Mathews #1-1	4632	Eagle Ford	1.46	-6.89	6.766
Mathews #1-1	4633	Eagle Ford	1.30	-7.10	5.647
Mathews #1-1	4634	Eagle Ford	0.69	-7.16	7.748
Mathews #1-1	4635	Eagle Ford	1.02	-7.14	7.281
Mathews #1-1	4636	Eagle Ford	1.02	-6.94	6.842

Mathews #1-1	4637	Eagle Ford	0.46	-7.28	7.389
Mathews #1-1	4637.3	Eagle Ford Concretion	1.86	-5.41	11.205
Mathews #1-1	4638	Eagle Ford	0.35	-7.08	7.114
Mathews #1-1	4639	Eagle Ford	0.51	-6.97	8.958
Mathews #1-1	4640	Eagle Ford	1.04	-7.72	7.138
Mathews #1-1	4641	Eagle Ford	1.18	-7.86	8.245
Mathews #1-1	4642	Eagle Ford	1.30	-7.52	7.449
Mathews #1-1	4643	Eagle Ford	1.47	-7.50	7.022
Mathews #1-1	4644	Eagle Ford	1.24	-7.66	6.823
Mathews #1-1	4645	Eagle Ford	1.37	-7.38	6.662
Mathews #1-1	4646	Eagle Ford	1.15	-7.39	7.254
Mathews #1-1	4647	Eagle Ford	1.54	-7.67	6.222
Mathews #1-1	4648	Eagle Ford	1.29	-7.25	6.082
Mathews #1-1	4649	Eagle Ford	1.23	-7.30	6.412
Mathews #1-1	4650	Eagle Ford	1.21	-7.53	6.044
Mathews #1-1	4651	Eagle Ford	0.79	-7.68	7.057
Mathews #1-1	4651.2	Eagle Ford Concretion	2.19	-4.69	10.860
Mathews #1-1	4652	Eagle Ford	-0.86	-7.05	6.723
Mathews #1-1	4653	Eagle Ford	-0.73	-6.55	1.373
Mathews #1-1	4654	Eagle Ford	1.15	-7.58	5.350
Mathews #1-1	4655	Eagle Ford	1.32	-7.22	7.000
Mathews #1-1	4656	Eagle Ford	1.21	-7.64	6.736
Mathews #1-1	4657	Eagle Ford	1.15	-7.21	6.806
Mathews #1-1	4658	Eagle Ford	1.18	-7.30	5.201
Mathews #1-1	4659	Eagle Ford	1.31	-7.57	5.608
Mathews #1-1	4660	Eagle Ford	0.19	-7.31	0.296
Mathews #1-1	4661	Eagle Ford	1.07	-7.38	6.233
Mathews #1-1	4662	Eagle Ford	1.27	-7.36	6.016
Mathews #1-1	4663	Eagle Ford	1.14	-7.49	5.590
Mathews #1-1	4664	Eagle Ford	1.20	-7.27	5.919
Mathews #1-1	4665	Eagle Ford	0.33	-6.73	2.157
Mathews #1-1	4666	Eagle Ford	0.76	-7.52	5.688
Mathews #1-1	4667	Eagle Ford	0.56	-7.24	4.501
Mathews #1-1	4668	Eagle Ford	0.50	-7.46	4.722
Mathews #1-1	4669	Eagle Ford	-0.18	-6.63	4.445
Mathews #1-1	4670	Eagle Ford Concretion	2.79	-6.38	9.309
Mathews #1-1	4671	Eagle Ford	-1.59	-7.22	6.204
Mathews #1-1	4672	Eagle Ford	-1.23	-7.22	5.341
Mathews #1-1	4673	Eagle Ford	-1.06	-7.56	6.497
Mathews #1-1	4674	Eagle Ford	-0.83	-7.26	5.139
Mathews #1-1	4674.7	Eagle Ford Concretion	1.78	-6.67	9.845
Mathews #1-1	4675	Eagle Ford	-0.88	-7.40	5.273
Mathews #1-1	4676	Eagle Ford	-0.55	-7.19	5.850
Mathews #1-1	4677	Eagle Ford	-0.67	-7.27	5.695
Mathews #1-1	4678	Eagle Ford	-0.42	-7.23	4.597
Mathews #1-1	4679	Eagle Ford	-0.97	-7.48	5.659
Mathews #1-1	4680	Eagle Ford	0.24	-7.76	5.662
Mathews #1-1	4681	Eagle Ford	-0.51	-7.55	5.972
Mathews #1-1	4682	Eagle Ford	0.56	-7.73	4.897
Mathews #1-1	4683	Eagle Ford	0.44	-7.57	5.617
Mathews #1-1	4684	Eagle Ford	-2.50	-6.79	5.736
Mathews #1-1	4685	Eagle Ford	-0.21	-7.44	5.307

Orts #2					
Core	Depth (ft)	Formation	$\delta^{13}C$ PDB	$\delta^{18}O$ PDB	%TIC
Orts #2	7681	Austin	0.89	-4.62	10.2351
Orts #2	7682	Austin	0.58	-4.69	10.4740
Orts #2	7683	Austin	0.31	-4.44	10.8770
Orts #2	7684	Eagle Ford	1.06	-5.37	8.0011
Orts #2	7685	Eagle Ford	0.65	-5.37	10.6365
Orts #2	7686	Eagle Ford	0.80	-5.41	8.3841
Orts #2	7687	Eagle Ford	0.77	-5.29	7.2950
Orts #2	7688	Eagle Ford	0.95	-3.37	11.2803
Orts #2	7689	Eagle Ford	0.69	-5.22	7.4835
Orts #2	7690	Eagle Ford	0.32	-4.47	7.2689
Orts #2	7691	Eagle Ford	0.26	-4.30	7.0507
Orts #2	7692	Eagle Ford	-0.28	-4.65	7.7802
Orts #2	7693	Eagle Ford	0.28	-5.35	7.3929
Orts #2	7694	Eagle Ford	-0.64	-4.53	9.5670
Orts #2	7695	Eagle Ford	-1.34	-4.75	7.3706
Orts #2	7696	Eagle Ford	-0.49	-4.74	6.5550
Orts #2	7697	Eagle Ford	0.85	-3.90	1.7553
Orts #2	7698	Eagle Ford	-0.06	-4.83	5.9202
Orts #2	7699	Eagle Ford	-0.72	-5.61	8.9175
Orts #2	7700	Eagle Ford	-0.06	-5.69	7.2357
Orts #2	7701	Eagle Ford	-0.24	-5.75	7.7783
Orts #2	7702	Eagle Ford	-0.21	-5.83	7.8507
Orts #2	7703	Eagle Ford	0.11	-5.74	6.8720
Orts #2	7704	Eagle Ford	0.11	-5.62	5.4590
Orts #2	7705	Eagle Ford	0.52	-5.89	6.1729
Orts #2	7706	Eagle Ford	0.58	-5.65	5.8939
Orts #2	7707	Eagle Ford	0.10	-6.15	8.4479
Orts #2	7708	Eagle Ford	-0.30	-6.23	8.1525
Orts #2	7709	Eagle Ford	0.18	-6.05	6.9007
Orts #2	7710	Eagle Ford	0.06	-6.22	8.3150
Orts #2	7711	Eagle Ford	-0.03	-5.92	6.2262
Orts #2	7712	Eagle Ford	0.19	-6.40	8.1281
Orts #2	7713	Eagle Ford	-0.98	-5.86	8.7017
Orts #2	7714	Eagle Ford	-0.14	-6.08	6.8860
Orts #2	7715	Eagle Ford	0.23	-6.47	7.8655
Orts #2	7716	Eagle Ford	0.27	-6.76	6.2005
Orts #2	7717	Eagle Ford	0.12	-6.48	6.6966
Orts #2	7718	Eagle Ford	-0.36	-5.95	5.6859
Orts #2	7719	Eagle Ford	-0.07	-6.10	7.3312
Orts #2	7720	Eagle Ford	0.23	-6.24	6.1880
Orts #2	7721	Eagle Ford	-0.28	-6.18	5.8130
Orts #2	7722	Eagle Ford	-0.13	-6.36	6.3102
Orts #2	7723	Eagle Ford	-0.21	-5.41	4.6451
Orts #2	7724	Eagle Ford	-0.28	-5.64	5.2765
Orts #2	7724.7	Eagle Ford Concretion	-3.77	-3.94	11.1959
Orts #2	7725	Eagle Ford	0.09	-5.54	5.1705
Orts #2	7726	Eagle Ford	-0.29	-6.11	6.9781
Orts #2	7727	Eagle Ford	-0.06	-6.05	6.1525
Orts #2	7728	Eagle Ford	-0.76	-6.01	7.3233
Orts #2	7729	Eagle Ford	0.14	-6.28	6.0662

Orts #2	7730	Eagle Ford	-0.39	-5.94	6.7448
Orts #2	7731	Eagle Ford	-0.26	-5.85	6.7251
Orts #2	7732	Eagle Ford	0.25	-6.12	5.5893
Orts #2	7733	Eagle Ford	0.12	-6.20	6.2660
Orts #2	7733.8	Eagle Ford Concretion	-0.09	-4.41	10.7887
Orts #2	7734	Eagle Ford	-0.85	-5.86	7.5464
Orts #2	7735	Eagle Ford	-0.84	-5.82	7.5349
Orts #2	7735.2	Eagle Ford Concretion	0.06	-4.66	10.8428
Orts #2	7736	Eagle Ford	0.11	-6.08	5.9725
Orts #2	7737	Eagle Ford	0.17	-5.85	5.9739
Orts #2	7738	Eagle Ford	-0.10	-6.34	7.2405
Orts #2	7739	Eagle Ford	0.61	-6.44	6.0739
Orts #2	7740	Eagle Ford	0.00	-6.57	8.5984
Orts #2	7741	Eagle Ford	-0.51	-5.97	7.5939
Orts #2	7742	Eagle Ford	-0.45	-6.26	5.1662
Orts #2	7743	Eagle Ford	0.01	-6.02	6.0955
Orts #2	7744	Eagle Ford	0.46	-6.18	5.6324
Orts #2	7745	Eagle Ford	0.39	-6.01	5.7148
Orts #2	7746	Eagle Ford	0.13	-6.00	6.7584
Orts #2	7747	Eagle Ford	0.19	-6.18	7.7170
Orts #2	7748	Eagle Ford	0.26	-5.39	1.0878
Orts #2	7749	Eagle Ford	-0.28	-5.95	1.1328
Orts #2	7750	Eagle Ford	0.60	-5.48	0.3410
Orts #2	7751	Eagle Ford	-0.14	-5.30	1.9186
Orts #2	7752	Eagle Ford	0.10	-6.23	0.9462
Orts #2	7753	Eagle Ford	-0.25	-8.54	0.1302
Orts #2	7754	Eagle Ford	-0.32	-7.68	0.4731
Orts #2	7755	Eagle Ford	0.34	-6.02	0.4091
Orts #2	7756	Eagle Ford	0.18	-5.19	2.2190
Orts #2	7757	Eagle Ford	0.41	-4.67	3.8872
Orts #2	7758	Buda	-0.14	-2.89	11.2526
Orts #2	7759	Buda	0.39	-4.23	11.2504
Orts #2	7760	Buda	0.65	-3.54	11.2086
Orts #2	7761	Buda	0.66	-3.65	11.2853
Orts #2	7762	Buda	1.19	-4.22	10.9304
Orts #2	7763	Buda	1.03	-3.64	11.0591
Orts #2	7764	Buda	0.92	-3.14	10.9818
Orts #2	7765	Buda	1.03	-3.71	8.7019
Orts #2	7766	Buda	0.93	-3.58	11.3345
Orts #2	7767	Buda	1.00	-3.20	10.2801
Orts #2	7768	Buda	0.90	-2.92	11.0539
Orts #2	7769	Buda	-0.17	-3.96	11.2901
Orts #2	7770	Buda	1.50	-3.29	10.4180
Orts #2	7771	Buda	1.44	-3.04	10.7784
Orts #2	7772	Buda	1.30	-3.54	10.7938
Orts #2	7773	Buda	1.48	-3.42	9.2500
Orts #2	7774	Buda	1.06	-3.48	10.4777
Orts #2	7775	Buda	1.12	-3.61	11.0653
Orts #2	7776	Buda	1.46	-3.09	9.9610
Orts #2	7777	Buda	1.45	-3.06	10.3568
Orts #2	7778	Buda	1.76	-2.48	8.7690
Orts #2	7779	Buda	1.70	-2.73	9.0210

Orts #2	7780	Buda	1.82	-2.57	7.2393
Orts #2	7781	Buda	2.01	-2.20	8.0001
Orts #2	7782	Buda	1.62	-2.99	11.4554
Orts #2	7783	Buda	1.93	-2.48	6.8577
Orts #2	7784	Buda	1.40	-3.54	10.4077
Orts #2	7785	Buda	2.37	-2.20	8.3451
Orts #2	7786	Buda	2.33	-2.27	8.1109
Orts #2	7787	Buda	1.93	-3.05	10.5494
Orts #2	7788	Buda	1.63	-3.41	9.7275

Shanklin #1-A					
Core	Depth (ft)	Formation	$\delta^{13}C$ PDB	$\delta^{18}O$ PDB	%TIC
Shanklin #1-A	2102	Austin	1.44	-2.59	8.397
Shanklin #1-A	2103	Austin	1.22	-3.13	9.650
Shanklin #1-A	2104	Austin	1.45	-2.59	8.833
Shanklin #1-A	2105	Austin	1.37	-2.71	8.955
Shanklin #1-A	2106	Austin	1.25	-3.34	9.334
Shanklin #1-A	2107	Austin	1.31	-3.38	10.027
Shanklin #1-A	2108	Austin	1.35	-3.07	9.938
Shanklin #1-A	2109	Austin	1.28	-3.62	9.706
Shanklin #1-A	2110	Eagle Ford	1.43	-3.19	7.975
Shanklin #1-A	2111	Eagle Ford	1.41	-3.78	8.283
Shanklin #1-A	2112	Eagle Ford	1.24	-3.61	10.159
Shanklin #1-A	2113	Eagle Ford	1.22	-4.28	9.733
Shanklin #1-A	2114	Eagle Ford	0.06	-3.24	9.618
Shanklin #1-A	2115	Eagle Ford	0.88	-3.60	5.637
Shanklin #1-A	2116	Eagle Ford	0.61	-3.64	6.225
Shanklin #1-A	2117	Eagle Ford	0.69	-3.73	9.134
Shanklin #1-A	2118	Eagle Ford	1.26	-4.71	9.359
Shanklin #1-A	2119	Eagle Ford	1.47	-4.58	8.224
Shanklin #1-A	2120	Eagle Ford	1.59	-4.68	7.176
Shanklin #1-A	2121	Eagle Ford	1.57	-4.79	6.419
Shanklin #1-A	2122	Eagle Ford	1.42	-4.79	7.073
Shanklin #1-A	2123	Eagle Ford	1.41	-4.78	8.537
Shanklin #1-A	2124	Eagle Ford	1.56	-5.14	8.390
Shanklin #1-A	2125	Eagle Ford	1.67	-4.68	5.765
Shanklin #1-A	2126	Eagle Ford	1.42	-4.70	7.079
Shanklin #1-A	2127	Eagle Ford	1.33	-4.69	7.936
Shanklin #1-A	2128	Eagle Ford	1.46	-5.02	7.228
Shanklin #1-A	2129	Eagle Ford	1.46	-4.99	7.011
Shanklin #1-A	2129.3	Eagle Ford Concretion	-0.58	-3.23	10.706
Shanklin #1-A	2130	Eagle Ford	1.43	-5.15	6.973
Shanklin #1-A	2130.4	Eagle Ford Concretion	-0.86	-2.97	10.732
Shanklin #1-A	2131	Eagle Ford	1.37	-5.12	7.608
Shanklin #1-A	2132	Eagle Ford	1.14	-5.07	7.123
Shanklin #1-A	2133	Eagle Ford	1.61	-4.93	7.991
Shanklin #1-A	2134	Eagle Ford	1.32	-4.97	6.212
Shanklin #1-A	2135	Eagle Ford	-1.46	-6.41	0.280
Shanklin #1-A	2136	Eagle Ford	1.38	-3.79	10.338
Shanklin #1-A	2137	Eagle Ford	0.47	-3.99	8.698
Shanklin #1-A	2138	Eagle Ford	0.81	-3.41	11.251
Shanklin #1-A	2138.1	Eagle Ford	1.14	-3.80	9.242

Shanklin #1-A	2139	Eagle Ford	0.89	-6.17	0.554
Shanklin #1-A	2140	Eagle Ford	0.81	-6.23	0.544
Shanklin #1-A	2141	Eagle Ford	0.71	-6.65	0.403
Shanklin #1-A	2142	Eagle Ford	1.00	-5.55	0.625
Shanklin #1-A	2143	Buda	1.43	-3.78	11.394
Shanklin #1-A	2144	Buda	1.70	-3.47	11.318
Shanklin #1-A	2145	Buda	1.59	-3.93	11.700
Shanklin #1-A	2146	Buda	1.73	-3.45	10.827
Shanklin #1-A	2147	Buda	1.61	-3.68	11.441
Shanklin #1-A	2148	Buda	1.46	-3.61	11.655
Shanklin #1-A	2149	Buda	1.60	-3.72	11.514
Shanklin #1-A	2150	Buda	1.80	-3.97	11.095
Shanklin #1-A	2151	Buda	1.70	-3.70	11.382
Shanklin #1-A	2152	Buda	1.83	-3.48	11.124
Shanklin #1-A	2153	Buda	1.48	-3.62	10.685
Shanklin #1-A	2154	Buda	1.64	-3.18	10.958
Shanklin #1-A	2155	Buda	1.75	-3.80	11.313
Shanklin #1-A	2156	Buda	1.70	-3.49	11.086
Shanklin #1-A	2157	Buda	1.69	-3.29	11.215
Shanklin #1-A	2158	Buda	1.46	-3.11	10.716
Shanklin #1-A	2159	Buda	1.79	-3.03	10.486
Shanklin #1-A	2160	Buda	1.71	-3.56	10.762
Shanklin #1-A	2161	Buda	1.85	-3.25	10.936
Shanklin #1-A	2162	Buda	1.85	-3.35	10.325
Shanklin #1-A	2163	Buda	1.94	-3.38	10.540
Shanklin #1-A	2164	Buda	1.82	-3.15	11.013
Shanklin #1-A	2165	Buda	2.11	-3.10	11.224
Shanklin #1-A	2166	Buda	1.83	-3.37	9.497

REFERENCES

Addy, S.K., and Buffler, R.T., 1984, Seismic stratigraphy of shelf and slope, northeastern Gulf of Mexico: American Association of Petroleum Geologists Bulletin, v. 68, p. 1782-1789.

Adkins, W.S., 1932, The Mesozoic systems in Texas, in Sellards, E.H., Adkins, W.S., and Plummer, F.B., eds.,The Geology of Texas, v. 1, University of Texas Bulletin No. 3232, p. 239-518.

Allan, J.R., and Wiggins, W.D., 1993, Dolomite reservoirs: Geochemical techniques for evaluating origin and distributions: AAPG Continuing Education Course Notes Series, no. 36, 129 p.

Ambrose, W.A., Hentz, T.F., Bonnaffe, F., Loucks, R.G., Brown Jr., F.B., Wang, F.P., and Potter, E.C., 2009, Sequence-stratigraphic controls on complex reservoir architecture of highstand fluvial-dominated deltaic and lowstand valley-fill deposits in the Upper Cretaceous (Cenomanian) Woodbine Group, East Texas field: Regional and local perspectives: American Association of Petroleum Geologists Bulletin, v. 93, p. 231-269.

Arthur, M.A., Dean, W.E., and Schlanger, S.O., 1985, Variations in the global carbon cycle during the Cretaceous related to climate, volcanism, and changes in atmospheric CO_2, in Sundquist, E.T., and Broecker, W.S., eds., The Carbon Cycle and Atmospheric CO_2: Natural Variations Archean to Present, Geophysical Monograph Series. AGU, Washington, D.C., p. 546-553.

Arthur, M.A., Dean, W.E., and Pratt, L.M., 1988, Geochemical and climatic effects of increased marine organic carbon burial at the Cenomanian/Turonian boundary: Nature, v. 335, p. 714-717.

Arthur, M.A. and Sageman, B.B., 1994, Marine Black Shales: Depositional Mechanisms and Environments of Ancient Deposits: Annual Reviews of Earth Planetary Science, v. 22, p. 499-551.

Bailey, T.L., Evans, F.G., and Adkins, W.S., 1945, Revision of Stratigraphy of Part of Cretaceous in Tyler Basin, Northeast Texas: American Association of Petroleum Geologists Bulletin, v. 29, no. 2, p. 170-186.

Barker, C., 1979, Organic Geochemistry in petroleum exploration: American Association of Petroleum Geologists Course Notes Series No. 10, 159 p.

Beall, A.O., 1964, Stratigraphy of the Taylor Formation (Upper Cretaceous), east-central Texas: Baylor Geological Studies Bulletin, v. 54, p. 289-308.

Bertrand, S., Charlet, F., Charlier, B., Renson, V., Fagel, N., Climate variability of southern Chile since the Last Glacial Maximum: a continuous sedimentological record from Lago Puyehue (40°S): Journal of Paleolimnology, v. 39, p. 179-195.

Blakey, R., 1994, Global Paleogeography, Northern Arizona University. <http://www2.nau.edu/rcb7/nam.html>, Accessed February 15, 2011.

Brown, C.W., and Pierce, R.L., 1962, Palynologic correlations in Cretaceous Eagle Ford Group, northeast Texas: American Association of Petroleum Geologists Bulletin, v. 46, p. 2133-2147.

Brughmans, N., 2003, Marine productivity and terrigenous matter supply: The variability of the Subtropical Convergence around Tasmania during the last 500 ka: Phd Dissertation, Christian-Albrechts-University, Kiel, Germany, 68 p.

Bureau of Economic Geology, The University of Texas at Austin, 1992, Geology of Texas Map.

Charvat, W.A., 1985, The nature and origin of the bentonite rich Eagle Ford rocks, central Texas: M.S. Thesis, Baylor University, Waco, Texas, 136 p.

Charvat, W.A., and Grayson, R.C., 1981, Anoxic sedimentation in the Eagle Ford Group (Upper Cretaceous) of central Texas: Gulf Coast Association of Geological Societies Transactions, v. 31, p. 256

Cherry, M., 2011, A case history of the Eagle Ford oil shale play, South Texas: AAPG Search and Discovery Article #90122, <http://www.searchanddiscovery.com/abstracts/pdf/2011/hedberg-texas/abstracts/ndx_cherry.pdf>, accessed June 9, 2011.

Coleman, M.L., 1993, Microbial processes: Controls on the shape and composition of carbonate concretions: Marine Geology, v. 113, p.127-140.

Corbett, K., 2010, Eagleford Shale Exploration Models: Depositional Controls on Reservoir Properties: Search and Discovery Article #10242.

Cotera, A.S., Jr., 1956, Petrology of the Cretaceous Woodbine Sand in Northeast Texas: M.S. Thesis, The University of Texas, Austin, Texas.

Curtis, C.D., Petrowski, C., and Oertel, G., 1972, Stable carbon isotope ratios within carbonate concretions: a clue to place and time of formation: Nature, v. 235, p. 98-100.

Dawson, W.C., 1997, Limestone microfacies and sequence stratigraphy: Eagle Ford Group (Cenomanian-Turonian) north-central Texas outcrops: Gulf Coast Association of Geological Societies Transactions, v. 47, p. 99-105.

Dawson, W.C., 2000, Shale microfacies: Eagle Ford Group (Cenomanian-Turonian) north-central Texas outcrops and subsurface equivalents: Gulf Coast Association of Geological Societies Transactions, v. 50, p. 607-621.

Dawson, W.C., and Almon, W.R., 2010, Eagle Ford Shale Variability: Sedimentologic influences on source and reservoir character in an unconventional resource unit: Gulf Coast Association of Geological Societies Transactions, v. 60, p. 181-190.

Donovan, A.D., and Staerker, T.S., 2010, Sequence Stratigraphy of the Eagle Ford (Boquillas) Formation in the Subsurface of South Texas and Outcrops of West Texas: Gulf Coast Association of Geological Societies Transaction, v. 60, p. 861-899.

Doronzo, D.M., 2010, A fluid dynamic model of volcaniclastic turbidity currents based on the similarity with the lower part of dilute pyroclastic density currents; evaluation of the ash dispersal from ash turbidites: Journal of Volcanology and Geothermal Research, v. 191, p. 193-204.

Dow, W.G., 1977, Kerogen studies and geological interpretations: Journal of Geochemical Exploration, v. 7, p. 79-99.

Dravis, J.J., 1980, Sedimentology and diagenesis of the Upper Cretaceous Austin Chalk Formation, South Texas and northern Mexico: Phd Dissertation, Rice University, Houston, Texas, 532 p.

Dunham, R.J., 1962, Classification of carbonate rocks according to depositional texture, in Ham, W.E., ed., Classification of Carbonate Rocks: American Association of Petroleum Geologists Memoir, v. 1, p. 108-121.

Durham, L.S., 2010, Eagle Ford joins shale elite: AAPG Explorer, <http://www.aapg.org/explorer/2010/01jan/eagleford0110.cfm>, accessed June 9, 2011.

Eaton, R.W., 1956, Resume of subsurface geology of Northeast Texas with emphasis on salt structures: Gulf Coast Association of Geological Societies Transactions, p. 79-84.

EOG Resources, 2011, EOG Resources Reports First Quarter 2011 Results, <http://investor.shareholder.com/eogresources/releasedetail.cfm?sh_print=yes&ReleaseID=575030>, accessed June 10, 2011.

Flügel, E., 2009, Microfacies of Carbonate Rocks: New York, Springer, 921 p.

Galloway, W.E., 2008, Depositional Evolution of the Gulf of Mexico Sedimentary Basin, in Miall, A.D., eds., The Sedimentary Basins of the United States and Canada: New York, Elsevier, 610 p.

Gary, M., McAfee Jr., R., Wolf, C.L., eds., Glossary of Geology: American Geological Institute, Washington, D.C., 805 p.

Grabowski, G.J., 1984, Generation and migration of hydrocarbons in Upper Cretaceous Austin Chalk, south-central Texas, in Palacas, J.G., ed., Petroleum geochemistry and source rock potential of carbonate rocks: AAPG Studies in Geology 18, p. 97-115.

Handford, C.R., 1986, Facies and bedding sequences in shelf-storm-deposited carbonates — Fayetteville Shale and Pitkin Limestone (Mississippian), Arkansas: Journal of Sedimentary Petrology, v. 56, no. 1, p. 123-137.

Hentz, T.F., and Ruppel, S.C., 2010, Regional lithostratigraphy of the Eagle Ford Shale: Maverick Basin to East Texas Basin: Gulf Coast Association of Geological Societies Transactions, v. 60, p. 325-337.

Hill, R.T., 1887a, The topography and geology of the Cross Timbers and surrounding regions in northern Texas: American Journal of Science, 3rd series, v. 33, p. 291-303.

Hill, R.T., 1887b, The Texas section of the American Cretaceous: American Journal of Science, 3rd series, v. 34, p. 287-309.

Hill, R.T., 1901, Geography and geology of the Black and Grand Prairies, Texas: USGS 21st Annual Report, pt. 7, 666 p.

Hudson, J.D., 1977, Stable isotopes and limestone lithification: Journal of the Geological Society, v. 133, p. 637-660.

Hughes, E.N., 2011, Chemostratigraphy and paleoenvironment of the Smithwick Formation, Fort Worth Basin, San Saba County, Texas: M.S. Thesis, The University of Texas, Arlington, Texas.

Irwin, H., Curtis, C., and Coleman, M., 1977, Isotopic evidence for source of diagenetic carbonates formed during the burial of organic-rich sediments: Nature, v. 269, p. 209-213.

Jackson, E.D., and Schlanger, S.O., 1976, Regional Synthesis, Line Islands Chain, Tuamotu Island Chain, and Manihiki Plateau, Central Pacific Ocean: Initial Reports of the Deep Sea Drilling Project 33, p. 915-927.

Jenkyns, H.C., 1980, Cretaceous anoxic events: from continents to oceans: Journal of the Geological Society, London, v. 37, p. 171-188.

Jenkyns, H.C., 2010, Geochemistry of oceanic anoxic events: Geochemistry Geophysics Geosystems, v. 11, no. 3, 30 p.

Jiang, M., 1989, Biostratigraphy and geochronology of the Eagle Ford Shale, Austin Chalk, and lower Taylor Marl in Texas based on calcareous nannofossils: Phd Dissertation, Texas A&M University, College Station, Texas, 524 p.

Kreisa, R.D., 1981, Storm-generated sedimentary structures in subtidal marine facies with examples from the middle and upper Ordovician of Southwest Virginia: Journal of Sedimentary Petrology, v. 51, p. 823-848.

Kreisa, R.D., and Bambach, R.K., 1982, The role of storm processes in generating shell beds in Paleozoic shelf environments, in Einsele, G., and Seilacher, A., eds., Cyclic and Event Stratification: New York, Springer-Verlag, 536 p.

Kuroda, J., Ogawa, N.O., Tanimizu, M., Coffin, M.F., Tokuyama, H., Kitazato, H., and Ohkouchi, N., 2007, Contemporaneous massive subaerial volcanism and late cretaceous Oceanic Anoxic Event 2: Earth and Planetary Science Letters 256, p. 211-223.

Lash, G.G., and Blood, D., 2004, Geochemical and textural evidence for early (shallow) diagenetic growth of stratigraphically confined carbonate concretions, Upper Devonian Rhinestreet black shale, western New York: Chemical Geology, v. 206, p. 407-424.

Liro, L.M., Dawson. W.C., Katz, B.J., and Robison, V.D., 1994, Sequence Stratigraphic Elements and Geochemical Variability within a "Condensed Section": Eagle Ford Group, East-Central Texas: Gulf Coast Association of Geological Societies Transactions, v. 44, p. 393-402.

Lock, B.E., Fleur, S.B., and Glaser, R.A., 2007, The Cenomanian Sequence Stratigraphy of Central to West Texas: AAPG Search and Discover Article #90069.

Loucks, R.G., and Ruppel, S.C., 2007, Mississippian Barnett Shale: Lithofacies and depositional setting of a deep-water shale-gas succession in the Fort Worth Basin, Texas: American Association of Petroleum Geologists Bulletin, v. 91, no. 4, p. 579-601.

Loutit, T.S., Hardenbol, J., and Vail, P.R., 1988, Condensed sections: the key to age determination and integrated approach: Society of Economic Paleontologists and Mineralogists Special Publication 42, p. 393-402.

Ludvigson, G.A., Witzke, B.J., González, L.A., Hammond, R.H., and Plocher, O.W., 1994, Sedimentology and carbonate geochemistry of concretions from the Greenhorn marine cycle (Cenomanian-Turonian), eastern margin of the Western Interior Seaway, in Shurr, G.W., Ludvigson, G.A., and Hammond, R.H., eds., Perspectives on the Eastern Margin of the Cretaceous Western Interior Basin: Boulder, Colorado, Geological Society of America Special Paper 287. p. 145-173.

Manville, V., and Wilson, C.J.N., 2004, Vertical density currents: a review of their potential role in the deposition and interpretation of deep-sea ash layers: Journal of the Geological Society, v. 161, no. 6, p. 947-958.

Montgomery, S.L., ed., 1990, Horizontal drilling in the Austin Chalk; Part 1, Geology, drilling history and field rules: Petroleum Frontiers, v. 7, no. 3, 44 p.

Montgomery, S.L. 1991, Horizontal drilling in the Austin Chalk; Part 2, Patterns of production: Petroleum Frontiers, v. 7, no. 4, 58 p.

Muehlberger, W.R., and Kurie, A.E., 1956, Fracture study of central Travis county, Texas, a preliminary statement: Gulf Coast Association of Geological Societies Transactions, v. 6, p. 43-49.

Mulder, T., and Alexander, J., 2001, The physical character of subaqueous sedimentary density flows and their deposits: Sedimentology, v. 48, p. 269-299.

Murray, G.E., 1961, Geology of the Atlantic and Gulf Coast Province of North America: New York, Harper Brothers, 692 p.

Narayana, A.C., Naidu, P.D., Shinu, N., Nagabhushanam, P., Sukhija, B.S., 2009, Carbonate and organic carbon content changes over the last 20 ka in the Southeastern Arabian Sea: Paleoceanographic implications: Quaternary International, v. 206, p. 72-77.

Nichols, P.H., 1964, The remaining frontiers for exploration in Northeast Texas: Gulf Coast Association of Geological Societies Transactions, v. 14, p. 7-22.

Oliver, W.B., 1971, Depositional systems in the Woodbine Formation (Upper Cretaceous), northeast Texas: University of Texas at Austin, Bureau of Economic Geology Report of Investigations No. 73, 28 p.

Pessagno, E.A., 1969, Upper Cretaceous stratigraphy of the western Gulf Coast area of Mexico, Texas, and Arkansas: Geological Society of America Memoir 111, 139 p.

Phelps, R.M., 2011, Middle-Hauterivian to Lower-Campanian Sequence Stratigraphy and Stable Isotope Geochemistry of the Comanche Platform, South Texas: Phd Dissertation, The University of Texas, Austin, Texas, 240 p.

Pioneer Natural Resources, 2011, Eagle Ford Shale (South Texas), <http://www.pioneernrc.com/operations/eagle_ford.htm>, accessed June 10, 2011.

Potter, P.E., Maynard, J.B., and Depetris, P.J., 2005, Mud & Mudstones: Springer-Verlag, New York, 297 p.

Prather, J.K., 1902, A preliminary report on the Austin chalk underlying Waco, Texas, and the adjoining territory: Transactions and Proceedings of the Texas Academy of Science, p. 115-122.

Railroad Commission of Texas, 2011, Eagle Ford Information, <http://www.rrc.state.tx.us/eagleford/index.php#general>, accessed June 10, 2011.

Robinson, C.R., 1997, Hydrocarbon source rock variability within the Austin Chalk and Eagle Ford Shale (Upper Cretaceous), East Texas, U.S.A.: International Journal of Coal Geology, v. 34, p. 287-305.

Reaser, D.F., 1961, Balcones Fault System: its northeast extent: Bulletin of the American Association of Petroleum Geologists, v. 45, p. 1759-1762.

Rose, P.R., 1972, Edwards Group, surface and subsurface, Central Texas: University of Texas at Austin, Bureau of Economic Geology Report of Investigations No. 74, 198 p.

Salvador, A., 1991, Origin and development of the Gulf of Mexico Basin, in Salvador, A., ed., The Gulf of Mexico Basin: Boulder, Colorado, Geological Society of America, The Geology of North America, v. J., p. 389-444.

Salvador, A. and Muñeton, J.M. Q., 1989, Stratigraphic Correlation Chart Gulf of Mexico Basin, in Salvador, A., ed., The Gulf of Mexico Basin: Boulder Colorado, Geological Society of America, The Geology of North America, v. J., plate 5.

Sarg, J.F., 1988, Carbonate sequence stratigraphy: Special Publication- Society of Economic Paleontologists and Mineralogists, v. 42, p. 155-181.

Schieber, J., 1999, Distribution and deposition of mudstone facies in the Upper Devonian Sonyea Group of New York: Journal of Sedimentary Research, v. 69, p. 909-925.

Schlanger, S.O., and Jenkyns, H.C., 1976, Cretaceous oceanic anoxic events: causes and consequences: Geologie en Mijnbouw, v. 55, p. 179-184.

Schlanger, S.O., Arthur, M.A., Jenkyns, H.C., and Scholle, P.A., 1987, in Brooks, J., and Fleet, A.J., eds., Marine Petroleum Source Rocks: Geological Society Special Publication No. 26, p. 371-399.

Seewald, K.O., 1958, The Austin Chalk: Guide to the Mid-Cretaceous Geology of Central Texas, Baylor Geologic Society, p. 75-78.

Sellards, E.H., Adkins, W.S., and Plummer, F.B., 1932, The Geology of Texas, Volume I, Stratigraphy: University of Texas Bulletin 3232, 1007 p.

Sepkoski, J.J., Jr., and Bambach, R.K., 1979, The temporal restriction of flat-pebble conglomerates: an example of co-evolution of organisms and sediments: Geological Society of America Abstracts with Programs, v. 11, p. 256.

Siegel, D.I., Chamberlain, S.C., and Dossert, W.P., 1987, The isotopic and chemical evolution of mineralization in septarian concretions: Evidence for episodic paleohydrogeologic methanogenesis: Geological Society of America Bulletin, v. 99, p. 385-394.

Siemers, C.T., 1978, Submarine Fan Deposition of the Woodbine-Eagle Ford Interval (Upper Cretaceous), Tyler County, Texas: Gulf Coast Association of Geological Societies Transactions, v. 28, p. 493-533.

Silver, B.A., 1963, The Bluebonnet Member, Lake Waco Formation (Upper Cretaceous), Central Texas- a lagoonal deposit: Baylor Geological Studies Bulletin, v. 4, 46 p.

Sinton, C.W., and Duncan, R.A., 1997, Potential links between ocean plateau volcanism and global anoxia at the Cenomanian-Turonian boundary: Economic Geology, v. 92, p. 836-842.

Snyder, R.H., and Craft, M., 1977, Evaluation of Austin and Buda Formations from core and fracture analysis: Gulf Coast Association of Geological Societies Transactions, v. 37, p. 376-385.

Sohl, N.F., Martinez, R.E., Salmeron-Urena, P., and Soto-Jaramillo, F., 1991, Upper Cretaceous, in Salavador, A., ed., The Gulf of Mexico Basin: Boulder, Colorado, Geological Society of America, The Geology of North America, v. J., p. 205-244.

Surles, M.A., Jr., 1987, Stratigraphy of the Eagle Ford Group (Upper Cretaceous) and its source-rock potential in the East Texas Basin: Baylor Geological Studies Bulletin, v. 45, 57 p.

Treadgold, G., Campbell, B., McLain, B., Sinclair, S., and Nicklin, D., 2011, Eagle Ford shale prospecting with 3D seismic data within a tectonic and depositional system framework: The Leading Edge, v. 30, no. 1, p. 48-53.

Tsikos, H., Jenkyns, H.C., Walsworth-Bell, B., Petrizzo, M.R., Forster, A., Kolonic, S., Erba, E., Premoli Silva, I., Baas, M., Wagner, T., and Sinninghe Damsté, J.S., 2004, Carbon-isotope stratigraphy recorded by the Cenomanian-Turonian Oceanic Anoxic Event: correlation and implications based on three key localities: Journal of the Geological Society, London, v. 161, p. 711-719.

Tyler, N., and Ambrose, W.A., 1986, Depositional Systems and Oil and Gas Plays in the Cretaceous Olmos Formation, South Texas: Bureau of Economic Geology, University of Texas at Austin, Report of Investigation No. 152, 41 p.

Waters, J.A., McFarland, P.W., and Lea, J.W., 1955, Geologic framework of gulf coastal plain of Texas: Bulletin of the American Association of Petroleum Geologists, v. 39, no. 9, p. 1821-1850.

Weeks, L.G., 1953, Environment and mode of origin and facies relationships of carbonate concretions in shales: Journal of Sedimentary Petrology, v. 23, no. 3, p. 162-173.

Wignall, P.B., 1994, Black Shales: Geology and Geophysics Monographs, 30. Oxford, Oxford University Press, 130 p.

Wingall, P.B., and Newton, R., 1998, Pyrite framboid diameter as a measure of oxygen deficiency in ancient mudrocks: American Journal of Science, v. 298, p. 537-552.

Winter, J.A., 1961, Stratigraphy of the lower Cretaceous (subsurface) of South Texas: Gulf Coast Association of Geological Societies, v. 11, p. 15-24.

Wu, X., and Galloway, W.E., 2002, Upper Miocene depositional history of the central Gulf of Mexico basin: Gulf Coast Association of Geological Societies Transactions, v. 50, p. 1019-1030.

Zink, E.R., 1957, Resume of the Lower Cretaceous of South Texas: Gulf Coast Association of Geological Societies Transactions, v. 7, p. 13-22.

Vita

Ryan Lee Harbor was born in West Columbia, South Carolina. After completing his work at Lexington High School, Lexington, South Carolina in 2002, he entered the University of South Carolina in Columbia, South Carolina. From 2003-2005, Ryan served a mission for the Church of Jesus Christ of Latter-Day Saints in New Zealand. Upon his return, Ryan transferred to Brigham Young University in Provo, Utah. In 2009, he received the degree of Bachelor of Science in geology with a minor in business management. In August 2009, Ryan entered the Graduate School at the University of Texas at Austin pursuing a master's degree in geology.

Permanent email: ryanharbor@yahoo.com

This thesis was typed by the author.